Experimental study of third (HFC) and fourth generation (HFO) refrigerants during flow boiling in singularities

Miguel David Padilla Gomez

To cite this version:

Miguel David Padilla Gomez. Experimental study of third (HFC) and fourth generation (HFO) refrigerants during flow boiling in singularities. Other. INSA de Lyon, 2011. English. NNT : 2011ISAL0121 . tel-00715788

HAL Id: tel-00715788
https://theses.hal.science/tel-00715788

Submitted on 9 Jul 2012

N° d'ordre : 2011ISAL0121 Année 2011

THÈSE

Experimental study of third (HFC) and fourth generation (HFO) refrigerants during flow boiling in singularities

présentée devant

L'INSTITUT NATIONAL DE SCIENCES APPLIQUÈES DE LYON

pour obtenir le grade de

Docteur

École Doctorale MEGA

(Mécanique, Énergétique, Génie Civil, Acoustique)

Spécialité : THERMIQUE ET ÉNERGÉTIQUE

par

Miguel David PADILLA GOMEZ

Soutenue le 18 Novembre 2011 devant la commission d'examen :

BONJOUR Jocelyn	Professeur (INSA de Lyon)	-	*Directeur de Thèse*
HABERSCHILL Philippe	Maître de Conférences HDR (INSA de Lyon)	-	*Invité*
INFANTE FERREIRA Carlos	Associate Professor (Delft University of Technology)	-	*Rapporteur*
MARTY Philippe	Professeur (Université de Grenoble)	-	*Rapporteur*
MARVILLET Christophe	Professeur (CNAM Paris)	-	*Examinateur*
REVELLIN Rémi	Maître de Conférences (INSA de Lyon)	-	*Co-directeur de Thèse*

Thèse préparée au Centre de Thermique de Lyon - CETHIL UMR 5008
Université de Lyon

Acknowledgments

This study has been carried out at the Centre de Thermique de Lyon (CETHIL UMR-5008), National Institute of Applied Sciences (INSA de Lyon), under the direction of Prof. Jocelyn Bonjour and Dr. Rémi Revellin. This PhD Thesis has been supported financially by the scholarship-salary program of the Council of Development Scientific and Humanistic of the Central University of Venezuela (CDCH-UCV), which are gratefully acknowledged.

I would like to thank Prof. Jocelyn Bonjour and Dr. Rémi Revellin for their advices and for giving me the opportunity and motivation to undertake this work. They were all the time available for fruitful research discussions and their guidance and encouragement during this period were a beneficial contribution to this study. Finally, I appreciate their total confidence and the responsibility they granted me throughout this period.

I thank Prof. Carlos Infante Ferreira of Delft University of Technology, Prof. Philippe Marty of Grenoble University and Prof. Christophe Marvillet of CNAM-Paris for being the examiners of this thesis.

Special thanks to my colleagues of the CETHIL for their cooperation and friendship.

I also acknowledge Prof. Philippe Haberschill, Ing. Jean-Dominique Chantelot and our technicians Joël, Nicolas, Jean, Antoine and Bernard who have skillfully participated to the construction of the experimental facility.

Last, but not least, many thanks to my family and my lovely wife Carmen Rosa for their support and encouragement during this work.

Experimental study of third (HFC) and fourth generation (HFO) refrigerants during flow boiling in singularities

Abstract:

The refrigerant charge reduction HVAC & R systems is an important issue because it falls within environmental policies regarding refrigerants contributions to the greenhouse effect. A way to move toward charge reduction is to increase the compactness of heat exchangers, which means more complex designs of the evaporators. Nevertheless, while a large amount of studies have been published on the thermal and hydraulic analysis of flow boiling of refrigerants in horizontal tubes, very little attention has been given to flow boiling in geometries different from straight tubes. This PhD thesis aims at studying the flow boiling characteristics of third generation (HFC) and fourth generation fluids such as HFO-1234yf in geometries which modify the fluid dynamics and two-phase flow with respect to horizontal straight tubes. To achieve this goal, an experimental test facility was specifically designed and built to conduct refrigerant evaporation experiments. This test facility allowed to perform flow regime visualizations and pressure drop measurements in singularities (such as sudden contractions and return bends).

First, two-phase flow regimes visualizations have been carried out using HFO-1234yf, R-134a and R-410A either in straight tubes or in singularities. A qualitative analysis of the flow behavior and also several comparisons to flow pattern prediction methods from the literature were conducted.

The second objective of this work was to characterize the flow disturbances caused by singularities such as sudden contractions and return bends, and to study their effects on the hydrodynamic performance (e.g. pressure drop) of refrigerants. An experimental study has been carried out to determine the perturbation lengths up- and downstream of the singularities. For return bends, both for horizontal and vertical cases, it is noted that there is no significant difference in the return bend pressure drop above $20D$ downstream and $10D$ upstream of the return bend. For the sudden contraction, the results obtained showed that there is no significant difference for the sudden contraction pressure drop measured above $70D_2$ downstream and above $28D_1$ upstream of it.

Lastly, pressure drop databases for third and fourth generation refrigerants are presented. Experimental values of pressure drops in straight tube were compared against 10 methods found in the literature, the measured return bend pressure drop values were compared against 4 methods and for the sudden contraction pressure drop database has been compared to 6 prediction methods from the literature. These databases have been used to develop new two-phase pressure drop prediction methods in singularities such as return bends and sudden contractions.

Keywords: Refrigerant, return bend, straight tube, sudden contraction, experimentation, flow pattern, two-phase flow, visualization, pressure drop

Etude expérimentale des fluides frigorigènes de troisième (HFC) et quatrième (HFO) génération lors de l'ébullition convective dans des singularités

Résumé:

La réduction de charge de fluides frigorigènes dans les systèmes de production de froid est un enjeu important s'inscrivant dans les politiques environnementales sur la contribution de ces fluides à l'effet de serre. Une des voies menant à la réduction de charge est l'augmentation de la compacité des échangeurs de chaleur, conduisant inévitablement à la conception d'évaporateurs plus complexes. Néanmoins, si de nombreuses études ont été publiées sur l'analyse thermo-hydraulique de l'ébullition convective de frigorigènes dans les tubes horizontaux, très peu ont été menées sur des écoulements diphasiques dans des géométries non conventionnelles.

Cette thèse vise à étudier les caractéristiques des écoulements diphasiques avec changement de phase des frigorigènes de troisième (HFC) et de quatrième génération tels que le HFO-1234yf dans des singularités (coudes de retour, contractions). Ainsi, un banc d'essais expérimental a été spécifiquement conçu et construit pour mener des expériences sur l'ébullition convective. Ce banc d'essais a permis de visualiser les régimes d'écoulement et de mesurer les chutes de pression dans les singularités.

Des visualisations de régimes d'écoulement ont été réalisées pour les frigorigènes HFO-1234yf, R-134a et R-410A dans des tubes droits et dans des singularités. Les résultats ont été confrontés avec diverses méthodes de prédiction de la littérature.

Les perturbations sur l'écoulement causées par ces singularités et leurs effets sur le comportement hydrodynamique des fluides frigorigènes ont également été étudiées. Une série d'expériences a été menée pour déterminer la longueur de perturbation en amont et en aval des singularités. Au-delà de 20 D en aval et 10 D en amont, le gradient de pression dans une section droite n'est pas affecté par la présence d'un coude de retour. Pour les contractions, les résultats obtenus ont montré qu'il n'y avait pas de différence significative pour la chute de pression au-delà de 70 D_2 en aval et 28 D_1 en amont.

Finalement, les valeurs expérimentales des chutes de pression ont été confrontées à différentes corrélations de la littérature. Des nouvelles méthodes de prédiction de la chute de pression pour des écoulements diphasiques dans des singularités telles que des coudes de retour et des réductions de section ont été proposées.

Mots clés: Fluide frigorigène, coude de retour, tube droit, contraction, expérimentation, régime d'écoulement, écoulement diphasique, visualisation, chute de pression

Contents

List of Figures

List of Tables

CHAPTER 1

Introduction

Contents

1.1 Background

Refrigeration is the process of extracting heat from one medium. This process usually involves the transportation of heat from one location to another by use of refrigerant in a closed cycle. Refrigeration is found everyday in several applications, which include air conditioning, commercial refrigeration, and industrial refrigeration. Commercial refrigeration was born in 1844, when Dr. John Gorrie designed the first commercial refrigerating machine based on reciprocating compressors in the United States. The hermetically sealed motor-compressor was first developed by General Electric Company for domestic refrigerators and sold in 1924.

In late 1920s and 1930s, several companies such as Carrier and Trane introduced the first centrifugal chillers and up to 1937, the capacity of centrifugal chillers had increased to 2500 kW. During the 1930s, one of the outstanding developments in refrigeration was the invention by [Midgley & Henne 1930] of the non-toxic, nonflammable, fluorinated hydrocarbon refrigerant family called Freon in 1930. The chlorofluorocarbons (CFCs), being the first generation of synthetic refrigerants, became widely adopted commercial products in reciprocating and centrifugal compressors.

The dominating market position of chlorofluorocarbons (CFCs) such as R-11 and R-12 and hydro-chlorofluorocarbons (HCFCs), also known as the second generation of synthetic refrigerants, was unchallenged until their implication in the depletion of the ozone layer, as first suggested by [Rowland & Molina 1974]. The authors described a chemical reaction as a photo-dissociation of man-made chlorofluorocarbons in the stratosphere which produces significant amounts of chlorine atoms and leads to the destruction of the stratospheric ozone, that could result in depleting the ozone layer for decades. The concerns raised by the data in their article grew over time, ultimately leading to the Montreal Protocol in 1987, which mandated the phase-out of CFCs and HCFCs. Several reviews of the Protocol followed that established a more stringent phase-out schedule. This led to an intense research to find alternative working fluids. The alternative refrigerants that emanated from these research efforts are predominantly hydrofluorocarbons (HFCs).

A third generation of synthetic refrigerants, the hydrofluorocarbons (HFCs), such as R-134a with zero Ozone Depletion Potential (ODP), have emerged as candidates for CFCs refrigerants substitution in refrigeration systems. But even with its ODP equal to zero, R-134a has a relatively high Global Warming Potential (GWP) (1300 times that of CO_2). A variety of studies have been carried out worldwide which have reported HFC refrigerants as alternative substitutes for CFC and HCFC. In these investigations are discussed several topics related to the influence of refrigerant substitutes on the energy efficiency and global warming, the use of hydrocarbon refrigerants (HC) as possible CFCs and HCFCs substitutes and on the refrigerant miscibility with the lubricant oils.

To expand the range of possible replacement fluids with desired properties, mixtures of refrigerants were investigated. A mixture can be formulated to obtain a saturation curve similar to the saturation curve of the original refrigerant, to suppress flammability or toxicity of one of the components that otherwise has excellent thermophysical properties.

The phase-out of CFCs, HCFCs and also some of HFCs such as R-134a due to their high GWP, provides the opportunity to a demand of new environmental friendly refrigerants with low GWP, without having an adverse effect on the refrigeration system performance. These new environmental friendly refrigerants, the HydroFluoroOlefins (HFOs), also called "fourth-generation" refrigerants with low GWP represent a significant reduction of the environmental footprint associated with air conditioning, heat pump and refrigeration systems. In 2007 were developed refrigerants that should meet the new regulations related to environmental impact, such as a GWP below 150. In this sense, the HFO-1234yf, with a GWP of 4, was the result of the industrial efforts to give a solution able to provide efficient and effective cooling with a near drop-in replacement for the current refrigerant R-134a. Among its interesting characteristics, HFO-1234yf has an atmospheric lifetime of only 11 days, compared to 13 years for R-134a.

Apart from environmental concerns raised by the depletion of the ozone layer and global warming, energy efficiency and refrigerant charge also came to the forefront. In response to that, the National Appliance Energy Conservation Act of 1987 promulgated a wide range of increases in minimum energy efficiency standards for heat pumps, refrigerators, freezers, and air-conditioners in the United States of America.

The impact of these regulatory decisions on the heating and cooling industry is very important, specifically regarding heat exchanger technology. Combined with space (volume) and materials (mass) saving considerations, as well as present-day global economics, there has been an expansion in efforts to produce more efficient heat exchange equipment for a given heat duty. Therefore the main thermal-hydraulic economic objectives are to reduce the size of a heat exchanger required for a specific heat duty, to upgrade the capacity of an available heat exchanger and its operation with smaller approach temperature differences, or to reduce the pumping power [Didion 1997].

Apart from the economic benefits of operating smaller and more efficient systems, material conservation would be implicit, thus benefiting society, due to the minimization of adverse environmental impacts [Ohadi & Buckley 2001]. However, size reduction should not be achieved at the expense of coefficient of performance (COP).

1.2 Motivation of the study

The refrigerant charge reduction in heating, ventilation, air conditioning and refrigeration systems (HVAC & R) is an important issue because it falls within environmental policies regarding refrigerants contributions to the greenhouse effect. A way to move toward charge reduction is to increase the compactness of heat exchangers, which means more complex designs of the evaporators. Besides, the development of new applications of refrigeration plants, such as geothermal heat pumps for which horizontal space may be limited, also requires some specific arrangements for the evaporators. Following this, prediction of two-phase pressure drop in direct-expansion evaporators, condensers and two-phase refrigerant transfer lines is important in order to design and optimize the refrigeration, air-conditioning and heat pump systems.

Nevertheless, while a large amount of studies have has been published on the thermal and hydraulic analysis of flow boiling of refrigerants in horizontal tubes (Fig. 1.1), very little attention has been given to flow boiling in geometries different from straight tubes. The main aim of this PhD work is to study the flow boiling characteristics of HFC refrigerants and new-generation fluids such as HFO-1234yf in geometries which will modify the fluid dynamics and two-phase flow with respect to horizontal straight tubes.

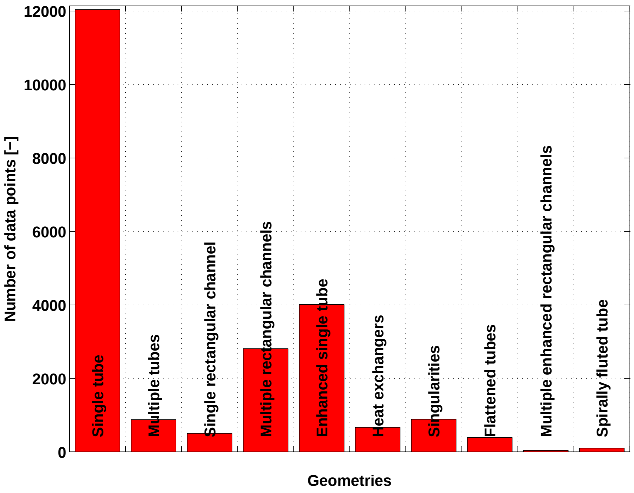

Figure 1.1: Number of experimental data points (22363 data points in total) for each geometry published in 122 articles since 1980 for flow boiling. [Charnay *et al.* 2011]

Most of the published research works on in-tube evaporation deal with refrigeration mass fluxes (also called mass velocity) in the range from 150 to 700 kg·m^{-2}·s^{-1}. Modern evaporators such as those used in typical heat pump water heater applications, however, usually operate in the mass flux range of 500 to 1000 kg·m^{-2}·s^{-1}. There is therefore a need to perform in-tube evaporation in a much wider mass flux range, viz. 150 - 1000 kg·m^{-2}·s^{-1}.

The majority of in-tube evaporation works use unrealistic evaporator tube dimensions, e.g. too short evaporator tubing (so that entrance effects play a prominent role on the flow recovery length). Researchers may also use too small diameter tubing in their research work (e.g 3.00 mm), while most conventional tubes used for evaporation in the HVAC & R industry, have a range from 9.52 mm (3/8") to 12.70 mm (1/2") outside diameters. Because this study is motivated by "real world" applications, use is made of 9.52 mm and 12.70 mm outside diameter refrigerant tubing. The fact that the evaporators are made of several sub-sections, implies the use of return bends connectors.

Most of the existing works carried out to develop predictive models for in-tube evaporation, are of an empirical nature, although several researchers have recently advanced in the development of semi-empirical based models. But, reliable predictions of two-phase pressure drop characteristics are still mainly experimental because of the complexity of the fluid dynamic involved.

Frictional pressure drop correlations, in several cases, still rely on two-phase multipliers to predict the effect of the vapor and liquid phases. The main problem is that two-phase multipliers artificially assume a homogeneous flow, which is only suitable for high mass velocities ([Thome 2004]). Distinct mathematical models for the pressure drop along straight tubes considering flow patterns and parameters such as void fraction that would be analogous to the models for return bends and sudden contractions have not been developed. Almost all empirical correlations that have been developed so far rely on the same form of the two-phase multipliers, with differing constant coefficients and exponents. This is probably because the empirical models are the easiest to implement and provide a reasonable accuracy within the range of database used in their implementation. In contrast, the analytical approach provides general models, since no empirical information is used, but their implementation is very complex and time consuming even just to make a single calculation. A good trade off between purely empirical and purely analytical seems to be the phenomenological approach (e.g [Moreno Quibén & Thome 2007] method). This later preserves the model of general applicability, as it is based on theory and, introducing some empiricism it overcomes complex calculations resulting in somewhat easy to use models.

The available correlations also satisfy only limited experimental data with a narrow range of applicability. There is no real unanimity for a unique correlation. In some cases, significant discrepancies are apparent when comparing experimental data to the correlations. This present work aims at consolidating various research efforts, and at generating an unambiguous, unified correlation for pressure drop in return bends on the one side and sudden contractions on the other side, using empirical and semi-empirical (analytic) means.

1.3 Objectives of the study

The experimental test facility used in this study was first developed by [Branescu 2000] and was specifically designed and built to conduct refrigerant evaporation experiments. This test facility was modified during the present PhD work in order to perform pressure drop measurements in singularities (such as sudden contractions and return bends).

The first objective of this experimental investigation is to visualize flow regimes using HFC and fourth-generation refrigerants either in straight tubes or in singularities and to compare them to flow pattern prediction methods from the literature.

The second objective is to characterize the flow disturbances caused by singularities such as sudden contractions and return bends, and to study their effects on the hydrodynamic performance (i.e. pressure drop) of refrigerants. The characterization of the perturbation lengths up- and downstream of the singularity to make a correct pressure drop measurement is necessary to be investigated.

The third objective is to develop a pressure drop database for third and fourth generation refrigerants which allows to develop reliable pressure drop predictive methods in singularities.

1.4 Layout of the thesis

The thesis is divided into eight chapters with several appendices. It is organized as follows:

- *Chapter 1* provides a background to the study, by motivating the study and stating the research objectives.

- In *Chapter 2*, the definition of the main parameters and basic equations used in two-phase flow and two-phase pressure drop analysis are presented.
- *Chapter 3* gives an overview of the state-of-the-art of two-phase pressure drop models and flow pattern maps for in-tube evaporation using straight tubes, return bends and sudden contractions. The experimental database collected from the literature is also presented.
- *Chapter 4* describes the experimental test facility as well as the test sections used for visualization and pressure drop measurements. The experimental methodology and data reduction procedure are also described.
- *Chapter 5* presents the experimental results of the two-phase pressure drop measurements and visualizations in straight tubes. Several comparisons to the existing most accurate pressure drop correlations for smooth straight tubes are carried out.
- *Chapter 6* presents original experimental two-phase flow regime visualizations and two-phase pressure drop data points in horizontal and vertical return bends for the fourth generation HFO-1234yf and for the well known R-134a and R-410A conventional refrigerants. In this chapter, the perturbation lengths encountered up- and downstream of the return bend are discussed. The new experimental database (1087 data points) measured for two-phase flow of HFO-1234yf, R-134a and R-410A refrigerants in horizontal and vertical return bends are presented and compared against 4 prediction methods from the literature. Based on the present visualizations and experimental measurements, a new correlation is proposed for predicting the pressure drop in return bends.
- *Chapter 7* gives qualitative two-phase flow visualizations of R-134a. In addition, the effect of perturbation lengths up- and downstream of the sudden contraction is also presented. 360 pressure drop data points measured for two-phase flow of HFO-1234yf, R-134a and R-410A refrigerants in horizontal sudden contractions are presented and compared against 6 prediction methods from the literature. Based on this database, a new method is proposed for predicting the pressure drop in sudden contractions.
- *Chapter 8* presents the general conclusions of this study and the perspectives.

CHAPTER 2

Fundamental definitions

Contents

This chapter presents the fundamentals two-phase fluid mechanics and provides information on the primary parameters used throughout this work and derives some simple relationships between them for the case of one-dimensional flow.

To distinguish between vapor and liquid the subscripts "l" for liquid and "v" for vapor will be used. Basic equations for two-phase flows are also introduced at the end of the chapter.

2.1 Two-phase flow

A phase, from Classical thermodynamics view, is a macroscopic state of matter which is homogeneous in chemical composition and physical structure; e.g. a gas, a liquid or solid of a pure component. Two-phase flow is the simplest case of multiphase flow in which two phases are present for a pure component.

In internal flow boiling processes, the vapor and liquid are in simultaneous motion inside the pipe. The resulting two-phase flow is generally more complicated physically than single-flow. In addition to the usual inertia, viscous, and pressure forces present in single-phase flow, two-phase flows are also affected by interfacial tension forces, the flow regime, the thermodynamic and transport properties of both the vapor and the liquid, the wetting characteristics of the surface-liquid pair, and other parameters.

Two-phase flow is encountered extensively in the air-conditioning, heating, and refrigeration industries. A combination of liquid and vapor refrigerant exists in coolers (e.g direct-expansion coolers), plate evaporators and condensers (e.g brazed plates), and tube-in-tube evaporators and condensers, as well as in air-cooled evaporators and condensers.

2.2 Flow boiling in Tubes

Boiling occurs when a liquid is in contact with a surface maintained at a temperature T_s sufficiently above the saturation temperature T_{sat} of the liquid. Boiling is classified as *pool boiling* or *flow boiling*, depending on the presence of bulk fluid motion. Boiling is called pool boiling in the absence of bulk fluid flow and flow boiling (or forced convection boiling) in the presence of it. Pool boiling involves a pool of seemingly motionless liquid, with vapor bubbles rising to the top as a result of buoyancy effects. In flow boiling, the fluid is forced to move by an external source such as a pump as it undergoes a phase-change process. The boiling in this case exhibits the combined effects of convection and pool boiling.

In *Internal flow boiling*, which is the case of study of the present investigation, both the liquid and the vapor are forced to flow together inside a duct.

2.3 Vapor quality

The vapor quality x is defined as the vapor mass flow rate $\dot{m}_{\mathrm{v}}$ ($\mathrm{kg{\cdot}s^{-1}}$) divided by the total mass flow rate $\dot{m}_{\mathrm{v}} + \dot{m}_{\mathrm{l}}$:

$$x = \frac{\dot{m}_{\mathrm{v}}}{\dot{m}_{\mathrm{v}} + \dot{m}_{\mathrm{l}}} \tag{2.1}$$

When phase change does not take place in the tube, one needs to measure the mass flow rate of each phase, and the quality is then determined for the entire tube. In case there is a phase change in the tube, e.g. if the tube is heated and boiling takes place, then the quality will increase downstream with the flow. Since often there is no thermal equilibrium between the phases, one cannot calculate the quality merely by knowing the inlet quality and the heat flux from the wall. Unfortunately, it is very difficult to measure or calculate with precision the quality of the liquid vapor mixture flowing in a tube where a change of phase takes place. However a fictitious quality, the so called thermodynamic equilibrium quality, can be calculated by assuming that both phases are saturated, e.g., that their temperatures are equal to the saturation temperature corresponding to their common pressure. The so-called thermodynamic equilibrium quality can be calculated as:

$$x = \frac{h_\mathrm{z} - h_\mathrm{l}}{h_\mathrm{lv}} \tag{2.2}$$

where h_l (J·kg^{-1}) is the enthalpy of the saturated liquid, h_lv is the latent heat of vaporization, and h_z is the enthalpy at a cross section z. This can be calculated from:

$$h_\mathrm{z} = h_\mathrm{in} + \frac{1}{\dot{m}} \int_\mathrm{in}^\mathrm{z} q(z)dz \tag{2.3}$$

where h_in is the enthalpy of the fluid at the inlet and $q(z)$ (W·m^{-1}) is the heat input per unit length of tube.

2.4 Void fraction

In two-phase flow, void fraction is one of the most important parameters to be determined. It defines the cross-sectional area occupied by each phase (Fig. 2.1) As it determines mean velocities of the liquid and the vapor, it represents a fundamental parameter in the calculation of pressure drop, flow pattern transitions and heat transfer coefficients.

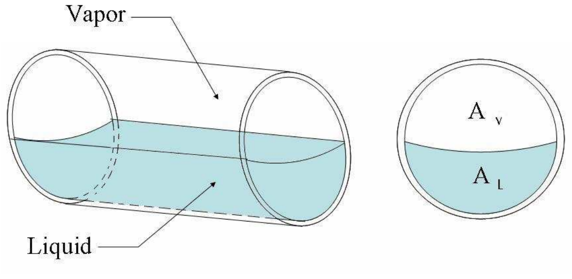

Figure 2.1: Void fraction representation.

The void fraction of the vapor is defined as:

$$\varepsilon = \frac{A_\mathrm{v}}{A_\mathrm{v} + A_\mathrm{l}} \tag{2.4}$$

where A_v is the sum of areas occupied by the vapor and A_l is the sum of areas occupied by the liquid. The total cross-sectional area of the tube is called A.

2.5 Velocities

There are a number of velocities which can be defined in a two-phase flow. In general, the two phases will not have the same velocity, and there will be a relative velocity between them, as discussed below.

2.5.1 Mass velocity

The **mass Velocity**, also known as mass flux, is defined to the mass flow rate divided by the total cross-sectional area:

$$G = \frac{\dot{m}}{A} \tag{2.5}$$

The principal unit of the mass velocity is $[\mathrm{kg{\cdot}m^{-2}{\cdot}s^{-1}}]$. Considering the continuity law, the mass velocity is also the expression of the mean flow velocity multiplied by the mean density.

2.5.2 Actual velocities

The **actual velocities** (or true mean velocities) of the phases u_v and u_l, are the mean velocities at which the phases actually travel. The cross-sectional velocities are determined by the volumetric flow rates $\dot{Q}_\mathrm{v}$ and $\dot{Q}_\mathrm{l}$ ($\mathrm{m^3 \cdot\ s^{-1}}$ and divided by the cross-sectional areas which are actually occupied by the phases as:

$$u_\mathrm{v} = \frac{\dot{Q}_\mathrm{v}}{A_\mathrm{v}} = \frac{\dot{Q}_\mathrm{v}}{\varepsilon A} \tag{2.6}$$

$$u_\mathrm{l} = \frac{\dot{Q}_\mathrm{l}}{A_\mathrm{l}} = \frac{\dot{Q}_\mathrm{l}}{(1-\varepsilon) A} \tag{2.7}$$

From the continuity law, it is possible to define both liquid and vapor actual velocities:

$$u_\mathrm{v} = \frac{x}{\varepsilon}\frac{\dot{m}}{\rho_\mathrm{v} A} = \frac{G}{\rho_\mathrm{v}}\frac{x}{\varepsilon} \tag{2.8}$$

$$u_\mathrm{l} = \frac{(1-x)}{(1-\varepsilon)}\frac{\dot{m}}{\rho_\mathrm{l} A} = \frac{G}{\rho_\mathrm{l}}\frac{(1-x)}{(1-\varepsilon)} \tag{2.9}$$

2.5.3 Superficial velocities

The **superficial velocities** (also called volumetric flux densities) J_v and J_l are the velocities of the phases as if they were each flowing alone in the tube, occupying the total cross-sectional area. The are defined as:

$$J_\mathrm{v} = \frac{\dot{Q}_\mathrm{v}}{A} = \varepsilon u_\mathrm{v} \tag{2.10}$$

$$J_\mathrm{l} = \frac{\dot{Q}_\mathrm{l}}{A} = (1-\varepsilon)\, u_\mathrm{l} \tag{2.11}$$

and the **total superficial velocity** is the sum of the vapor and liquid superficial velocities:

$$J = J_\mathrm{v} + J_\mathrm{l} \tag{2.12}$$

2.6 Basic equations of two-phase flow

Developments of the full governing equations for three-dimensional, time-varying two-phase flow can be found in [Ishii 1975], [Bouré 1978] and [Delhaye 1990]. The form of the governing equations can be simplified by invoking time and/or space averaging. The averaging processes make the equations more tractable but, at the same time, useful information about the flow is lost at each simplifying step. In the present context, for sake of simplicity, the flow is considered to be steady and one-dimensional in the sense that all dependent variables are idealized as being constant over any section of the tube, varying only in the axial direction.

To facilitate development of a one-dimensional analysis of multi-phase flow, we will consider the system shown in Fig. 2.2.

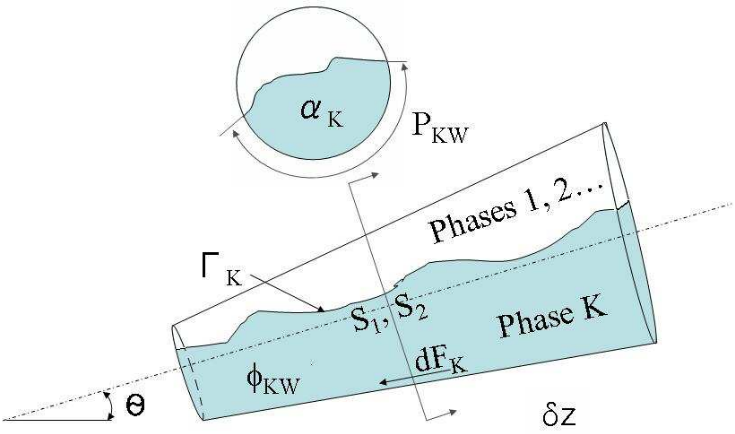

Figure 2.2: Idealized model for multiphase-flow in an inclined tube.

A stratified flow is chosen to allow the equations to be derived for the general case where each phase is in contact with the tube wall as well as having a common interface. It is further assumed that the pressure across any phase normal to the channel is uniform. Mean values of velocity and density of each phase are assumed to exist across any phase normal to the flow.

2.6.1 Conservation of mass

The equation expressing the conservation of mass in the absence of any removal or addition of fluid through the channel walls for phase k is:

$$\frac{\partial}{\partial t}(A\varepsilon_{\mathrm{k}}\rho_{\mathrm{k}}) + \frac{\partial}{\partial z}(A\varepsilon_{\mathrm{k}}\rho_{\mathrm{k}}u_{\mathrm{k}}) = \Gamma_{\mathrm{k}} \tag{2.13}$$

where ε_{k} is the void fraction of phase k, ρ_{k} is the density of phase k, u_{k} is the actual velocity of phase k and Γ_{k} is the mass transfer (mass flow rate $\dot{m}$ per unit length) to phase k from the various interphase mass transfer, where:

$$\sum_k \Gamma_{\mathrm{k}} = 0 \tag{2.14}$$

For the particular case of steady state two-phase vapor (v)/liquid (l) flow in a constant area tube this reduces to two expressions:

$$\frac{\partial}{\partial z}(A\varepsilon_{\mathrm{v}}\rho_{\mathrm{v}}u_{\mathrm{v}}) = \Gamma_{\mathrm{v}} \tag{2.15}$$

$$\frac{\partial}{\partial z}(A\varepsilon_{\mathrm{l}}\rho_{\mathrm{l}}u_{\mathrm{l}}) = \Gamma_{\mathrm{l}} \tag{2.16}$$

and

$$\Gamma_{\mathrm{v}} + \Gamma_{\mathrm{l}} = 0 \tag{2.17}$$

2.6.2 Conservation of momentum

The rate of creation of momentum of phase k plus the rate of inflow of momentum is balanced against the sum of the forces acting on that phase plus the momentum generation due to mass transfer, as follows:

$$M_1 = M_2 - M_3 - M_4 + M_5 + M_6 \tag{2.18}$$

where M_1

$$M_1 = \frac{\partial}{\partial t}(\dot{m}_{\mathrm{k}}\delta z) + \left(\dot{m}_{\mathrm{k}}u_{\mathrm{k}} + \delta z\frac{\partial}{\partial z}(\dot{m}_{\mathrm{k}}u_{\mathrm{k}})\right) - \dot{m}_{\mathrm{k}}u_{\mathrm{k}} \tag{2.19}$$

represents the rate of creation of momentum plus the rate of inflow of momentum within the control element. The term M_2,

$$M_2 = \left[A\varepsilon_{\mathrm{k}}p - \left(A\varepsilon_{\mathrm{k}}p\delta z\frac{\partial}{\partial z}(A\varepsilon_{\mathrm{kp}})\right) + \left\{p\left(-\delta z\frac{\partial}{\partial z}(A\varepsilon_{\mathrm{k}})\right)\right\}\right] \tag{2.20}$$

represents the pressure forces in the control element. The term M_3,

$$M_3 = A\varepsilon_{\mathrm{k}}\rho_{\mathrm{k}}\delta z g \sin\theta \tag{2.21}$$

represents the gravitational forces. The term M_4,

$$M_4 = \tau_{\mathrm{kw}}P_{\mathrm{kw}}\delta z \tag{2.22}$$

represents the wall shear force (dF_{k}), where τ_{kw} is the wall shear stress between the phase k and the channel wall and P_{kw} is the contact perimeter between the wall and phase k.

The term M_5,

$$M_5 = \sum_{1}^{n}\tau_{\mathrm{knz}}P_{\mathrm{kn}}\delta z \tag{2.23}$$

represents the sum of the interfacial shear forces (S_1, S_2, . . .), where where τ_{knz} is the z component of the interfacial shear stress between phase k and phase n and P_{kn} is the contact perimeter between phase k and phase n.

The term M_6 represents the rate of generation of momentum of phase k due to mass transfer assuming that the mass transferred across the interface is accelerated to the mean velocity of the receiving phase.

$$M_6 = u_{\mathrm{k}}\Gamma_{\mathrm{k}} \tag{2.24}$$

Rearranging terms, equation (2.18) can be written as:

$$\frac{\partial}{\partial t}(\dot{m}_{\mathrm{k}}\delta z) + \delta z\frac{\partial}{\partial z}(\dot{m}_{\mathrm{k}}u_{\mathrm{k}}) = -A\varepsilon_{\mathrm{k}}\frac{\partial p}{\partial z} - \tau_{\mathrm{kw}}P_{\mathrm{kw}}\delta z$$

$$+\sum_{1}^{n}\tau_{\mathrm{knz}}P_{\mathrm{kn}}\delta z - A\varepsilon_{\mathrm{k}}\rho_{\mathrm{k}}\delta z g \sin\theta + u_{\mathrm{k}}\Gamma_{\mathrm{k}} \tag{2.25}$$

Thus for a steady-state two-phase vapor (v) / liquid (l) flow in a constant area tube, for the vapor phase

$$\dot{m}_{\mathrm{v}} du_{\mathrm{v}} = -A_{\mathrm{v}} dp - \tau_{\mathrm{vw}} P_{\mathrm{vw}} dz - A_{\mathrm{v}} \rho_{\mathrm{v}} dz g \sin\theta + u_{\mathrm{v}} \Gamma_{\mathrm{v}} \tag{2.26}$$

and for the liquid phase

$$\dot{m}_{\mathrm{l}} du_{\mathrm{l}} = -A_{\mathrm{l}} dp - \tau_{\mathrm{lw}} P_{\mathrm{lw}} dz - A_{\mathrm{l}} \rho_{\mathrm{l}} dz g \sin\theta + u_{\mathrm{l}} \Gamma_{\mathrm{l}} \tag{2.27}$$

Adding equations (2.26) and (2.27) and using the conservation of momentum across the interface

$$\tau_{\mathrm{vl}} P_{\mathrm{vl}} dz + u_{\mathrm{v}} \Gamma_{\mathrm{v}} = \tau_{\mathrm{lv}} P_{\mathrm{lv}} dz + u_{\mathrm{l}} \Gamma_{\mathrm{l}} \tag{2.28}$$

The following equation is obtained, which represents the basic differential equation for this simplified approach

$$d\left(\dot{m}_{\mathrm{l}} u_{\mathrm{l}} + \dot{m}_{\mathrm{v}} u_{\mathrm{v}}\right) = A dp + \tau_{\mathrm{vw}} P_{\mathrm{vw}} dz - \tau_{\mathrm{lw}} P_{\mathrm{lw}} dz - g \sin\theta \left[A_{\mathrm{v}} \rho_{\mathrm{v}} + A_{\mathrm{l}} \rho_{\mathrm{l}}\right] \tag{2.29}$$

The net frictional force acting on each phase may be expressed in terms of the ones occupied by each phase:

$$(dF_{\mathrm{v}} + \mathrm{S}) = -\tau_{\mathrm{vw}} P_{\mathrm{vw}} dz - \tau_{\mathrm{vl}} P_{\mathrm{vl}} dz = -A_{\mathrm{v}} \left(\frac{dp}{dz}\right)_{F,\mathrm{v}} dz \tag{2.30}$$

$$(dF_{\mathrm{v}} - \mathrm{S}) = -\tau_{\mathrm{lw}} P_{\mathrm{lw}} dz + \tau_{\mathrm{vl}} P_{\mathrm{vl}} dz = -A_{\mathrm{l}} \left(\frac{dp}{dz}\right)_{F,\mathrm{l}} dz \tag{2.31}$$

Adding equations (2.30) and (2.31), the expression for the total net frictional force is obtained as:

$$(dF_{\mathrm{v}} + dF_{\mathrm{l}}) = -\tau_{\mathrm{vw}} P_{\mathrm{vw}} dz - \tau_{\mathrm{lw}} P_{\mathrm{lw}} dz = -A \left(\frac{dp}{dz}\right)_{F} dz \tag{2.32}$$

where the term $\left(\frac{dp}{dz}\right)_F$ represents the part of the overall pressure gradient required to overcome friction. Substitution of equation (2.32) into equation (2.29) and rearrangement yields:

$$\left(\frac{dp}{dz}\right) = \left(\frac{dp}{dz}\right)_F + \left(\frac{dp}{dz}\right)_a + \left(\frac{dp}{dz}\right)_z \tag{2.33}$$

where the term $\left(\frac{dp}{dz}\right)_a$ reflects the change in momentum of the flow and can be expressed, using relationships introduced in this chapter, as:

$$-\left(\frac{dp}{dz}\right)_a = \frac{1}{A}\frac{d}{dz}\left(\dot{m}_{\mathrm{v}} u_{\mathrm{v}} + \dot{m}_{\mathrm{l}} u_{\mathrm{l}}\right) = G^2 \frac{d}{dz}\left[\frac{x^2}{\varepsilon \rho_{\mathrm{v}}} + \frac{(1-x)^2}{(1-\varepsilon)\rho_{\mathrm{l}}}\right] \tag{2.34}$$

and the term $\left(\frac{dp}{dz}\right)_z$ reflects the change in static head and can be expressed as:

$$-\left(\frac{dp}{dz}\right)_z = g \sin\theta \left[\frac{A_{\mathrm{v}}}{A}\rho_{\mathrm{v}} + \frac{A_{\mathrm{l}}}{A}\rho_{\mathrm{l}}\right] = g \sin\theta \left[\varepsilon \rho_{\mathrm{v}} + (1-\varepsilon)\rho_{\mathrm{l}}\right] \tag{2.35}$$

The above derivation introduces the use of the momentum equation to relate the total pressure gradient in terms of its three separate components: friction, acceleration and static head. It should be explained at this point that the frictional component has been derived in terms of the total wall shear force $(dF_{\mathrm{v}} + dF_{\mathrm{l}})$.

2.6.3 Conservation of energy

The rate of increase of total energy for phase k (internal plus kinetic energy) within the control element plus the rate at which total energy is convected into the control element is balanced against the rate at which heat is added to phase k plus the rate at which work is done on phase k plus the rate at which energy is transferred across the interface to the control element. The equation expressing the differential energy balance is:

$$E_1 = E_2 + E_3 - E_4 + E_5 + E_6 \tag{2.36}$$

where E_1

$$\begin{aligned} E_1 = {} & \frac{\partial}{\partial t}\left[\varepsilon_\mathrm{k}\rho_\mathrm{k}\left(e_\mathrm{k} + \frac{u_\mathrm{k}^2}{2}\right)A\delta z\right] + \dot{m}_\mathrm{k}\left(e_\mathrm{k} + \frac{u_\mathrm{k}^2}{2}\right)\delta z \\ & - \left[\dot{m}_\mathrm{k}\left(e_\mathrm{k} + \frac{u_\mathrm{k}^2}{2}\right) - \delta z\frac{\partial}{\partial z}\dot{m}_\mathrm{k}\left(e_\mathrm{k} + \frac{u_\mathrm{k}^2}{2}\right)\right] \end{aligned} \tag{2.37}$$

represents the rate of increase of total energy plus the rate at which energy enters within the control element in the absence of the addition or subtraction of mass through the tube walls.

The term E_2,

$$E_2 = \phi_\mathrm{kw}P_\mathrm{kw}\delta z + \sum_1^n \phi_\mathrm{kn}P_\mathrm{kn}\delta z + \dot{\phi}_\mathrm{k}A\varepsilon_\mathrm{k}\delta z \tag{2.38}$$

represents the rate at which heat enters phase k within the control volume, namely: the heat flow via the channel wall over the perimeter P_kw, the heat flow via the various interfaces with the other n phases and the internal heat generation for phase k within the control element itself.

The terms E_3, E_4 and E_5 represent the work done by pressure forces, the work done by body forces and the work done by shear and pressure forces at the interface with other phases respectively.

$$E_3 = \left[\frac{\dot{m}_\mathrm{k}p}{\rho_\mathrm{k}} - \left\{\frac{\dot{m}_\mathrm{k}p}{\rho_\mathrm{k}} + \delta z\frac{\partial}{\partial z}\left(\frac{\dot{m}_\mathrm{k}p}{\rho_\mathrm{k}}\right)\right\}\right] \tag{2.39}$$

$$E_4 = \dot{m}_\mathrm{k}g\sin\theta\delta z - pA\delta z\frac{\partial \varepsilon_\mathrm{k}}{\partial t} \tag{2.40}$$

$$E_5 = \Gamma_\mathrm{k}\frac{\delta z p}{\rho_\mathrm{k}} + u_\mathrm{k}\sum_1^n \tau_\mathrm{kn}P_\mathrm{kn}\delta z \tag{2.41}$$

Finally, the term E_6 represents the rate at which energy is added to phase k by virtue of mass transfer across the interface.

$$E_6 = \Gamma_\mathrm{k}\delta z\left(e_\mathrm{k} + \frac{u_\mathrm{k}^2}{2}\right) \tag{2.42}$$

Rearranging terms, equation (2.36) may be written as

$$\frac{\partial}{\partial t}A\varepsilon_\mathrm{k}\rho_\mathrm{k}\left(e_\mathrm{k} + \frac{u_\mathrm{k}^2}{2}\right) + \frac{\partial}{\partial z}\dot{m}_\mathrm{k}\left(h_\mathrm{k} + \frac{u_\mathrm{k}^2}{2}\right) = -\dot{m}_\mathrm{k}g\sin\theta + \phi_\mathrm{kw}P_\mathrm{kw}$$

$$+\sum_{1}^{n} \phi_{\mathrm{kn}} P_{\mathrm{kn}} + \dot{\phi}_{\mathrm{k}} A \varepsilon_{\mathrm{k}} - pA\frac{\partial \varepsilon_{\mathrm{k}}}{\partial t} + \Gamma_{\mathrm{k}}\left(h_{\mathrm{k}} + \frac{u_{\mathrm{k}}^2}{2}\right) + u_{\mathrm{k}}\sum_{1}^{n} \tau_{\mathrm{kn}} P_{\mathrm{kn}} \tag{2.43}$$

where h_{k} represents the enthalpy of phase k per unit of mass

$$h_{\mathrm{k}} = e_{\mathrm{k}} + \frac{p}{\rho_{\mathrm{k}}} \tag{2.44}$$

For the particular case of steady-state, two-phase vapor(v)/liquid(l) flow in a constant area tube with no internal heat generation (ϕ_{k}), equation (2.43) reduces to the following expressions for the vapor and liquid phases:

$$d\left[\dot{m}_{\mathrm{v}}\left(h_{\mathrm{v}} + \frac{u_{\mathrm{v}}^2}{2}\right)\right] + \dot{m}_{\mathrm{v}} g \sin\theta \delta z =$$

$$\phi_{\mathrm{wv}} P_{\mathrm{wv}} \delta z + \phi_{\mathrm{vl}} P_{\mathrm{vl}} \delta z + u_{\mathrm{v}} \tau_{\mathrm{vl}} P_{\mathrm{vl}} \delta z + \Gamma_{\mathrm{v}} \delta z\left(h_{\mathrm{v}} + \frac{u_{\mathrm{v}}^2}{2}\right) \tag{2.45}$$

$$d\left[\dot{m}_{\mathrm{l}}\left(h_{\mathrm{l}} + \frac{u_{\mathrm{l}}^2}{2}\right)\right] + \dot{m}_{\mathrm{l}} g \sin\theta \delta z =$$

$$\phi_{\mathrm{wl}} P_{\mathrm{wl}} \delta z + \phi_{\mathrm{lv}} P_{\mathrm{lv}} \delta z + u_{\mathrm{l}} \tau_{\mathrm{lv}} P_{\mathrm{lv}} \delta z + \Gamma_{\mathrm{l}} \delta z\left(h_{\mathrm{l}} + \frac{u_{\mathrm{l}}^2}{2}\right) \tag{2.46}$$

Adding equations (2.45) and (2.46) and taking into account the conservation of energy across the interface, the results gives:

$$\Gamma_{\mathrm{v}}\left(h_{\mathrm{v}} + \frac{u_{\mathrm{v}}^2}{2}\right) + \phi_{\mathrm{vl}} P_{\mathrm{vl}} + u_{\mathrm{v}} \tau_{\mathrm{vl}} P_{\mathrm{vl}} = \Gamma_{\mathrm{l}}\left(h_{\mathrm{l}} + \frac{u_{\mathrm{l}}^2}{2}\right) + \phi_{\mathrm{lv}} P_{\mathrm{lv}} + u_{\mathrm{l}} \tau_{\mathrm{lv}} P_{\mathrm{lv}} \tag{2.47}$$

Now it can be obtained the following differential equation for this simplified approach:

$$\frac{d}{dz}\left[\dot{m}_{\mathrm{v}} h_{\mathrm{v}} + \dot{m}_{\mathrm{l}} h_{\mathrm{l}}\right] + \frac{d}{dz}\left[\frac{\dot{m}_{\mathrm{v}} u_{\mathrm{v}}^2}{2} + \frac{\dot{m}_{\mathrm{l}} u_{\mathrm{l}}^2}{2}\right] + \left(\dot{m}_{\mathrm{v}} + \dot{m}_{\mathrm{l}}\right) g \sin\theta = Q_{\mathrm{wl}} \tag{2.48}$$

where the term $Q_{\mathrm{wl}} = \phi_{\mathrm{wl}} P_{\mathrm{wl}} + \phi_{\mathrm{wv}} P_{\mathrm{wv}}$ represents the heat transferred to the fluid across the wall per unit of tube length.

Using relationships introduced in this chapter, equation (2.48) may be written

$$-\frac{dp}{dz}\left[\frac{x}{\rho_{\mathrm{v}}} + \frac{(1-x)}{\rho_{\mathrm{l}}}\right] = \left\{\frac{dE}{dz} - \frac{Q_{\mathrm{wl}}}{(\dot{m}_{\mathrm{v}} + \dot{m}_{\mathrm{l}})}\right\}$$

$$+\left\{p\frac{d}{dz}\left[\frac{x}{\rho_{\mathrm{v}}} + \frac{(1-x)}{\rho_{\mathrm{l}}}\right] + \frac{G^2}{2}\frac{d}{dz}\left[\frac{x^3}{\rho_{\mathrm{v}}^2 \varepsilon^2} + \frac{(1-x)^3}{\rho_{\mathrm{l}}^2 (1-\varepsilon)^2}\right]\right\} + g \sin\theta \tag{2.49}$$

where $E = xe_{\mathrm{v}} + (1-x)e_{\mathrm{l}}$ is the flow-weighted mixture internal energy per unit of mass.

The above equation shows that the total pressure gradient can be expressed in terms of a frictional dissipation term (first bracketed term), an accelerational term (second bracketed term) and a static head term (final term). It should pointed out that the frictional dissipation term $\left(\frac{dE}{dz} - \frac{Q_{\mathrm{wl}}}{(\dot{m}_{\mathrm{v}} + \dot{m}_{\mathrm{l}})}\right)$ includes the dissipation of mechanical energy not only within the fluid due to friction at the tube walls but also at the interface due to the relative motion of the phases.

2.6.3.1 Flashing effect

The pressure drop related to frictional dissipation term can reach non-negligible values and provoke a so-called flashing (increase of the vapor quality due to expansion) and a temperature difference. The flashing effect may easily be calculated using the relation developed by [Revellin *et al.* 2009b], which is expressed (for constant properties) as follows:

$$\Delta x = -\frac{\upsilon_{\mathrm{lv}} T_{\mathrm{sat}} c_{\mathrm{x,tp}} + h_{\mathrm{lv}} \upsilon_{\mathrm{tp}}}{h_{\mathrm{lv}}^2} \Delta p_f \tag{2.50}$$

where $c_{\mathrm{x,tp}}$ corresponds to the specific heat capacity of the two-phase flow at constant vapor quality, calculated by the following relation:

$$c_{\mathrm{p,tp}} = x c_{\mathrm{x,v}} + (1-x) c_{\mathrm{x,l}} \text{ ; where } c_{\mathrm{x}} = T \left(\frac{\partial s}{\partial T} \right)_x \tag{2.51}$$

The induced temperature difference is obtained using the Clapeyron equation ($\mathrm{d}p/\mathrm{d}T_{\mathrm{sat}} = h_{\mathrm{lv}}/(T_{\mathrm{sat}} \upsilon_{\mathrm{lv}})$).

2.7 Non-dimensional numbers

The main non-dimensional numbers used in the present study are defined below. Different definitions of main non-dimensional numbers, particularly for the Reynolds and Froude number, can be found in the literature. In order to be consistent in this work, the corresponding definitions used in this work are introduced.

2.7.1 Reynolds number

The Reynolds number represents the ratio of the inertial forces to the viscous forces. For the particular case of forced convection inside a tube, the liquid Reynolds number for a single-phase in a tube can be expressed in the following form:

$$\mathrm{Re}_{\mathrm{l}} = \frac{\rho_{\mathrm{l}} u_{\mathrm{l}} D}{\mu_{\mathrm{l}}} \tag{2.52}$$

Considering one-dimensional flow and using the definition of the actual velocity from Eq. (2.7), the liquid Reynolds number in a two-phase flow can be expressed as:

$$\mathrm{Re}_{\mathrm{l}} = \frac{GD}{\mu_{\mathrm{l}}} \frac{(1-x)}{(1-\varepsilon)} \tag{2.53}$$

The same approach will be used for the vapor Reynolds number which is defined as:

$$\mathrm{Re}_{\mathrm{v}} = \frac{GD}{\mu_{\mathrm{v}}} \frac{x}{\varepsilon} \tag{2.54}$$

In the literature, other definitions of the Reynolds number may be found. As the void fraction is difficult to determine, the following expressions are also used for circular tubes:

$$\mathrm{Re}_{\mathrm{l}} = \frac{G(1-x)D}{\mu_{\mathrm{l}}} \tag{2.55}$$

$$\mathrm{Re}_{\mathrm{v}} = \frac{GxD}{\mu_{\mathrm{v}}} \tag{2.56}$$

Another type of Reynolds number may be calculated when considering each phase flows alone in the complete cross-section of the tube at its own velocity:

$$\mathrm{Re}_{\mathrm{lo}} = \frac{GD}{\mu_{\mathrm{l}}} \tag{2.57}$$

$$\mathrm{Re}_{\mathrm{vo}} = \frac{GD}{\mu_{\mathrm{v}}} \tag{2.58}$$

It represents the liquid (or the vapor) phase only flowing alone in the complete cross-section of the tube at the total mass velocity.

2.7.2 Froude number

The Froude number represents the ratio of the inertia forces to the gravitational forces. The general expression is:

$$\mathrm{Fr} = \frac{G^2}{gD\rho^2} \tag{2.59}$$

The liquid Froude number for the liquid phase in a tube can be expressed in the following form:

$$\mathrm{Fr}_{\mathrm{l}} = \frac{G^2}{gD\rho_{\mathrm{l}}^2} \tag{2.60}$$

and for the vapor Froude number is defined as:

$$\mathrm{Fr}_{\mathrm{v}} = \frac{G^2}{gD\rho_{\mathrm{v}}^2} \tag{2.61}$$

2.7.3 Weber number

The Weber number expresses the ratio of inertia to surface tension forces. The reference length is the tube diameter. It is expressed for liquid phase as:

$$\mathrm{We}_{\mathrm{l}} = \frac{\rho_{\mathrm{l}} u_{\mathrm{l}}^2 D}{\sigma} \tag{2.62}$$

2.7.4 Martinelli parameter

The Martinelli parameter [Lockhart & Martinelli 1949] is defined as the ratio between the theoretical pressure gradients which would occur if each phase would flow alone in the pipe with the original flow rate of each phase. The Martinelli parameter X_{tt}^2 is calculated as:

$$\mathrm{X}_{\mathrm{tt}}^2 = \frac{\left(\frac{dp_{\mathrm{f}}}{dz}\right)_{\mathrm{lo}}}{\left(\frac{dp_{\mathrm{f}}}{dz}\right)_{\mathrm{vo}}} \tag{2.63}$$

$\mathrm{X}_{\mathrm{tt}}^2$ is void fraction independent and is a measure of the degree to which the two-phase mixture is close to being a liquid, e.g. $\mathrm{X}_{\mathrm{tt}}^2 >> 1$, or to being a vapor, e.g. $\mathrm{X}_{\mathrm{tt}}^2 << 1$. The subscript tt signifies that both phases are turbulent. Modeling the pressure drop of each phase with its superficial velocity and friction factors in the classical form:

$$f_{\mathrm{l}} = C_{\mathrm{l}}\mathrm{Re}_{\mathrm{l}}^{-n} \tag{2.64}$$

$$f_{\mathrm{v}} = C_{\mathrm{v}}\mathrm{Re}_{\mathrm{v}}^{-m} \tag{2.65}$$

and assuming the same friction model for both phases (both turbulent or both laminar) which means that m = n and $C_{\mathrm{l}} = C_{\mathrm{v}}$, Eq. (2.63) reduces to:

$$\mathrm{X}_{\mathrm{tt}} = \left(\frac{1-x}{x}\right)^{-n+2/2} \left(\frac{\mu_{\mathrm{l}}}{\mu_{\mathrm{v}}}\right)^{n/2} \left(\frac{\rho_{\mathrm{v}}}{\rho_{\mathrm{l}}}\right)^{1/2} \tag{2.66}$$

In this work, the following expression will be used:

$$\mathrm{X}_{\mathrm{tt}} = \left(\frac{1-x}{x}\right)^{0.9} \left(\frac{\rho_{\mathrm{v}}}{\rho_{\mathrm{l}}}\right)^{0.5} \left(\frac{\mu_{\mathrm{l}}}{\mu_{\mathrm{v}}}\right)^{0.1} \tag{2.67}$$

2.8 Geometrical parameters

2.8.1 Return bends

Figure 2.3 shows the geometrical parameters of a 180° return bend, where D is the tube inside diameter, R the curvature radius, L_1 and L_2 are inlet and outlet straight section lengths, respectively.

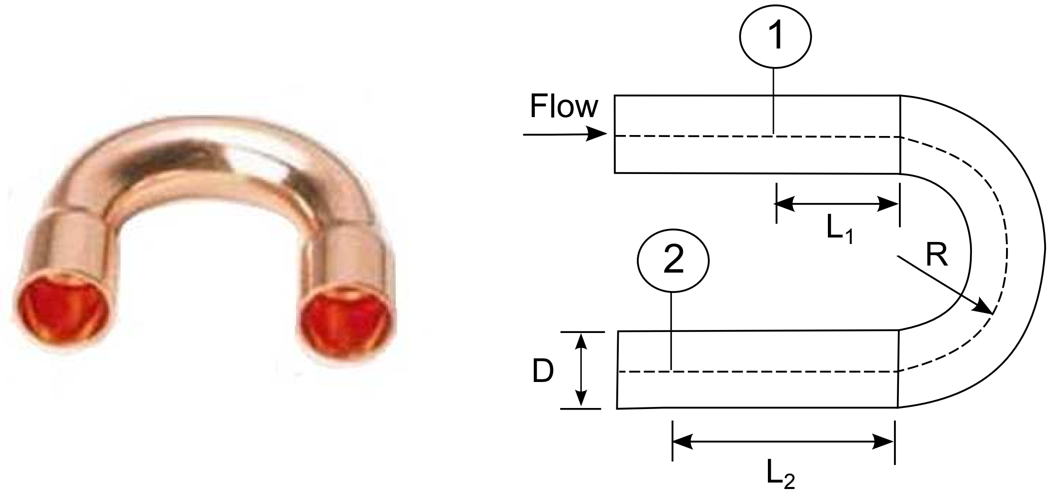

Figure 2.3: 180° Return bend.

The curvature ratio in a return bend is defined as $\dfrac{2R}{D}$.

2.8.2 Sudden contractions

Figure 2.4 shows the flow through a sudden contraction of a duct area (based on measurements in single-phase water flow).

In a distance of about 1.5 times the entrance-pipe diameter in front of the transitional cross section the flow separates from the inner wall and contracts to a jet with a narrowest

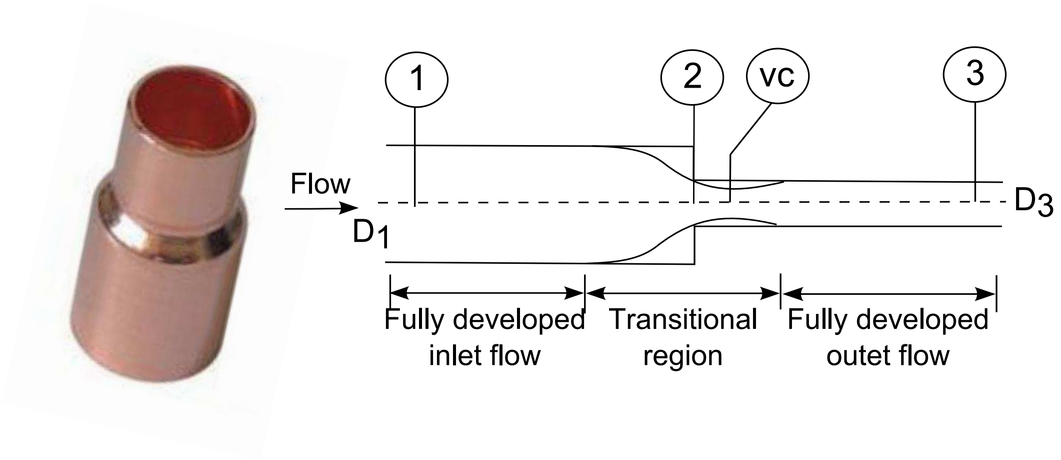

Figure 2.4: Single-phase flow through a sudden contraction.

cross section immediately behind the transition. Hereafter, the jet enlarges and the main flow reattaches to the pipe wall in a distance of less than 14 times the outlet-pipe diameter, depending on the flow condition. In the contracted flow region the static pressure in the inlet line decreases more rapidly than in fully developed flow. In the narrowest cross section, the so-called *vena contracta* it attains the (locally) smallest value. Then, the pressure gradually increases and, after reaching its maximum, it merges into the curve of the pipe frictional pressure drop.

The area ratio in a sudden contraction is defined as $\frac{A_3}{A_1} = \frac{D_3^2}{D_1^2}$.

2.9 Chapter conclusions

Fundamental parameters and basic principles of two-phase flow used throughout this work have been presented. Relevant information on the primary variables and some simple relationships between them are derived for the case of one-dimensional flow.

CHAPTER 3

State of the art review

Contents

Two-phase flow pressure drop depends on a large number of independent parameters like geometric configuration of the duct, mass and volume fractions of the individual phases, pressure, fluid properties, mass velocity, orientation of the duct (e.g horizontal, vertical or inclined), flow direction (e.g vertical upflow, downflow or counter-current flow) and flow patterns. Further, in many engineering applications, such as refrigeration, two-phase flow systems can be adiabatic, diabatic, one-component, two-component or multi-component. To cater for the needs of these diverse applications, a very large number of two-phase pressure drop prediction tools are reported in the literature. Many of them are correlations, empirical in nature, that are applicable only for limited parameter ranges. Even mechanistic models are based on certain assumptions and careful examination of the particular application if necessary to ensure that the assumptions made in deriving the model hold good. For many practical situations, designers and analysts often require some guidance to choose the appropriate correlation.

In this chapter, an overview of the state-of-the-art of two-phase pressure drop models and flow pattern maps are given.

3.1 Two-phase flow in straight macro channels

Many classifications of channels have been proposed. Many authors consider the channels of diameter greater than 6 mm to be macro channels and smaller than 6 mm as small (micro, mini, etc.) channels. This classifications is arbitrary, without any physical basis.

[Cheng & Wu 2006] have given the following criteria based on an analysis considering the magnitudes of gravity and surface tension effects:

- Micro channel, if $\mathrm{Bo} < 0.5$ (negligible effect of gravity).
- Mini channel , if $0.5 < \mathrm{Bo} < 3.0$ (both gravity and surface tension have significant effect).
- Macro channel, if $\mathrm{Bo} > 3.0$ (surface tension has negligible effect).

where Bo is the Bond number defined as:

$$\mathrm{Bo} = \frac{g(\rho_\mathrm{l} - \rho_\mathrm{v})D^2}{\sigma} \tag{3.1}$$

3.1.1 Flow patterns

When a mixture of liquid and vapor flows inside a tube, a variety of *flow patterns* may occur, depending among other parameters, on the mass fraction of liquid, the fluid properties of each phase, and the flow rate. In an evaporator tube, the mass fraction of liquid decreases along the circuit length, resulting in a series of successive vapor-liquid flow patterns. If the fluid enters as a subcooled liquid, the first indications of vapor generation are bubbles forming at the heated tube wall (nucleation). Subsequently, *bubble*, *plug*, *churn* (or semi-annular), *annular*, *spray-annular*, and *mist* flows can occur as the vapor content increases along the tubes.

Idealized flow patterns are illustrated in Figure 3.1 for a horizontal heated channel.

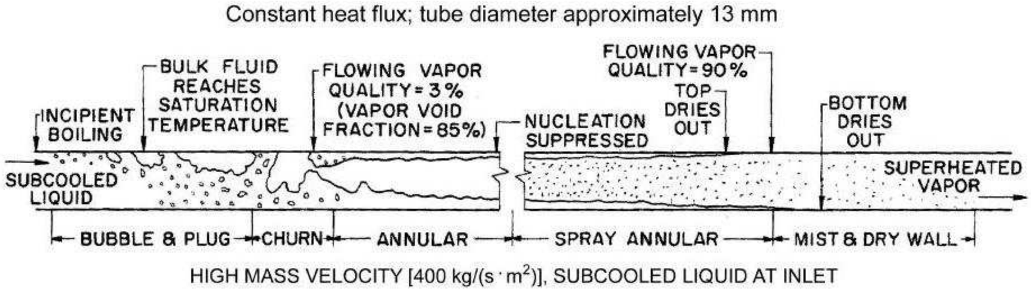

Figure 3.1: Flow regimes in typical evaporator smooth horizontal tube [ASHRAE 2001].

Because nucleation occurs at the heated surface in a thin sublayer of superheated liquid, boiling in forced convection may begin while the bulk of the liquid is still subcooled. Depending on the nature of the fluid and the subcooling, the bubbles formed can either collapse or continue to grow and coalesce (Figure 3.1), as [Gouse & Coumou 1965] observed for R-113. [Bergles & Rohsenow 1964] developed a method to determine the point of incipient surface boiling.

After nucleation begins, bubbles quickly agglomerate to form vapor plugs at the center of a vertical tube, or, as shown in Figure 3.1, vapor plugs form along the top surface of a horizontal tube. At the point where the bulk of the fluid reaches saturation temperature, which corresponds to local static pressure, there can up to 1%, vapor quality because of the preceding surface boiling [Guerrieri & Talty 1956].

Further coalescence of vapor bubbles and plugs results in churn, or semi-annular flow. If the fluid velocity is high enough, a continuous vapor core surrounded by a liquid annulus at the tube wall soon forms. This annular flow occurs when the ratio of the tube cross section filled with vapor to the total cross section is approximately 85%. With common refrigerants, this equals a vapor quality of about 0% to 30%.

If two-phase mass velocity is high (i.g greater than 200 $\mathrm{kg{\cdot}m^{-2}{\cdot}s^{-1}}$ for a 12 mm tube), annular flow with small drops of entrained liquid in the vapor core (spray) can persist over a vapor quality range from about 10% to more than 90%. Refrigerant evaporators are fed from an expansion device at vapor qualities of typically 20-30%, so that annular and spray annular flow predominate in most tube lengths. In a vertical tube, the liquid annulus is distributed uniformly over the periphery, but it is somewhat asymmetric in a horizontal tube (Figure 3.1). As vapor quality reaches about 80%, the surface dries out. [Chaddock & Noerager 1966] found that in a horizontal tube, dryout occurs first at the top of the tube and progresses toward the bottom with increasing vapor quality (Figure 3.1).

Flow patterns for co-current flow of gas and liquid in a horizontal tube are strongly influenced by gravity that acts to stratify the liquid to the bottom of the tube and the gas to the top. The liquid and gas phases distribute into several recognizable flow structures that present certain analogies with those observed during flow boiling (Fig. 3.2):

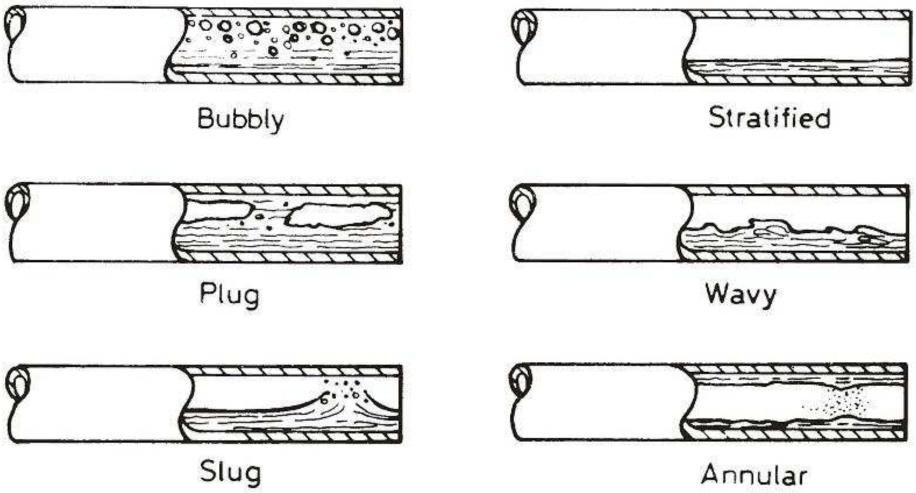

Figure 3.2: Two-phase flow patterns in horizontal flow [Collier & Thome 1994].

- **Bubbly flow**: The vapor bubbles are dispersed in the liquid with a high concentration of bubbles in the upper half of the tube due to their buoyancy. When shear forces are dominant, the bubbles tend to disperse uniformly in the tube. For horizontal flows, this regime only occurs at high mass flow rates.

- **Stratified flow**: At low liquid and vapor velocities, complete separation of the two phases occurs. The vapor goes to the top and the liquid to the bottom of the tube. Both phases are separated by an undisturbed flat interface. Therefore, the liquid and vapor are fully stratified in this regime.

- **Stratified-wavy flow**: When increasing the vapor velocity in a stratified flow, waves are formed on the interface and travel in the direction of the flow. The amplitude of the waves is notable and depends on the relative velocity of the two phases; however, their crests do not reach the top of the tube. The waves climb up the sides of the tube, leaving behind thin films of liquid on the wall.

- **Intermittent flow**: Further increasing the vapor velocity, these interfacial waves become large enough to wash the top of the tube. This regime is characterized by large amplitude waves intermittently washing the top of the tube with smaller amplitude waves in between. Large amplitude waves often contain entrained bubbles. The top wall is nearly continuously wetted by the large amplitude waves and thin liquid films are left behind. Intermittent flow can also be described as a composite of the plug and slug flow regimes. These subcategories are characterized as follows:

  - **Plug flow**: This regime presents liquid plugs that are separated by elongated bubbles. The diameter of the elongated bubbles is much smaller than the tube so that the liquid phase is continuous along the bottom of the tube below the elongated bubbles.
  - **Slug flow**: At higher vapor velocities, the diameter of elongated bubbles becomes similar to the channel height. The liquid slugs separating such elongated bubbles can also be described as large amplitude waves.

- **Annular flow**: At even larger vapor flow rates, the liquid forms a continuous film around the perimeter of the tube. The interface between the liquid annulus and the vapor core is disturbed by small amplitude waves and droplets may be dispersed in the vapor core. At high vapor fractions, the top of the tube with its thinner film becomes dry first, so that the annular film covers only part of the tube perimeter. This behavior is thus classified as stratified-wavy flow. At very high velocities most of the liquid is entrained as spray by the vapor. The spray appears to be produced by the high velocity vapor ripping the annular liquid film off from the wall. When this occurs, it is then classified as **Mist flow**.

The distribution of the phases in vertical upward two-phase flow is no more influenced by the gravity. The most common flow patterns encountered in vertical upward flow are shown in Fig. (3.3) and presented below:

- **Bubbly flow**: The vapor or vapor phase is dispersed in the liquid as discrete bubbles. The bubbles may have different shapes and sizes but they are much smaller than the pipe diameter.

- **Slug flow**: When the quality increases, the bubbles coalesce and form larger bubbles, of a size similar to the pipe diameter. These are called Taylor bubbles and have a characteristic spherical cap nose and are somewhat abruptly terminated. The elongated vapor bubbles are separated by liquid slugs, which may have smaller bubbles in them. The Taylor bubbles are separated from the wall by a thin liquid film.

- **Churn flow**: When the velocity of the flow is increased, the slugs break-down into a seemingly unstable regime. This is a flow regime between the slug flow and the annular flow regime, where the liquid phase is displaced to the tube wall.
- **Wispy-annular flow**: When the liquid flow rate is increased, a considerable amount of liquid may be entrained in the vapor core. These liquid droplets may then coalesce to form larger lumps or liquid wisp. This regime occurs at high mass velocities.
- **Annular flow**: At even larger vapor flow rates, the bulk of the liquid flows on the wall as a film, and the vapor is the continuous phase at the center of the tube. Normally, there is some liquid entrained in the continuous vapor in the form of small droplets, and there may be some vapor in the liquid film in the form of bubbles.

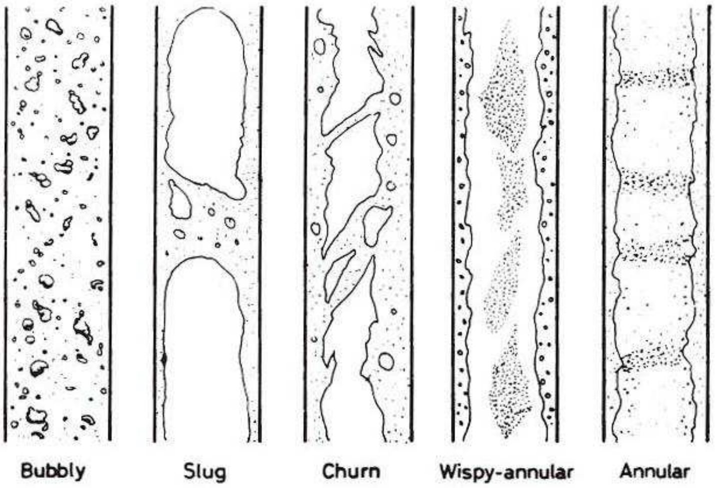

Figure 3.3: Two-phase flow patterns in vertical flow [Collier & Thome 1994].

3.1.2 Flow pattern maps

For evaporation in horizontal tubes, Fig.3.4 from [Thome 2004] depicts the typical flow regimes, including cross-sectional views of the flow structure.

To predict the local flow pattern in a tube, a flow pattern map is used. It is a diagram that displays the transition boundaries between the flow patterns. The most widely quoted flow pattern maps for predicting the transition between two-phase flow regimes for adiabatic flow in horizontal tubes are those of [Baker 1954] and [Taitel & Dukler 1976].

[Baker 1954] was the first to recognize the importance of the flow pattern as a starting point for the calculation of pressure drop, void fraction, and heat and mass transfer. He published the earliest flow pattern map for horizontal flow. The [Taitel & Dukler 1976] map is based on their analytical analysis of the flow transition mechanisms together with empirical selection of several parameters. The proposed map has a better scientific basis than many of the previous attempts and thus extrapolates better than the others maps.

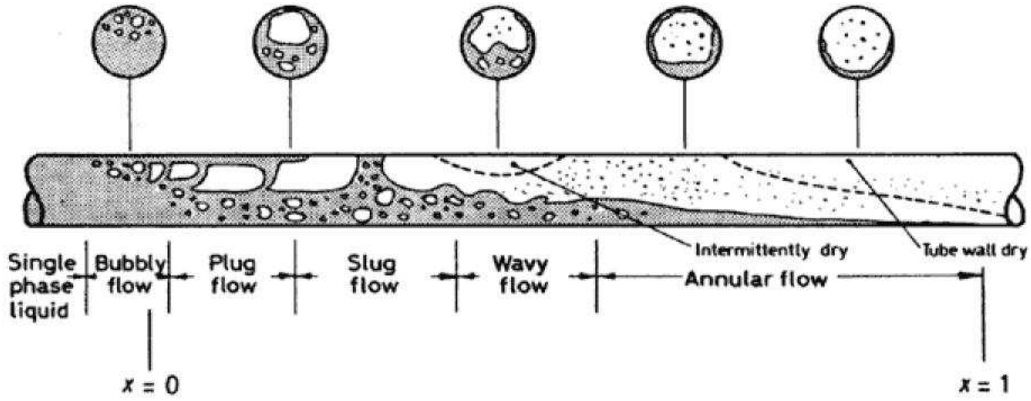

Figure 3.4: Flow patterns during evaporation in a horizontal tube [Thome 2004].

The map uses the Martinelli parameter X_{tt}, the vapor Froude number Fr_{v} and is composed of three graphs.

Later, [Hashizume 1983] performed flow pattern observation experiments for refrigerant two-phase flow in a horizontal tube. He showed that the flow pattern boundaries of refrigerant two-phase flows differ considerably from those of Baker map, which was based on air-water data. He concluded that the flow patterns of refrigerant two-phase flows can be presented on a revised Baker map, where the property correction factor on surface tension was modified.

These flow patterns maps were all developed for adiabatic two-phase flows but are often extrapolated to the case of diabatic process of evaporation. As with any extrapolation, this may or may not produce reliable results. Important factors influencing the flow during evaporation, which may have an effect on transition between flow regimes, are nucleate boiling, evaporation of liquid films and the acceleration of the flow due to the phase change. It is desirable to define for this type of flow a flow pattern map that includes the influences of heat flux and dryout on the flow pattern transition boundaries and one which is also easier to implement than the frequently used log - log format. As a first step in this direction, for small diameter tubes, [Kattan *et al.* 1998a, Kattan *et al.* 1998b, Kattan *et al.* 1998c] proposed a modification of the [Steiner 1993] map, which itself is a modified Taitel-Duckler map, and included a method for predicting the onset of dryout at the top of the tube in evaporating annular flows.

A more recent version of the Kattan et al. flow map, based on information obtained from dynamic void fraction measurements and observations of the cross-sectional locus of the liquid-vapor interface has been proposed by [Wojtan *et al.* 2005a], This flow pattern map also includes the effect of heat flux on the transition to mist flow.

This new map is illustrated in Fig. 3.5 where **S**= stratified flow, **SW**= stratified-wavy flow, **I**= intermittent flow, **A**= annular flow, **M**= mist flow and **D** represents the transition zone between annular and mist flow.

The implementation procedure for the updated version is as follows:

First, the geometrical parameters ε, A_{lD}, A_{vD}, θ_{strat}, h_{lD} and P_{iD} that are showed in Fig. 3.6, are calculated from the following equations:

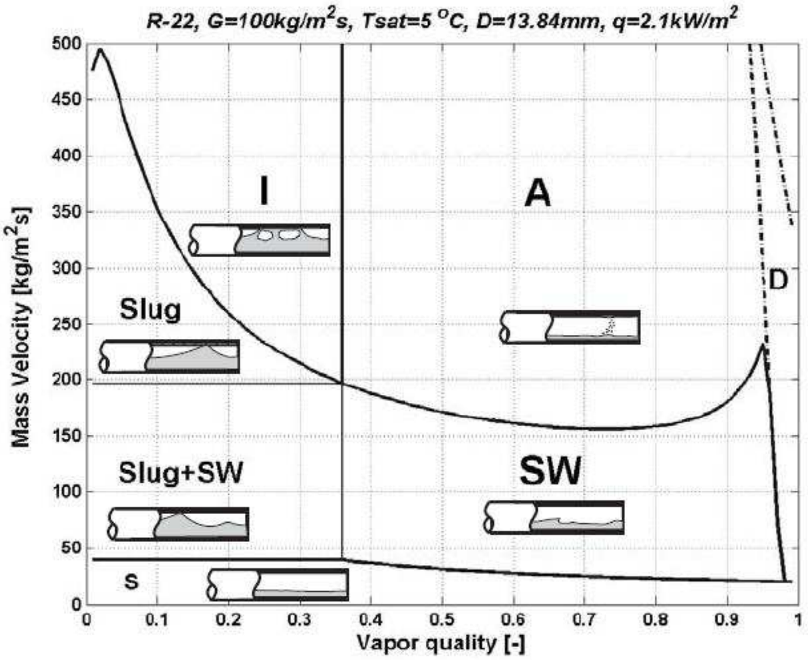

Figure 3.5: Flow pattern map of [Wojtan *et al.* 2005a] for R-22 at $T_{\text{sat}} = 5^{\circ}$C in a 13.84 mm internal diameter tube at $G = 100$ kg·m^{-2}·s^{-1} and q = 2.1 kW· m^{-2}. [Quibén 2005]

$$h_{\mathrm{lD}} = \frac{h_\mathrm{l}}{D};\; P_{\mathrm{lD}} = \frac{P_\mathrm{l}}{D};\; P_{\mathrm{vD}} = \frac{P_\mathrm{v}}{D};\; P_{\mathrm{iD}} = \frac{P_\mathrm{i}}{D};$$
$$A_{\mathrm{lD}} = \frac{A(1-\varepsilon)}{D^2}$$
$$A_{\mathrm{vD}} = \frac{A\varepsilon}{D^2} \tag{3.2}$$

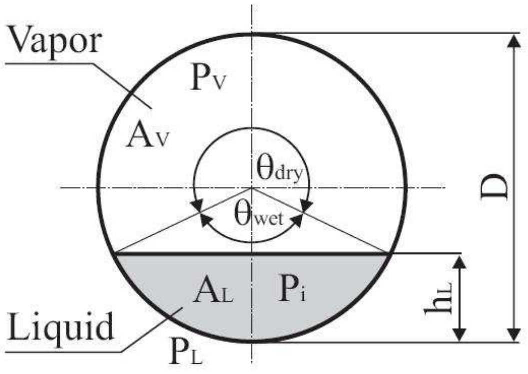

Figure 3.6: Cross-sectional and peripheral fractions in a circular tube. [Quibén 2005]

$$\theta_{\mathrm{strat}} = 2\pi - 2\left\{\pi(1-\varepsilon) + \left(\frac{3\pi}{2}\right)^{1/3}\left[1 - 2(1-\varepsilon) + (1-\varepsilon)^{1/3} - \varepsilon^{1/3}\right]\right\}$$
$$- 2\pi - 2\left\{\frac{1}{200}(1-\varepsilon)\varepsilon\left[1 - 2(1-\varepsilon)\left[1 + 4\left((1-\varepsilon)^2 - \varepsilon^2\right)\right]\right]\right\} \tag{3.3}$$

$$h_{\mathrm{lD}} = 0.5\left[1 - \cos\left(\frac{2\pi - \theta_{\mathrm{strat}}}{2}\right)\right] \tag{3.4}$$

$$P_{\mathrm{iD}} = \sin\left(\frac{2\pi - \theta_{\mathrm{strat}}}{2}\right) \tag{3.5}$$

where the void fraction (ε) can be calculated with the [Steiner 1993] version of the [Rouhani & Axelsson 1970] equation for horizontal tubes, Eq. (3.68). The **S-SW** transition is calculated from:

$$G_{\mathrm{strat}} = \left[\frac{226.3^2 A_{\mathrm{lD}} A_{\mathrm{vD}}^2 \rho_\mathrm{v}(\rho_\mathrm{l} - \rho_\mathrm{v}) g \mu_\mathrm{l}}{x^2(1-x)\pi^3}\right]^{1/3} \tag{3.6}$$

The flow is stratified whenever $G < G_{\mathrm{strat}}$.

The **SW-I/A** boundary is calculated from the following equation:

$$G_{\mathrm{wavy}} = \left\{\frac{16 A_{\mathrm{vD}}^3 g D \rho_\mathrm{l} \rho_\mathrm{v}}{x^2\pi^2\left(1 - (2h_{\mathrm{lD}} - 1)^2\right)^{0.5}} + \left[\frac{\pi^2}{25 h_{\mathrm{lD}}^2}\left(\frac{We}{Fr}\right)_l^{-1} + 1\right]\right\}^{0.5} + 50 \tag{3.7}$$

The stratified-wavy region lies above the stratified region and is then subdivided into three zones:

- $G > G_{\mathrm{wavy}}(x_{\mathrm{IA}})$ gives the SLUG zone;
- $G_{\mathrm{strat}} < G < G_{\mathrm{wavy}}(x_{\mathrm{IA}})$ and $x < x_{\mathrm{IA}}$ give the SLUG/STRATIFIED-WAVY zone;
- $x \geq x_{\mathrm{IA}}$ gives the STRATIFIED-WAVY zone.

- $G > G_{\mathrm{wavy}}(x_{\mathrm{IA}})$ gives the SLUG zone;
- $G_{\mathrm{strat}} < G < G_{\mathrm{wavy}}(x_{\mathrm{IA}})$ and $x < x_{\mathrm{IA}}$ give the SLUG/STRATIFIED-WAVY zone;
- $x \geq x_{\mathrm{IA}}$ gives the STRATIFIED-WAVY zone.

The **I-A** transition is calculated from the equation below and is extended down to its intersection with G_{strat}:

$$x_{\mathrm{IA}} = \left\{ \left[0.34^{1/0.875} \left(\frac{\rho_{\mathrm{v}}}{\rho_{\mathrm{l}}} \right)^{-1/1.75} \left(\frac{\mu_{\mathrm{v}}}{\mu_{\mathrm{l}}} \right)^{1/7} \right] + 1 \right\}^{-1} \tag{3.8}$$

The **A-D** boundary is calculated from:

$$G_{\mathrm{dryout}} = \left[\frac{\frac{1}{0.235} \left(\mathrm{Ln}\left(\frac{0.58}{x}\right) + 0.52 \right) \left(\frac{D}{\rho_{\mathrm{v}} \sigma} \right)^{-0.17}}{\left(\frac{1}{D \rho_{\mathrm{v}} (\rho_{\mathrm{l}} - \rho_{\mathrm{v}})} \right)^{0.37} \left(\frac{\rho_{\mathrm{v}}}{\rho_{\mathrm{l}}} \right)^{0.25} \left(\frac{\phi}{\phi_{\mathrm{crit}}} \right)^{0.70}} \right]^{0.926} \tag{3.9}$$

and the **D-M** is calculated from:

$$G_{\mathrm{mist}} = \left[\frac{\frac{1}{0.0058} \left(\mathrm{Ln}\left(\frac{0.61}{x}\right) + 0.57 \right) \left(\frac{D}{\rho_{\mathrm{v}} \sigma} \right)^{-0.38}}{\left(\frac{1}{D \rho_{\mathrm{v}} (\rho_{\mathrm{l}} - \rho_{\mathrm{v}})} \right)^{0.15} \left(\frac{\rho_{\mathrm{v}}}{\rho_{\mathrm{l}}} \right)^{-0.09} \left(\frac{\phi}{\phi_{\mathrm{crit}}} \right)^{0.27}} \right]^{0.943} \tag{3.10}$$

The following conditions are then applied to define the transitions in the high quality range:

- If $G_{\mathrm{strat}} \geq G_{\mathrm{dryout}}$, then $G_{\mathrm{dryout}} = G_{\mathrm{strat}}$;
- If $G_{\mathrm{wavy}} \geq G_{\mathrm{dryout}}$, then $G_{\mathrm{dryout}} = G_{\mathrm{wavy}}$.

The maximum values of x to use in Eqs. (3.9) and (3.10) are 0.99. This updated version provides a more accurate prediction of different flow regimes (in particular the onset and completion of dryout around the tube perimeter) and does not require any iterative calculations. Therefore, it can be easily used for flow regime identification.

3.1.3 Flow boiling pressure drop in straight tubes

Frictional two-phase pressure drops in internal geometries have been experimentally investigated over the last 30 years by several authors. Figure 3.7 presents the number of data points found in the open literature (122 articles for 23 refrigerants since 1980) only for refrigerants flow boiling ([Charnay *et al.* 2011, Revellin *et al.* 2009a]). As can be noted, almost all studies were carried out using R-134a which can be considered as a reference fluid since it has been extensively studied over the last 15 to 20 years.

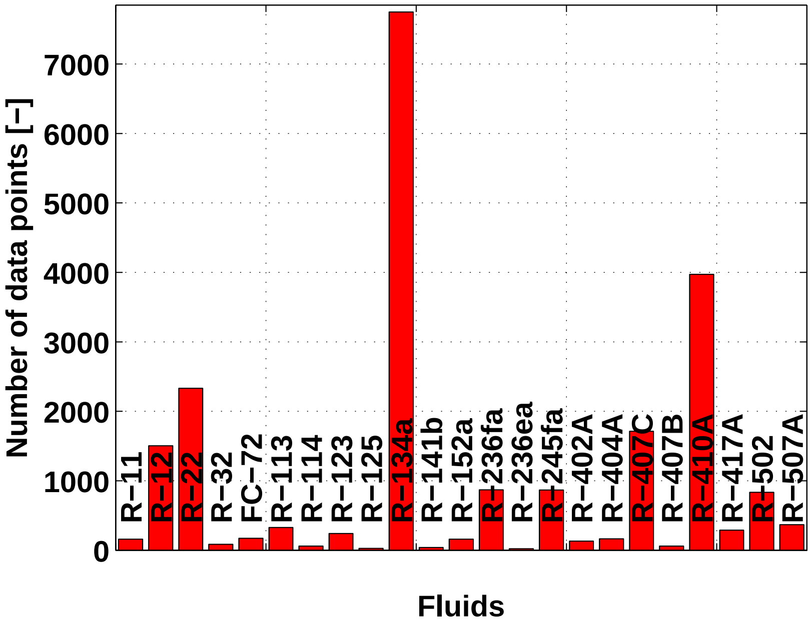

Figure 3.7: Number of pressure drop data points (22363 data points in total) for each synthetic refrigerant published in 122 articles since 1980 for flow boiling. ([Charnay *et al.* 2011],[Revellin *et al.* 2009a])

3.1.3.1 Most representative experimental studies for pressure drop prediction in straight tubes

[Ould Didi *et al.* 2002] compared the two-phase pressure gradient data obtained in two horizontal tubes (D = 10.92 mm and D = 12.00 mm) for five refrigerants (R-134a, R-123, R-402A, R-404A and R-502). They found that the methods proposed by [Müller-Steinhagen & Heck 1986] and that developed by [Grönnerud 1979] provide the most accurate predictions. Later, [Wongsa-ngam *et al.* 2004] experimentally investigated two-phase heat transfer coefficient and pressure drop during evaporation of R-134a in smooth and microfin tubes. The outer diameter was 9.52 mm and the evaporating temperatures ranged between 10 and 20 °C. They also proposed their own modified Martinelli correlation by fitting their database.

[Bandarra Filho *et al.* 2004] presented a pressure drop study of R-134a under flow boiling conditions in horizontal smooth and microfin copper tubes. According to the authors, the method by [Jung & Radermacher 1989] was found to be the best prediction method for smooth tubes. These authors also proposed their own modified Martinelli's parameter to fit their data. [Greco & Vanoli 2006] reported the results of an experimental study on pressure drop during horizontal flow boiling of refrigerants R-22, R-507, R-404A, R-134a, R-407C and R-410A in a smooth, horizontal, stainless steel tube (D = 6.00 mm). The experimental tests were carried out varying the mass velocity from 280 to 1080 kg m^{-2} s^{-1}. They found that the pressure drop of R-22 is significantly higher as compared to all the other fluids.

[Mauro *et al.* 2007] compared their experimental pressure drop data for different refrigerants (R-22, R-134a, R-404A, R-407C, R-410A, R-417A and R-507A) and different experimental conditions to four methods and to the phenomenological model by [Moreno Quibén & Thome 2007]. They statistically showed that the method by Grönnerud and that by Moreno Quibén and Thome were equally the best. [Park & Hrnjak 2007] investigated flow boiling pressure drops in a horizontal smooth tube of 6.10 mm inner diameter for R-744, R-410A, and R-22 refrigerants. The tested saturation temperatures were -30 °C and -15 °C. They found that the method by [Müller-Steinhagen & Heck 1986] was the best for predicting their data.

[Kuo & Wang 1996], reported adiabatic and diabatic experimental pressure drop data for R-22 and R-407C in a microfin tube with nominal diameter of 9.52 mm. They concluded by saying that their pressure drop data for R-407C were 30-50% lower as compared to R-22. They proposed their own two-phase friction factor for predicting their data. [Wang & Chiang 1997] reported in their study the measurement of adiabatic two-phase frictional pressure drop and heat transfer characteristics for R-22 and R-407C inside a 6.5mm smooth tube for a mass velocity varying from 100 to 700 kg m^{-2} s^{-1}. They found a lower pressure drop for R-407C than for R-22.

[Haberschill *et al.* 2003] studied the influence of different parameters (nature of fluid, mass velocity and heat flux) on the local pressure drop during flow boiling inside smooth and microfin tubes. However, they did not compare their data to existing prediction methods. They found no effect of the heat flux on the pressure drop. Their penalty factor was varying between 1.46 and 1.63.

Very recently, [Padilla *et al.* 2011a] presented 819 pressure drop data points measured during two-phase flow of refrigerants HFO-1234yf, R-134a and R-410A in horizontal straight tubes. The tube diameter (D) varies from 7.90 to 10.85 mm. The mass velocity ranges from 187 to 1702 kg m^{-2} s^{-1} and the saturation temperatures from 4.8 °C to 20.7 °C. This database was compared against 10 well-known two-phase frictional pressure drop prediction methods. The best accuracy is given by the method of [Müller-Steinhagen & Heck 1986] with around 90% of the data predicted within a ±30% error band. An analysis was carried out on the maximum pressure gradient and on the corresponding vapor quality. A statistical analysis for each flow regime was also carried out.

Note that the information available in the literature related to slug flow are for vertical, horizontal, and inclined straight tubes. For the last one, very little attention has been given to downward gas-liquid flows. [Roitberg *et al.* 2008] carried out an study on the effect of pipe inclination angle (θ) focused on the slug flow regimes. The pipe inclination angles considered were from -7.5° to -1°. Results show that the pipe inclination affects mainly the bubble length, while the liquid slug length remains insensitive to the variation of the inclination angle. The elongated bubble and the liquid slug length grow with gas flow rate. The slug head is affected by the pipe's inclination and gas flow rate, while the shape of the slug tail seems to remain approximately normal to the pipe axis for all experimental conditions considered

3.1.3.2 Overview of existing two-phase frictional pressure gradient prediction methods in straight tubes

As expressed in Eq.(2.33), the pressure gradient during flow boiling in horizontal tubes is the sum of the frictional, acceleration and static head contributions. The momentum pressure drop results from the change in momentum of both phases consequent to the change of the mass and velocity of each phase caused by evaporation. When the flow is adiabatic, $\left(\frac{dp}{dz}\right)_a = 0$.

The frictional pressure drop results from the shear stress between the flowing fluid and the tube wall. Despite numerous theoretical and experimental investigations, no general model is available to reliably predict two-phase frictional pressure drops. A reason for this is that two-phase flow includes all the complexities of single-phase like non-linearities, transition to turbulence and instabilities plus additional two-phase characteristics like motion and deformation of the interface, non-equilibrium effects and interactions between phases. This term can be calculated following three different approaches of prediction methods for smooth tubes: empirical correlations, analytical models or phenomenological models.

- The analytical approach, which is general since no empirical information is used in its development.
- The empirical approach is the most widely used as it requires a minimum knowledge of flow characteristics. However, it is restricted by its underlying database. Furthermore, no single correlation is currently able to reach an acceptable accuracy for general use.
- The phenomenological approach is based on the knowledge of each flow regime and the interfacial structure is taken into account. This method is physically based on several simplified interfacial two-phase flow structures.

Due to its extensive historical use and the continued references to it in the literature, the first method to be considered is that of [Lockhart & Martinelli 1949]. In this treatment they postulated that two-phase flow could be divided into four flow regimes: (1) liquid and vapor both turbulent (tt), (2) liquid turbulent and vapor viscous (tv), (3) liquid viscous and vapor turbulent (vt), (4) liquid and vapor both viscous (vv).

There are two basic postulates on which the analysis is based: (1) The static pressure drop for liquid and vapor phases must be equal regardless of the flow pattern; (2) The volume occupied by the liquid plus the vapor at any instant (position) must equal the total volume of the pipe. These postulates imply that the flow pattern does not change along the tube length. In effect they eliminate those flows which have large pressure fluctuations, such slug and intermittent flows, and those with radial pressure gradients, such as stratified and stratified-wavy flows.

In the final correlation, the two-phase frictional pressure drop based on a two-phase multiplier for the liquid-phase, or the vapor-phase, respectively, is:

$$\left(\frac{\mathrm{d}p}{\mathrm{d}z}\right)_{\mathrm{st}} = \left(\frac{\mathrm{d}p}{\mathrm{d}z}\right)_{\mathrm{v}} \Phi^2_{\mathrm{Vtt}} \tag{3.11}$$

$$\left(\frac{\mathrm{d}p}{\mathrm{d}z}\right)_{\mathrm{st}} = \left(\frac{\mathrm{d}p}{\mathrm{d}z}\right)_{\mathrm{l}} \Phi^2_{\mathrm{Ltt}} \tag{3.12}$$

where the terms $\left(\frac{\mathrm{d}p}{\mathrm{d}z}\right)_{\mathrm{l}}$ and $\left(\frac{\mathrm{d}p}{\mathrm{d}z}\right)_{\mathrm{v}}$ represent the frictional two-phase pressure drop that would exist if the the flow as a liquid or vapor, respectively, were assumed to flow alone in the entire cross-section of the tube, and are calculated as:

$$\left(\frac{\mathrm{d}p}{\mathrm{d}z}\right)_{\mathrm{l}} = \frac{2 f_{\mathrm{l}} G^2 (1-x)^2}{D \rho_{\mathrm{l}}} \tag{3.13}$$

$$\left(\frac{\mathrm{d}p}{\mathrm{d}z}\right)_{\mathrm{v}} = \frac{2 f_{\mathrm{v}} G^2 x^2}{D \rho_{\mathrm{v}}} \tag{3.14}$$

The corresponding Φ^2_{Ltt} and Φ^2_{Vtt} can be related to the Martinelli parameter (2.67) by relationships of the form:

$$\Phi^2_{\mathrm{Ltt}} = 1 + \frac{C}{X_{\mathrm{tt}}} + \frac{1}{X^2_{\mathrm{tt}}} \tag{3.15}$$

$$\Phi^2_{\mathrm{Vtt}} = 1 + C X_{\mathrm{tt}} + X^2_{\mathrm{tt}} \tag{3.16}$$

The single-phase friction factors of the liquid f_{l} and vapor f_{v} are calculated using the Blasius correlations as a function of the Reynolds number given by:

$$f_{\mathrm{l}} = \frac{0.079}{\mathrm{Re}_{\mathrm{l}}^{0.25}} \tag{3.17}$$

$$f_{\mathrm{v}} = \frac{0.079}{\mathrm{Re}_{\mathrm{v}}^{0.25}} \tag{3.18}$$

where Reynolds numbers are calculated using Eqs. (2.55) and (2.56).

The correlation was developed for horizontal two-phase flow of two-component (benzene-air, kerosene-air, water-air and various oils-air) systems at low pressures (close to atmospheric), saturation temperatures from 15.5 to 29.5°C and inner tube diameters from 1.49 to 25.83 mm. Its application to situations outside of this range of conditions is not recommended.

A different approach for modeling two-phase pressure drops is by considering a homogeneous fluid, which is a pseudo-fluid that obeys the conventional design equations for single-phase fluids and is characterized by suitably averaged properties of the liquid and vapor phases. The two-phase frictional pressure gradient is:

$$\left(\frac{\mathrm{d}p}{\mathrm{d}z}\right)_{\mathrm{st}} = \frac{2 f_{\mathrm{tp}} G^2}{D \rho_{\mathrm{tp}}} \tag{3.19}$$

where the two-phase friction factor is given by:

$$f_{\mathrm{tp}} = \frac{0.079}{\mathrm{Re}_{\mathrm{tp}}^{0.25}} \tag{3.20}$$

when $Re_{\mathrm{tp}} > 2300$ and

$$f_{\mathrm{tp}} = \frac{16}{\mathrm{Re}_{\mathrm{tp}}} \tag{3.21}$$

when $Re_{\mathrm{tp}} \leq 2300$. The two-phase Reynolds number is calculated as:

$$\mathrm{Re}_{\mathrm{tp}} = \frac{GD}{\mu_{\mathrm{tp}}} \tag{3.22}$$

and the averaged two-phase properties are:

$$\mu_{\mathrm{tp}} = x\mu_{\mathrm{v}} + (1-x)\mu_{\mathrm{l}} \text{ ; ([Chicchitti } et\ al. \text{ 1960])} \tag{3.23}$$

$$\rho_{\mathrm{tp}} = \left(\frac{x}{\rho_v} + \frac{(1-x)}{\rho_l}\right)^{-1} \tag{3.24}$$

According to [Thome 2004], the homogeneous flow model applied to in-tube flow is suitable for mass velocities greater than 2000 kg·m^{-2}·s^{-1} in the case of the friction factor calculations and for mass velocities less than 2000 kg·m^{-2}·s^{-1} and $\rho_{\mathrm{l}}/\rho_{\mathrm{v}} < 10$ for gravitational pressure drop calculations.

[Bankoff 1960] made an extension of the homogeneous two-phase model by including some two-dimensional effects. He derived expressions for the axial variation of velocity and void fraction in a tube. The assumption was that the axial variation could be determined using a power law function. The resulting two-phase frictional pressure gradient is:

$$\left(\frac{\mathrm{d}p}{\mathrm{d}z}\right)_{\mathrm{st}} = \left(\frac{\mathrm{d}p}{\mathrm{d}z}\right)_{\mathrm{lo}} \Phi_{\mathrm{tp}}^{7/4} \tag{3.25}$$

The liquid frictional pressure gradient is:

$$\left(\frac{\mathrm{d}p}{\mathrm{d}z}\right)_{\mathrm{lo}} = f_{\mathrm{lo}} \frac{2G^2}{D\rho_{\mathrm{l}}} \tag{3.26}$$

and the liquid friction factor f_{lo} is calculated using Eq.(3.17). The two-phase multiplier is:

$$\Phi_{\mathrm{tp}} = \frac{1}{1-x}\left[1-\gamma\left(1-\frac{\rho_{\mathrm{v}}}{\rho_{\mathrm{l}}}\right)\right]^{3/7}\left[1+x\left(\frac{\rho_{\mathrm{l}}}{\rho_{\mathrm{v}}}\right)-1\right] \tag{3.27}$$

where

$$\gamma = \frac{0.71 + 2.35\left(\frac{\rho_{\mathrm{v}}}{\rho_{\mathrm{l}}}\right)}{1+\left(\frac{1-x}{x}\right)\left(\frac{\rho_{\mathrm{v}}}{\rho_{\mathrm{l}}}\right)} \tag{3.28}$$

This method was derived using 375 data points for steam-water mixtures in horizontal and vertical tubes in a range of mass velocities from 950 to 1220 kg·m^{-2}·s^{-1}, pressures from 0.01 to 17.23 MPa and is applicable to vapor qualities from $0.00 < x < 0.90$.

In his work, [Chawla 1967] suggested the following method based on the vapor pressure gradient:

$$\left(\frac{\mathrm{d}p}{\mathrm{d}z}\right)_{\mathrm{st}} = \left(\frac{\mathrm{d}p}{\mathrm{d}z}\right)_{\mathrm{vo}} \Phi_{\mathrm{tp}}^{2} \tag{3.29}$$

The two-phase multiplier is:

$$\Phi_{\mathrm{tp}} = x^{1.75}\left[1 + S\left(\frac{1-x}{x}\right)\left(\frac{\rho_{\mathrm{v}}}{\rho_{\mathrm{l}}}\right)\right]^{2.375} \tag{3.30}$$

and the slip ratio S is:

$$S = 1/9.1\left[\frac{1-x}{x}(\mathrm{Re}_{\mathrm{vo}}\mathrm{Fr}_{\mathrm{h}})^{-0.167}\left(\frac{\rho_{\mathrm{l}}}{\rho_{\mathrm{v}}}\right)^{-0.9}\left(\frac{\mu_{\mathrm{l}}}{\mu_{\mathrm{v}}}\right)^{-0.5}\right] \tag{3.31}$$

where Fr_{h} is determining using the following expression:

$$\mathrm{Fr}_{\mathrm{h}} = G^2/gD\rho_{\mathrm{tp}}^2 \tag{3.32}$$

$$\mathrm{Re}_{\mathrm{vo}} = \frac{GD}{\mu_{\mathrm{v}}} \; ; \; \rho_{\mathrm{tp}} = \left(\frac{x}{\rho_{\mathrm{v}}} + \frac{1-x}{\rho_{\mathrm{l}}}\right)^{-1}$$

This method was derived using 88 data points for R-11 in horizontal tubes in a range of mass velocities from 20 to 200 kg·m^{-2}·s^{-1}, saturation temperatures from 0.0 to 20.0°C, inner diameter from 6.00 to 25.00 mm and is applicable to vapor qualities from $0.10 < \mathrm{x} < 0.95$.

[Chisholm 1973a] transformed the graphical procedure of [Baroczy 1965] to enable a more convenient application to the case of evaporating turbulent flow of two-phase mixtures in smooth tubes. The two-phase frictional pressure gradient is given as:

$$\left(\frac{\mathrm{d}p}{\mathrm{d}z}\right)_{\mathrm{lo}} = f_{\mathrm{lo}}\frac{2G^2}{D\rho_{\mathrm{l}}} \; ; \; \left(\frac{\mathrm{d}p}{\mathrm{d}z}\right)_{\mathrm{vo}} = f_{\mathrm{vo}}\frac{2G^2}{D\rho_{\mathrm{v}}} \tag{3.33}$$

friction factors are calculated for turbulent flows using Eqs.(3.17) and (3.18):

$$f_{\mathrm{lo}} = \frac{0.079}{\mathrm{Re}_{\mathrm{lo}}^{0.25}} \; ; \; f_{\mathrm{vo}} = \frac{0.079}{\mathrm{Re}_{\mathrm{vo}}^{0.25}} \quad \text{for Re} > 2000$$

and for Re< 2000 are used the following relations:

$$f_{\mathrm{lo}} = \frac{16}{\mathrm{Re}_{\mathrm{lo}}} \; ; \; f_{\mathrm{vo}} = \frac{16}{\mathrm{Re}_{\mathrm{vo}}} \; ; \text{ for Re} < 2000 \tag{3.34}$$

Reynolds numbers are obtained using Eqs. (2.57) and (2.58):

$$\mathrm{Re}_{\mathrm{lo}} = \frac{GD}{\mu_{\mathrm{l}}} \; ; \mathrm{Re}_{\mathrm{vo}} = \frac{GD}{\mu_{\mathrm{v}}}$$

The parameter Y is obtained from the ratio of the frictional pressure drops as follows:

$$Y^2 = \frac{\left(\frac{\mathrm{d}p}{\mathrm{d}z}\right)_{\mathrm{vo}}}{\left(\frac{\mathrm{d}p}{\mathrm{d}z}\right)_{\mathrm{lo}}} \tag{3.35}$$

Then, the two-phase multiplier is determined as:

$$\Phi_l^2 = 1 + (Y^2 - 1)\left[Bx^{2-n/2}(1-x)^{2-n/2} + x^{2-n}\right] \tag{3.36}$$

where n is the exponent from the friction factor expression of Blasius (n = 0.25). Finally, Chisholm parameter B is then determined following the procedure described below:

For $0 < Y < 9.5$, B is calculated as:

$$B = \frac{55}{G^{1/2}} \text{ for } G \geq 1900\text{kg}\cdot\text{m}^{-2}\cdot\text{s}^{-1} \tag{3.37}$$

$$B = \frac{2400}{G} \text{ for } 500 < G < 1900\text{kg}\cdot\text{m}^{-2}\cdot\text{s}^{-1} \tag{3.38}$$

$$B = 4.8 \text{ for } G \leq 500\text{kg}\cdot\text{m}^{-2}\cdot\text{s}^{-1} \tag{3.39}$$

For $9.5 < Y < 28$, B is calculated as:

$$B = \frac{520}{YG^{1/2}} \text{ for } G \leq 600\text{kg}\cdot\text{m}^{-2}\cdot\text{s}^{-1} \tag{3.40}$$

$$B = \frac{21}{Y} \text{ for } G > 600\text{kg}\cdot\text{m}^{-2}\cdot\text{s}^{-1} \tag{3.41}$$

For $Y > 28$, B is calculated as:

$$B = \frac{1500}{Y^2 G^{1/2}} \tag{3.42}$$

Once the value of B is determined, the two-phase multiplier can be calculated and therefore the frictional pressure drop can be determined.

This method was derived using 459 data points for steam-water in horizontal and vertical tubes in a range of mass velocities from 520 to 640 kg·m^{-2}·s^{-1}, pressures from 0.64 to 4.0 MPa, inner diameter from 26.00 to 27.00 mm and is applicable to vapor qualities from $0.10 < x < 0.75$.

It is important to note that, while the procedures developed for smooth tubes gave satisfactory agreement with steam/water mixtures in vertical channels, these procedures considerably underestimated experimental air-water flow data in horizontal tubes when the mass velocity was below 700 kg·m^{-2}·s^{-1}.

One of the most accurate two-phase pressure drop correlations is said to be that of [Friedel 1979]. It was obtained by optimizing an equation for Φ_{lo}^2 using a large data base of two-phase pressure drop measurements. This method is for any vapor qualities and utilizes a two-phase multiplier as:

$$\left(\frac{\mathrm{d}p}{\mathrm{d}z}\right)_{\text{st}} = \left(\frac{\mathrm{d}p}{\mathrm{d}z}\right)_{\text{lo}} \Phi_{\text{lo}}^2 \tag{3.43}$$

where $\left(\frac{\mathrm{d}p}{\mathrm{d}z}\right)_{\text{lo}}$ is determined from:

$$\left(\frac{\mathrm{d}p}{\mathrm{d}z}\right)_{\text{lo}} = f_{\text{lo}}\frac{2G^2}{D\rho_{\text{l}}} \tag{3.44}$$

and the corresponding values of liquid friction factor and liquid Reynolds numbers are given by:

$$f_{\text{lo}} = \frac{0.079}{\text{Re}_{\text{lo}}^{0.25}} \; ; \text{Re}_{\text{lo}} = \frac{GD}{\mu_{\text{l}}} > 2000$$

$$f_{\mathrm{lo}} = \frac{16}{\mathrm{Re}_{\mathrm{lo}}} \text{ ; for } \mathrm{Re}_{\mathrm{lo}} < 2000$$

The two-phase multiplier is correlated as:

$$\Phi_{\mathrm{lo}}^2 = C_{F1} + \frac{3.24 C_{F2}}{\mathrm{Fr}_{\mathrm{tp}}^{0.045}\mathrm{We}_{\mathrm{l}}^{0.035}} \tag{3.45}$$

where $\mathrm{Fr}_{\mathrm{tp}}$, C_{F1}, C_{F2} and ρ_{tp} are as follows:

$$\mathrm{Fr}_{\mathrm{tp}} = G^2/gD\rho_{\mathrm{tp}}^2 \text{ ; } \mathrm{We}_{\mathrm{l}} = G^2 D/\sigma\rho_{\mathrm{tp}} \tag{3.46}$$

$$C_{F1} = (1-x)^2 + x^2\left(\frac{\rho_{\mathrm{l}}}{\rho_{\mathrm{v}}}\right)\left(\frac{f_{\mathrm{v}}}{f_{\mathrm{l}}}\right) \tag{3.47}$$

$$C_{F2} = x^{0.78}(1-x)^{0.224}\left(\frac{\rho_{\mathrm{l}}}{\rho_{\mathrm{v}}}\right)^{0.91}\left(\frac{\mu_{\mathrm{v}}}{\mu_{\mathrm{l}}}\right)^{0.19}\left(1-\frac{\mu_{\mathrm{v}}}{\mu_{\mathrm{l}}}\right)^{0.7} \tag{3.48}$$

$$\rho_{\mathrm{tp}} = \left(\frac{x}{\rho_{\mathrm{v}}} + \frac{(1-x)}{\rho_{\mathrm{l}}}\right)^{-1}$$

The correlation is applicable to vertical upflow and to horizontal flow. This method is known to work well when the ratio $\mu_{\mathrm{l}}/\mu_{\mathrm{v}} < 1000$, which is the case for most working fluids and operating conditions.

The method presented by [Grönnerud 1979] was developed specifically for refrigerants by using around 1000 data points for R-12 and R-717 in a 26.2 mm inner diameter horizontal tube. This method is for vapor qualities from 0 to 1 and utilizes a two-phase multiplier as:

$$\left(\frac{\mathrm{d}p}{\mathrm{d}z}\right)_{\mathrm{st}} = \left(\frac{\mathrm{d}p}{\mathrm{d}z}\right)_{\mathrm{lo}}\Phi_{\mathrm{lo}}^2 \tag{3.49}$$

where $\left(\frac{\mathrm{d}p}{\mathrm{d}z}\right)_{\mathrm{lo}}$ is determined from:

$$\left(\frac{\mathrm{d}p}{\mathrm{d}z}\right)_{\mathrm{lo}} = f_{\mathrm{lo}}\frac{2G^2}{D\rho_{\mathrm{l}}} \tag{3.50}$$

$$f_{\mathrm{lo}} = \frac{0.079}{\mathrm{Re}_{\mathrm{lo}}^{0.25}} \text{ ; } \mathrm{Re}_{\mathrm{lo}} = \frac{GD}{\mu_l} > 2000$$

$$f_{\mathrm{lo}} = \frac{16}{\mathrm{Re}_{\mathrm{lo}}} \text{ ; for } \mathrm{Re}_{\mathrm{lo}} < 2000$$

and the two-phase multiplier is:

$$\Phi_{\mathrm{lo}}^2 = 1 + \left(\frac{\mathrm{d}p}{\mathrm{d}z}\right)_{\mathrm{Fr}}\left[\left(\frac{\rho_{\mathrm{l}}}{\rho_{\mathrm{v}}}\right)\left(\frac{\mu_{\mathrm{l}}}{\mu_{\mathrm{v}}}\right)^{0.25} - 1\right] \tag{3.51}$$

The frictional pressure gradient depends on the Froude number and is given as:

$$\left(\frac{\mathrm{d}p}{\mathrm{d}z}\right)_{\mathrm{Fr}} = f_{\mathrm{Fr}}\left(x + 4(x^{1.8} - x^{10} f_{\mathrm{Fr}}^{0.5})\right) \tag{3.52}$$

When applying this expression, if the liquid Froude number $\mathrm{Fr}_{\mathrm{l}} = G^2/gD\rho_{\mathrm{l}}^2 \geq 1$, then the friction factor $f_{\mathrm{Fr}} = 1.0$, or if $\mathrm{Fr} \leq 1$, then:

$$f_{\mathrm{Fr}} = \mathrm{Fr}_{\mathrm{l}}^{0.3} + 0.0055 \left(\ln \frac{1}{\mathrm{Fr}_{\mathrm{l}}} \right)^2 \tag{3.53}$$

This method was derived in a range of mass velocities from 20 to 1600 $\mathrm{kg \cdot m^{-2} \cdot s^{-1}}$, and saturation temperatures from -45.0 to 5.0 °C.

A new correlation for the prediction of frictional pressure drop for two phase flow in pipes was developed by [Müller-Steinhagen & Heck 1986]. This correlation and fourteen correlations from the literature were checked against a data bank containing 9300 measurements of frictional pressure drop for a variety of fluids and flow conditions. They found that the best agreement between predicted and measured values was obtained by the correlation of [Bandel. 1973] which, however, is quite complex to implement and use. The correlation proposed in their paper still predicted the frictional pressure drop with reasonable accuracy. It includes single-phase liquid and vapor pressure drops and predicts correctly the influence of flow parameters.

The correlation developed by [Müller-Steinhagen & Heck 1986] is in essence a clever empirical interpolation between all liquid flow and all vapor flow:

$$\left(\frac{\mathrm{d}p}{\mathrm{d}z} \right)_{\mathrm{st}} = M (1-x)^{1/3} + \left(\frac{\mathrm{d}p}{\mathrm{d}z} \right)_{\mathrm{vo}} x^3 \tag{3.54}$$

where the factor M is:

$$M = \left(\frac{\mathrm{d}p}{\mathrm{d}z} \right)_{\mathrm{lo}} + 2 \left(\left(\frac{\mathrm{d}p}{\mathrm{d}z} \right)_{\mathrm{vo}} - \left(\frac{\mathrm{d}p}{\mathrm{d}z} \right)_{\mathrm{lo}} \right) x \tag{3.55}$$

the frictional pressure gradients for all liquid $\left(\frac{\mathrm{d}p}{\mathrm{d}z} \right)_{\mathrm{lo}}$ and all vapor $\left(\frac{\mathrm{d}p}{\mathrm{d}z} \right)_{\mathrm{vo}}$ flow and are defined as:

$$\left(\frac{\mathrm{d}p}{\mathrm{d}z} \right)_{\mathrm{lo}} = f_{\mathrm{lo}} \frac{2G^2}{D\rho_{\mathrm{l}}} \; ; \; \left(\frac{\mathrm{d}p}{\mathrm{d}z} \right)_{\mathrm{vo}} = f_{\mathrm{vo}} \frac{2G^2}{D\rho_{\mathrm{v}}} \tag{3.56}$$

The friction factors are obtained with:

$$\mathrm{Re}_{\mathrm{lo}} = \frac{GD}{\mu_{\mathrm{l}}} \; ; \; \mathrm{Re}_{\mathrm{vo}} = \frac{GD}{\mu_{\mathrm{v}}}$$

$$f_{\mathrm{lo}} = \frac{0.079}{\mathrm{Re}_{\mathrm{lo}}^{0.25}} \; ; \; f_{\mathrm{vo}} = \frac{0.079}{\mathrm{Re}_{\mathrm{vo}}^{0.25}} \quad \text{for Re} > 2000$$

$$f_{\mathrm{lo}} = \frac{16}{\mathrm{Re}_{\mathrm{lo}}} \; ; \; f_{\mathrm{vo}} = \frac{16}{\mathrm{Re}_{\mathrm{vo}}} \; ; \text{ for Re} < 2000$$

This method was derived using 7851 data points for several mixtures (air-water, steam-water,hydrocarbons-air, oils-air,R-11, R-12, R-22, Neon, N_2) in horizontal tubes and 1462 data points in vertical tubes including air-water, steam-water, R-12 and argon combinations.

In general, the methods that follow an empirical approach, such as [Grönnerud 1979], [Friedel 1979] and [Müller-Steinhagen & Heck 1986] for example, do not account for flow pattern effects on the process, which are particularly important at low flow rates (stratification effects) and high vapor qualities (dry-out effects). Furthermore, they do not use the actual velocities of liquid and vapor phases by introduction of the local void fraction in the method.

[Moreno Quibén & Thome 2007] carried out an analytical study in order to develop a new two-phase frictional prediction method. Their model has been developed following a phenomenological approach as the interfacial structure between the phases is taken into account. They selected the [Wojtan *et al.* 2005a] diabatic two-phase flow pattern map to provide the corresponding interfacial structure. The model treats each flow regime separately and then insures a smooth transition at the transition boundary, in agreement with the experimental observations. Next, based on a statistical comparison, they concluded that the two-phase frictional pressure drop flow pattern map based model successfully predicts the new experimental database and captures the numerous trends observed in the data.

The complete set of equations will not be given here due to their complexity and length but the calculating procedure is given in the paper by [Moreno Quibén & Thome 2007]. Below, the Moreno-Quibén and Thome model and its calculation procedure for the annular flow regime is presented and described.

$$\left(\frac{\mathrm{d}p}{\mathrm{d}z}\right)_{\mathrm{st}} = \frac{2G^2 f_{\mathrm{annular}} x^2}{D\rho_{\mathrm{v}}\varepsilon^2} \tag{3.57}$$

where the friction factor is obtained by:

$$f_{\mathrm{annular}} = 0.67\left[\frac{1-\varepsilon}{4}\right]^{1.2}\left[\frac{gD^2(1-\varepsilon)^2(\rho_{\mathrm{l}}-\rho_{\mathrm{v}})}{16\sigma}\right]^{-0.4}\left(\frac{\mu_{\mathrm{v}}}{\mu_{\mathrm{l}}}\right)^{0.08}\mathrm{We}^{-0.034} \tag{3.58}$$

and the Weber number is given by Eq.(2.62):

$$\mathrm{We} = \frac{\rho_{\mathrm{l}} u_{\mathrm{l}}^2 D}{\sigma}$$

where the void fraction ε can be calculated with the [Steiner 1993] version of the [Rouhani & Axelsson 1970] equation for horizontal tubes.

The [Moreno Quibén & Thome 2007] model was developed for R-22, R-410A and R-134a during flow boiling in horizontal tube. The model was based on diameters comprised between 8 and 13.8 mm over the entire range of vapor quality.

In the article of [Revellin & Haberschill 2009], a simple linear function was developed for predicting the frictional pressure drop based on an explicit expression for the vapor quality corresponding to the maximum pressure drop (x_{M}) and on the pressure drop for liquid and vapor phases.

In order to develop their method, the authors first proposed an explicit expression for the vapor quality corresponding to the maximum pressure drop (x_{M}) which is given by three cases ($x_{\mathrm{M1}}, x_{\mathrm{M2}}$ and x_{M3}):

$$x_{\mathrm{M1}} = -\frac{a_2}{3a_3} + 2\sqrt{\frac{-p_1}{3}}\cos\left[\frac{1}{3}\arccos\left(\frac{-p_2}{2}\sqrt{\frac{27}{-p_1^3}}\right) + \frac{4\pi}{3}\right] \tag{3.59}$$

where x_{M1} is the vapor quality corresponding to the maximum pressure drop in the annular flow regime.

$$x_{\mathrm{M2}} = 0.58e^{\left[0.52-0.23We_{\mathrm{v}}^{0.17}Fr_{\mathrm{v}}^{0.37}(\frac{\rho_{\mathrm{v}}}{\rho_{\mathrm{l}}})^{0.25}(\frac{q}{q_{\mathrm{crit}}})^{0.70}\right]} \tag{3.60}$$

x_{M2} corresponds to the expression of the annular-to-dryout transition vapor quality according to the flow pattern map of [Wojtan *et al.* 2005a].

x_{M3} is the annular-to-mist flow transition vapor quality given by [Wojtan *et al.* 2005a] and is expressed as follows:

$$x_{\mathrm{M3}} = 0.61e^{\left[0.57-0.0058We_{\mathrm{v}}^{0.38}Fr_{\mathrm{v}}^{0.15}(\frac{\rho_{\mathrm{v}}}{\rho_{\mathrm{l}}})^{-0.09}(\frac{q}{q_{\mathrm{crit}}})^{0.27}\right]} \tag{3.61}$$

Finally, according to [Moreno Quibén & Thome 2007], x_{M} is based on flow regimes and is retained as:

$$x_{\mathrm{M}} = \min(x_{\mathrm{M1}}, x_{\mathrm{M2}}, x_{\mathrm{M3}}) \tag{3.62}$$

The procedure to calculate the parameters a_2, a_3, p_1, p_2, q_{crit} is described in the article of [Revellin & Haberschill 2009].

The values of $\left(\frac{\mathrm{d}p}{\mathrm{d}z}\right)_{\mathrm{lo}}$ for $x = 0$, $\left(\frac{\mathrm{d}p}{\mathrm{d}z}\right)_{\max}$ for $x = x_{\mathrm{M}}$ and $\left(\frac{\mathrm{d}p}{\mathrm{d}z}\right)_{\mathrm{vo}}$ for $x = 1$ are known. As a first approximation, the authors developed a simple mathematical function to predict the frictional pressure drop by assuming a linear variation of the pressure drop as a function of x for $0 \leq x < x_{\mathrm{M}}$ and another linear variation of the pressure drop as a function of x for $x_{\mathrm{M}} \leq x \leq 1$. As a result, the approximation was:

For $0 \leq x < x_{\mathrm{M}}$

$$\left(\frac{\mathrm{d}p}{\mathrm{d}z}\right)_{\mathrm{st}} = \left[\left(\frac{\mathrm{d}p}{\mathrm{d}z}\right)_{\mathrm{l}} - \left(\frac{\mathrm{d}p}{\mathrm{d}z}\right)_{\max}\right] \frac{x}{x_{\mathrm{M}}} - \left(\frac{\mathrm{d}p}{\mathrm{d}z}\right)_{\mathrm{l}} \tag{3.63}$$

For $x_{\mathrm{M}} \leq x \leq 1$

$$\left(\frac{\mathrm{d}p}{\mathrm{d}z}\right)_{\mathrm{st}} = \left[\left(\frac{\mathrm{d}p}{\mathrm{d}z}\right)_{\mathrm{v}} - \left(\frac{\mathrm{d}p}{\mathrm{d}z}\right)_{\max}\right] \frac{x-1}{x_{\mathrm{M}}-1} - \left(\frac{\mathrm{d}p}{\mathrm{d}z}\right)_{\mathrm{v}} \tag{3.64}$$

The linear approach proposed by [Revellin & Haberschill 2009] presented the best statistics for each flow regime reporting almost 86% of the data within a ± 30% error band.

The methods that follow a phenomenological approach ([Moreno Quibén & Thome 2007, Revellin & Haberschill 2009]) give an acceptable representation of the pressure gradient trend versus vapor quality and they go to acceptable limits at $x = 0$ and $x = 1$. They are also able to capture reasonably well the position and magnitude of the characteristic peak at high vapor qualities.

3.1.4 Void fraction

The void fraction ε is one of the most important parameters used to characterize two-phase flows. It is the key physical value for determining numerous other important parameters, such as two-phase density and the two-phase viscosity, and is of fundamental importance in models for predicting flow pattern transitions and pressure drop. The most widely used is the cross-sectional average void fraction which is usually predicted by several methods.

The general velocity ratio model is defined as:

$$\varepsilon = \left[1 + \left(\frac{1-x}{x}\right)\frac{\rho_{\mathrm{v}}}{\rho_{\mathrm{l}}} S\right]^{-1} \tag{3.65}$$

The first method to be introduced is the homogeneous void fraction model. From the definition of the cross-section void fraction of a tube of area A, the mean vapor and liquid velocities are given by Eqs. (2.8) and (2.9) in terms of the vapor quality. The basis of the homogeneous void fraction model is that it assumes that the liquid and the vapor phase travel at the same velocity ($S = 1$). From that assumption, the homogeneous void fraction, denoted by ε_{H}, is expressed as:

$$\varepsilon_{\mathrm{h}} = \left[1 + \left(\frac{1-x}{x}\right)\frac{\rho_{\mathrm{v}}}{\rho_{\mathrm{l}}}\right]^{-1} \tag{3.66}$$

This model is reasonably accurate for a limited range of circumstances, among very large mass velocities or at high vapor qualities.

For horizontal co-current flows, u_{v} is generally greater than u_{l}, such that $S > 1$. Numerous analytical and empirical methods have been proposed to calculate the velocity ratio S

[Zivi 1964] proposed a model for annular flow, assuming that no liquid is entrained in the central vapor core. Later, [Chisholm. 1973b] proposed a new expression for the velocity ratio S based on a simple annular flow theory and application of the homogeneous theory on the fluid density, producing approximately equal frictional pressure gradients in each phase.

[Zuber & Findlay 1965] proposed the original form of the well known drift flux model. This model takes into account both the effect of nonuniform flow and void fraction profiles as well as the effect of the relative velocity between the phases. In contrast to previous analysis, [Zuber & Findlay 1965] derived an expression which is applicable to any two-phase flow regime. As can be seen, the drift flux model of [Zuber & Findlay 1965] allows one to calculate the void fraction ε taking into account numerous aspect occurring in two-phase flow.

[Rouhani & Axelsson 1970] presented a drift flux model based on that of [Zuber & Findlay 1965] in the form of:

$$\varepsilon = \frac{x}{\rho_{\mathrm{v}}}\left[C_o\left(\frac{x}{\rho_{\mathrm{v}}} + \frac{1-x}{\rho_{\mathrm{l}}}\right) + \frac{V_{\mathrm{vj}}}{G}\right]^{-1} \tag{3.67}$$

substitution of the weighted mean drift flux velocity $\vec{V}_{\mathrm{vj}}$ and the distribution parameter C_o into equation (3.67), results in expression:

$$\varepsilon = \frac{x}{\rho_{\mathrm{v}}}\left[(1+0.12(1-x))\left(\frac{x}{\rho_{\mathrm{v}}} + \frac{1-x}{\rho_{\mathrm{l}}}\right) + \frac{1.18(1-x)[g\sigma(\rho_{\mathrm{l}}-\rho_{\mathrm{v}})]^{0.25}}{G\rho_{\mathrm{l}}^{0.5}}\right]^{-1} \tag{3.68}$$

This form of the [Rouhani & Axelsson 1970] model was proposed for general use by [Steiner 1993] irrespective of flow pattern but for horizontal flows.

[Taitel & Dukler 1976] proposed a model for predicting flow regimes transitions. Starting from a momentum balance of each phase in an equilibrium stratified flow and assuming the same pressure gradient in both phases, they obtained a set of dimensionless equations in which can be obtained a relationship between the void fraction and the liquid height.

Recently, [Wojtan *et al.* 2005b] measured the dynamic void fraction in stratified types of flow utilizing an optical image analysis technique developed by [Ursenbacher *et al.* 2004, Wojtan *et al.* 2004] inside round horizontal 8.0 mm sight-glass tube. This experimental void fraction data and also the previous results for a 13.6 mm sight-glass tube presented by [Wojtan *et al.* 2004] have been compared to the predictions given by [Rouhani & Axelsson 1970, Taitel & Dukler 1976, Zivi 1964] and the homogeneous void fraction model. Results of this comparison showed that the drift flux model of [Rouhani & Axelsson 1970] for horizontal flows was the best of the four models tested and accurately predicts the stratified flow void fraction data.

3.2 Two-phase flow in return bends

To cater to the needs of diverse engineering applications, such as refrigeration, two-phase pressure drops in return bends in HVAC&R systems have been studied by several authors in the open literature. These studies highlight the impact of the large number of independent parameters governing the flow among which geometric configuration of the tube such as the curvature ratio, mass and volume fractions of the individual phases, pressure, fluid properties, mass velocity, orientation of the return bend (i.e horizontal, vertical or inclined) and flow patterns. Since the 60's, several refrigerants have been studied, among which CFCs, HCFCs and HFCs ([Pierre 1964, Traviss & Rohsenow 1973, Geary 1975]. Most recent researches have been carried out for R-134a and R-410A([Chen *et al.* 2008b, Silva-Lima & Thome 2010, Padilla *et al.* 2011b]).

One of the most important parameters when designing an experimental bench for measuring two-phase pressure drop in singularities is the perturbation lengths up- and downstream of them. Indeed, the location of the pressure taps before and after the return bend is important.

3.2.1 Perturbation lengths up- and downstream of a return bend

In the study of [Traviss & Rohsenow 1973] on R-12 two-phase flow in straight tubes with inner diameters of 12.70 mm and 25.40 mm, the pressure drop was measured incrementally along the test section with the first pressure tap located approximately $10D$ downstream of the return bend. They found that the amount of pressure recovery in the test section downstream of the return bend was negligible. The pressure gradient in the first downstream increment did not deviate significantly (±10%) from the fully developed pressure gradient.

In the article of [Hoang & Davis 1984], the authors suggested that a length equal to $9D$ is required to complete the remixing process of the phases after leaving a return bend.

Recently, [Padilla *et al.* 2011b] carried out preliminary tests which show that the recovery length necessary for a correct pressure drop measurement downstream of the return bend is less than $20D$. These results are consistent with the few information available in the literature. Nevertheless, further work is called for to more thoroughly investigate the perturbation lengths up- and downstream of a return bend and this is one of the aims of this thesis.

3.2.2 Pressure drop in return bends

3.2.2.1 Existing experimental studies for pressure drop prediction in horizontal return bends

Two-phase flow pressure drop in return bends in refrigeration systems have been experimentally investigated by several authors in the open literature. [Pierre 1964] studied the pressure drop of R-12 in return bends with two-phase flow for the oil-free fluid and for oil-refrigerant mixtures. He used a test section which consisted of a straight tube and an evaporator, made with six 180° return bends in copper tubing. The evaporation temperature was 0°C and -10°C, and the vapor quality in the bend was between 0.30 and 0.98. The refrigerant mass flux was comprised between 134 and 208 $\text{kg}\cdot\text{m}^{-2}\cdot\text{s}^{-1}$. The author made a calculation diagram for pressure drop in evaporators with an experimental resistance factor for different types of return bends.

Using the same fluid (R-12), [Traviss & Rohsenow 1973] measured two-phase pressure drops in a 8 mm tube in order to determine whether the disturbance caused by a return bend was only a localized effect or extended over a significant length of the condenser tube. They found that the effect of a return bend on the downstream pressure drop was negligible when averaged over a length of 90 tube diameters or more.

[Geary 1975] investigated the two-phase adiabatic flow pressure drop in return bends based on his R-22 data with tube diameters from 11.05 mm to 11.63 mm with curvature ratios ($2R/D$) from 2.317 to 6.54. He proposed a correlation for predicting the two-phase pressure drop for design purposes in typical air-conditioning applications. In this paper, the author also proposes two-phase frictional pressure drop data for straight tubes.

Later, [Chen *et al.* 2004] presented single-phase and two-phase frictional data of R-410A in four types of return bends with tube diameters ranging from 3.3 and 5.07 mm and curvature ratios varying from 3.91 to 8.15. They proposed a modified two-phase friction factor based on the Geary's correlation. Then, [Chen *et al.* 2007a] presented a study with single-phase and two-phase pressure drop data for R-134a/oil mixture with oil concentration of 0%, 1%, 3% and 5%, flowing in a wavy tube with an inner diameter of 5.07 mm and a curvature ratio of 5.18.

Very recently, [Chen *et al.* 2008b] presented measurements of R-134a two-phase frictional pressure gradients for vertical and horizontal arrangements of a U-type copper wavy tube which contained nine consecutive return bends with an inner diameter of 5.07 mm and a curvature ratio of 5.18. The working temperature was near 25°C, the mass flux ranged from 200 to 700 $\text{kg}\cdot\text{m}^{-2}\cdot\text{s}^{-1}$ and the vapor quality varied from 0.1 to 0.9. They conducted their tests for vertical arrangement by selecting the inlet flow at the upper tube or at the lower tube in the return bend. They found that the pressure gradients in the return bend of vertical arrangement were always higher than those of horizontal arrangement regardless the flow entry was at the upper or at the lower tube. Furthermore, the pressure gradient for a flow entering at the upper tube was higher than that for a flow entering at the lower tube because of the influence of buoyancy.

3.2.2.2 Existing experimental studies for pressure drop prediction in vertical return bends

Two-phase pressure drops in return bends in refrigeration systems have been investigated by several authors in the open literature. So far, experimental studies dealing with two-phase flow in return bends are relatively scarce, especially in the case of vertical return bends.

In general, two-phase flow in vertical return bends involves the combined action of gravitational, centrifugal and buoyant forces, which tends to produce such complications as inhomogeneous phase distribution, flow reversal, flooding, secondary flow and coalescence. When positioned vertically, a greater pressure drop should be incurred through the curved channel than when the curve is in the horizontal plane ([Usui 1980]).

[Usui 1980, Usui 1981] conducted experiments on the flow behavior, average void fraction and pressure drop in air-water two-phase flow flowing upward and downward through a C-shaped bend in vertical plane. The test tubes inner diameters were $D = 16$ and 24 mm, curvature ratios ($2R/D$) ranging from 11.25 to 22.5. Consequently, some complex flow phenomena such as flow reversal and flooding are encountered due, among others, to interactions of gravity and centrifugal force. The combined action of gravity and centrifugal force was expressed in term of the so-called "modified Froude number" in both upward and downward flows. The author also observed that the average void fraction of the downward flow in the U-bend was very different from that in the straight tube, in contrast to the case of upward flow.

For single-phase flow, it is well known that a secondary flow is generated when fluid flows across the curved channel ([Dean 1927]. The fluid flow characteristics are rather complicated since the centrifugal force drives the more rapid fluid in the concave part of the curve channel while the fluid in the convex parts is slowing down. The magnitude of such secondary flows is reduced with an increase of bend curvature (R), and with a decrease of fluid velocity. For two-phase flow across the curved channel, the study is more complex because of the unequal values of velocity, density and other phase properties.

There are some studies related to the frictional characteristics in U-type return bends. For detailing the flow patterns across return bend, [Chen *et al.* 2002] and [Wang *et al.* 2003] conducted visualizations for air-water mixtures through horizontal return bends ($D = 3$, 5 and 6.9 mm) having curvature ratios of 3 and 7.1. They provided some qualitative description about the two-phase flow across the horizontal return bends. However, their studies were pertinent to horizontal arrangement only and no detailed quantitative description of the slug flow pattern was reported. In this sense, [Wang *et al.* 2005] conducted a study to examine some characteristics of the slug flow such as change of flow pattern and the translational velocities across the vertical return bend.

[Wang *et al.* 2008] performed visual observations of the two-phase flow patterns of the air-water mixtures inside two 3.0 mm and two 6.9 mm smooth tubes forming vertical return bends. Flow reversal and freezing slug phenomena were observed for the vertical return bend having $D = 6.9$ mm. According to the authors, apparently this “freezing slug” phenomenon is related to the buoyancy force in the return bend which contributes to slow down the motion of the vapor slug. Those phenomena were absent in previously reported results for horizontal configurations. The authors also observed that with $D = 3.0$ mm, at the same mass flux and vapor quality, there was no great difference between the two-phase flow patterns developed with the flow entering in the upper tube or in lower tube.

Flow pattern and bubble behavior are the fundamentals to better understand the dynamics of the two-phase flow in a return bend. For investigations of the slug flow in vertical, horizontal, and inclined tubes, many researches were available in the literature([Hout *et al.* 2002, Sun *et al.* 2004, Roitberg *et al.* 2008]). Note that the existing studies concerning slug flow pattern are only for straight tubes. However, in real thermo-fluids systems, exploitation of the curved tubes for connection is very common. Very little information has been found in the literature which reveals the behavior of a bubble under the effects of the dynamic forces of the fluid. [Yeh & Yang 1968] carried out an analytical study of the time history of the velocity, size and deformation of a bubble moving in the flow field around a point source or sink by considering the case where the changes in the bubble velocity, size and deformation are caused by the dynamic forces of the fluid, rather than the initial perturbation of the bubble shape. The analysis presented is general and may be applied to an initially spherical as well as non-spherical bubble.

Recently, [Meng *et al.* 2009] reported bubble dynamical behavior in 180° return bend. To describe this behavior, the test section is divided into four zones to understand the bubble detachment mechanism. These four zones were identified to describe bubble behavior according to the experimental observations of flow pattern and bubble size: the secondary flow zone, the transition zone, the inertia zone and the buoyancy zone. Each of them was combined with unique interaction between two phases.

To better understand the dynamics of bubbles, a review of some of the most representative works in this domain has been carried out. However, most published works are focused to the dynamics of a rising bubble in a static liquid, nevertheless, the information may be very useful in the present study.

3.2.2.3 Bubble dynamical behavior in a return bend

The understanding of the motion of gas bubbles in a liquid depends on appropriate expressions for the drag, lift, and apparent mass forces on the bubble. Experimental studies ([Ford & Loth 1997, Shew *et al.* 2006, Lakshmanan *et al.* 2011]) have shown distinctly different shape and trajectory oscillations depending on the bubble size, as well as the bubble and liquid properties, e.g. density, viscosity, and surface tension. There are small bubbles with an almost spherical shape that have linear rising trajectories, or big bubbles that rise on a helical path, while at the same time change their shape periodically. The relationship between the bubble size and the rising trajectory and its dependency on the bubble peak velocity is well described by [Peebles & Garber 1953] correlation for adiabatic bubble rise and experimentally validated by [Siedel *et al.* 2011].

Closed form analytical expressions for the hydrodynamic forces currently exist only for low Reynolds numbers and minimal shape deformations. In [Auton *et al.* 1988], assuming that the bubble equivalent radius is small compared with the scale over which the strain rate changes, the authors presented a general expression for the fluid force on a bubble as a body of simple shape moving through inviscid fluid in which there is an unsteady non-uniform rotational velocity field in three dimensions. The equation of motion for bubbles formulated by [Auton *et al.* 1988] describes the contributions to the bubble's acceleration from inertial forces (e.g pressure gradient and added mass), buoyancy forces, drag forces and lift forces. To use this formulation, it is also necessary to know the drag function f_{D} which depends on the drag coefficient. One early work in the search for the drag coefficients of (solid) particles in liquids goes back to [Stokes 1851], who derives an analytical solution for the flow around a spherical, solid particle in the creeping-flow limit. Very small air bubbles in the range $D_{\mathrm{eq}} < 0.3$ mm in water are found to behave like solid spheres; their drag coefficient can be expressed by Stokes' law. Later, the [Stokes 1851] correlation is empirically extend to higher Reynolds numbers in the range of $\mathrm{Re} < 800$ by [Schiller & Naumann 1933]. This correlation gives a very good approximation for the drag of solid spheres and is still commonly used in engineering applications due to its accuracy and simplicity. However, analytical formulations are far from being able to handle general situations of turbulent flow with substantive deformation, and the assumptions of each formulation must be carefully considered. For such conditions empirical relations must typically suffice and be continually enhanced through new experimental data until new analytical formulations can be derived and validated.

Despite some studies were oriented toward the fundamental aspects of two-phase flow across return bends, the majority of the previous experimental studies have been conducted with air-water mixtures. Very recently, in order to extend the existing database available in the literature toward different synthetic fluids such as HFC refrigerants, [Padilla *et al.* 2011b] presented 238 pressure drop data points measured for two-phase flow of R-410A in horizontal return bends of diameter (D) from 7.9 to 10.85 mm and the curvature ratio ($2R/D$) from 3.68 to 4.05. This study showed the influence of mass velocity, saturation temperature and inner diameter on the return bend pressure drop. Besides, a next generation refrigerant has been developed by the refrigeration industry for environmental reasons, namely the HydroFluoroOlefin (HFO) 1234yf. The two-phase flow characteristics of this fluid need to be investigated.

Moreover, the return bends used in heat transfer equipment may be vertically arranged rather than horizontally arranged. However, rather rare studies are investigated about the basic aspect of the two-phase flow characteristics in vertical return bends. It is obvious that the flow patterns are strongly related to the pressure drop characteristics. As a consequence, it is of great interest to examine the two-phase flow characteristics inside the vertical return bend subject to the tube size and various curvature ratios.

3.2.2.4 Two-phase frictional pressure drop prediction methods in return bends

In the open literature, among the articles presenting correlations for two-phase pressure drop of refrigerants in return bends, only six provide complete information (fluid, saturation temperature, mass velocity, diameter, etc.). [Pierre 1964] proposed a correlation, only valid for horizontal tubes, based on his experiments carried out with R-12 by assuming that the total flow resistance is divided into two part: the first one corresponds to the turning of the flow, and the second one to the friction only. This is expressed as follows:

$$\Delta p_{\mathrm{rb}} = \Delta p_{\mathrm{o}} + \Delta p_{\mathrm{f}} \tag{3.69}$$

where Δp_{rb} is the total pressure drop in the return bend, Δp_{o} is the pressure drop due to the turning of the flow and Δp_{f} is the pressure drop due to the friction. For the calculation of Δp_{o} and Δp_{f}, one needs to refer to two different graphs so as to determine the corresponding resistance factor. Those values of the resistance factors obtained by Pierre showed not to be much influenced by the center-to-center distance of the bend ($2R$). In that sense, Pierre concluded that this parameter was not of major importance and did not include it in his pressure drop correlation.

[Geary 1975] presented a correlation (using 4 empirical constants) by using the friction factor approach for straight tubes. The correlation of the two-phase pressure drop in return bends consisted in a single-phase pressure drop equation for vapor flow only. He included a dimensionless friction factor depending on the effects of the vapor quality and the center-to-center distance in return bends. The pressure drop induced by the return bends was expressed as:

$$\Delta p_{\mathrm{rb}} = f \frac{L}{D} \frac{G^2 x^2}{2\rho_{\mathrm{v}}} \tag{3.70}$$

where L is the bend length, D is the tube diameter, ρ_{v} is the density of the vapor phase and f is a dimensionless friction factor given by:

$$f = \frac{8.03 \times 10^{-4} \mathrm{Re}_{\mathrm{v}}^{0.5}}{\exp(0.215(\frac{2R}{D}))x^{1.25}} \tag{3.71}$$

In Eq. (3.71), Re_{v} is the Reynolds number (GDx/μ_{v}) of the vapor phase and the term $2R/D$ represents the curvature ratio of the return bend.

[Chisholm 1983] proposed a correlation (using 5 empirical constants) to calculate the pressure drop in return bends Δp_{rb} by using a two-phase multiplier Φ and the single-phase flow liquid pressure drop in the return bend Δp_{sp}:

$$\Delta p_{\mathrm{rb}} = \Phi \Delta p_{\mathrm{sp}} \tag{3.72}$$

where Δp_{sp} is expressed as follows:

$$\Delta p_{\mathrm{sp}} = K_{\mathrm{sp}} \frac{G^2}{2\rho_{\mathrm{l}}} \tag{3.73}$$

In Eq. (3.73), K_{sp} is the all-liquid local pressure drop coefficient obtained for single-phase flows. To estimate the value of K_{sp}, [Idelshik 1986] suggested the following expression:

$$K_{\mathrm{sp}} = f_{\mathrm{l}} \frac{L}{D} + 0.294 \left(\frac{R}{D}\right)^{0.5} \tag{3.74}$$

where R is the curvature radius and f_{l} is the single-phase friction factor calculated from the Blasius equations.

The two-phase multiplier Φ in (3.72) is given by:

$$\Phi = 1 + \left(\frac{\rho_{\mathrm{l}}}{\rho_{\mathrm{v}}} - 1\right) x \left[b\left(1-x\right) + x\right] \tag{3.75}$$

where b is expressed as:

$$b = 1 + \frac{2.2}{K_{\mathrm{sp}}\left(2 + \frac{R}{D}\right)} \tag{3.76}$$

The [Chisholm 1983] and [Idelshik 1986] method did not provide validation against experimental measurements. Based on Geary's correlation and using Geary's R-22 database and their own R-410A database, [Chen *et al.* 2004] presented a new correlation for the friction factor from the empirical fit, including new parameters such as the Weber number and a combined vapor and liquid Reynolds number as well as the vapor quality and the curvature ratio $2R/D$. The expression of the friction fraction is written as:

$$f = \frac{10^{-2}\mathrm{Re}_{\mathrm{mix}}^{0.35}}{\mathrm{We}_{\mathrm{v}}^{0.12}\exp\left(0.194(\frac{2R}{D})\right) x^{1.26}} \tag{3.77}$$

where $\mathrm{Re}_{\mathrm{mix}} = \mathrm{Re}_{\mathrm{v}} + \mathrm{Re}_{\mathrm{l}} = GD\left(x/\mu_{\mathrm{v}} + \left(1-x\right)/\mu_{\mathrm{l}}\right)$ is a combined vapor and liquid Reynolds number and $\mathrm{We}_{\mathrm{v}} = G^2 D/\rho_v \sigma$ is the Weber number which takes into account the influence of the surface tension in the two-phase frictional pressure drop. The authors reported a good agreement with their own R-410A database and with Geary's R-22 database, with a mean deviation of 19.1%.

Recently, [Domanski & Hermes 2008] proposed a correlation for the calculation of the two-phase pressure gradient in return bends based on 241 experimental data points from Geary's R-22 database and [Chen *et al.* 2004] R-410A database. The correlation allowed predicting the two-phase pressure gradient in a straight tube using the [Müller-Steinhagen & Heck 1986] correlation and using a multiplier that accounted for the bend curvature:

$$\left(\frac{\mathrm{d}p}{\mathrm{d}z}\right)_{\mathrm{rb}} = \Psi \left(\frac{\mathrm{d}p}{\mathrm{d}z}\right)_{\mathrm{st}} \tag{3.78}$$

The multiplier Ψ includes five empirical constants and takes into account the influence of the vapor velocity and the mass distribution in each phase. The multiplier Ψ is given by:

$$\Psi = 6.5 \times 10^{-3} \left(\frac{GxD}{\mu_{\mathrm{v}}}\right)^{0.54} \left(\frac{1}{x} - 1\right)^{0.21} \left(\frac{\rho_{\mathrm{l}}}{\rho_{\mathrm{v}}}\right)^{0.34} \left(\frac{2R}{D}\right)^{-0.67} \tag{3.79}$$

The [Domanski & Hermes 2008] correlation predicted 75% of the 241 experimental data points within a ± 25 % error band and exhibited a RMS deviation of 25%.

In order to propose a new prediction method, [Padilla *et al.* 2009] collected a total of 690 experimental data points from the literature: [Pierre 1964, Traviss & Rohsenow 1973, Geary 1975, Wang *et al.* 2003, Chen *et al.* 2004, Chen *et al.* 2007a, Chen *et al.* 2008b]. These data came from four different laboratories and the database included four different refrigerants. However, some of these data were removed from the collected database for the following reasons:

- The pressure drop measurements in the return bend were lower than those in the straight tube which is obviously not realistic and probably is a clue for too low accuracy.
- The length between two consecutive return bends was less than $4.8D$. In the literature, a length between $9D$ ([Hoang & Davis 1984]) and 90D ([Traviss & Rohsenow 1973]) was proposed to let the flow regimes recover after the return bend. Nevertheless, the [Padilla *et al.* 2009] correlation allows predicting the data down to $4.8D$.
- The R-22 data from Geary were finally removed. As a matter of fact, it was proven impossible to predict Geary's data for straight tubes (Fig. 3.8) by using the [Müller-Steinhagen & Heck 1986] correlation whereas this correlation is now often considered as very efficient for such conditions. Especially it has been shown to work satisfactorily with R-22 ([Revellin & Haberschill 2009]).

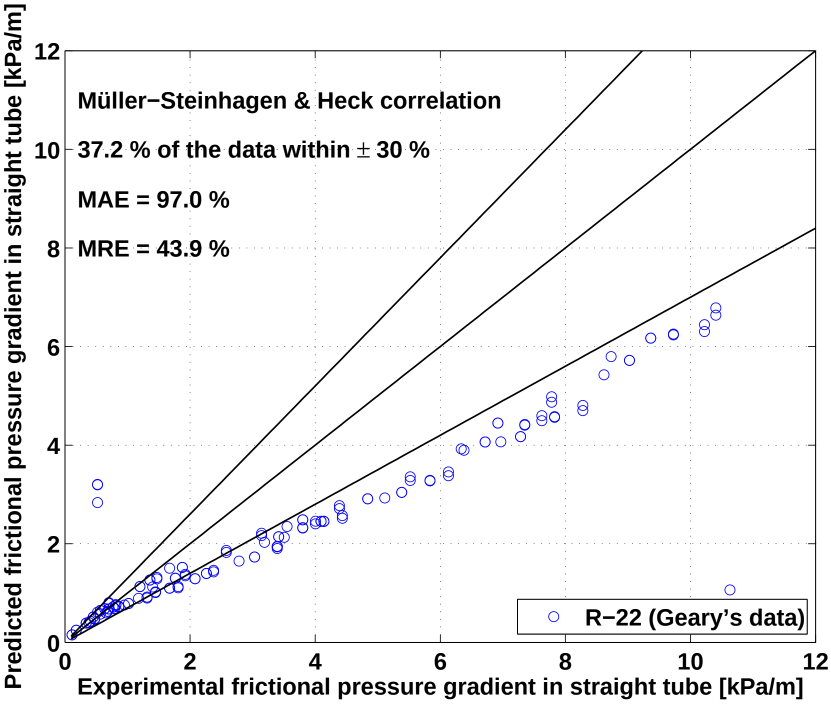

Figure 3.8: Comparison made by [Padilla *et al.* 2009] between the experimental frictional pressure gradient in straight tubes from [Geary 1975] and the predicted one by [Müller-Steinhagen & Heck 1986].

Finally, the database used for developing the [Padilla *et al.* 2009] prediction method includes 325 data points from [Traviss & Rohsenow 1973] for R-12, [Chen *et al.* 2004] for R410A and [Chen *et al.* 2007a] and [Chen *et al.* 2008b] for R-134a. The ranges of the experimental parameters are presented in Table (3.1).

As can be observed, the tube diameter varies from 3.25 to 8 mm, the curvature ratios from 3.175 to 8.15, the mass velocity ranges from 150 to 900 kg·m^{-2}·s^{-1} and the vapor quality from 0.0095 to 0.9367. The saturation temperature varies from 10 to 39°C. It is

Table 3.1: Experimental conditions of [Traviss & Rohsenow 1973], [Chen *et al.* 2008b], [Chen *et al.* 2007a] and [Chen *et al.* 2004].

Authors	Refrigerant	D (mm)	$2R/D$	G (kg·m^{-2}·s^{-1})	T_{sat} (°C)	x	Number of data points
[Traviss & Rohsenow 1973]	R-12	8	3.175	155	34	0.218 - 0.77	21
				300	38	0.0095 - 0.9367	35
				500	39	0.147 -0.928	24
			6.35	150	34	0.154 - 0.935	24
				300	34	0.046 - 0.932	35
[Chen *et al.* 2007a]	R-134a	5.07	5.18	200 - 700	20	0.1 - 0.9	27
[Chen *et al.* 2008b]	R-134a	5.07	5.18	200 - 700	25	0.1 - 0.9	25
				200 - 700	20	0.1 - 0.9	25[a]
				200 - 700	25	0.1 - 0.9	26[a]
[Chen *et al.* 2004]	R-410A	3.25	3.91	300 - 900	25	0.1 - 0.9	33
		3.3	8.15	300 - 900	10 - 25	0.1 - 0.9	50
	Total	3.25 - 8.00	3.175 - 8.15	150 - 900	10 - 39	0.0095 - 0.9367	325

[a] Vertical orientation

worth mentioning that the data correspond to the total pressure gradient in return bends, e.g. the sum of the frictional pressure gradient in straight tubes plus the singular pressure gradient.

The method of [Padilla *et al.* 2009] has been proposed for predicting the pressure gradient in return bends considering the sum of the frictional pressure gradient that would be obtained in straight tubes (predicted by [Müller-Steinhagen & Heck 1986] correlation) and the singular pressure gradient.

$$\left(-\frac{\mathrm{d}p}{\mathrm{d}z}\right)_{\mathrm{rb}} = \left(-\frac{\mathrm{d}p}{\mathrm{d}z}\right)_{\mathrm{st}} + \left(-\frac{\mathrm{d}p}{\mathrm{d}z}\right)_{\mathrm{sing}} \tag{3.80}$$

where $\left(-\frac{\mathrm{d}p}{\mathrm{d}z}\right)_{\mathrm{st}}$ is the frictional pressure gradient that would be reached in straight tubes calculated by the [Müller-Steinhagen & Heck 1986] correlation (plus eventually the static pressure gradient for vertical orientation [Thome 2004]). The second term $\left(-\frac{\mathrm{d}p}{\mathrm{d}z}\right)_{\mathrm{sing}}$ is the singular pressure gradient. From the whole database, the authors proposed to express it by the following relation:

$$\left(\frac{\mathrm{d}p}{\mathrm{d}z}\right)_{\mathrm{sing}} = a\left[\frac{\rho_{\mathrm{v}} J_{\mathrm{v}}^2}{R}\right]\left[\frac{J_{\mathrm{l}}^2}{R}\right]^b \tag{3.81}$$

where a = 0.047 ($\mathrm{s}^{2/3}\cdot\mathrm{m}^{-1/3}$) and b = 1/3. This constant and this exponent were obtained from the least square method based on the experimental data shown in Table (3.1), R is the radius of the curvature, J_{v} is the superficial velocity of the vapor written as:

$$J_{\mathrm{v}} = \frac{Gx}{\rho_{\mathrm{v}}} \tag{3.82}$$

and J_{l} is the superficial velocity of the liquid expressed as:

$$J_{\mathrm{l}} = \frac{G(1-x)}{\rho_{\mathrm{l}}} \tag{3.83}$$

G represents the mass velocity, x the vapor quality and ρ_{v} and ρ_{l} are the densities of the vapor and the liquid, respectively.

The comparison between the [Padilla *et al.* 2009] prediction method and the database from the literature (Fig. 3.9) showed that almost 67% of the data are predicted within a ±30% error band. The mean absolute error was less than 23.5% and the mean relative error is around −8%.

Using the same singular pressure gradient correlation but the [Friedel 1979] correlation instead of the [Müller-Steinhagen & Heck 1986] relation for the straight tube yields a MAE of 26% which is still correct. In addition, the authors used the [Revellin & Haberschill 2009] model and the [Grönnerud 1979] correlation, obtaining respectively MAE = 32.7% and MAE = 35.7%. Equation (3.81) presents many advantages:

- only two empirical constants have been used for developing this equation (instead of five for [Domanski & Hermes 2008] and [Chen *et al.* 2004])
- the relation has been developed based on a large database: 325 data points for three different fluids obtained in two different laboratories.
- the equation works for horizontal and vertical return bends

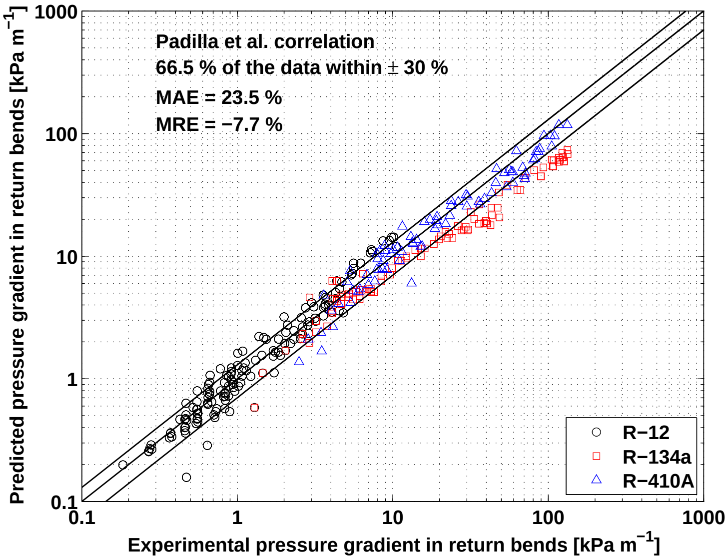

Figure 3.9: Experimental pressure gradient data for return bends (Table 3.1) compared to the [Padilla *et al.* 2009] prediction method.

- the relation has been developed over a wide range of tube diameters (3.25 – 8.00 mm), mass velocities (150 – 900 kg·m^{-2}·s^{-1}), saturation temperatures (10 – 39°C) and over a large range of vapor quality (0.0095 – 0.9367).
- the term $\left[\frac{\rho_\mathrm{v} J_\mathrm{v}^2}{R}\right]$ represents the centrifugal force acting on the vapor phase due to the return bend
- the term $\left[\frac{J_\mathrm{l}^2}{R}\right]$ takes into account the centrifugal and gravitational forces acting on the liquid phase due to the return bend
- the relation is independent of the diameter which is logical in view of the following reasoning: Equation (3.81) predicts the curvature effect on the pressure gradient in a straight tube. The diameter effect is thus directly taken into account by the [Müller-Steinhagen & Heck 1986] correlation.
- there is no constant including the properties such as $\mu_\mathrm{v}/\mu_\mathrm{l}$ or σ.

Rearranging Eq. (3.80), it comes:

$$\left(\frac{\mathrm{d}p}{\mathrm{d}z}\right)_\mathrm{rb} = \left(\frac{\mathrm{d}p}{\mathrm{d}z}\right)_\mathrm{st} \left[1 + \frac{\left(\frac{\mathrm{d}p}{\mathrm{d}z}\right)_\mathrm{sing}}{\left(\frac{\mathrm{d}p}{\mathrm{d}z}\right)_\mathrm{st}}\right] = \left(\frac{\mathrm{d}p}{\mathrm{d}z}\right)_\mathrm{st} \Psi \tag{3.84}$$

In Eq. (3.84), the curvature multiplier Ψ represents the ratio between the pressure gradient in return bends and that in straight tubes calculated by the [Müller-Steinhagen & Heck 1986] correlation. When the curvature radius $R \rightarrow +\infty$, the curvature multiplier $\Psi \rightarrow 1$ and the resulting pressure gradient in return bends tends toward the pressure gradient in straight tubes. Furthermore, when $R \rightarrow 0$, the curvature multiplier $\Psi \rightarrow +\infty$ (This is an hypothetical limit because the real limit is $R \rightarrow D/2$) and the pressure gradient in return bends tends toward infinity. To illustrate this, Fig. (3.10) shows the curvature multiplier Ψ as a function of the curvature ratio for four different return bend pressure gradient correlations (the [Chisholm 1983] and [Idelshik 1986] method, the [Chen *et al.* 2004], the [Domanski & Hermes 2008] and [Padilla *et al.* 2009] correlations).

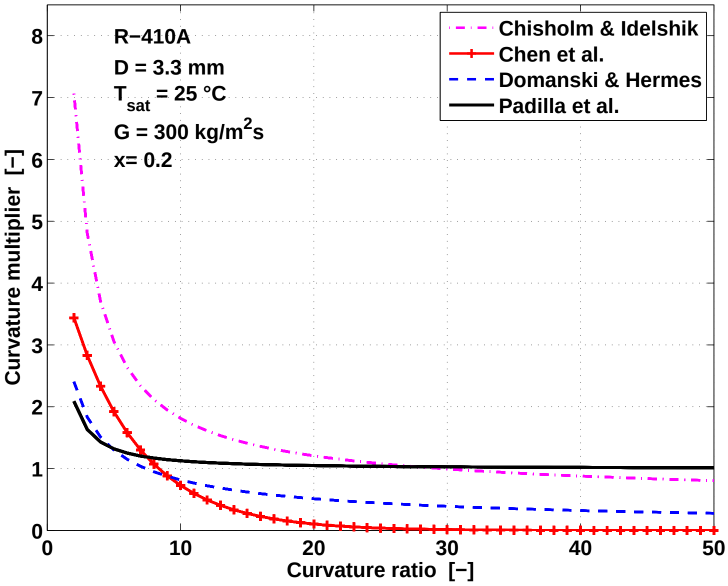

Figure 3.10: Curvature multiplier $\left(\frac{\mathrm{d}p}{\mathrm{d}z}\right)_{\mathrm{rb}} / \left(\frac{\mathrm{d}p}{\mathrm{d}z}\right)_{\mathrm{st}}$ as a function of the curvature ratio $(2R/D)$ for the [Padilla *et al.* 2009] prediction method and different correlations from the literature. [Padilla *et al.* 2009]

3.3 Two-phase flow in sudden contractions

In HVAC & R applications, the two-phase mixture can flow through sudden changes of cross-section, the flow might form a separation region at the sharp corner and an irreversible pressure loss is induced. This singular loss often occurs in orifices, valves, connections and heat exchangers with round or rectangular configurations.

3.3.1 Pressure drop in sudden contractions

The flow channel normally involves several geometrical singularities such as abrupt changes of cross-sections (sudden enlargement, sudden contraction, valve or orifice). At an abrupt change of cross-section, eddies are formed in the separation region which is a clear sign of the irreversibility for a large pressure loss. Some correlations applicable to the pressure change with respect to mini channels ([Abdelall *et al.* 2005, Chen *et al.* 2007b]) have been developped.

For single-phase flow through contractions, the flow separates from the inner wall and eddy zones are developed just at the front of transitional cross-section. The contracted flow forms into a small jet flow pattern with the narrowest cross-section of the jet being called *vena-contracta* which is located immediately after the transition cross-section. In the contracted flow region the static pressure decreases more rapidly than for the fully developed flow at the upstream and downstream. After the *vena-contracta*, the pressure gradually increases and reaches its maximum, and then merges into the fully developed pressure gradient line at the downstream.

In contrast to the well-known pressure profile in the transitional region between the flow separation and reattachment for single-phase liquid flow, the pressure profile and the shape of streamlines in two-phase flow are unknown. At an abrupt change of flow cross-section due to geometrical singularities, eddies are formed in the separation region which is a clear sign of the irreversibility for a large pressure loss. Many investigations were based on the assumption that the occurrence of the *vena-contracta* phenomenon is associated to energy dissipation at the downstream of the contraction point. However, [Schmidt & Friedel 1997] reported that a local pressure minimum was not detectable in the two-phase tests, thus the axial pressure profile and the shape of streamlines in two-phase flow are still unknown. There is no evidence whether or not the profile is similar to the one in single phase flow, nor even if a flow contraction occurs at all. In fact, [Schmidt & Friedel 1997] concluded that unlike single-phase flow a two-phase flow does not contract behind the edge of the transition at least in a range of mass flow quality between 1 and 97%.

There are various models from the open literature which aim at predicting the single- and two-phase pressure drops in pipe contractions. In the 50's, in order to determine the pressure drop across a pipe contraction with low Reynolds number flow, [Kays 1950] measured the axial pressure profiles in the regions of fully developed pipe flow upstream and downstream of the pipe contraction. He extrapolated these (linear) pressure courses to the transitional cross section.

In subsequent years, some studies ([Richardson 1958, Chisholm 1968, Geiger 1964, McGee 1966, Janssen 1966, Husain 1975]) have been conducted in order to propose new experimental data and prediction methods. Most of these authors have recommended a homogeneous flow model to calculate the pressure drop, although they agreed that this is physically not correct; the assumption of equal mean velocities of gas and liquid phase implied by the homogeneous flow model is highly questionable. Additionally, a flow contraction downstream of the transitional cross section in analogy to single-phase liquid flow is assumed and the liquid flow contraction coefficient is used for simplicity. Some prediction methods found in the literature are described below.

For two-phase flow, the change in static pressure at a sudden contraction can be estimated using a homogeneous flow model as recommended by [Collier & Thome 1994]:

$$\Delta p_{\mathrm{c}} = \frac{G_2^2}{2\rho_{\mathrm{l}}}\left[(C_{\mathrm{c}}^{-1}-1)^2 + (1-\sigma_{\mathrm{A}}^2)\right]\left[1 + x\left(\frac{\rho_{\mathrm{l}}}{\rho_{\mathrm{v}}}-1\right)\right] \tag{3.85}$$

where $\sigma_{\mathrm{A}} = D_2^2/D_1^2$ is defined as the passage cross-section area ratio. The contraction coefficient C_{c} can be calculated using the expression given by [Geiger 1964]:

$$C_{\mathrm{c}} = 1 - \frac{1-\sigma_{\mathrm{A}}}{2.08(1-\sigma_{\mathrm{A}}) + 0.5371} \tag{3.86}$$

[Chisholm 1983] introduced a constant B coefficient for flow through a discrete interval in evaluating the contraction pressure change:

$$\Delta p_{\mathrm{c}} = \Delta p_{\mathrm{cl}}\left[1 + \left(\frac{\rho_{\mathrm{l}}}{\rho_{\mathrm{v}}}-1\right)(Bx(1-x)+x^2)\right] \tag{3.87}$$

where the total static pressure drop at the contraction considering only liquid (Δp_{cl}) is:

$$\Delta p_{\mathrm{cl}} = \frac{G_2^2}{2\rho_{\mathrm{l}}}\left[\frac{1}{(\sigma_{\mathrm{A}} C_{\mathrm{c}})^2} - 1 - \frac{2(C_{\mathrm{c}}^{-1} - 1)}{\sigma_{\mathrm{A}}^2}\right] \tag{3.88}$$

and the contraction coefficient (C_{c}) is given as follows:

$$C_{\mathrm{c}} = \frac{1}{[0.639(1-\sigma_{\mathrm{A}})^{0.5} + 1]} \tag{3.89}$$

The constant B coefficient is calculated as follows:

$$B = \frac{\left\{\frac{1}{K_0}\left(\frac{1}{(C_{\mathrm{c}}\sigma_{\mathrm{A}})^2} - 1\right) - \frac{2}{(K_0 C_{\mathrm{c}}\sigma_{\mathrm{A}}^2)} + \frac{2}{(K_0^{0.28}\sigma_{\mathrm{A}}^2)}\right\}}{\left(\frac{1}{(C_{\mathrm{c}}\sigma_{\mathrm{A}})^2} - 1\right) - \frac{2}{(C_{\mathrm{c}}\sigma_{\mathrm{A}}^2)} + \frac{2}{\sigma_{\mathrm{A}}^2}} \tag{3.90}$$

where Δp_{cl} is the contraction pressure drop for total flow assumed liquid across the same sudden contraction, and K_0 is given as:

$$K_0 = \left[1 + x\left(\frac{\rho_{\mathrm{l}}}{\rho_{\mathrm{v}}} - 1\right)\right]^{0.5} \quad \text{for } \mathrm{X_{tt}} > 1 \tag{3.91}$$

$$K_0 = \left(\frac{\rho_{\mathrm{l}}}{\rho_{\mathrm{v}}}\right)^{0.25} \quad \text{for } \mathrm{X_{tt}} \leq 1 \tag{3.92}$$

where $\mathrm{X_{tt}}$ is the Martinelli parameter Eq.(2.63):

$$\mathrm{X_{tt}} = \left(\frac{1-x}{x}\right)^{0.9}\left(\frac{\rho_{\mathrm{v}}}{\rho_{\mathrm{l}}}\right)^{0.5}\left(\frac{\mu_{\mathrm{l}}}{\mu_{\mathrm{v}}}\right)^{0.1}$$

The [Chisholm 1983] correlation does not take into account the physical limit when $\sigma_{\mathrm{A}} = 1$ since the B parameter is not defined for this case.

Some mechanistic models for two-phase pressure drop across sudden contractions have been developed by [Al'Ferov & Shul'Zhenko 1977, Attou & Bolle 1995, Schmidt & Friedel 1997]. [Al'Ferov & Shul'Zhenko 1977, Attou & Bolle 1995] assumed the occurrence of the vena-contracta phenomenon in complete analogy with single-phase flow, and considered a dispersed droplet flow pattern downstream of the vena-contracta point. However, [Schmidt & Friedel 1997] have shown that the vena-contracta phenomenon may actually not occur in two-phase flow at all. Based on the momentum and mass transfer balance, the latter developed a new pressure drop model for sudden contraction which is given by:

$$\Delta p_{\mathrm{c}} = \frac{G_2^2\left[\frac{1}{\rho_{\mathrm{eff}}} - \frac{\sigma_{\mathrm{A}}}{\rho_{\mathrm{eff}}} + f_{\mathrm{c}}\rho_{\mathrm{eff}}\left(\frac{x}{\rho_{\mathrm{v}}\varepsilon} - \frac{1-x}{\rho_{\mathrm{l}}(1-\varepsilon)}\right)^2\left(1-\sigma_{\mathrm{A}}^{1/2}\right)^2\right]}{1 + \Omega_{\mathrm{c}}\left(\frac{1}{\sigma_{\mathrm{A}}} - 1\right)} \tag{3.93}$$

where

$$\frac{1}{\rho_{\mathrm{eff}}} = \frac{x^2}{\rho_{\mathrm{v}}\varepsilon} + \frac{(1-x)^2}{\rho_{\mathrm{l}}(1-\varepsilon)} + \rho_{\mathrm{l}}(1-\varepsilon)\left(\frac{\alpha_{\mathrm{E}}}{1-\alpha_{\mathrm{E}}}\right)\left[\frac{x}{\rho_{\mathrm{v}}\varepsilon} - \frac{1-x}{\rho_{\mathrm{l}}(1-\varepsilon)}\right]^2 \tag{3.94}$$

$$\varepsilon = 1 - \frac{2(1-x)^2}{1 - 2x + \sqrt{1 + 4x(1-x)(\frac{\rho_\mathrm{l}}{\rho_\mathrm{v}} - 1)}} \tag{3.95}$$

$$\alpha_\mathrm{E} = \frac{1}{S}\left[1 - \frac{1-x}{1 - x(1 - 0.18\mathrm{We}^{0.27}\mathrm{Re}^{0.5})}\right] \tag{3.96}$$

$$S = \frac{x}{1-x}\frac{1-\varepsilon}{\varepsilon}\frac{\rho_\mathrm{l}}{\rho_\mathrm{v}} \tag{3.97}$$

$$\mathrm{We} = G_2^2 x^2 \frac{D_2}{\rho_\mathrm{v}\sigma}\frac{(\rho_\mathrm{l} - \rho_\mathrm{v})}{\rho_\mathrm{v}} \tag{3.98}$$

$$\mathrm{Re} = \frac{G_2(1-x)D_2}{\mu_\mathrm{l}}$$

$$\Omega_\mathrm{c} = 0.77\sigma_\mathrm{A}(1 - \sigma_\mathrm{A}^{0.306}) \tag{3.99}$$

$$f_\mathrm{c} = 0.0052\, x^{0.1}(1-x)\left(\sigma_\mathrm{A}\frac{\mu_\mathrm{l}}{\mu_\mathrm{v}}\right)^{0.8} \tag{3.100}$$

The comparison of the [Schmidt & Friedel 1997] model and their test results is fair with 80% of the data sets being predicted within ±30%. However, this correlation uses more than 15 empirical parameters and some physical limits are not described correctly. For example, when $x = 1$, S and ε are not defined.

The predictions of the homogeneous flow model, when no vena-contracta is assumed (i.e. $C_\mathrm{c} = 1$) are also shown in the work of [Chalfi & Ghiaasiaan 2008], and it is indicated that the homogeneous flow model over predicts the pressure drop very significantly. Similar comparison have been made between the data and the predictions of the homogeneous flow model, as well as the slip flow model along with the [Zivi 1964] slip ratio expression, but assuming that the vena-contracta phenomenon occurred according to Geiger's expression (Eq. 3.86). The results once again showed that the homogeneous model over predicted the pressure drop very significantly everywhere, typically by a factor of five. The slip flow model also over predicted the data consistently, typically by a factor of two.

[Abdelall *et al.* 2005] investigated air-water pressure drops at 25°C caused by abrupt flow area expansion and contraction in a small test section with $\sigma_\mathrm{A} = 0.26$. The tube diameters were 0.84 and 1.60 mm and the mass velocities spanned from 2700 to 6200 kg$\cdot$ m$^{-2}\cdot$ s^{-1}. Assuming incompressible gas and liquid phases, and assuming x and ε remained constant across the sudden contraction, the pressure drop across the sudden contraction was written as:

$$\Delta p_\mathrm{c} = G_2^2\left[\frac{\rho_\mathrm{tp}\left(\frac{1}{C_c^2} - \sigma_\mathrm{A}^2\right)}{2\rho''^2} + \frac{1 - C_c}{\rho'}\right] \tag{3.101}$$

where ρ_tp is obtained using Eq. (3.24):

$$\rho_\mathrm{tp} = \left[\frac{x}{\rho_\mathrm{v}} + \frac{1-x}{\rho_\mathrm{l}}\right]^{-1}$$

$$\rho^{'} = \left[\frac{1-x^2}{\rho_{\mathrm{l}}(1-\varepsilon)} + \frac{x^2}{\rho_{\mathrm{v}}\varepsilon}\right]^{-1} \quad (3.102)$$

$$\rho^{''} = \left[\frac{(1-x)^3}{\rho_{\mathrm{l}}^2(1-\varepsilon)^2} + \frac{x^3}{\rho_{\mathrm{v}}^2\varepsilon^2}\right]^{-1/2} \quad (3.103)$$

The parameter C_{c} is estimated from the correlation of [Geiger 1964], and the void fraction (ε) is calculated from the slip ratio model presented by [Zivi 1964]:

$$S = \frac{x}{1-x}\frac{1-\varepsilon}{\varepsilon}\frac{\rho_{\mathrm{l}}}{\rho_{\mathrm{v}}} = \left(\frac{\rho_{\mathrm{l}}}{\rho_{\mathrm{v}}}\right)^{1/3} \quad (3.104)$$

[Chen *et al.* 2008a] studied the pressure drop at the sudden contraction from small rectangular channels (3 × 9 mm and 3 × 6 mm) into a 3 mm diameter tube. They proposed a correction factor accounting for the influence of surface tension (Bond number and contraction ratio) to the original homogeneous model. The proposed modification takes the following form:

$$\Delta p_{\mathrm{c}} = \Delta p_{\mathrm{h}}\Omega \quad (3.105)$$

$$\Omega = 1 + e^{\left(\frac{-0.1\mathrm{Bo}}{1+e^{-\sigma_{\mathrm{A}}}}\right)}\left(-4.22 - 7.29(\mathrm{Bo}\sigma_{\mathrm{A}})^{0.5}\mathrm{Ln}(\mathrm{Bo}\sigma_{\mathrm{A}}))^{-1}\right) \quad (3.106)$$

where the Bond number (Bo) defined in section 3.1, represents the balance of buoyancy and surface tension forces. It can be expressed as:

$$\mathrm{Bo} = \frac{g(\rho_{\mathrm{l}}-\rho_{\mathrm{v}})(D_2/2)^2}{\sigma} \quad (3.107)$$

The mean deviation of this correlation is 26% applicable to an air-water database (437 points) available in the literature.

Finally, [Chen *et al.* 2009] investigated the pressure drop and flow pattern for two-phase flow in sudden contractions. They carried out experiments with air and water mixtures from small rectangular channels (2 × 4, 2 × 6, 4 × 4 and 4 × 6 mm, respectively) into a 2 mm diameter tube. The total mass velocity ranged from 100 to 700 $\mathrm{kg{\cdot}m^{-2}{\cdot}s^{-1}}$ with gas quality comprised between 0.001 and 0.8. In general the contraction pressure drop increases with the rise of mass velocity, and gas quality but as unique deflection of contraction pressure drop pertaining to liquid vena-contracta at a very low gas quality is encountered at a very low gas quality in the 4 × 6 mm test section. For a low gas quality, elongated bubble prevails after the contraction, yet the size of elongated bubbles is reduced when the aspect ratio is increased. Comparisons amid the pressure change data of this study and available literature data with the predictions of existing model/correlations indicated that none of them can accurately predict the data.

It was found that surface tension and outlet tube size, or equivalently the Bond number, play a major role for the departure of various models/correlations. Among the models/correlations being examined, the homogeneous model showed a little better than the others. Hence, by taking into account the influences of gas quality, Bond number, Weber number and area contraction ratio into the homogeneous model, a modified homogeneous correlation was proposed by [Chen *et al.* 2009]:

$$\Delta p_{\mathrm{c}} = \Delta p_{\mathrm{h}}(1+\Omega_1)(1+\Omega_2)(1+\Omega_3)^{-0.08} \quad (3.108)$$

$$
\begin{aligned}
\Omega_1 &= -0.99e^{\frac{-13.1C_1}{C_2}} \\
\Omega_2 &= -39.4e^{C_1^{-0.25}}(16.1C_3^{-1.5} - 13.2C_3^{-1.8} - 4.2C_3^{-1}) \\
\Omega_3 &= 0.1C_3^{-13}C_4^{-3} \\
C_1 &= \mathrm{Bo}^{1.1}(1-x)^{0.9} \\
C_2 &= 470e^{-\sigma_{\mathrm{A}}^{-0.2}} \\
C_3 &= \mathrm{WeBo}\sigma_{\mathrm{A}}(1-x)^{-3} \\
C_4 &= \sigma_{\mathrm{A}}^{2.5}(1-x)^{-1}
\end{aligned}
\tag{3.109}
$$

Note that this correlation includes 21 empirical constants. Although the [Chen *et al.* 2009] correlation has been compared against available air-water data in the literature and the predictions show a satisfactory accuracy, this correlation and also the method presented by [Chen *et al.* 2008a] are modifications of the homogeneous model in order to improve the predictions, but fall into the same physical inconsistencies when considering pseudo-homogeneous fluid where the *vena-contracta* phenomenon exists throughout its entire range of application.

Most experiments on the two-phase flow pressure drop in sudden contractions referred to in the literature have been carried out with steam/water and air/water mixtures. Thus, the physical properties of the fluids were not systematically varied and, additionally, flow parameters like mass flow quality and area ratio have been changed only in minor ranges.

Very little information for synthetic fluids have been found, and generally is for small rectangular channels. Furthermore, the majority of correlations are based on the homogeneous model and does not give more physical information of the phenomena. As a consequence, the prediction of measured pressure drops by using available models will lead to inadequate results for refrigerants. The equations differ mostly in the definition of the mixture properties and a reliable model for calculating the contraction coefficient in two-phase flow. In summary, with the available experimental data it does not seem possible to reliably determine the pressure drop in a sudden contraction for refrigerants as a function of primary parameters. Further, experimental investigations and theoretical analysis for two-phase flow in sudden contractions are necessary.

3.3.2 Up- and downstream perturbation effects on the sudden contraction pressure drop

According to [Collier & Thome 1994], in single-phase flow the velocity profile becomes fully developed at a maximum of 10 to 12 pipe diameters downstream of the singularity. In two-phase flow, the distance downstream over which the influence of the singularity is felt is greatly increased by up to ten times. [Schmidt & Friedel 1997] suggested that for single-phase flow, in a distance of about 1.5 times the entrance-pipe diameter in front of the transitional cross section the flow separates from the inner wall and contracts to a jet with a narrowest cross section immediately behind the transition. Hereafter, the jet enlarges and the main flow reattaches to the pipe wall in a distance of less than 14 times the outlet-pipe diameter, depending on the flow condition.

In general, the perturbation lengths up- and downstream of the sudden contraction depend on the passage cross-section area ratio (σ_{A}), fluid properties and flow conditions. There is a lack of experimental data on this topic in the literature, especially for synthetic refrigerants; as a result, experimental tests will be performed to determine the perturbation lengths in our conditions.

3.4 Chapter Conclusion

An extensive review of the existing two-phase flow models to predict pressure drops in straight tubes, return bends and sudden contractions was presented. The models were classified according to the different approaches used for their development. The main experimental conditions (where available) of those methods were recalled.

A state-of-the-art review related to the existing studies on void fraction and flow pattern maps in straight tubes and flow visualization in return bends has also been carried out. The following conclusions may be drawn from this literature review:

- The two-phase pressure drop prediction methods for water are not suitable for refrigerants. For these fluids (which is the topic of the thesis), five main prediction methods may be used: [Friedel 1979], [Grönnerud 1979], [Müller-Steinhagen & Heck 1986], [Moreno Quibén & Thome 2007] and [Revellin & Haberschill 2009]. These methods are still based on numerous empirical constants.
- The [Wojtan *et al.* 2005a] flow pattern map for flow pattern prediction of refrigerants in straight tube is, so far, the most accurate available in the literature. This map adds new transition curves to define annular-dryout and dryout-mist flow transitions which have been integrated into the Thome-El Hajal version of the [Kattan *et al.* 1998a] flow pattern map. These modifications provide a more accurate prediction of the flow regimes and significantly improve the identification the inception of dryout.
- The void fraction prediction in straight tubes is still under investigation because no general method exists so far. The most accurate method available for horizontal flows seems to be that of [Rouhani & Axelsson 1970]
- No void fraction measurements were performed so far in return bends nor in sudden contractions.
- No two-phase flow visualizations were carried out for refrigerant flowing in sudden contraction.
- So far, the best prediction method for predicting the two-phase pressure drop in return bend seems to be that of [Padilla *et al.* 2009]. However, this method should be checked with different geometries and refrigerants.
- In general, there are very little information in the literature on the perturbation lengths up- and downstream of a singularity. Furthermore, there is a lack of experimental data on this topic, especially for synthetic refrigerants.
- As mentioned above, the two-phase pressure drop prediction methods for water in sudden contractions are not suitable for refrigerants. The existing prediction methods are mainly developed for small rectangular channels. No two-phase pressure drop prediction method in sudden contraction for refrigerants has been found in the literature. Hence, further work is called for to more thoroughly investigate these points, which is the objective of this thesis.

Chapter 4

Description of the experiments

Contents

This chapter describes the conceptualization, construction, components assembly and commissioning of the experimental setup used during the present PhD work. It was built in such a way that flow visualization and two-phase pressure drop measurements in different geometries could be done on the same system. The experimental stand was based on the existing setup used by [Branescu 2000] at Centre de Thermique de Lyon (CETHIL UMR-5008), National Institute of Applied Sciences (INSA de Lyon).

4.1 Description of the experimental test facility

The present experimental facility consists of two parallel circuits: the refrigerant circuit and the water-glycol circuit. The test facility is designed to allow single-phase and two-phase tests using various refrigerants.

4.1.1 Refrigerant circuit

The refrigerant circuit (Fig. 4.1), which can be used to perform both pressure drop and visualization tests, allows for the test section's inlet and outlet properties (vapor quality, mass flow rate, temperature) of the refrigerant flow to be controlled. This circuit consists of a refrigerant pump (Verder, model 3LS7, 0.37 kW nominal power) which delivers subcooled refrigerant to the electrical heater. The refrigerant line splits into two branches after the pump. The main line continues on to the Coriolis-type mass flow meter (Danfoss MASSFLO 2100). The by-pass line contains two valves which are used to divert flow from the test section for low mass flow tests. Both the main test line and by-pass line have ball valves (quarter turn valves). In addition, the by-pass line has a needle valve which allows to control the refrigerant mass flow with an accuracy of ±5 kg·s^{-1}.

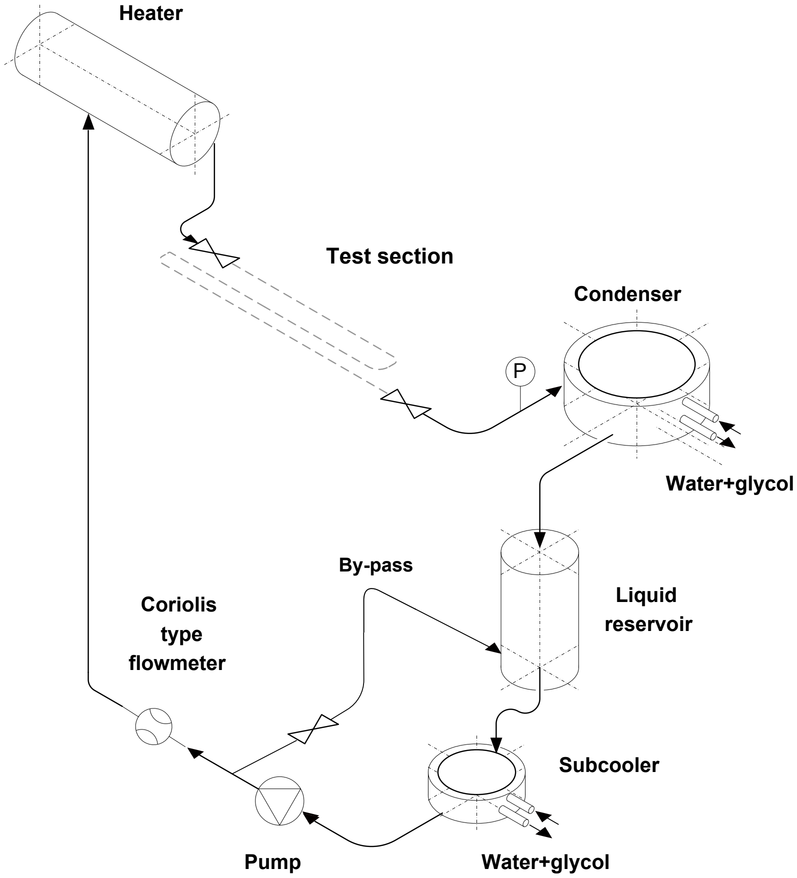

Figure 4.1: Sketch of the refrigerant cycle.

After the Coriolis-type mass flow meter, the main line continues to the electrical heater, which is used to control the vapor quality at the inlet of the test section. The refrigerant thermal properties are measured at the outlet of the heater. The state of the liquid refrigerant before the electrical heater is used as the starting point for calculations of properties for the energy balance in the electrical heater.

Some corrections on the fluid characteristics (x, T_{sat}) can be conducted following the procedure explained in section 2.6.3.1. The refrigerant is preheated and partially evaporated in the electrical heater to the desired vapor quality. The vapor quality entering the test section is calculated from the energy balance on the electrical heater given by Eq. (4.1). The measurement devices used are discussed later, in Section 4.3.1.

$$x = \frac{\left(\frac{\mathrm{P}_{\mathrm{heater}}}{\dot{m}}\right) + h_{\mathrm{heater,in}} - h_{\mathrm{l}}}{h_{\mathrm{lv}}} \tag{4.1}$$

$h_{\mathrm{lv}} = h_{\mathrm{v}} - h_{\mathrm{l}}$ is the latent heat of vaporization and $-(h_{\mathrm{heater,in}} - h_{\mathrm{l}})$ corresponds to the subcooling sensible heat. $\mathrm{P}_{\mathrm{heater}}$ is the electric power of the heater. As the electrical heater is well-insulated, heat losses on it may be neglected as compared to the total heat electrical power. The single-phase energy balance carried out on the heater is described in appendix B.

The fluid passes through the test section and is then cooled and condensed in the condenser. The condenser pressure is controlled by means of a water-glycol (20% V/V glycol concentration) flow in the water-glycol circuit, with a temperature comprised between -6.0 °C and 20.0 °C, that can be chosen by the operator. The condenser is followed by a liquid receiver and a sub-cooler, whose two-phase conditions are also controlled by the water-glycol flow. The liquid receiver is used as a reservoir to ensure that sub-cooled liquid enters the refrigerant pump and the coriolis flow meter to measure the flow of refrigerant in the test line.

Before returning to the pump, the refrigerant is subcooled to ensure that no vapor flows into the pump. The refrigerant mass flow rate is adjusted by the operator using a by-pass and measured by means of a Coriolis-type mass flow meter described below. All components and tubes are well insulated with foam material.

The test section was constructed to the required length that would allow for the flow to fully develop. It can be shut off with valves and is equipped with a Schrader valve for refrigerant recovery. The test section is instrumented with the necessary temperature and pressure measurement devices. Two sight-glasses/moisture-indicators are used directly upstream of the electrical heater and refrigerant pump for visual verification of the refrigerant state.

The system is currently usable with most common refrigerants and evaporation tests are planned using R-410A, R-134a and HFO-1234yf.

4.1.2 Water-glycol circuit

The water-glycol circuit consists of a hot and cold side (heating loop and cooling loop). All the equipment of the water-glycol circuit are independent of the refrigerant circuit. The water-glycol mixture is used to exchange heat with the refrigerant side at the condenser and the sub-cooler. The supply of high and low temperature flows is controlled by a Danfoss AMB 162 actuated 4-ways valve which, ultimately, controls the saturation pressure at the condenser. To increase the saturation pressure in the condenser, the 4-ways valve opens the heating loop allowing the high temperature flow to enter to the condenser. To decrease the saturation pressure the 4-ways valve closes the heating loop and the low temperature flow from the cooling loop enters into the condenser. A PID controller (West model 6100+) drives the 4-ways valve in order to obtain a specific saturation pressure for the tests.

The water-glycol heating loop, consists of a centrifugal pump (Pedrollo model CP-130, 0.37 kW nominal power) which delivers water-glycol mixture to the first water electrical heater (Vulcanic model DN80, 9 kW nominal power), namely a 9 kW electrical heater. The mixture is heated to a maximum value of 50 °C and then the flow at high temperature enters to the 4-ways valve.

In the water-glycol cooling loop, after the 4-ways valve, the water-glycol mixture enters into the second water electrical heater (Vulcanic model DN80, 30 kW nominal power), namely a 30 kW electrical heater. This electrical heater is placed to avoid the freezing of the water-glycol mixture and the low pressure cut-off of the chiller. After the second electrical heater, the mixture is cooled in a TRANE outdoor chiller (model VGA 100, 25.7 kW cooling capacity) to a minimum temperature of -6 °C. To avoid temperature oscillations at the chiller outlet, a liquid vessel (40 l) has been placed downstream of the chiller. After the liquid vessel, a PT-100 probe driven by a second PID control (West model 6100+), regulates the water-glycol mixture temperature by modifying the heating power in the second electrical heater. Finally, the flow at low temperature enters the 4-ways valve.

4.2 Description of the test sections

The experimental setup is designed to perform flow regime visualizations and pressure drop measurements. The test sections conceived to this end are presented below.

4.2.1 Test section for flow regime visualizations

4.2.1.1 Flow regime visualizations in straight tubes

Figure 4.2 shows the test section for visualizing flow regimes. This section consists in a 6.70 mm inner diameter glass tube which has been discretized into three sections (1-2, 2-3 and 3-4, see Fig. 4.2(a)).

In order to visualize flow regimes simultaneously from the top and the side views of the straight tube section 1-2, a mirror was settled down behind the glass tube. Figure 4.2(b) shows a sketch of the array glass tube - mirror for visualizing both top and side views of the flow regimes in straight tube section. Observations of flow patterns are obtained from images given by a high speed high resolution camera (Photron model Fastcam 1024 PCI). Relevant specifications of the high speed camera are listed in Table 4.1.

Table 4.1: Relevant information of the high speed camera.

Camera Type :	FASTCAM-1024PCI
Model :	100K
Record Rate(fps) :	2000
Shutter Speed(s) :	1/40000
Total Frame :	3072
Image Width (px) :	1024
Image Height (px) :	512
Color Bit :	8
File Format :	Jpeg

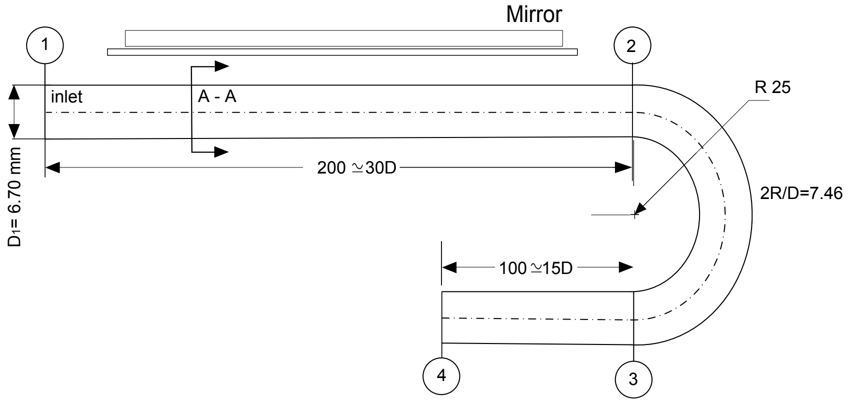

(a)

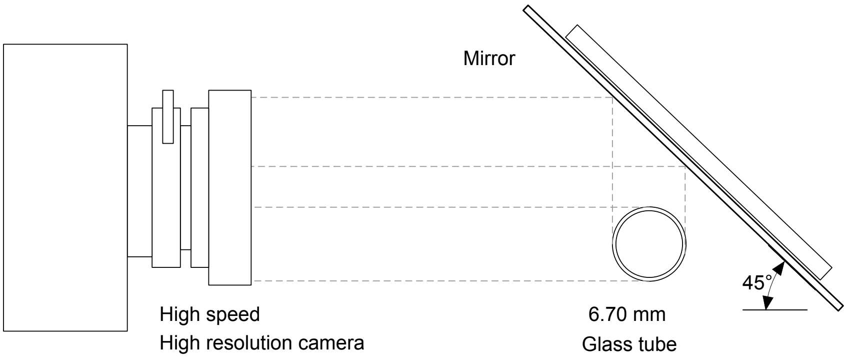

(b)

Figure 4.2: Sketch of the test section for flow regime visualizations in straight tubes. [Padilla *et al.* 2011a].

4.2.1.2 Flow regime visualizations in return bends

To visualize flow regimes in return bends, the same glass tube utilized to visualize the flow regimes in straight tubes was used. Tube orientation was also changed (see Fig. 4.3) to get the inlet flow in the short section of the glass tube (section 1-2). This arrangement allows to visualize the flow regimes upstream (section 1-2), along the entire return bend (section 2-3) and also the flow recovery downstream of the return bend (section 3-4). In addition, Fig. 4.3 shows the glass tube disposition to visualize horizontal or vertical flow regimes in the return bend.

4.2.1.3 Flow regime visualizations in sudden contraction

A similar arrangement to that used for visualize flow regimes in straight tubes is used to visualize simultaneously from the top and the side views in a sudden contraction (Fig. 4.4). A 10 mm inner diameter glass tube with $\sigma_{\mathrm{A}} = 0.49$ was used as a section to visualize

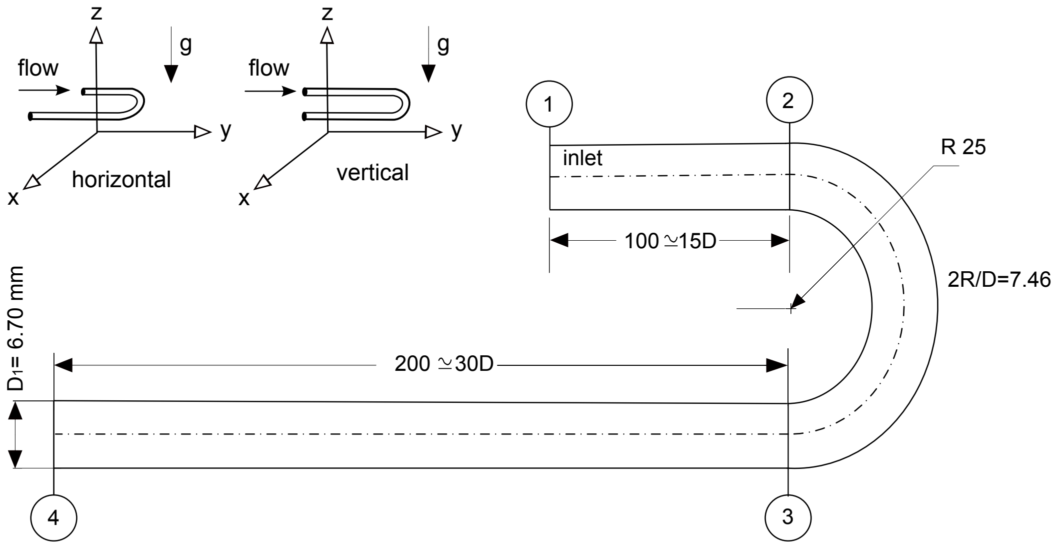

Figure 4.3: Sketch of the test section for flow regime visualizations in return bends.

horizontal two-phase flow in a sudden contraction.

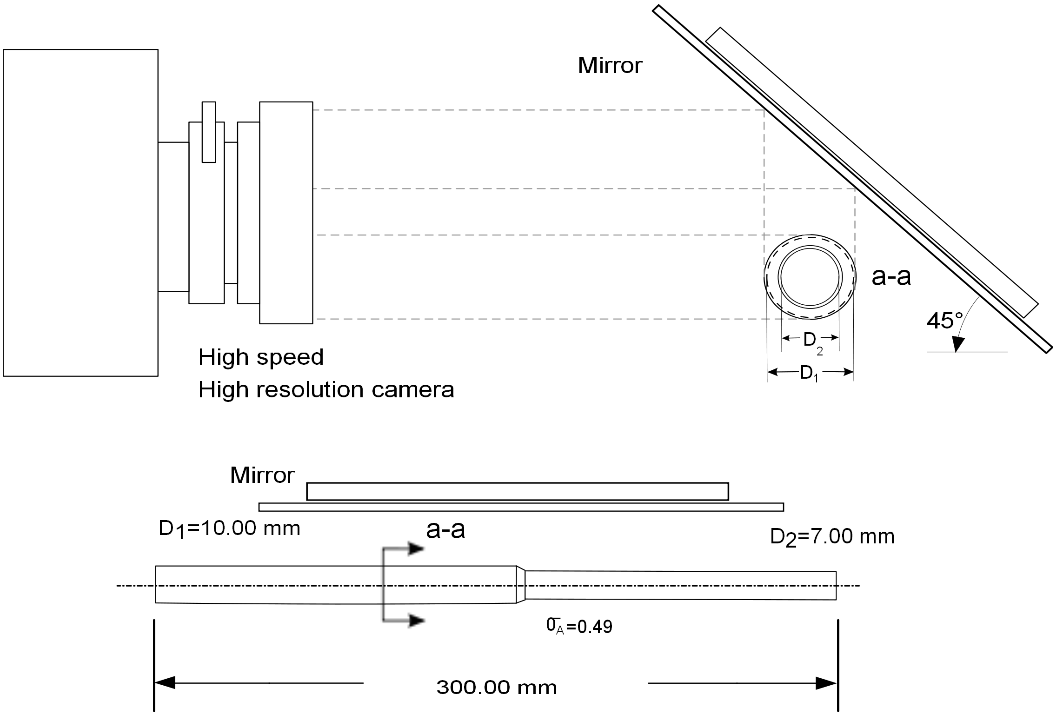

Figure 4.4: Sketch of section a-a used to visualize flow regimes in sudden contraction.

4.2.2 Test section for perturbation lengths measurements

In order to determine the flow recovery length necessary to make a correct pressure drop measurement downstream of singularities such as return bends or the sudden contraction, [Padilla *et al.* 2011b] presented two adiabatic test sections for flow recovery length measurements downstream of a return bend (Fig. 4.5). This section was made of smooth copper tubes (D = 7.90 mm) and two thermocouples were placed at the inlet and the outlet of the test section in the center of the flow. The desired vapor quality at the inlet of the test section was obtained by adjusting the power of the electrical heater.

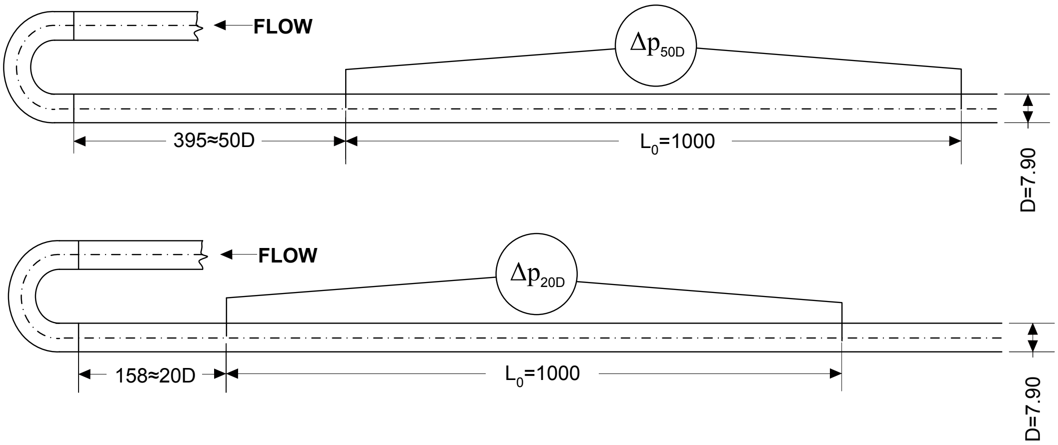

Figure 4.5: Sketch of the sections used to determine the flow recovery length downstream of the return bend. [Padilla *et al.* 2011b]

As explained in [Padilla *et al.* 2011b], to check if the perturbation length upward the pressure tap was sufficient to make a correct pressure drop measurement downstream of the return bends, two pressure drop tests in straight tubes using refrigerant HFO-1234yf were carried out by considering two different inlet pressure tap locations. In the first test, the pressure drop was measured along the straight tube (D = 7.90 mm, L_0 = 1000 mm) with the first pressure tap located approximately $50D \approx 400$ mm downstream of the return bend. For the second test, the first pressure tap was located approximately $20D \approx 160$ mm downstream of the return bend. Figures (4.6(a)) and (4.6(b)) show the results of these tests. The straight tube pressure drop measured for a recovery length of $20D$ does not deviate significantly ($\pm 5\%$) from the straight tube pressure drop measured at $50D$. In this sense, to minimize the test section size, the minimal flow recovery length of $20D$ was selected to locate the pressure taps downstream of the return bends. In addition, authors compared the straight tube pressure gradients to the models of [Müller-Steinhagen & Heck 1986] and [Moreno Quibén & Thome 2007]. Results showed that the data were comprised between these two models.

In order to double-check the perturbation effects up- and downstream of the singularity (return bends, sudden contractions), two test sections for perturbation lengths measurements have been developed.

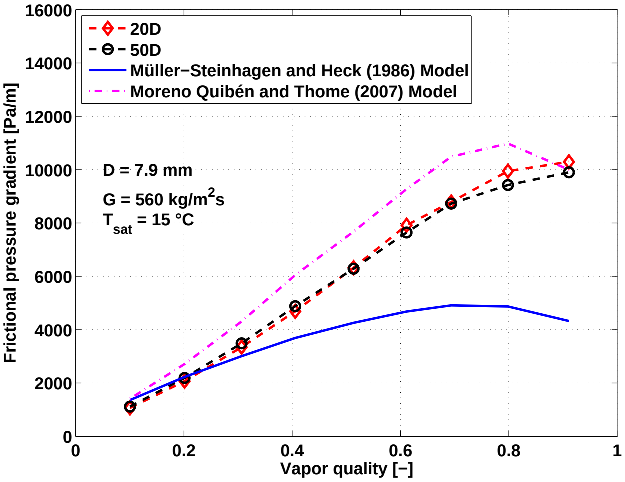

(a)

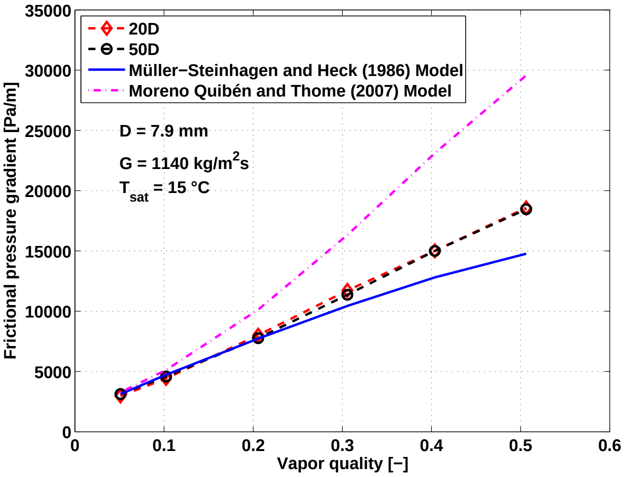

(b)

Figure 4.6: HFO-1234yf frictional pressure drop in straight tubes vs. vapor quality for two flow recovery lengths upstream of the straight tube, namely $20D$ and $50D$. [Padilla *et al.* 2011b]

4.2.2.1 Test section for perturbation length measurements up- and downstream of a return bend

Figure 4.7, shows the test section for perturbation length measurements up- and downstream of a return bend. This test section leads to measure the total pressure drop along the return bend with the pressure taps placed at different up- and downstream locations. In this sense, to determine the perturbation length downstream of the return bend, the total pressure drop is measured from a pressure tap positioned $50D$ upstream of the return bend to different pressure taps located at $5D$, $10D$, $20D$, $30D$ and $50D$ downstream of the return bend. A similar procedure has been conducted to determine the upstream perturbation length measuring the total pressure drop from different pressure taps located at five different lengths upstream of the return bend to the pressure tap located $50D$ downstream of the return bend.

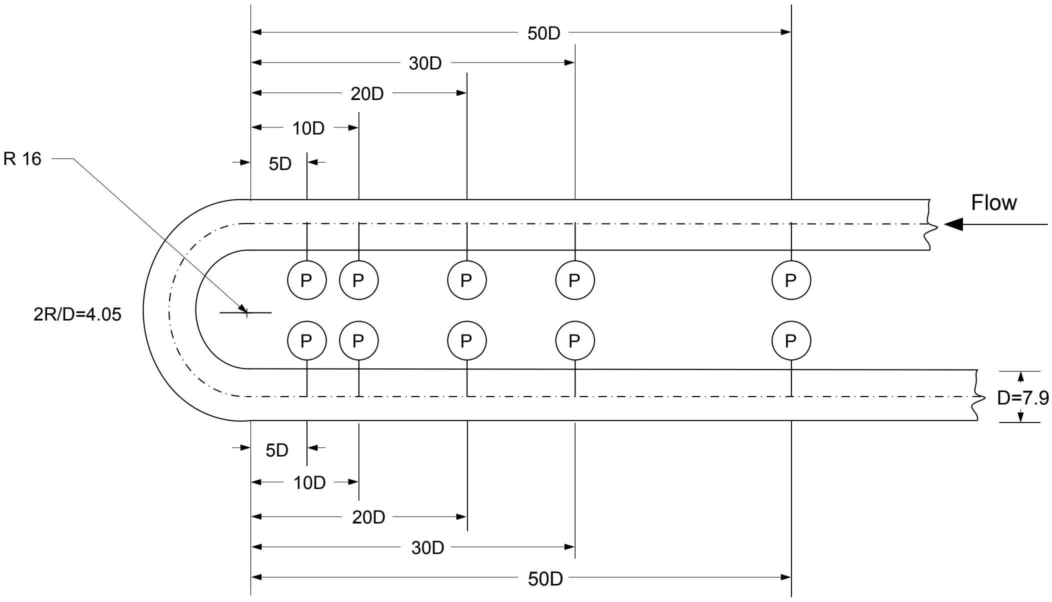

Figure 4.7: Test section used to measure the perturbation lengths up- and downstream of a return bend.

4.2.2.2 Test section for perturbation length measurements up- and downstream of a sudden contraction

To make a correct pressure drop measurement which includes the effects caused by abrupt flow area changes upstream and downstream of the sudden contraction, a specific test section was developed (Fig. 4.8). This test section was made of smooth copper tubes and includes two straight tubes ($D = 7.90$ mm and $D = 5.30$ mm), one sudden contraction and two return bends. The downstream segment of the test section has 4 pressure taps spaced $15D_2$, $30D_2$, $70D_2$ and $100D_2$ from the singularity, and the upstream one has 4 pressure taps spaced $15D_1$, $28D_1$, $70D_1$ and $100D_1$ from the singularity. The pressure taps are connected to two manifolds by flexible plastic tubing and these manifolds are connected to a differential pressure transducer. Through this arrangement, the pressure difference between adjacent pairs of pressure taps can be measured using the same transducer. Contrary to the return bends, no perturbation lengths information for two-phase flow up- or downstream of the sudden contraction were found in the literature.

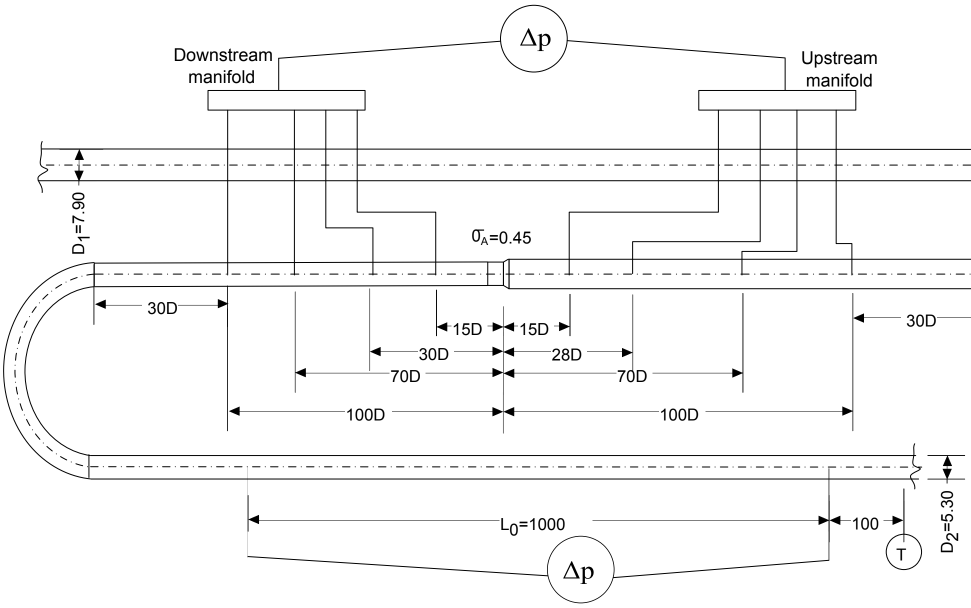

Figure 4.8: Test section used to measure the perturbation lengths up- and downstream of a sudden contraction.

This arrangement allows to compare several lengths in order to determine which is the minimal length needed to locate the pressure taps in the test section. Several tests have been carried out to determine these lengths. The complete description (experimental conditions and results) is given in Chapter 7. For two different fluids such as R-134a and R-410A refrigerants, the results obtained show that there was no significant difference for the sudden contraction pressure drop measured above $70D$ downstream and above $28D$ upstream of the singularity.

4.2.3 Test section for pressure drop measurements

For pressure drop measurements, the experimental setup used a 3105 mm long adiabatic test section (Fig. 4.9) which is made of smooth copper tubes and includes two straight tubes, two return bends and one sudden contraction. The test tubes can be set horizontally or vertically. The saturation pressure is measured using an absolute pressure transducer (JPB model Tb233) located at the outlet of the test section. In addition, two thermocouples are placed at the inlet and the outlet of the test section in the center of the flow. The desired vapor quality at the inlet of the test section is obtained by adjusting the power of the electric heater.

A straight entrance tube of inner diameter 10.85 mm and 550 mm ($50D$) long is located upstream of the first straight tube of the test section to achieve a fully-developed flow condition. A differential pressure transducer (Rosemount 3051C) is used to measure the pressure drop across the first straight tube ($D = 10.85$ mm, $L_0 = 1000$ mm). The pressure gradient along the first return bend ($2R/D = 3.68$) is measured from a second differential

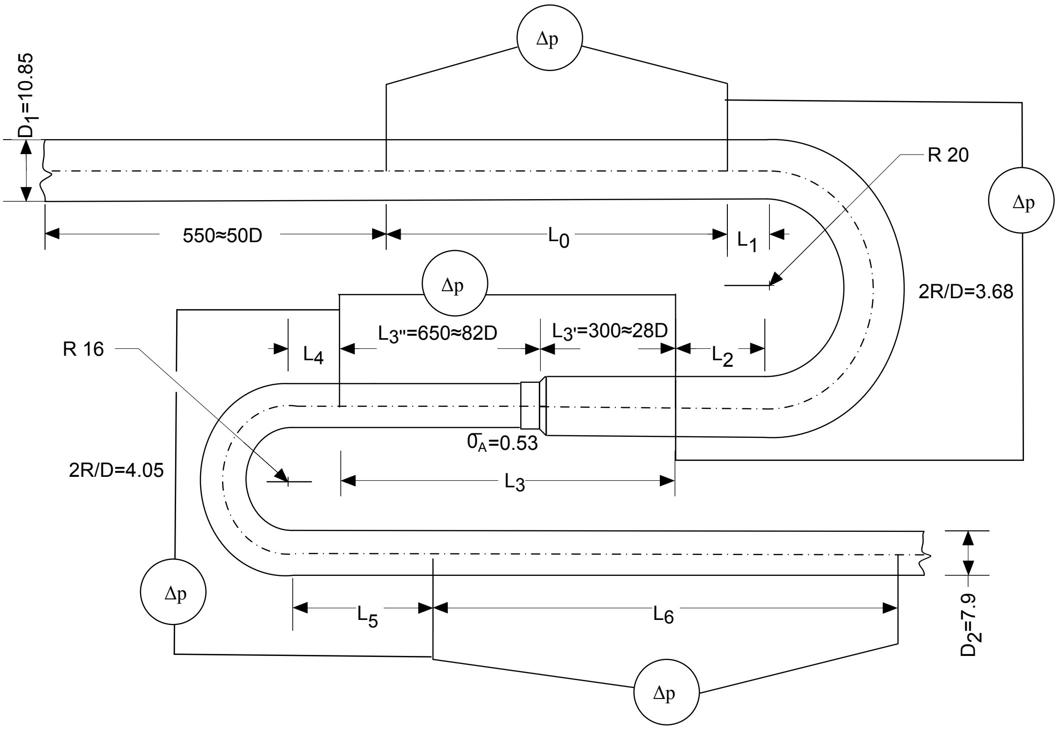

Figure 4.9: Test section for pressure drop measurements. L_0 = 1000 mm ≈ $92D$, L_1 = 110 mm ≈ $10D$, L_2 = 210 mm ≈ $20D$, L_3 = 950 mm, L_4 = 120 mm ≈ $15D$, L_5 = 160 mm ≈ $20D$, L_6 = 1000 mm ≈ $127D$.

pressure transducer (Elsag Baley type PTS). The pressure tap is located 210 mm ≈ $20D$ (L_2) downstream of the return bend. 300 mm ≈ $28D$ downstream of the pressure tap the flow passes across a sudden contraction to obtain a new tube diameter. A straight tube of length 650 mm ≈ $82D$ is directly connected downstream of the sudden contraction for the flow recovery.

The differential pressure transducers described above are used to measure the pressure drop across the second return bend ($2R/D = 4.05$) and the second straight tube ($D = 7.90$ mm, $L_6 = 1000$ mm) by using a set of 11 valves in two manifolds (Fig. 4.10). The pressure tap is located 165 mm ≈ $20D$ downstream of the second return bend. As explained in section 3.2.1, the flow recovery length of $9D$ downstream of the return bend is respected.

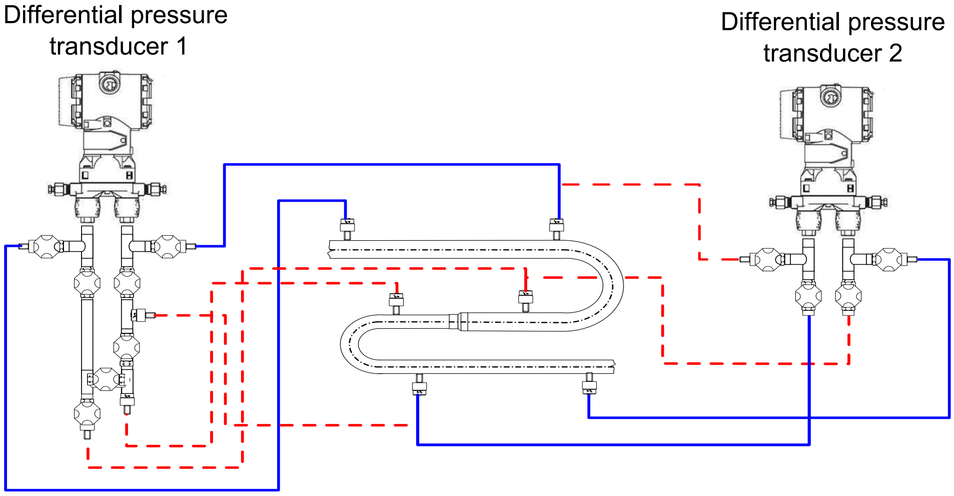

Figure 4.10: Details of the manifolds and valves arrangement for pressure drop measurements. Continuous lines show the connections for straight tube pressure drop measurements. Dashed lines show the connections for the return bends and the sudden contraction pressure drop measurements.

4.3 Instrumentation and data acquisition

The experimental setup, as described above, is completely monitored using a computer. Signals from the thermocouples, pressure transducers and the mass flow meter are collected by a computerized data acquisition system (Fig. 4.11). The entire acquisition system includes:

1. Laptop.
2. LabView 8.2, a graphical data acquisition programming language (National Instruments, 2006). A LabView program was written to perform system monitoring and data acquisition (Section 4.3.1).
3. One KEITHLEY Data Acquisition model 2701 with two slot cards allowing for multiple measurements up to 40 channels.
4. Two (2) DC/DV electric sources. These sources are capable of supplying 24 V. They are used to supply power to differential pressure transducers.

5. One Hyoki 3193 power tester unit to control the phases of the refrigerant electrical heater.
6. Two (2) PID controllers for the 4-ways valve and the PT-100 for the water-glycol cooling loop

4.3.1 The LabView program

The data acquisition program was developed in National Instruments' LabView. This interface utilizes the inputs received from sensors to achieve the data acquisition. The sensors utilized by the LabView software are presented in Table 4.2.

Table 4.2: Equipment utilized by the LabView software backbone in the two-phase experimental setup.

Equipment	Range	Incertitude
K-Type thermocouple:	-30 - 300 °C	±0.1K
PT-100 probe class B:	-50 - 450 °C	±0.1K
Rosemount 3051C pressure transducer:	25 Pa - 27.6 MPa	±0.04%
Elsag Baley pressure transducer:	0 - 33.29 kPa	±0.1%
Danfoss coriolis-type mass flow meter:	0 - 5600 $\text{kg}\cdot\text{h}^{-1}$	±0.15%
Hyoki power tester:	0 - 10 kW	±0.001 kW

The main LabView VI (Virtual Instrument) performs the data acquisition operations required. As shown in Figure 4.12, the program is divided into two 'tabs'; each one of these is utilized to show the salient information of each circuit described in section 4.1. It is important to note that there are several data which are not placed inside tabs; due to the fact that they are, in general, part of the calculation procedure to obtain the final parameters tabbed for monitoring purposes. These include the enthalpies for the energy balance, signal conversion from 4 - 20 mA to Pa, Reynolds number, etc.

The water-glycol circuit tab allows the operator to check the inlet and the outlet water-glycol temperatures in the condenser and the sub-cooler. In the refrigerant circuit tab (LabView front panel) are included:

- Refrigerant: for refrigerant selection (R-410A, R-134a or HFO-1234yf).
- Refrigerant electrical heater power supply: gives in real-time the corresponding power supply of each three phases of the electrical heater. In this sense, Phase 1 is a variable phase that let modify the power supply in a range from 0 to 3.4 kW. Phases 2 and 3 are fixed to 3.3 kW each one. The total power supply in the refrigerant electrical heater is up to 10 kW.
- Test section operational conditions: TC_{01}, TC_{02}, Δp, p_{abs}, $\Delta p_{\text{Rosemount}}$, $\Delta p_{\text{Elsag Baley}}$ and p_{abs} are calculated by the relations (4.2), (4.3) and (4.4) respectively. These relations are given by the manufacturer.

$$\Delta p_{\text{Rosemount}} = 25012.1485(I) - 5002.1176 \tag{4.2}$$

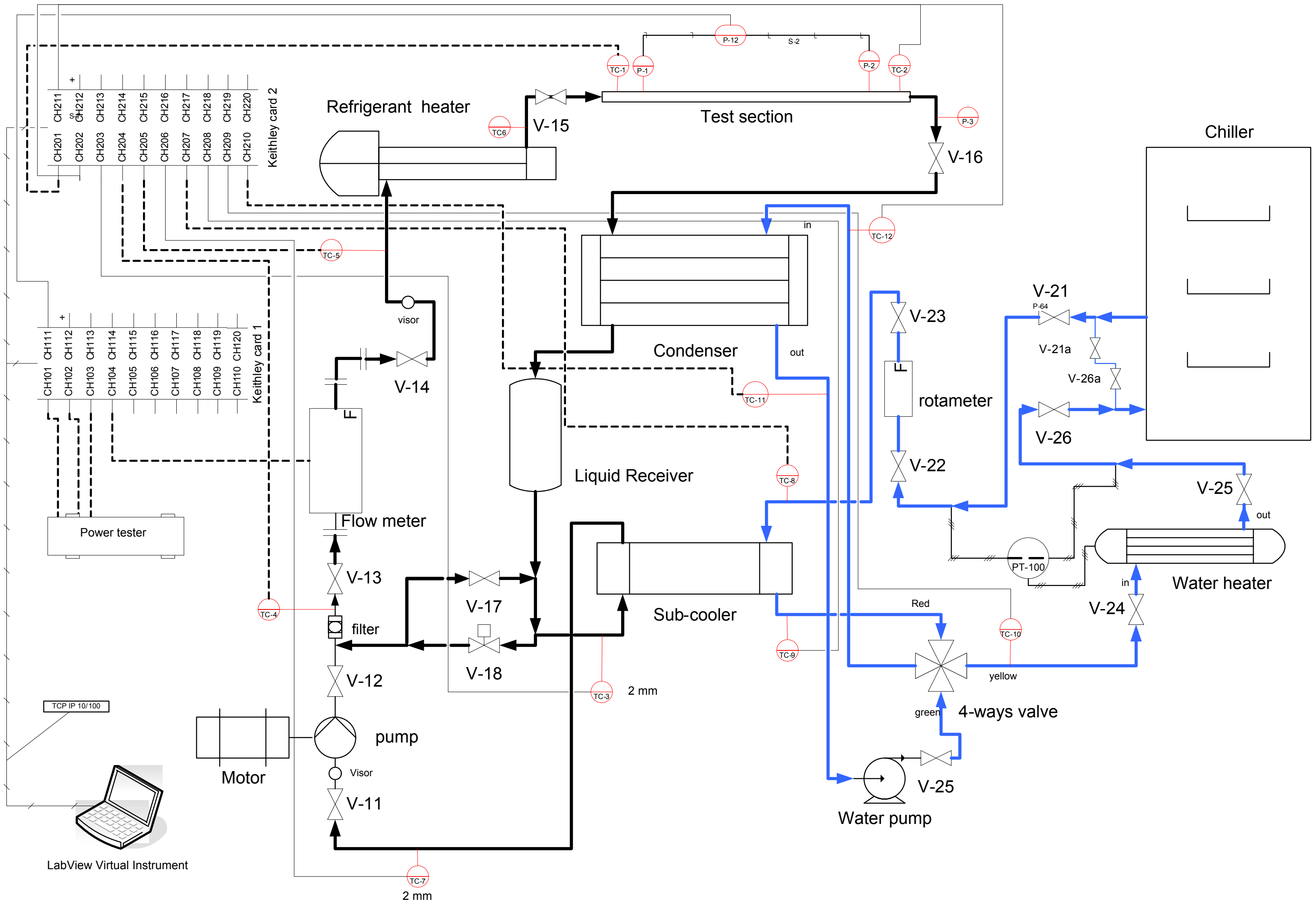

Figure 4.11: Experimental facility pipe and instrumentation diagram.

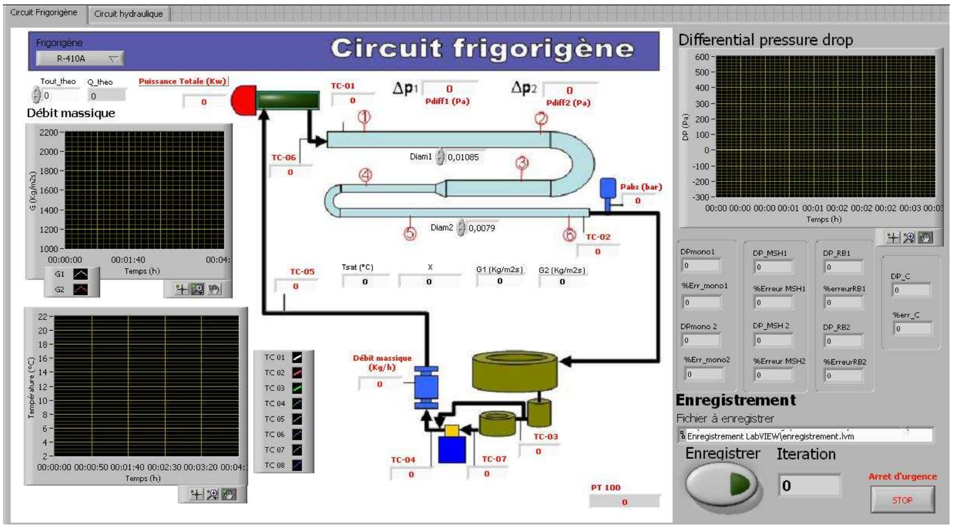

(a) Refrigerant circuit

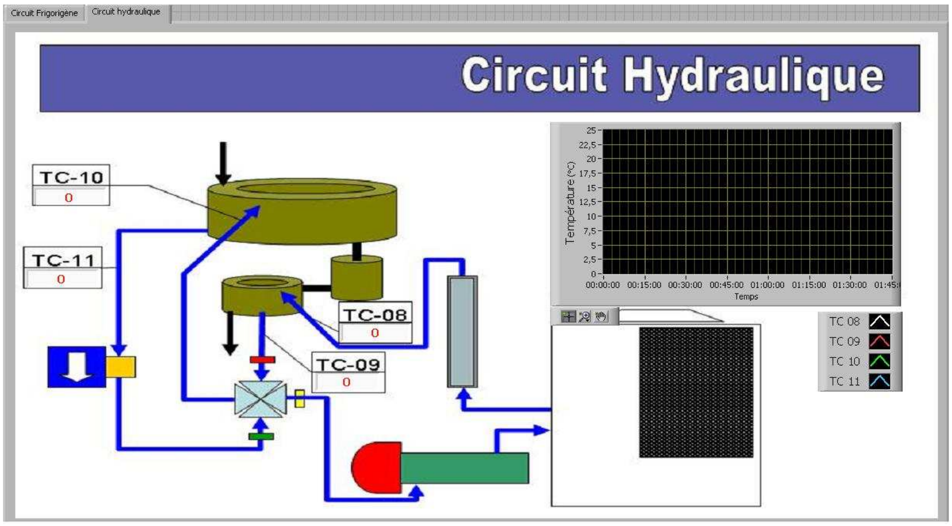

(b) Water-glycol circuit

Figure 4.12: LabView VI (Virtual Instrument).

$$\Delta p_{\text{Elsag Baley}} = 37349.390365(I) - 7529.71 \tag{4.3}$$

$$p_{\text{abs}} = 24.85165(I) - 3.10386 \tag{4.4}$$

where I is the current expressed in [A].

- Condenser outlet temperature: TC_{03}.
- Main liquid line temperature (before Coriolis mass flow meter): TC_{04}.
- Refrigerant electrical heater inlet and outlet temperatures: TC_{05} and TC_{06}.
- Sub-cooler water-glycol inlet and outlet temperatures: TC_{07} and TC_{08}.
- Condenser water-glycol inlet and outlet temperatures: TC_{09} and TC_{10}.
- Mass flow rate ($\dot{m}$): calculated by the relation (4.5) given by the manufacturer.

$$\dot{m} = 437.5(I) - 87.5 \tag{4.5}$$

- Mass velocity (G): mass velocity corresponding to each pipe inner diameter (D) is calculated following the expression introduced in section 2.5.1, where $A = \pi D^2/4$.
- Vapor quality (x): the vapor quality entering the test section is calculated from the energy balance on the electrical heater given by Eq. (4.6):

$$\Delta x = \frac{\left(\dfrac{\text{P}_{\text{heater}}}{\dot{m}}\right) - (h_{\text{l}} - h_{\text{heater,in}})}{h_{\text{lv}}} \tag{4.6}$$

  where $h_{\text{lv}} = h_{\text{v}} - h_{\text{l}}$ is the latent heat of vaporization and $(h_{\text{l}} - h_{\text{heater,in}})$ corresponds to the sub-cooling sensible heat. P_{heater} is the electrical power of the heater. When the pressure drop related to the frictional dissipation term reaches non-negligible values and provokes the so-called flashing (see section 2.6.3.1), the flashing effect is calculated using the relation (2.50).

- All thermodynamic properties such as saturation temperature (T_{sat}), enthalpy (h), density (ρ), viscosity (μ) and surface tension (σ) for refrigerants R-410A and R-134a have been obtained from the NIST thermodynamic properties of refrigerants and refrigerant mixtures database [McLinden *et al.* 2007]. The thermodynamic property tables of the refrigerant HFO-1234yf have been generated using the REFPROP software with the last updated properties library. Appendix C provides information about physical properties of these refrigerants.
- A running history of the mass velocities, pressure drops and fluids (both the refrigerant and the water-glycol mixture) temperatures are presented in time dependent graphs.
- Error indicators are also available. These indicators provides important information in order to notify if any system parameters falls over or runs over the specified safety limits.
- The 'Save' button is used to manually specify the file name convention, and the directory used for saving, as well as the number of samples to capture per saved data point (30 by defect).

4.4 Measurements and accuracy

This section introduces the root-sum-square (RSS) combination, the basic form used for combining uncertainty contributions in multiple-sample analysis. In this section, the term δX_{i} refers to the uncertainty in X_{i} in a general and nonspecific way: whatever is being dealt with at the moment (for example, fixed errors, random errors, or uncertainties).

Consider a variable X, which has a known uncertainty δX. The form for representing this variable and its uncertainty is:

$$X = X_{\mathrm{i(measured)}} \pm \delta X_{\mathrm{i}} \tag{4.7}$$

The value of $X_{\mathrm{i(measured)}}$ represents the observation in a single-sample experiment or the mean of a set of N observations in a multiple-sample experiment. The value of δX represents 2σ for a single-sample analysis, where σ is the standard deviation of the population of possible measurements from which the single sample X, was taken. For multiple-sample experiments, δX_{i} can have three meanings. It may represent $tS_{(N)}/\sqrt{N}$ for random error components, where $S_{(N)}$ is the standard deviation of the set of N observations used to calculate the mean value $\bar{X}_{\mathrm{i}}$ and t is the Student's t statistic appropriate for the number of samples N and the confidence level desired. Finally, δX_{i} may represent $U_{.95}$, the overall uncertainty in X_{i}.

The result R of the experiment is assumed to be calculated from a set of measurements using a data interpretation program (by hand or by computer) represented by:

$$\mathrm{R} = \mathrm{R}(X_1, X_2, X_3, X_4, \cdots, X_N) \tag{4.8}$$

The effect of the uncertainty in a single measurement on the calculated result, if only that one measurement were in error would be:

$$\delta \mathrm{R}_{X i} = \frac{\partial \mathrm{R}}{\partial X_{\mathrm{i}}} \delta X_{\mathrm{i}} \tag{4.9}$$

The partial derivative of R with respect to X_{i} is the sensitivity coefficient for the result R with respect to the measurement X_{i}. When several independent variables are used in the function R, the individual terms are combined by a root-sum-square method.

$$\delta \mathrm{R} = \left\{ \sum_{1}^{N} \left(\frac{\partial \mathrm{R}}{\partial X_{\mathrm{i}}} \delta X_{\mathrm{i}} \right)^2 \right\}^{1/2} \tag{4.10}$$

Equation (4.10) is the basic equation of uncertainty analysis. Each term represents the contribution made by the uncertainty in one variable, ∂X_{i}, to the overall uncertainty in the result, δ R. Each term has the same form: the partial derivative of R with respect to X_{i} multiplied by the uncertainty interval for that variable.

According to [Moffat 1988], in many applications, the uncertainty estimate is wanted as a fraction of reading, rather than in engineering units. While this can always be calculated, starting from the results of the general form in Eq. (4.10), it is sometimes possible to do the calculation of relative uncertainty directly. In particular, whenever the equation describing the result is a pure "product form," such as Eq. (4.11), or can be put into that form, then the relative uncertainty can be found directly. That is, if:

$$\mathrm{R} = \mathrm{R}(X_1^a, X_2^b, X_3^c, X_4^d, \cdots, X_M^m) \tag{4.11}$$

then

$$\frac{\delta \mathrm{R}}{\mathrm{R}}=\left\{\left(a\frac{\partial X_1}{X_1}\right)^2+\left(b\frac{\partial X_2}{X_2}\right)^2+\left(c\frac{\partial X_3}{X_3}\right)^2+\left(m\frac{\partial X_\mathrm{m}}{X_\mathrm{m}}\right)^2\right\}^{1/2} \tag{4.12}$$

This is a natural and convenient approach in situations when the uncertainties of the component measurements are described in terms of percent of reading and the result is needed in the same terms. The exponent of X_i becomes its sensitivity coefficient.

4.4.1 Tube diameter

Tube diameters have been measured with a digital vernier caliper with a resolution of ±0.03 mm. The measurements for each diameter have been carried out on two samples chosen among the same tube used in the test section fabrication. 8 measurements have been made for each diameter. The results are obtained using the Student distribution. The uncertainty obtained for the lower diameter used in the present study ($D = 5.30$ mm) is less that 0.6 %.

4.4.2 Tube lengths

Tube lengths are measured with an error less than 0.5 mm. This uncertainty comes directly from the measurement instrument.

$$\Delta L = 5 \times 10^{-4}\mathrm{m} \tag{4.13}$$

The minimal tube length measured is 100 mm, thus the relative error is 0.5 %.

4.4.3 Temperature

All the thermocouples are K-type and come from the company *Serv-Instrumentation*. They have been calibrated with two reference platinum probes in a temperature range from -20 °C to 40 °C. A second degree polynomial equation has been applied to correct the measurements. The absolute error is:

$$\Delta T = 0.1\mathrm{K} \tag{4.14}$$

4.4.4 Fluid properties

The fluid properties were calculated from a temperature measurement by applying a linear regression of the 3rd order determined with *REFPROP* software.

$$X = a_0 + a_1 T + a_2 T^2 + a_3 T^3 \tag{4.15}$$

and the corresponding uncertainty is:

$$\Delta X = \left[a_1 + 2a_2 T + 3a_3 T^2\right]\Delta T \tag{4.16}$$

The coefficients a_0, a_1, a_2 and a_3 for the R-134a enthalpy calculations are given in the Table 4.3.

For example, for a given temperature of 30 °C the results for the enthalpies for R-134a are h_l = 241712 J·kg^{-1} ±0.06% and h_v = 414853 J·kg^{-1} ±0.01%. As can be seen, the relative errors made on the enthalpy calculations are negligible.

Table 4.3: Coefficients for the refrigerants enthalpy calculations.

Fluid	R-134a		R-410A		HFO-1234yf	
	h_l	h_v	h_l	h_v	h_l	h_v
a_0	200002.6	398600.1	200007.3	421297.8	36922.1	200100.1
a_1	1343.4	583.6	1513.12	314.8	1296.5	656.2
a_2	1.3	-1.0	2.4	-3.4	1.7741	-0.817
a_3	0.0088	-0.0131	0.0316	-0.0518	0.0049	-0.0104

4.4.5 Mass flow

The specifications of the Danfoss MASSFLO 2100 Coriolis-type mass flow meter are indicated as follows:

$$\begin{aligned}&\text{for}\,\dot{m} \geq 5\%\,(\text{full scale})\,\mathrm{kg\cdot s^{-1}},\ \Delta\dot{m} = 0.15\%\dot{m} \qquad (4.17)\\ &\text{for}\,\dot{m} < 5\%\,(\text{full scale})\,\mathrm{kg\cdot s^{-1}},\ \Delta\dot{m} = \pm\sqrt{(0.15)^2 + \left(\frac{66}{\dot{m}}\right)^2}\,\%\end{aligned}$$

4.4.6 Mass velocity

The definition of the mass velocity G was introduced in section 2.5.1. It can be expressed for a circular pipe as:

$$G = \frac{4\dot{m}}{\pi D^2} \tag{4.18}$$

The uncertainty for G is:

$$\Delta G = G\sqrt{\left(\frac{\Delta\dot{m}}{\dot{m}}\right)^2 + \left(2\frac{\Delta D}{D}\right)^2} \tag{4.19}$$

The mass velocity ranges from 186.7 kg·m^{-2}·s^{-1} (for D = 10.45 mm) to 1702.2 kg·m^{-2}·s^{-1} (for $D = 7.90$ mm). Thus the uncertainties are:

$$G = 186.7\,\mathrm{kg\cdot m^{-2}\cdot s^{-1}} \pm 0.5\%\ \text{for}\, D = 10.45\mathrm{mm}$$

$$G = 1702.2\,\mathrm{kg\cdot m^{-2}\cdot s^{-1}} \pm 1.3\%\ \text{for}\, D = 7.90\mathrm{mm}$$

4.4.7 Pressure drop

The pressure transducers are connected to a Keithley data acquisition system. The nominal uncertainty given by the manufacturers are ± 0.10 % for the Elsag Baley transducer and ± 0.04 % for the Rosemount 3051CD in overall measure range. The total performance includes the errors due to nominal uncertainty, environment temperature effect and static pressure efect. This nominal uncertainty includes to the hysteresis errors, the linearity as a function of scale limit values and the repeatability of measurements.

4.4.8 Energy balance

The power supplied to the electrical heater in the refrigerant circuit is directly measured using the HIOKI 3193 POWER HiTESTER. The power measurements accuracy given by the manufacturer is ± 1 W. If considering the pressure drop measurements for R-410A, the entire range of power supplied to the electrical heater was from 0.311 ± 0.001 kW to 10.378 ± 0.001 kW. The uncertainty is less than 0.33 %. The description of the uncertainties of the single-phase energy balance carried out on the electrical heater is presented in Appendix B.

4.4.9 Vapor quality

The vapor quality entering the test section is calculated from the energy balance on the electrical heater given by Eq. (4.1):

$$x = \frac{\left(\dfrac{\mathrm{P}_{\mathrm{heater}}}{\dot{m}}\right) + h_{\mathrm{heater,in}} - h_{\mathrm{l}}}{h_{\mathrm{lv}}}$$

The absolute error is expressed as:

$$\Delta x = \frac{1}{h_{\mathrm{lv}}}\sqrt{\left(\frac{\Delta \mathrm{P}_{\mathrm{heater}}}{\dot{m}}\right)^2 + \left(\frac{\mathrm{P}_{\mathrm{heater}}\Delta\dot{m}}{\dot{m}^2}\right)^2 + (\Delta h_{\mathrm{heater,in}})^2 + (\Delta h_{\mathrm{l}})^2 + (x\Delta h_{\mathrm{lv}})^2} \quad (4.20)$$

where Δh_{l}, $\Delta h_{\mathrm{heater,in}}$ and Δh_{lv} are given by Eq. (4.16).

For example, if considering the most critical operation test conditions for R-410A (low mass velocity and high vapor quality) as $x = 0.96$, $T_{\mathrm{sat}} = 10.1$ °C, $\mathrm{P}_{\mathrm{heater}} = 3.965$ kW, $\dot{m} = 0.019$ kg·s^{-1}, $T_{\mathrm{l}} = 4.1$ °C and $T_{\mathrm{heater,in}} = 10.4$ °C, the uncertainty is less than 0.82 %.

4.5 Experimental procedure

Once the commissioning procedure is finished (the system is considered leak-free and is charged with the proper refrigerant) the system is ready to be started. It is necessary to check that the water-glycol supply temperatures are within tolerances. In the case of the cooling water-glycol supply, the mixture temperature should be between -3 - 0 °C, while in the heating water-glycol loop, the mixture temperature should be between 30 - 35 °C. To get these conditions, the first step is to start up the chiller and the 30 kW electrical heater in the cooling water-glycol loop (see section 4.1.2). Then, the centrifugal pump and the 9 kW electrical heater. For security reasons, it is very important not to start up the electrical heaters without having a proper water-glycol flow in both loops.

Before starting up the refrigerant circuit, all valves in the refrigerant loop need to be fully opened. In the main control panel, there are 9 switches which activate the refrigerant pump, the water-glycol pump, the Coriolis-type mass flow meter, the 4-ways valve, the absolute pressure transducer and each phase of the refrigerant electrical heater. The last switch governs the power supply to the experimental facility. An emergency stop button is also available. In the operation of this experimental facility, all protocols for industrial hygiene and safety (including those under special regulations related to refrigerants handling) have been respected.

4.6 Chapter Conclusion

The existing flow boiling test facility used by [Branescu 2000] at the Centre Thermique de Lyon (CETHIL UMR-5008) has been successfully modified and adapted to the different test conditions and measurement methods required by the present PhD work. Two new test sections for flow regime visualization and pressure drop measurements have been successively implemented into the modified test rig. The visualization test section allows to visualize flow regimes in straight tubes, sudden contractions and return bends. The latter can be placed horizontally and vertically. The test section for pressure drop measurements consists of five sections: two straight tubes (7.90 mm and 10.45 mm inner diameter), two return bends and one sudden contraction. This configuration allows the tests to be run in order to obtain experimental two-phase pressure drop values under adiabatic conditions.

Regarding the test section design, to minimize the test section length, the minimal flow recovery length of $20D$ was selected to locate the pressure taps downstream of the return bends. Concerning the sudden contraction, the minimal flow recovery length of $82D$ was selected to locate the pressure taps downstream of the singularity.

A mirror was settled down behind the glass tube in the visualization test section in order to visualize flow regimes simultaneously from the top and the side views of the straight tube and sudden contractions. Observations of flow patterns are obtained from images given by a high-speed high-resolution camera.

No two-phase flow regimes visualization of refrigerants in sudden contraction, return bends nor the top and the side views simultaneously of the straight tube have been found in the literature. Hence, investigations related to these points are one of the objectives of the present thesis.

CHAPTER 5

Two-phase flow in straight tubes

Contents

This chapter presents the results for two-phase flow regime visualizations for the next generation HFO-1234yf and the well known R-134a refrigerants in straight tubes. In addition, a new pressure drop database measured during two-phase flow of refrigerants HFO-1234yf, R-134a and R-410A in horizontal straight tubes is presented. The results are compared against 10 well-known two-phase frictional pressure drop prediction methods. A statistical analysis for each flow regime was also carried out.

5.1 Experimental procedure

5.1.1 Single-phase experiments

In order to check the measurements made with the present experimental facility, an energy balance and single-phase pressure drop measurements have been carried out. The energy balance (Fig. 5.1(a)) depicts a Mean Relative Error less than 1%. The single-phase pressure drop data have been compared to the Blasius correlation for smooth tubes with a MRE less than 0.5% (Fig. 5.1(b)). The test facility is thus validated.

5.1.2 Data reduction

In order to obtain the values of the straight tube pressure gradient, the pressure drops in straight tubes have been measured and divided by the appropriate length:

$$\left(-\frac{\mathrm{d}p}{\mathrm{d}z}\right)_{\mathrm{st}} = \frac{\Delta p_{\mathrm{st}}}{L_i} \tag{5.1}$$

where $L_i = L_0 = 1000$ mm for $D = 10.85$ mm and $L_i = L_6 = 1000$ mm for $D = 7.90$ mm, (see Fig. 4.9). For $D = 5.3$ mm, the test section depicted in Fig. 4.8 has been used considering $L_0 = 1000$ mm

In the experiments, the maximum pressure drop measured from the outlet of the electrical heater (where the vapor quality is calculated) to the outlet of the test section can

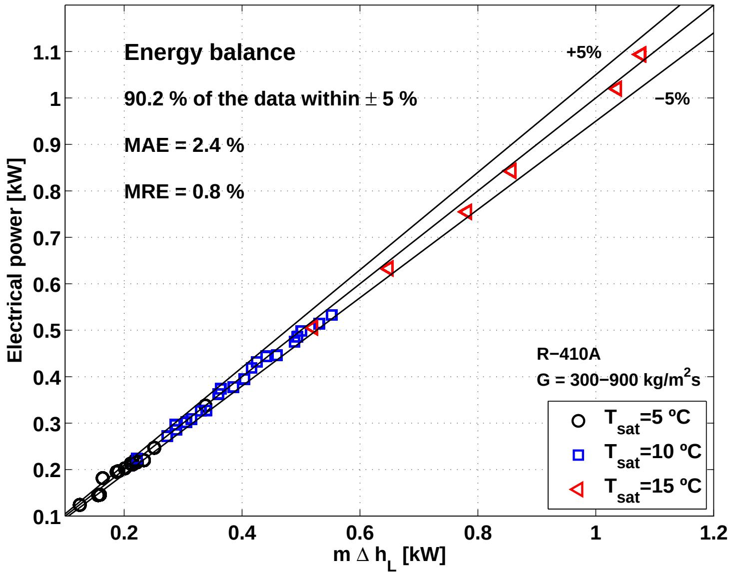

(a) Energy balance.

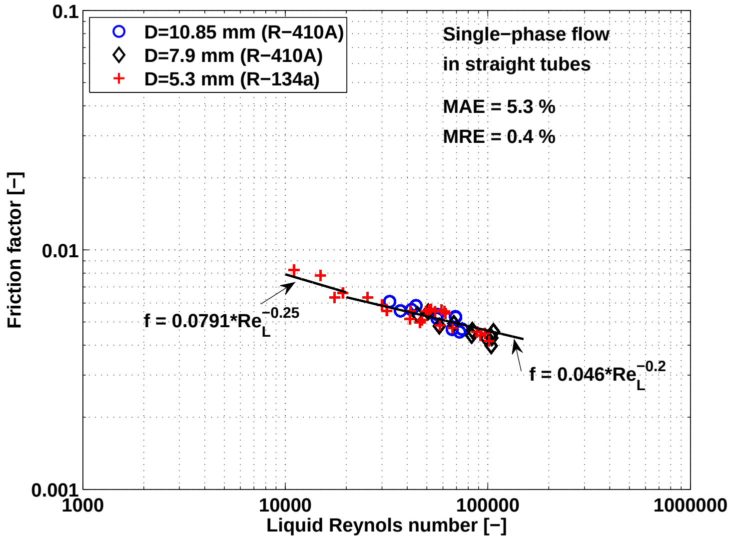

(b) Friction factor vs. Re for straight tube.

Figure 5.1: Energy balance and single-phase pressure drop measurements. [Padilla *et al.* 2011a]

reach up to 0.83 bar. This pressure drop is not negligible and provokes a flashing effect (see section 2.6.3.1) and a temperature difference. The flashing effect is calculated using the relation (2.50).

The maximum vapor quality variation Δx due to the flashing effect from the outlet of the electrical heater to the outlet of the test section is 0.02. As a consequence, the variation of the vapor quality along the tubes has been taken into account. This increase in the vapor quality induces a momentum pressure drop. The ratio of the momentum pressure drop to the total pressure drop over the whole length of the circuit from the outlet of the electrical heater to the outlet of the test section was found to be always lower than 2.6 %. As the test section used to obtain the pressure drop data is much shorter than the whole length of the circuit (about 4 times shorter), the additional momentum pressure drop in the test section can thus be neglected. In addition, the maximum temperature difference due to the pressure drop along the tube is up to 2.3 K. As a result, the saturation temperature is recalculated at the inlet of each straight tube,return bend and sudden contraction.

5.2 Experimental results

5.2.1 Two-phase flow visualization in straight tubes

Flow regimes of HFO-1234yf and R-134a have been observed in the range of mass velocities from 297 to 512 kg·m^{-2}·s^{-1}, vapor qualities from 5 to 90 % and T_{sat} from 9.5 to 10.5°C. Both top and side views were recorded simulaneously.

Flow regime visualizations of HFO-1234yf and R-134a have been compared to the [Wojtan *et al.* 2005a] flow pattern map. It is important to note, that this flow pattern map was developed for R-22 and R-410A inside a 13.6 mm horizontal smooth tube and further validated for R-134a and other fluids. Figure 5.2 presents the HFO-1234yf and R-134a visualization data points for D = 6.70 mm, and T_{sat} = 10 °C plotted on the [Wojtan *et al.* 2005a] flow pattern map.

As can be seen, no major difference was found between the experimental flow regimes (slug, intermittent and annular flows) and their transitions and those predicted by [Wojtan *et al.* 2005a]. As a result, the flow pattern map proposed by the latter was used to predict the flow pattern of the current experimental pressure drop database.

Figures 5.3 and 5.4 show the different flow regimes observed. The side view reveals the effect of gravity, e.g. the vapor is to a certain extend preferentially located at the upper part of the tube. From the top view, we see that the vapor phase is centered.

40 experimental videos have been taken in total for HFO-1234yf and R-134a. No major difference can be observed when comparing the flow patterns of both refrigerants for the same conditions of mass velocity, saturation temperature, inner diameter and vapor quality, which was desirable since HFO-1234yf was designed so that its properties would be close to those of R-134a.

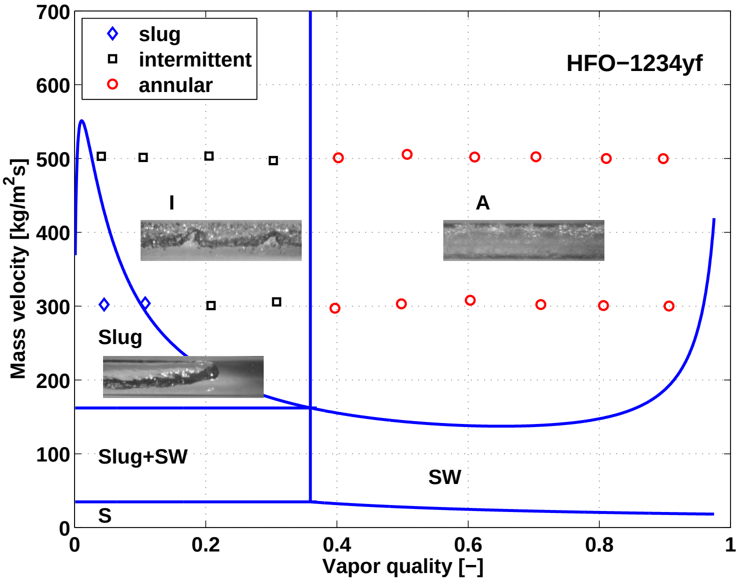

(a) $T_{\text{sat}} = 10$ °C, $G = 500$ kg·m^{-2}·s^{-1}, $D = 6.70$ mm and $q = 0$ kW·m^{-2}.

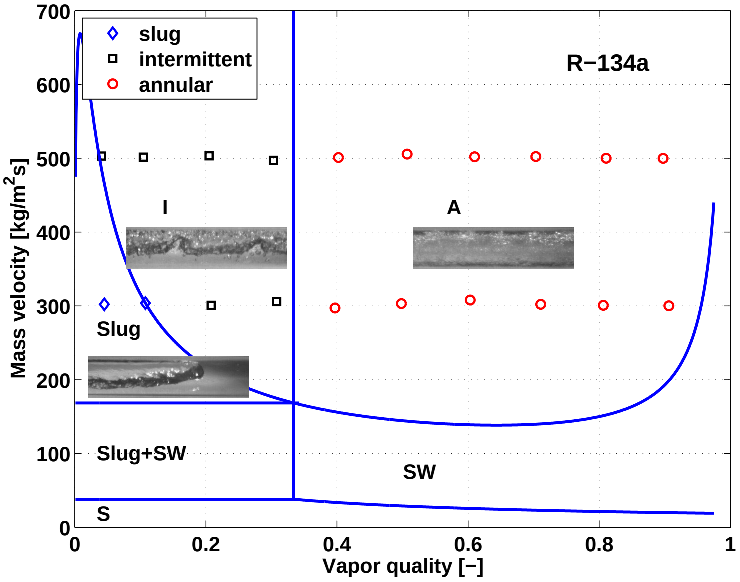

(b) $T_{\text{sat}} = 10$ °C, $G = 500$ kg·m^{-2}·s^{-1}, $D = 6.70$ mm and $q = 0$ kW·m^{-2}.

Figure 5.2: HFO-1234yf and R-134a visualizations plotted in the flow pattern map of [Wojtan *et al.* 2005a]. (I: intermittent, A: annular, Slug: slug, SW: stratified-wavy). [Padilla *et al.* 2011a]

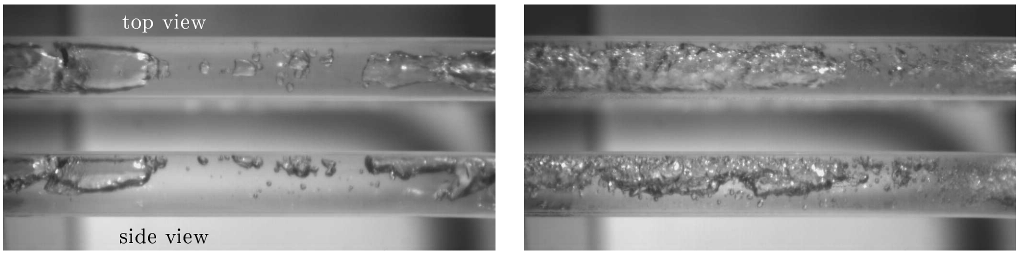

(a) Slug flow at $x = 5.2\%$ and $G = 306$ kg·m^{-2}·s^{-1}.

(b) Intermittent flow at $x = 19.1\%$ and $G = 306$ kg·m^{-2}·s^{-1}.

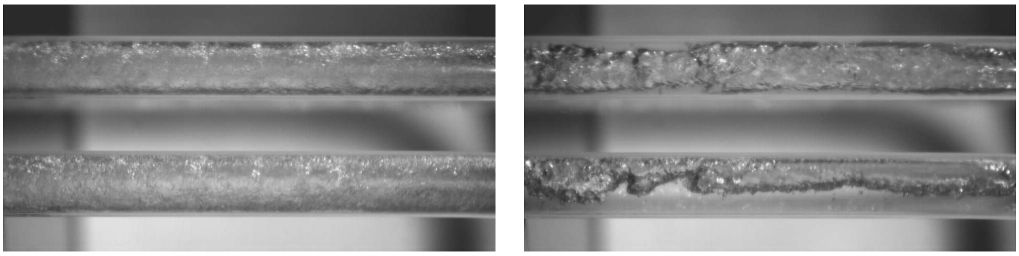

(c) Annular flow at $x = 61.0\%$ and $G = 307$ kg·m^{-2}·s^{-1}.

(d) Intermittent flow at $x = 6.7\%$ and $G = 512$ kg·m^{-2}·s^{-1}.

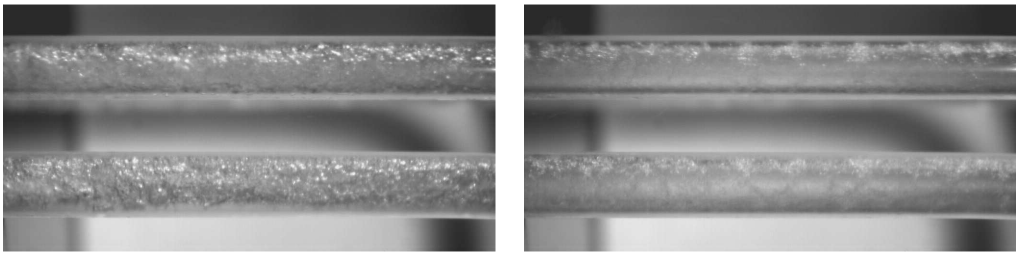

(e) Intermittent flow at $x = 21.8\%$ and $G = 497$ kg·m^{-2}·s^{-1}.

(f) Annular flow at $x = 58.9\%$ and $G = 506$ kg·m^{-2}·s^{-1}.

Figure 5.3: Top and side views of the HFO-1234yf flow patterns for $T_{\text{sat}} = 10$ °C and $D = 6.70$ mm. [Padilla *et al.* 2011a]

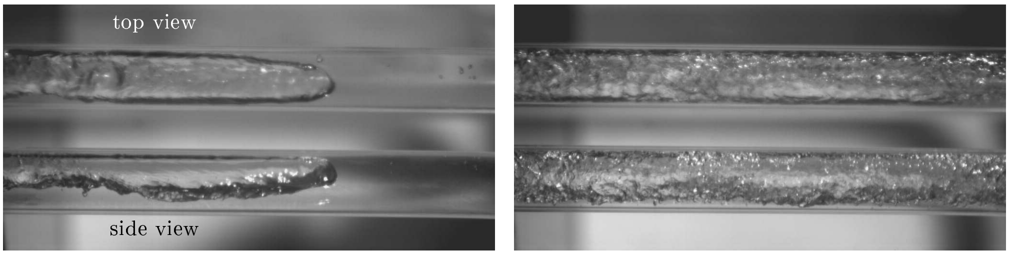

(a) Slug flow at $x = 4.8\%$ and $G = 302$ kg·m^{-2}·s^{-1}.

(b) Intermittent flow at $x = 20.7\%$ and $G = 310$ kg·m^{-2}·s^{-1}.

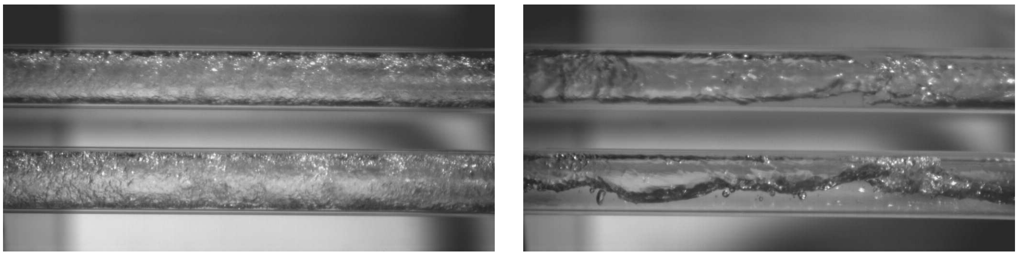

(c) Annular flow at $x = 60.0\%$ and $G = 301$ kg·m^{-2}·s^{-1}.

(d) Intermittent flow at $x = 4.8\%$ and $G = 496$ kg·m^{-2}·s^{-1}.

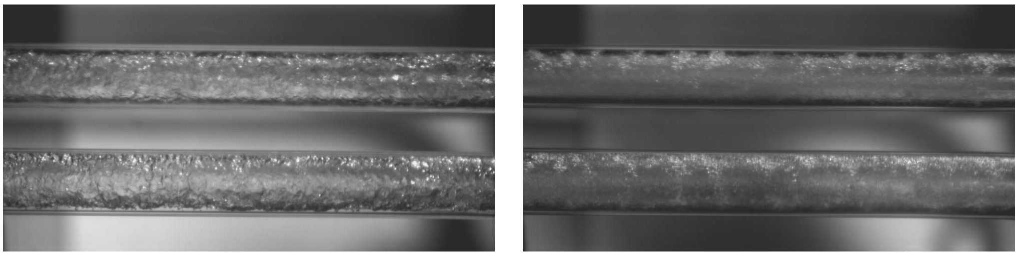

(e) Intermittent flow at $x = 20.4\%$ and $G = 498$ kg·m^{-2}·s^{-1}.

(f) Annular flow at $x = 59.4\%$ and $G = 494$ kg·m^{-2}·s^{-1}.

Figure 5.4: Top and side views of the R-134a flow patterns for $T_{\text{sat}} = 10$ °C and $D = 6.70$ mm. [Padilla *et al.* 2011a]

5.2.2 Two-phase pressure drop in straight tubes

5.2.2.1 Experimental conditions for the pressure drop measurements

Table 5.1 summarizes the experimental conditions of the present pressure drop database along with the corresponding uncertainties. The 884 experimental tests have been carried out using three different tube diameters (10.85, 7.90 and 5.30 mm) for three refrigerants (R-410A, R-134a and HFO-1234yf), saturation temperatures from 4.8 °C to 22.0 °C, and over the entire range of the vapor quality. The mass velocity ranges from 187 to 2146 kg·m^{-2}·s^{-1}.

Table 5.1: Experimental conditions and uncertainties of the present straight tube pressure drop database.

Parameters	Range	Uncertainties
Fluids	R-410A, R-134a, HFO-1234yf	
D	10.85, 7.90 and 5.3 mm	$\pm 0.6\%$
G	187 to 2146 kg m^{-2} s^{-1}	$< 1.3\%$
T_{sat}	4.8 - 22.0 °C	± 0.1K
P_{heater}	0 - 10 kW	± 1 W
x	0.04 - 0.98	$< 0.82\%$
p	3.48 - 14.50 bar	$\pm 0.1\%$
Δp	0 - 33.29 kPa	$\pm 0.1\%$
L_0	1000 mm	$\pm 0.5\%$
L_1	110 mm	$\pm 0.5\%$
L_2	210 mm	$\pm 0.5\%$
L_3	120 mm	$\pm 0.5\%$
L_4	165 mm	$\pm 0.5\%$
L_5	1000 mm	$\pm 0.5\%$

5.2.2.2 Flow regimes

Since the two-phase frictional pressure drop depends on the flow regime, one must first determine the flow pattern prior to reducing the measurement data. Figure 5.5 presents the HFO-1234yf pressure drop data points for $D = 10.85$ mm, $T_{sat} = 15$ °C and $D = 7.90$ mm, $T_{sat} = 10$ °C mapped on the [Wojtan *et al.* 2005a] flow pattern map. For the HFO-1234yf pressure drop database (308 points), 59 % (182 points) of the experiments are thus considered to belong to annular flow, whereas almost 39 % (118 points) are for intermitent flow, the rest (8 points around 2 %), is segregated between slug and stratified wavy. For the whole pressure drop database (884 points), almost 57% (501 points) of the experiments are for annular flow, whereas 39 % (340 points) are for intermitent flow. The rest, (43 points, around 4 %) is segregated between slug flow and stratified wavy.

Figure 5.6 presents a comparison between the three working fluids considered in this investigation for two different conditions. Figures 5.6(a) and 5.6(b) show that the pressure drop of R-134a is higher than the pressure drop of HFO-1234yf and is also significantly higher as compared to the R-410A results. This behavior occurs as a consequence of the

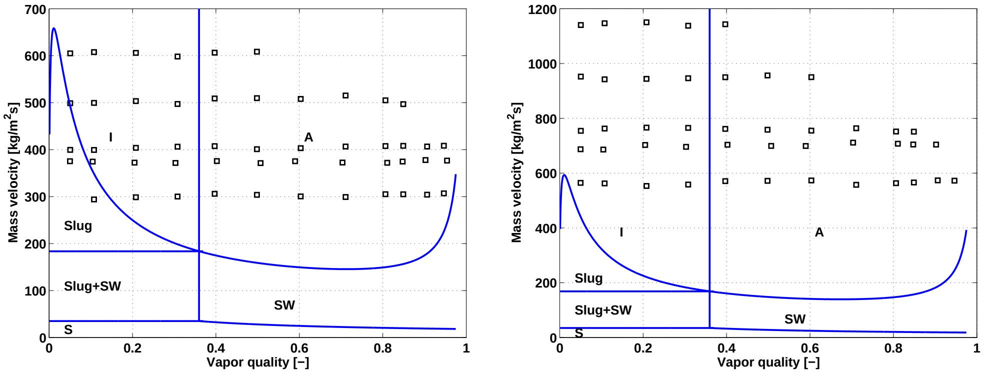

(a) $T_{\text{sat}} = 15$ °C, $G = 400$ kg·m^{-2}·s^{-1}, $D = 10.85$ mm and $q = 0$ kW·m^{-2}.

(b) $T_{\text{sat}} = 20$ °C, $G = 750$ kg·m^{-2}·s^{-1}, $D = 7.90$ mm and $q = 0$ kW·m^{-2}.

Figure 5.5: HFO-1234yf pressure drop data plotted in the flow pattern map of [Wojtan *et al.* 2005a]. (I: intermittent, A: annular, Slug: slug, SW: stratified-wavy). [Padilla *et al.* 2011a]

physical properties of the refrigerants. For $T_{\text{sat}} = 15$ °C, the working refrigerant with the highest pressure drop (R-134a), has the highest density ratio (ρ_l/ρ_v) and viscosity ratio (μ_l/μ_v). In addition R-410A shows lower two-phase frictional pressure drop than R-134a and HFO-1234yf, consequence of its properties.

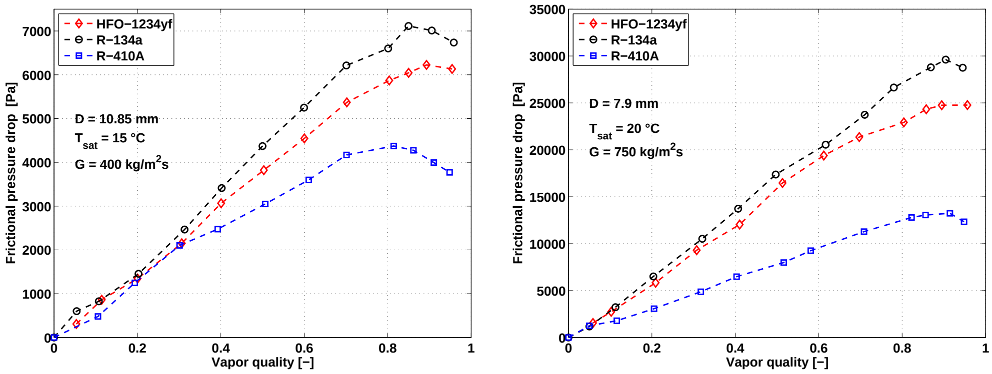

(a) Pressure drop vs. vapor quality. $T_{\text{sat}} = 15$ °C, $G = 400$ kg·m^{-2}·s^{-1}, $D = 10.85$ mm and $L = 1.0$ m.

(b) Pressure drop vs. vapor quality. $T_{\text{sat}} = 20$ °C, $G = 750$ kg·m^{-2}·s^{-1}, $D = 7.90$ mm and $L = 1.0$ m.

Figure 5.6: Pressure drop vs. vapor quality for 3 different fluids: R-134a, R-410A and HFO-1234yf. [Padilla *et al.* 2011a]

In addition, Figure 5.7 presents the effect of the mass velocity G, the saturation temperature T_{sat} and the inner diameter D on the frictional pressure drop for the HFO-1234yf.

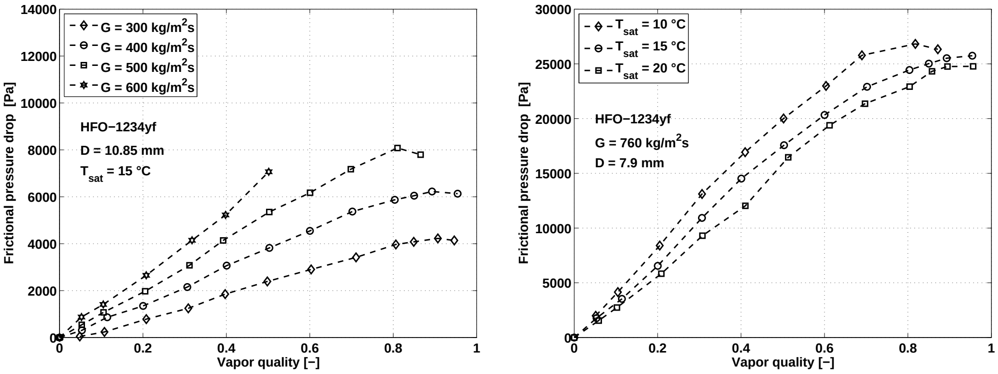

(a) Effect of the mass velocity G.

(b) Effect of the saturation temperature T_{sat}

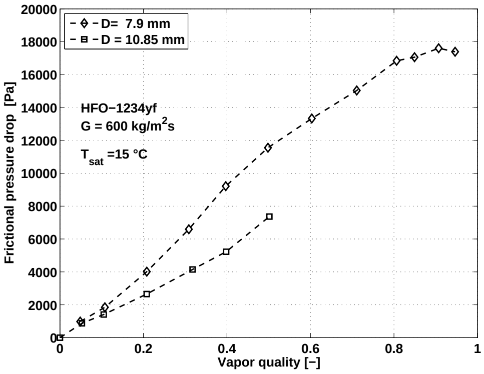

(c) Effect of the inner diameter D

Figure 5.7: Effect of the mass velocity, the temperature and the inner diameter on the frictional pressure drop. [Padilla *et al.* 2011a]

Figure 5.7(a) shows the effect of the increasing mass velocity on the frictional pressure drop. When the mass velocity increases, the frictional pressure drop increases. An increase in mass velocity results in a higher flow velocity and a higher flow inertia, which increases the frictional pressure drop. Figure 5.7(b) shows the influence of the saturation temperature. It can be observed that the frictional pressure drop increases when the saturation temperature decreases. This result can be explained by the effect of physical properties such as density and viscosity on the pressure drop at different temperatures. The liquid density ρ_{l} and liquid viscosity μ_{l}, increase as the temperature decreases, whereas the vapor density ρ_{v} and vapor viscosity μ_{v} decrease as the temperature decreases. Finally, in Fig. 5.7(c) when the inner diameter is smaller, it can be noted that the frictional pressure drop is higher. The pressure drop in the smallest diameter tube is higher than that in the largest one. This can be explained by the fact that smaller inner tube diameter results in a higher wall shear stress, leading to a higher friction, which then results in a higher frictional pressure drop.

As can be observed in the previous figures, maximum pressure drop occurs at a vapor quality of about 80%. According to the flow pattern map of [Wojtan *et al.* 2005a], this maximum occurs in annular flow regime. To better understand this maximum, an analysis on the maximum pressure gradient has been carried out.

5.2.2.3 Maximum two-phase pressure gradient

Figures 5.8(a) and 5.8(b) show predicted values of the maximum frictional pressure gradient using two methods [Müller-Steinhagen & Heck 1986, Revellin & Haberschill 2009] compared to experimental values. In a first approach, both methods lead to good predictions of the maximum pressure gradient. The method of [Müller-Steinhagen & Heck 1986] is however slightly better with 98.3 % of the data predicted within a ± 30 % error band. The method of [Revellin & Haberschill 2009] tends to over predict values of the maximum frictional pressure gradient for high mass velocities.

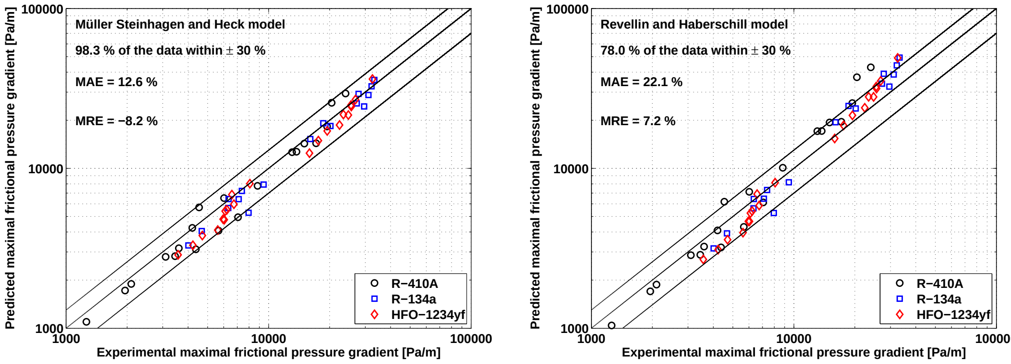

(a) [Müller-Steinhagen & Heck 1986] prediction method.

(b) [Revellin & Haberschill 2009] prediction method.

Figure 5.8: Comparison between predicted and experimental maximum frictional pressure gradients. [Padilla *et al.* 2011a]

Figures 5.9(a) and 5.9(b) show the predicted values of the vapor qualities corresponding to the maximum frictional pressure gradient, compared to experimental values. It can be noted that both methods predict almost constant values of the vapor qualities. In the case of [Müller-Steinhagen & Heck 1986] method, the vapor quality corresponding to the maximum pressure gradient is almost constant and is around 93%, and in the case of [Revellin & Haberschill 2009] it is near 80 %. Note that the experimental vapor quality corresponding to the maximum pressure gradient ranges from 77 % to 92 %. Even if the statistics indicate that both methods are able to fairly predict the data within a ± 10 % error band, the trend of the vapor quality corresponding to the maximum pressure gradient is in fact not well captured by these methods.

As a preliminary conclusion, future prediction methods should focus on the correct prediction of this maximum pressure drop. As explained by [Revellin & Haberschill 2009], when this maximum is known, the prediction is more accurate.

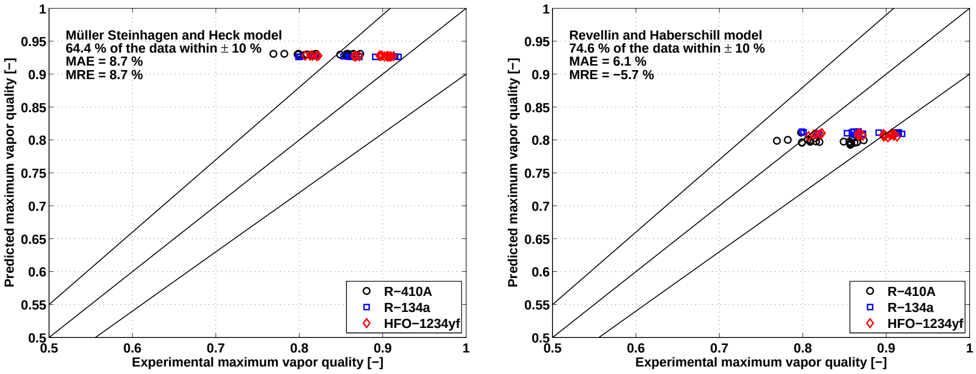

(a) [Müller-Steinhagen & Heck 1986] prediction method.

(b) [Revellin & Haberschill 2009] prediction method.

Figure 5.9: Comparison between predicted and experimental vapor qualities corresponding to the maximum pressure gradients. [Padilla *et al.* 2011a]

5.2.2.4 Comparison to prediction methods

The present database is now compared with existing prediction methods to give some indications on the best method to use. In this sense, the whole set of two-phase pressure drop data for the 3 fluids tested in this work was compared against available correlations: i.e. the methods developed by [Müller-Steinhagen & Heck 1986, Grönnerud 1979, Moreno Quibén & Thome 2007, Lockhart & Martinelli 1949, Chisholm 1973a, Friedel 1979, Revellin & Haberschill 2009, Bankoff 1960, Chawla 1967] and the Homogeneous Model (Cicchitti viscosity model). All these methods allow the calculation of the frictional pressure drop. The results of the comparison are summarized in Table 5.2 and some of these results are shown in Fig. 5.10. As can be observed in this figure, low mass velocities (200 kg·m^{-2}·s^{-1}) result in a very small pressure drop at low vapor qualities (below 400 Pa·m^{-1}). Under this threshold, the test facility is not stable enough for an accurate measurement.

The best accuracy is, by far, given by the method of [Müller-Steinhagen & Heck 1986]. The data predicted are around 90 % within a ± 30 % error band. The mean absolute error is near 18 % and the the mean relative error is around -4 %. Although the method proposed by [Müller-Steinhagen & Heck 1986] is a method which has been developed without considering flow pattern effects on the process, this method gives the best prediction for intermittent and annular flows, but also for the entire database.

The methods of [Lockhart & Martinelli 1949, Bankoff 1960, Chawla 1967] give particularly poor predictions. These methods are not reliable to predict frictional pressure drop of refrigerants and also are not suited to describe the behavior of refrigerant fluids at different evaporation pressures.

Nevertheless, the correlation of [Lockhart & Martinelli 1949] gives better predictions than the [Bankoff 1960], [Chawla 1967] and Homogeneous models. The best results for [Lockhart & Martinelli 1949] occur in annular flow with 44% of the data predicted within a ± 30 % error band.

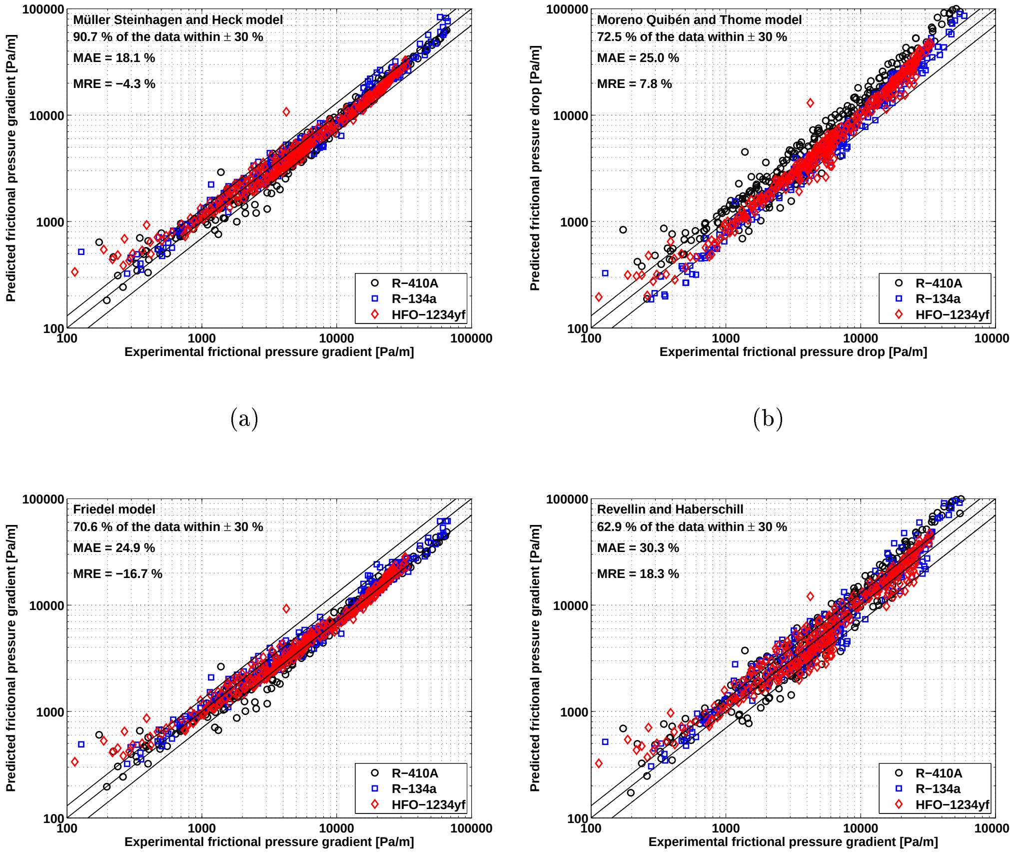

(a) (b)

(c) (d)

Figure 5.10: Experimental pressure gradient data (884 points) compared to prediction methods. [Padilla *et al.* 2011a]

Table 5.2: 884 experimental pressure drop data points for refrigerants HFO-1234yf, R-134a and R-410A in straight tubes compared to different correlations from the literature

	Number of points	Müller-Steinhagen and Heck	Grönnerud	Friedel	Revellin and Haberschill	Chawla	Chisholm	Bankoff	Homogeneous	Lockhart and Martinelli	Moreno and Thome
SLUG	39										
λ(%)		55.6	**75.0**	61.1	52.8	13.9	0.0	30.6	8.3	0.0	44.4
MAE(%)		45.9	35.3	42.4	46.7	633.7	452.6	113.3	60.8	239.1	35.9
MRE(%)		42.6	21.8	38.7	44.4	628.4	452.6	66.3	-60.8	238.2	-6.8
INTERMITTENT	340										
λ(%)		**88.6**	78.1	81.9	49.5	0.3	10.8	32.1	1.3	0.3	74.6
MAE(%)		18.5	22.9	20.8	36.1	>1000	143.5	317.9	77.8	164.5	25.9
MRE(%)		9.2	19.2	-6.3	34.2	863.5	143.2	301.1	-77.2	164.1	6.2
STRATIFIED-WAVY	2										
λ(%)		100.0	**100.0**	100.0	0.0	0.0	100.0	0.0	0.0	0.0	0.0
MAE(%)		19.2	8.3	20.9	41.7	>1000	24.4	>1000	73.1	64.2	41.5
MRE(%)		-19.2	-0.6	-20.9	-41.7	>1000	-24.4	>1000	-73.1	-64.2	-41.5
ANNULAR	501										
λ(%)		**95.3**	15.7	68.5	80.2	0.0	62.1	0.0	0.0	44.0	76.1
MAE(%)		16.7	54.7	26.3	19.8	>1000	37.1	>1000	88.7	36.1	20.0
MRE(%)		-15.0	54.2	-25.5	-0.4	>1000	20.7	>1000	-88.7	0.2	6.6
DRY-OUT	2										
λ(%)		50.0	50.0	100.0	100.0	0.0	**100.0**	0.0	0.0	0.0	100.0
MAE(%)		18.4	21.2	15.1	11.8	>1000	9.6	>1000	56.8	55.2	13.5
MRE(%)		18.4	21.2	15.1	-11.8	>1000	-9.6	>1000	-56.8	-55.2	-7.4
ALL DATA	884										
λ(%)		**90.7**	42.9	70.6	62.9	0.7	39.8	13.7	0.9	25.0	72.5
MAE(%)		18.1	41.4	24.9	30.3	>1000	96.2	>1000	83.2	94.6	25.0
MRE(%)		-4.3	39.1	-16.7	18.3	>1000	86.6	>1000	-82.9	73.4	7.8

The method proposed by [Friedel 1979] is a method developed using a large database valid for horizontal flows, which predicts around 70 % of the entire database within a ± 30 % error band. This method also gives good prediction for intermittent and annular regimes.

Regarding the phenomenological models, although the method proposed by [Moreno Quibén & Thome 2007] is not the best one, it gives reasonably good predictions for all flow regimes. Its best results are found for annular and intermittent regimes.

For slug flow, the best method is that of [Grönnerud 1979] with 75 % of the data within a ± 30 % error band.

Beyond the above statistics, Figs. 5.11(a) and 5.11(b) graphically show the comparison between the prediction methods with experimental data obtained for the most recently developed refrigerant, namely HFO-1234yf. Correlations of [Müller-Steinhagen & Heck 1986, Moreno Quibén & Thome 2007, Friedel 1979, Revellin & Haberschill 2009] better describe the behaviors of the data. On the contrary, using the methods of [Lockhart & Martinelli 1949, Chisholm 1973a] the calculation results are not in agreement with the data. It is also important to note that only the methods proposed by [Müller-Steinhagen & Heck 1986, Grönnerud 1979, Moreno Quibén & Thome 2007, Revellin & Haberschill 2009] give a good representation of the pressure gradient trend versus vapor quality. They also capture the peak in the pressure gradient at high vapor qualities.

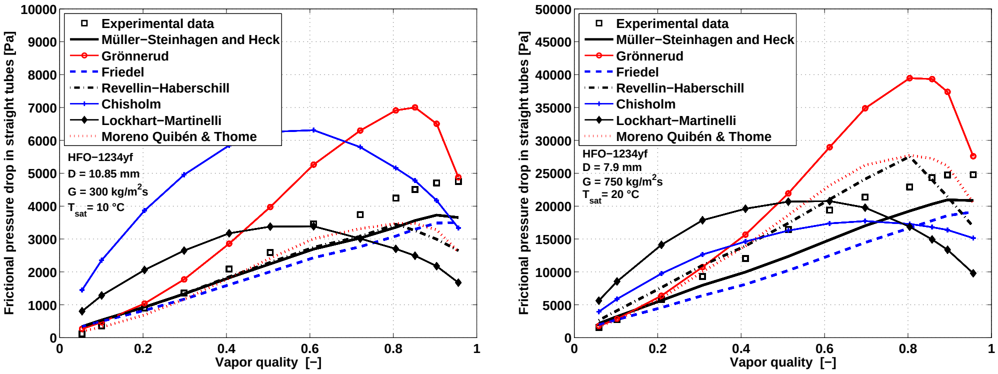

(a) (b)

Figure 5.11: Experimental pressure drop in straight tubes as a function of the vapor quality compared to different prediction methods. [Padilla *et al.* 2011a]

5.3 Chapter conclusions

Two-phase flow regime visualizations of HFO-1234yf and R-134a in a 6.70 mm inner diameter glass straight tube have been simultaneous performed by top and side views with a high-speed high-definition camera. These flow regimes have been observed in the range of mass velocities from 297 to 512 kg m^{-2} s^{-1}, vapor qualities from 5 to 90 % and T_{sat} from 9.5 to 10.5 °C. The different flow regimes observed were: slug, intermittent and annular flows. No major difference was observed between both refrigerants. Indeed HFO-1234yf properties are close to those of R-134a. It was found that the [Wojtan *et al.* 2005a] flow pattern map was able to satisfactorily predict the HFO-1234yf flow regimes.

884 pressure drop data points measured in horizontal straight tubes have been presented for refrigerants R-410A, R-134a and the next-generation refrigerant HFO-1234yf. The tube diameter (D) varied from 5.30 to 10.85 mm and the mass velocity (G) ranged from 187 to 2146 kg m^{-2} s^{-1}. Vapor quality (x) ranged from 0.04 to 0.98. Saturation temperatures were tested from 4.8 °C to 20.7 °C.

The 884 experimental data have been compared against selected correlations found in the literature. The best accuracy was given by [Müller-Steinhagen & Heck 1986] with around 90 % of the data predicted within a ± 30 % error band.

CHAPTER 6

Two-phase flow in return bends

Contents

The aim of this chapter is to present original experimental two-phase flow regime visualizations and two-phase pressure drop data points in horizontal and vertical return bends for the next generation HFO-1234yf and for well known R-134a and R-410A conventional refrigerants. This permits to extend the existing database available in the literature (presented in Table 3.1) and also to better understand the physical phenomena involved. In addition, this chapter aims at discussing the perturbation length encountered up- and downstream of the return bend. Furthermore, the new experimental data measured for two-phase flow of HFO-1234yf, R-134a and R-410A refrigerants in horizontal and vertical return bends are presented and compared against 4 prediction methods from the literature.

Based on the present database and as proposed by [Padilla *et al.* 2009], we suggest a correlation for predicting the pressure drop in return bends, which is understood as the sum of the regular pressure drop along the length πR and the frictional pressure drop due to the singularity and its perturbation effects up- and downstream (proposed equation).

6.1 Experimental procedure

To obtain the values of the return bend pressure drop Δp_{rb}, the total pressure drop and the horizontal straight tube pressure drops have been measured. Figure 6.1 shows a synthesis of the idealized pressure profile of the flow path along a vertical return bend (as explained later, horizontal return bends can be treated as a particular case of vertical return bends).

Δp_{tot} corresponds to the total pressure drop experimentally measured over the length $L_1 + \pi R_1 + L_2 = 0.383$ m for the first return bend and $L_3 + \pi R_2 + L_4 = 0.335$ m for the second return bend (Fig. 4.9). In Fig. 6.1, Δp_{tot} is measured along the length L_{io}.

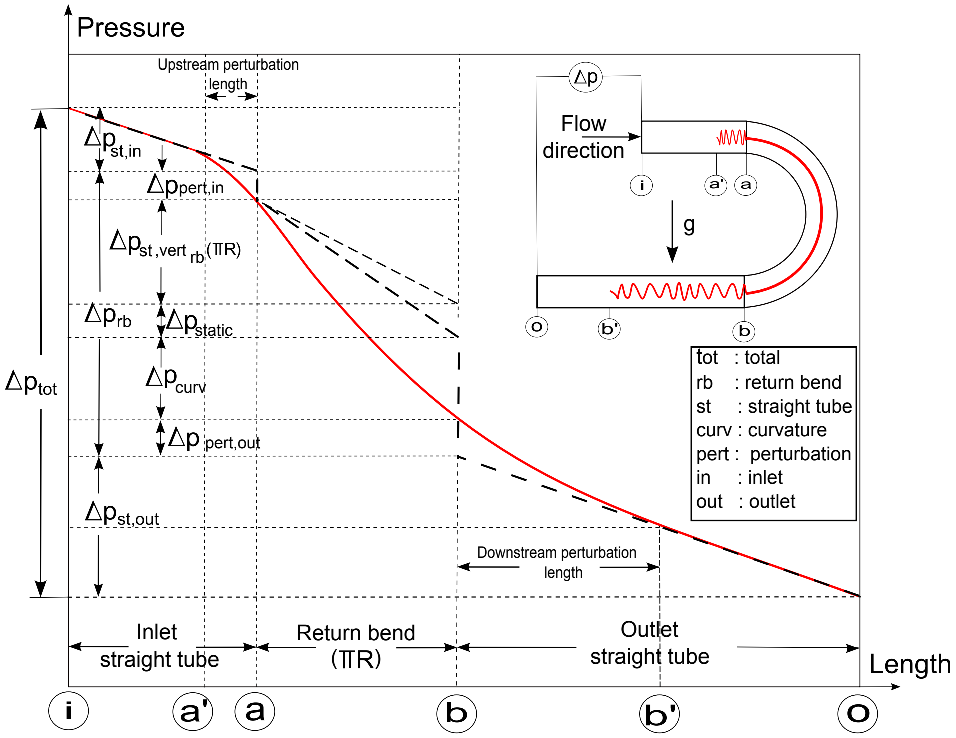

Figure 6.1: Idealized pressure profile along a vertical return bend.

The total pressure drop is expressed as follows:

$$\Delta p_{\mathrm{tot}} = \Delta p_{\mathrm{st,in}} + \Delta p_{\mathrm{rb}} + \Delta p_{\mathrm{st,out}} \tag{6.1}$$

The term $\Delta p_{\mathrm{st,in}} + \Delta p_{\mathrm{st,out}}$ is calculated by:

$$\Delta p_{\mathrm{st,in}} + \Delta p_{\mathrm{st,out}} = \left(-\frac{\mathrm{d}p}{\mathrm{d}z}\right)_{\mathrm{st}} L_{\mathrm{eq}} \tag{6.2}$$

where $L_{\mathrm{eq}} = L_1 + L_2 = 0.320$ m for the first return bend and $L_{\mathrm{eq}} = L_3 + L_4 = 0.285$ m for the second return bend.

The straight tube (regular) pressure gradients are experimentally measured along the length L_0 and L_6 (see Fig. 4.9) for inner tube diameters 10.85 mm and 7.90 mm. These gradients are calculated using Eq. (5.1).

The term Δp_{rb} corresponds to the return bend pressure drop. This term is the sum of the static pressure drop ($\Delta p_{\mathrm{static}}$), the regular pressure drop along the vertical bend of length πR ($\Delta p_{\mathrm{st,vert_{rb}}(\pi R)}$) and the singular pressure drop (Δp_{sing}) which can be viewed as the sum of the pressure drops due to the curvature effect (Δp_{curv}) and the perturbations up- and downstream of the return bend. ($\Delta p_{\mathrm{pert,in}}$, $\Delta p_{\mathrm{pert,out}}$).

$$\Delta p_{\mathrm{rb}} = \Delta p_{\mathrm{st,vert_{rb}}(\pi R)} + \Delta p_{\mathrm{static}} + \Delta p_{\mathrm{sing}} \tag{6.3}$$

$$\Delta p_{\text{sing}} = \Delta p_{\text{curv}} + \Delta p_{\text{pert,in}} + \Delta p_{\text{pert,out}} \tag{6.4}$$

Note that $\Delta p_{\text{st,vert}_{\text{rb}}(\pi R)}$ means that the corresponding length is πR and is thus a succession of elementary regular pressure drops at different orientations from 0° to 180° (Fig. 6.2). It can be expressed by the following relation:

$$\Delta p_{\text{st,vert}_{\text{rb}}(\pi R)} = \int_0^{\pi R} \frac{\mathrm{d}p_{\text{st,f}}(\theta)}{\mathrm{d}z}\mathrm{d}z = \int_0^{\pi} \frac{\mathrm{d}p_{\text{st,f}}(\theta)}{R\mathrm{d}\theta}R\mathrm{d}\theta = \int_0^{\pi} \frac{\mathrm{d}p_{\text{st,f}}(\theta)}{\mathrm{d}\theta}\mathrm{d}\theta \tag{6.5}$$

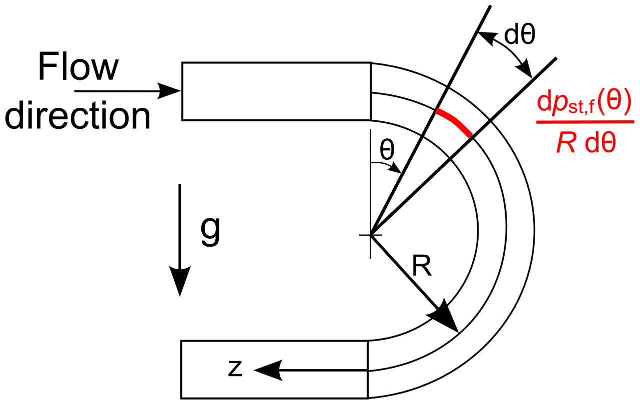

Figure 6.2: Description of the regular frictional pressure drop in a vertical return bend.

The static pressure drop is calculated as follows:

$$\Delta p_{\text{static}} = \rho_{\text{h}}\, g\, 2R \tag{6.6}$$

For the particular case of a horizontal return bend, $\Delta p_{\text{static}} = 0$. The homogeneous density ρ_{H} is:

$$\rho_{\text{h}} = \rho_{\text{l}}(1-\varepsilon) + \rho_{\text{v}}(\varepsilon) \tag{6.7}$$

The void fraction ε is calculated by the [Rouhani & Axelsson 1970] model (Eq.(3.68)).

In the experiments, as explained in [Padilla *et al.* 2011a], the maximum pressure drop measured from the outlet of the electrical heater (where the vapor quality is calculated) to the outlet of the test section can reach up to 0.84 bar. This pressure drop is not negligible and provokes a flashing effect (see section 2.6.3.1) and a temperature difference. The flashing effect is calculated using the relation (2.50).

As explained in section 5.1.2, from the outlet of the electrical heater to the outlet of the test section, the Δx and ΔT_{sat} variations due to the flashing effect have been taken into account. Both vapor quality and saturation temperature are recalculated at the inlet of each straight tube and return bend.

6.2 Experimental results

6.2.1 Two-phase flow visualization in return bends

6.2.1.1 Flow regimes at the return bend inlet

The flow regimes of HFO-1234yf and R-134a encountered at the inlet of the return bend for each visualization are presented in Figures 5.2(a) and 5.2(b) respectively. The corresponding experimental conditions are mapped in the flow pattern map proposed by [Wojtan *et al.* 2005a] only as information. It is important to note that this flow pattern map was developed for R-22 and R-410A inside a 13.6 mm horizontal smooth tube and further validated for R-134a and other fluids. Therefore, it can not strictly be used to determine the flow pattern in the return bend test section. Nevertheless, it gives an indication of the flow regimes encountered at the inlet of the return bend.

For the present visualization dataset, at the return bend inlet, 60.0% (24 points) of the experiments belong to annular flow, whereas 30.0% are for intermittent flow. The rest corresponds to slug flow. Note that the flow pattern map of [Wojtan *et al.* 2005a] was implemented by setting the heat flux to 0.00 kW$\cdot$m^{-2}, as the present experiment is performed in adiabatic conditions.

The flow regime visualizations at the inlet of the return bend for both refrigerants have been compared to the [Wojtan *et al.* 2005a] flow pattern map. As can be seen, no major difference was found between the experimental flow regimes (slug, intermittent and annular flows) and their transitions and those predicted by [Wojtan *et al.* 2005a]. As a result, the flow pattern map proposed by the latter could be used to predict the flow pattern at the inlet of the return bend for the current experimental database.

6.2.1.2 Two-phase flow visualization in horizontal return bends

Flow regimes of HFO-1234yf and R-134a have been observed using the test section depicted in Fig. 4.3. The range of mass velocities was from 297 to 512 kg$\cdot$m$^{-2}\cdot$s^{-1}, vapor qualities from 5 to 90 % and T_{sat} from 9.5 to 10.5 °C. As shown in Figs. 6.3 and 6.4, the different flow regimes observed are: slug, intermittent and annular flows. The liquid and vapor phases distribute naturally into several recognizable flow structures.

At the beginning of the curved section of the return bend, one can see that the vapor phase moves toward the inside of the curve, while the liquid phase moves to the outside due to the effect of the centrifugal force. After a length of about $20D$ from the return bend outlet, it appears that the flow pattern recovers the original shape it had before entering the return bend.

During intermittent flow (Figures 6.3(b), 6.3(d), 6.3(e), 6.4(b), 6.4(d) and 6.4(e)), there is a notable difference observed between the flow structure at $G = 300$ kg$\cdot$m$^{-2}\cdot$s^{-1} and $G = 500$ kg$\cdot$m$^{-2}\cdot$s^{-1}. Increasing the mass velocity provokes higher vapor velocity that distorts the interfacial waves. Large amplitude waves intermittently wash the top of the tube while smaller amplitude waves are also observed in between. Large amplitude waves often contain entrained bubbles. Figure 5.3 also presents images for annular flow regime at $G = 300$ kg$\cdot$m$^{-2}\cdot$s^{-1} and $G = 500$ kg$\cdot$m$^{-2}\cdot$s^{-1}. Annular flow images show that the liquid forms a continuous film around the perimeter of the tube. The interface between the liquid annulus and the vapor core is disturbed by small amplitude waves and droplets are observed to be dispersed in the vapor core.

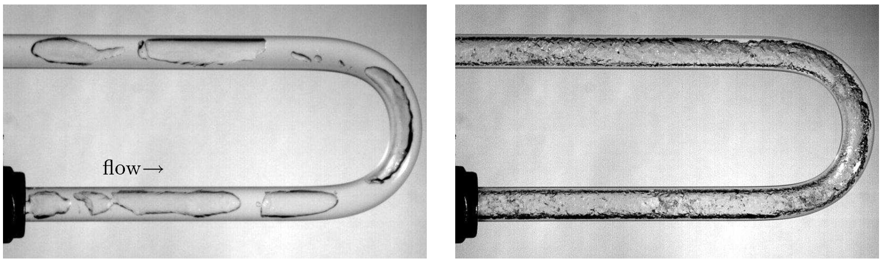

(a) Slug flow at $x = 5.2\%$ and $G = 306\ \mathrm{kg \cdot m^{-2} \cdot s^{-1}}$.

(b) Intermittent flow at $x = 19.1\%$ and $G = 306\ \mathrm{kg \cdot m^{-2} \cdot s^{-1}}$.

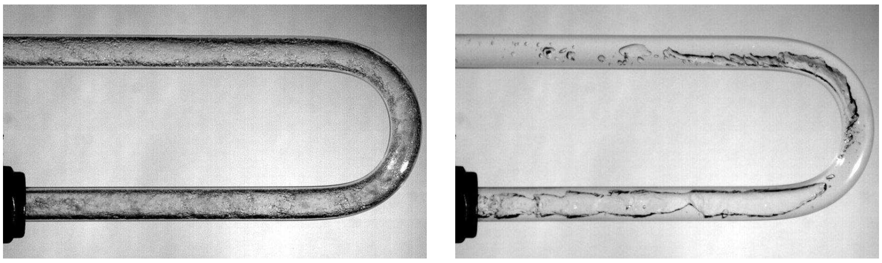

(c) Annular flow at $x = 61.0\%$ and $G = 307\ \mathrm{kg \cdot m^{-2} \cdot s^{-1}}$.

(d) Intermittent flow at $x = 6.7\%$ and $G = 512\ \mathrm{kg \cdot m^{-2} \cdot s^{-1}}$.

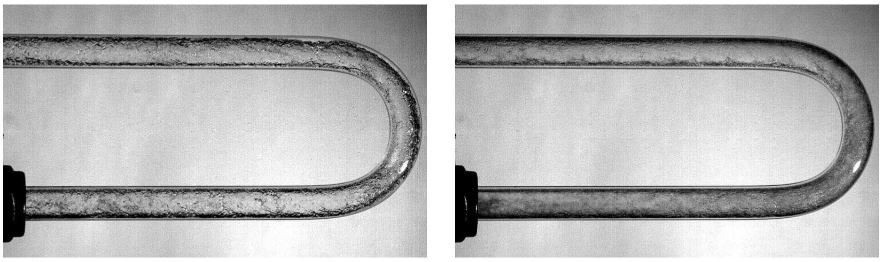

(e) Intermittent flow at $x = 21.8\%$ and $G = 497\ \mathrm{kg \cdot m^{-2} \cdot s^{-1}}$.

(f) Annular flow at $x = 59.0\%$ and $G = 506\ \mathrm{kg \cdot m^{-2} \cdot s^{-1}}$.

Figure 6.3: Top view of the HFO-1234yf flow patterns in a horizontal return bend for $T_{\mathrm{sat}} = 10$ °C and $D = 6.70$ mm.

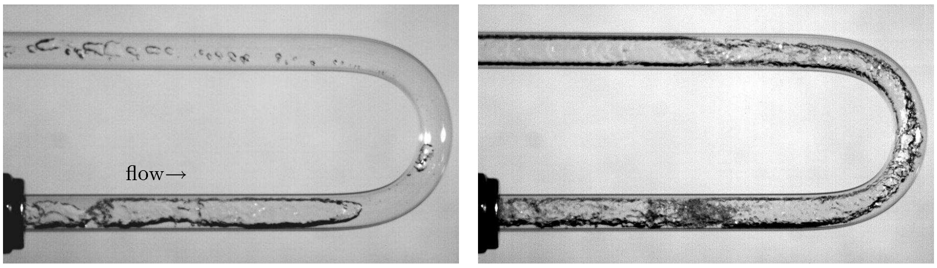

(a) Slug flow at $x = 4.9\%$ and $G = 301$ kg·m^{-2}·s^{-1}.

(b) Intermittent flow at $x = 19.8\%$ and $G = 303$ kg·m^{-2}·s^{-1}.

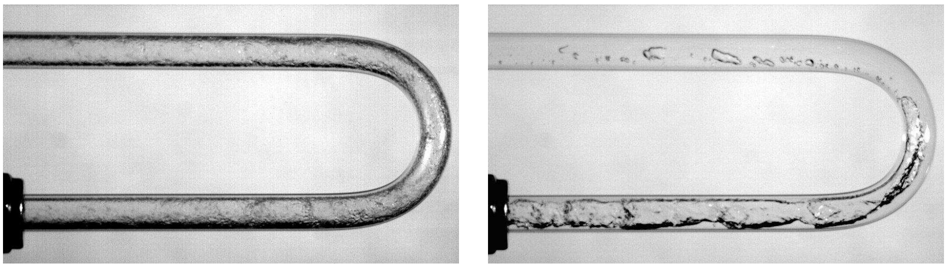

(c) Annular flow at $x = 61.2\%$ and $G = 307$ kg·m^{-2}·s^{-1}.

(d) Intermittent flow at $x = 4.8\%$ and $G = 509$ kg·m^{-2}·s^{-1}.

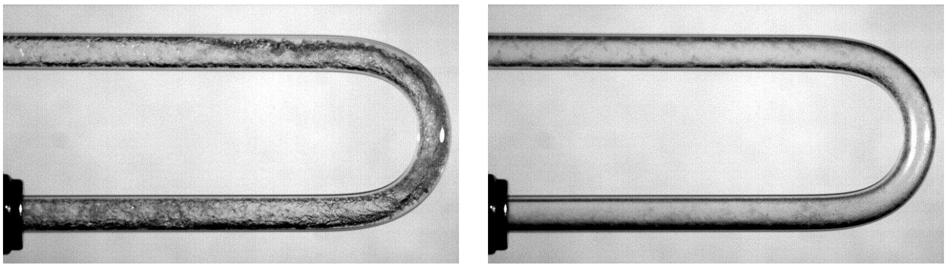

(e) Intermittent flow at $x = 20.1\%$ and $G = 503$ kg·m^{-2}·s^{-1}.

(f) Annular flow at $x = 59.7\%$ and $G = 502$ kg·m^{-2}·s^{-1}.

Figure 6.4: Top view of the R-134a flow patterns in a horizontal return bend for $T_{\text{sat}} = 10$ °C and $D = 6.70$ mm.

6.2.1.3 Two-phase flow visualization in vertical return bends

The test section depicted in Fig. 4.3 has been placed to allow flow regimes visualizations of HFO-1234yf and R-134a in vertical return bend. The range of mass velocities was from 300 to 500 kg·m^{-2}·s^{-1}, vapor qualities from 5 to 95 % and $T_{\text{sat}} = 10$ °C.

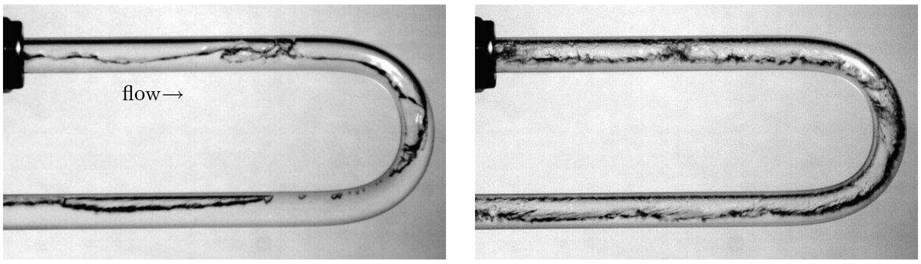

(a) Slug flow at $x = 5.4\%$ and $G = 306$ kg·m^{-2}·s^{-1}.

(b) Intermittent flow at $x = 20.1\%$ and $G = 306$ kg·m^{-2}·s^{-1}.

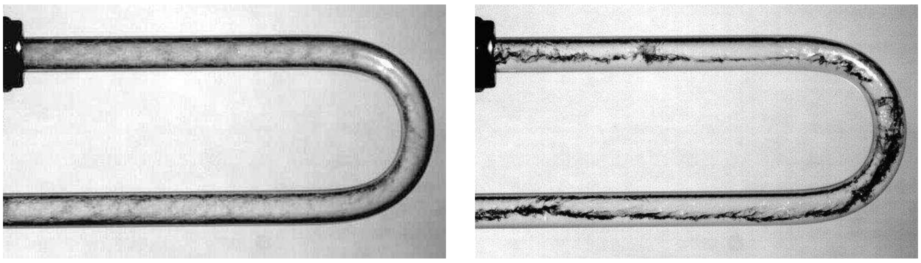

(c) Annular flow at $x = 61.0\%$ and $G = 302$ kg·m^{-2}·s^{-1}.

(d) Intermittent flow at $x = 4.9\%$ and $G = 505$ kg·m^{-2}·s^{-1}.

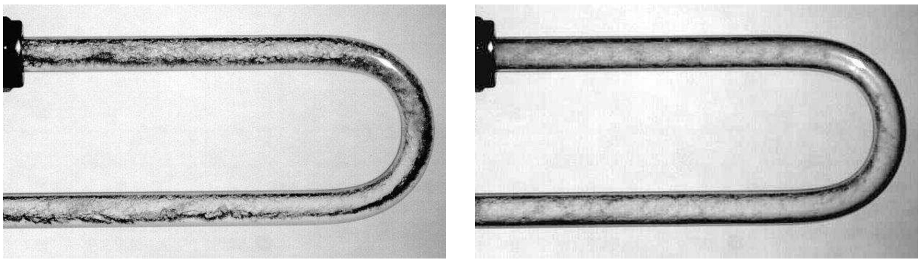

(e) Intermittent flow at $x = 21.1\%$ and $G = 496$ kg·m^{-2}·s^{-1}.

(f) Annular flow at $x = 61.0\%$ and $G = 504$ kg·m^{-2}·s^{-1}.

Figure 6.5: Side view of the HFO-1234yf flow patterns in a vertical return bend for $T_{\text{sat}} = 10$ °C and $D = 6.70$ mm.

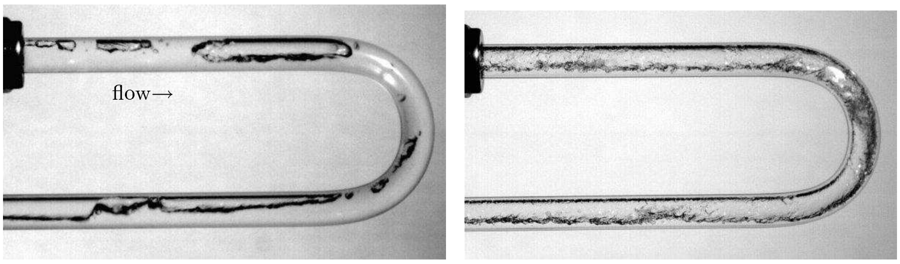

(a) Slug flow at $x = 5.5\%$ and $G = 308$ kg·m^{-2}·s^{-1}.

(b) Intermittent flow at $x = 22.0\%$ and $G = 301$ kg·m^{-2}·s^{-1}.

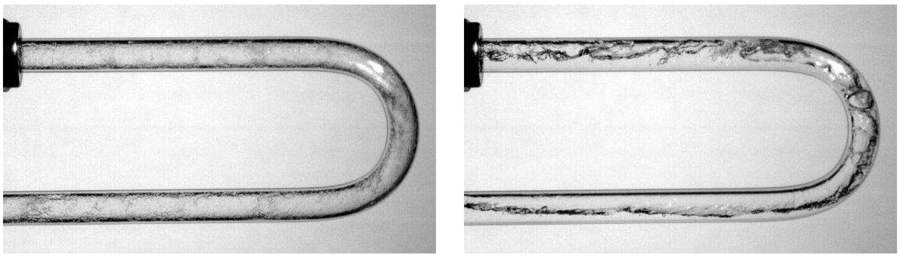

(c) Annular flow at $x = 62.0\%$ and $G = 297$ kg·m^{-2}·s^{-1}.

(d) Intermittent flow at $x = 5.4\%$ and $G = 498$ kg·m^{-2}·s^{-1}.

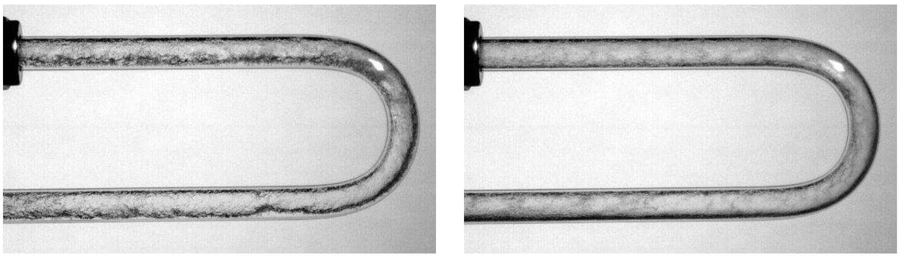

(e) Intermittent flow at $x = 20.1\%$ and $G = 501$ kg·m^{-2}·s^{-1}.

(f) Annular flow at $x = 61.2\%$ and $G = 503$ kg·m^{-2}·s^{-1}.

Figure 6.6: Side view of the R-134a flow patterns in a vertical return bend for $T_{\text{sat}} = 10$ °C and $D = 6.70$ mm.

As shown in Figs. 6.5 and 6.6, the different flow regimes observed are: slug, intermittent and annular flows. For slug flow regime, the co-current flow in the straight tube upstream of the vertical return bend is strongly influenced by gravity that acts to stratify the liquid to the bottom of the tube and the vapor to the top. The liquid and vapor phases distribute naturally into several recognizable flow structures.

At the beginning of the curved section of the return bend, one can see that the vapor phase tends toward the convex part of the curved section, while the liquid phase goes to the concave part due to the effect of the centrifugal force. Similar as observed for horizontal return bends, after a length of about $20D$ from the return bend outlet, it seems that the flow pattern recovers its original shape that it had before entering the return bend.

Figure 6.5 also presents images for intermittent and annular flow regimes at $G = 300$ kg·m^{-2}·s^{-1} and $G = 500$ kg·m^{-2}·s^{-1}. Similar behavior as shown for horizontal return bends, annular flow images for vertical return bends show that the liquid forms a continuous film around the perimeter of the tube. The interface between the liquid annulus and the vapor core is disturbed by small amplitude waves and droplets are observed to be dispersed in the vapor core.

6.2.2 Dynamical behavior of bubbles and vapor slugs in vertical return bends

The different flow patterns were found to be characterized by distinct dynamical bubble behaviors. In the general case of slug and bubbly flow regimes, when a bubble or a vapor slug travels along the curved section of the return bend, it first slides on the outer side tube wall for a distance, and then detaches. After a period of movement inside the curved section, it re-attaches to the inner side tube wall and then slides on the upper part of the tube wall along the liquid flow direction.

In the results that follow, an equivalent radius $R_{\text{eq}} = (3/4\pi \times \text{actual volume})^{1/3}$ is used as a measure of the bubble size. In bubbly flow regime, the observed bubbles have an equivalent radius inferior to 4 mm. They would depart away from the outer side tube wall before about 45° after they slide to the inner side tube wall (see Fig. 6.7(a)). Similar observations have been carried out by [Meng *et al.* 2009] with R-141b. The small bubbles (equivalent radius < 1.5 mm) are observed to follow an arc route, as shown in Fig. 6.7(g). These bubbles would detach from the outer side tube wall before a bend angle of 70° ([Meng *et al.* 2009]). In our case, the detachment point is not superior to 50°.

Figure 6.8(a) presents a superposition of 30 images (time lapse between images 15 ms) which allows to visualize the trajectory of a small bubble of HFO-1234yf (approx. $R_{\text{eq}} = 0.5$ mm) moving along the return bend. The flow conditions are $G = 300$ kg·m^{-2}·s^{-1}, $T_{\text{sat}} = 10$ °C and $x = 5\%$. As can be observed, the bubble slides from the outlet of the horizontal tube to the outer side wall of the curved tube. The bubble detaches at approx. 30° and then takes off. After a period of movement inside the curved section (between 40° and 130°), it re-attaches to the inner side tube wall at 135° and slides on the tube wall along the liquid flow direction.

Concerning the vapor slug behavior, although the size of the vapor phase is bigger, the detachment still happens before 50°. When the equivalent bubble radius grows up to greater than 3 mm, a vapor slug is relatively long and the detachment process is separated into two different parts, one concerning the vapor slug head detachment and the other regarding the vapor slug tail detachment.

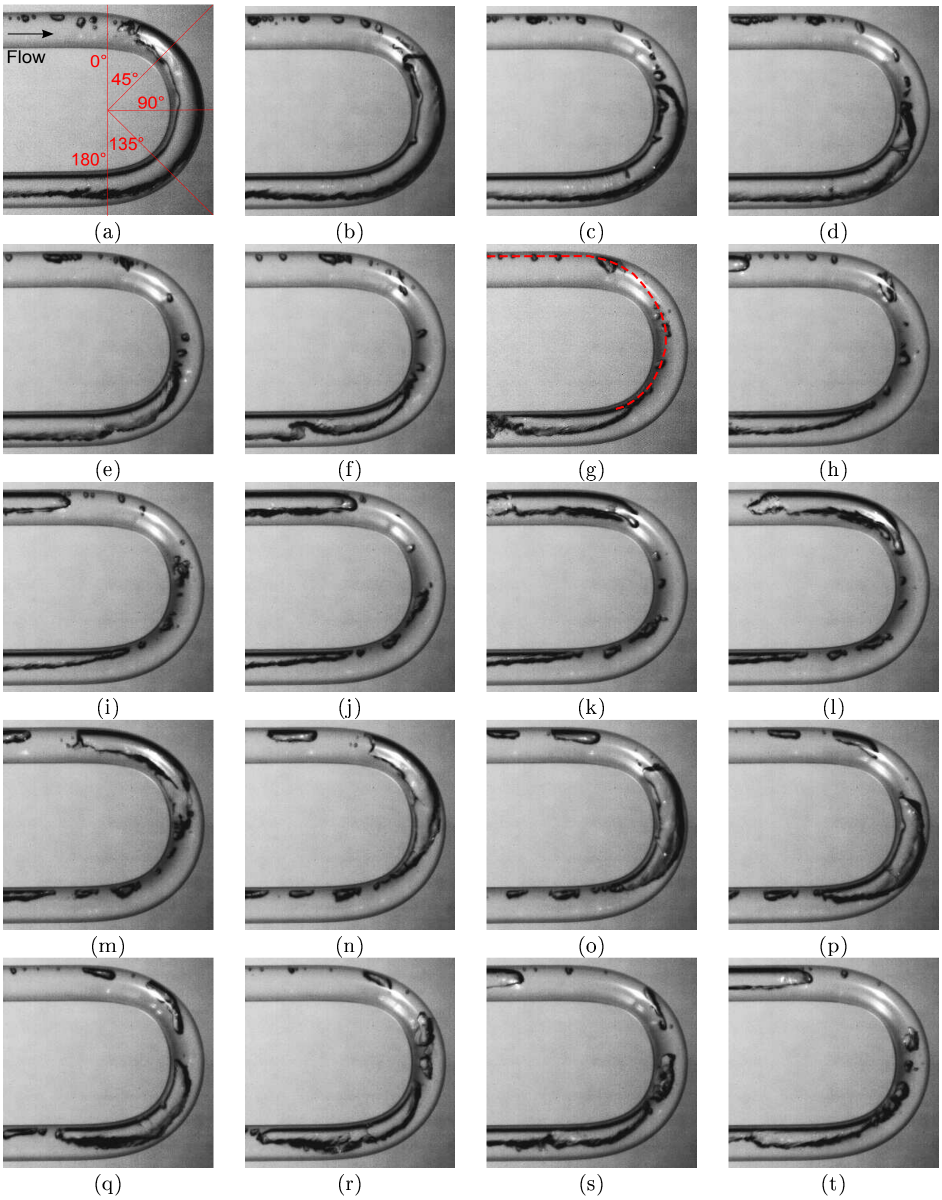

(a) (b) (c) (d)
(e) (f) (g) (h)
(i) (j) (k) (l)
(m) (n) (o) (p)
(q) (r) (s) (t)

Figure 6.7: Side view progress of HFO-1234yf slug flow entering at the higher tube (flowing downwards) in a vertical return bend for $x = 5\%$, $G = 300$ kg·m^{-2}·s^{-1}, $T_{\text{sat}} = 10$ °C and $D = 6.70$ mm (time lapse between images = 15 ms, total time lapse = 0.28 s).

As explained in section 3.1.3.1, the information available in the literature related to slug flow for inclined straight tubes give very little attention to downward gas-liquid flows. In analogy with the work by [Roitberg *et al.* 2008], a superposition of 7 images (time lapse between images 60 ms) for vapor slug head (6.8(b)) and vapor slug tail (6.8(c))of HFO-1234yf have been constructed in order to visualize the evolution of a slug along the return bend. Both head and tail depart from the outer side tube wall at different positions. Normally, vapor slug head is lifted up at about 80° of a bend, leaving a liquid film between it and the outer side tube wall. Sometimes the vapor slug head re-attaches to the inner side tube wall even before the vapor slug tail detaches the outer side tube wall. Note that the effect of the centrifugal force acting on the liquid phase produces a radial force over the vapor phase which lifts the vapor slug off the concave section of the curved tube and contributes to the detachment.

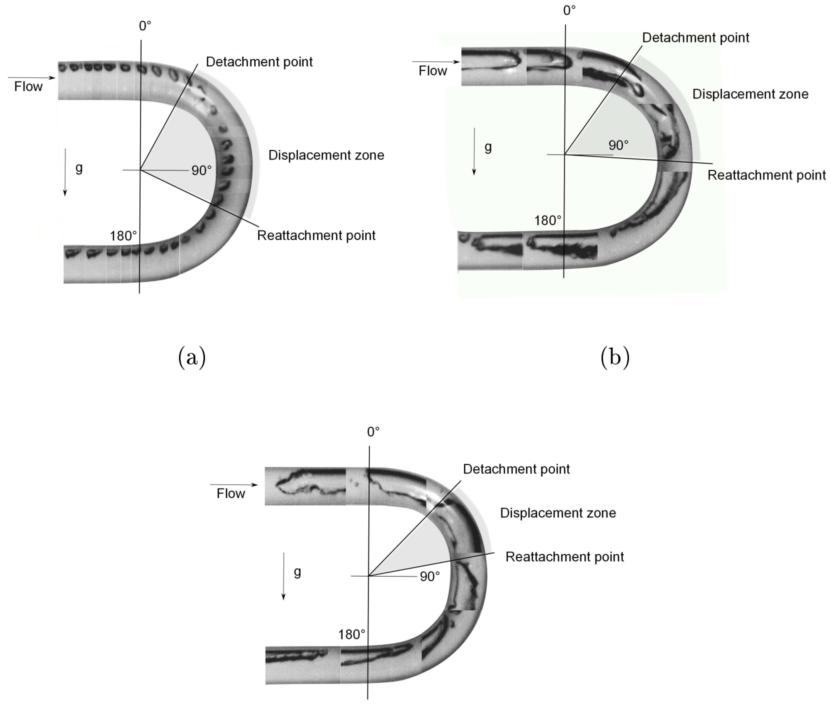

(a) (b)

(c)

Figure 6.8: Visual reconstitution of bubble, slug head and slug tail behaviors and trajectories during a vertical downward flow in a return bend. Test conditions are $x = 5\%$, $G = 300$ kg·m^{-2}·s^{-1}, $T_{\mathrm{sat}} = 10$ °C and $D = 6.70$ mm.

To better understand these observations, an analysis of forces acting on the bubble was performed. The forces are applied at the gravity center of a moving small vapor bubble induced by the flow field with a non uniform pressure gradient (Fig. 6.9), where the bubble experiences (i) buoyancy due to gravity (which comprises the effect of the bubble weight in the opposite direction); (ii) hydrodynamic drag which is opposed to the relative motion of the bubble through the liquid phase; (iii) a hydrodynamic lift force due to the shear within the liquid phase which is perpendicular to the flow direction; and (iv) buoyancy caused by the reaction of the liquid phase on the bubble due to the effect of the centrifugal acceleration acting on the liquid phase (which also comprises the effect of the centrifugal acceleration acting on the vapor phase in the opposite direction).

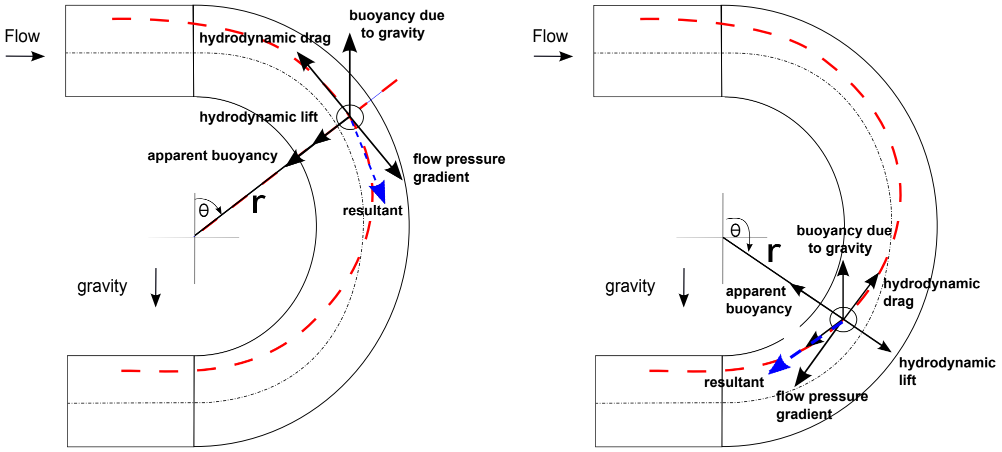

(a) Detachment (b) Re-attachment

Figure 6.9: Acting forces on a moving vapor bubble along a return bend.

The latter, is also known as "*apparent buoyancy*" and is described by [Batchelor 1967]. When the bubble touches the tube wall, a new force due to the contact pressure appears in the forces balance at the center of the bubble. A convenient strategy to identify this force is presented by [van der Geld 2009] by considering a bubble footed at a plane wall and symmetrical around the axis perpendicular to the wall through the center of the bubble. The time rate of change of the kinetic energy in the liquid is computed with the mechanical energy balance. This force represents the hydrodynamic force component of the bubble normal to the wall, and it depends on the dynamic contact angle and the surface tension.

The detachment is mainly controlled by the apparent buoyancy and hydrodynamic lift. The re-attachment is controlled by the apparent buoyancy and the radial component of buoyancy due to gravity. In general, the secondary flow in the liquid phase influences the trajectory of the small bubbles while it is probably negligible in the case of vapor slugs.

After detaching from the outer side tube wall, bubbles and vapor slugs experience a period of movement inside the tube before they re-attach to the inner side tube wall. The interval between detachment and re-attachment is shown in Fig. 6.8. It is also observed that the re-attachment of the slug head happens even before the detachment of the slug tail when the vapor slug is long enough.

Since the shape of the bubbles is rather complex during its evolution, the bubble size is characterized by an equivalent diameter which is defined as the radius of a disk with exactly the same projected area. The projected area is computed by an image processing software at 3 different locations upstream of the return bend.

Bubble detachment positions as a function of the bubble equivalent radius for HFO-1234yf and R-134a are plotted in Fig. 6.10(a). This figure also presents the results obtained by [Meng *et al.* 2009] for R-141b as comparison. The general trend is that bigger bubbles always detach later (at greater angle) than smaller ones. Considering a very small bubble, it is reasonable to believe that secondary flow would be strong enough to detach it from concave part of the curved tube before 40°, and further dominate its trajectory after departure.

It is also noted that for the same bubble size, the detachment point for R-134a occurs before that for HFO-1234yf, and both before those observed for R-141b. Although the temperature range for R-141b is different from that for the other fluids and the data reduction method employed by [Meng *et al.* 2009] is not the same as in the present work, the effect of the fluid on the detachment behavior is clearly shown. Figure 6.10(b) presents the bubble re-attachment positions as a function of the bubble equivalent radius for HFO-1234yf and R-134a. Results suggest that the re-attachment of the biggest bubbles occurs at a lower angle than for smaller ones.

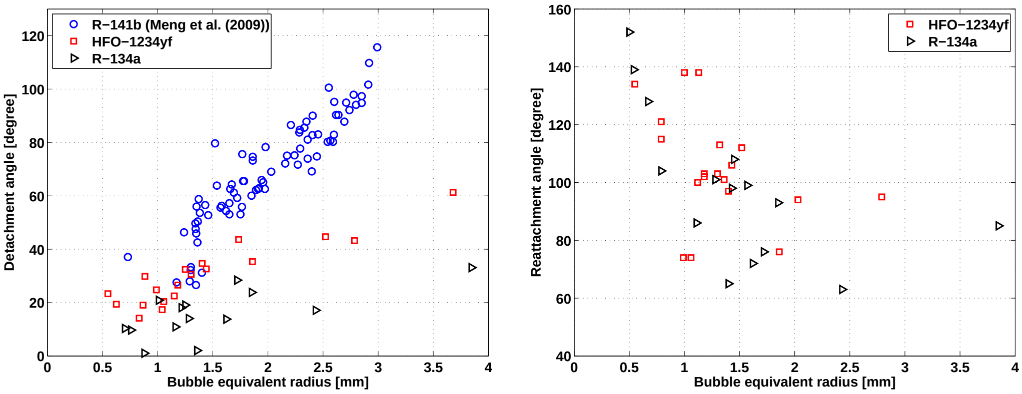

(a) Bubble detachment position vs. bubble equivalent radius

(b) Bubble re-attachment position vs. bubble equivalent radius

Figure 6.10: Bubble position vs. bubble equivalent radius. Test conditions are $x = 5\%$, $G = 300$ kg·m^{-2}·s^{-1}, $T_{\mathrm{sat}} = 10$ °C and $D = 6.70$ mm.

6.2.3 Determination of the perturbation lengths up- and downstream of a return bend

To determine the perturbation lengths up- and downstream of a return bend (sections a-a' and b-b', see Fig. 6.1), some experimental tests have been performed using the test section depicted in Fig. 4.7. As can be noted, this test section contains 10 pressure taps at several locations along the straight tubes up- and downstream of the return bend. Each measurement is made with a pressure transducer connected to a valve manifold which permits to isolate the pressure drop measurement at each location while maintaining the same measurement uncertainty.

The effect of the saturation temperature on the pressure drop in straight tubes and also in return bends was presented in [Padilla *et al.* 2011a] and [Padilla *et al.* 2011b] respectively. From these sets of experimental results, the saturation temperature of 10 °C was selected to perform the tests. As a matter of fact, this temperature corresponds to the condition which yielded the highest pressure drop for R-134a in our experimental facility.

Mass velocities of $G = 570$ kg·m^{-2}·s^{-1} and $G = 950$ kg·m^{-2}·s^{-1} correspond to the minimal and maximal mass velocities studied in the present work for an inner diameter of 7.90 mm.

The pressure drops presented in this section correspond to the return bend pressure drop ($\Delta p_{\mathrm{rb}} = \Delta p_{\mathrm{tot}} - \Delta p_{\mathrm{st,in}} - \Delta p_{\mathrm{st,out}}$, of Fig. 6.1). To compare the results up to an objective significance, the Wilcoxon matched-pairs signed rank tests for two-related samples ([Wilcoxon 1950]) were used in all experiments. This is a well-known non-parametric statistical test for the relative size of the scores of the same (or matched) subjects under two experimental conditions by comparing the distributions for positive and negative differences of the ranks of their absolute values. The significance criterion for two independent samples was set to $p = 0.05$.

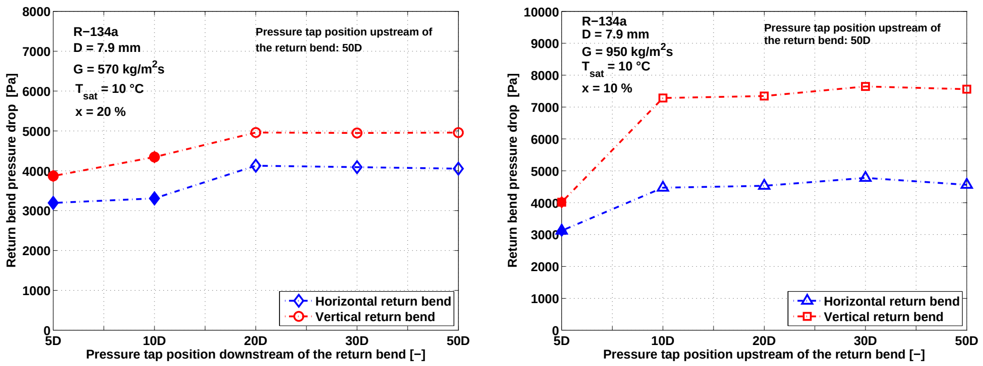

(a) (b)

Figure 6.11: Return bend pressure drop as measured at different pressure tap locations ($5D$, $10D$, $20D$, $30D$ and $50D$) up- and downstream on vertical and horizontal return bends. Filled markers correspond to measurements affected by the perturbation.

A comparison between the return bend pressure drop measured at different pressure tap locations up- and downstream for vertical and horizontal return bends is presented in Fig. 6.11. Each measurement presented corresponds to a mean of 30 data points measured during about 3 min.

In both horizontal and vertical cases, it is noted that there was no significant difference in the return bend pressure drop between any position from $20D$ to $50D$ downstream of the return bend ($p > 0.05$). Concerning the perturbation length upstream of the return bend, in both cases (horizontal and vertical) there was found a significant difference in the return bend pressure drop ($p < 0.05$) between the pressure taps located at $5D$ and $10D$.

6.2.4 Two-phase pressure drop in return bends

The pressure drops presented hereafter correspond to the return bend pressure drop (Δp_{rb}). Note that Δp_{rb} is obtained from $\Delta p_{\mathrm{rb}} = \Delta p_{\mathrm{tot}} - \Delta p_{\mathrm{st,in}} - \Delta p_{\mathrm{st,out}}$ and depends on the return bend orientation. The general formulation for Δp_{rb} has been presented for vertical return bends in Eq. (6.3). For horizontal return bends, $\Delta p_{\mathrm{rb}} = \Delta p_{\mathrm{st}(\pi R)} + \Delta p_{\mathrm{sing}}$.

Table 6.1 summarizes the experimental conditions of the return bend pressure drop database presented by [Padilla *et al.* 2011b, Padilla *et al.* 2012a, Padilla *et al.* 2012c] along with the corresponding uncertainties. The 1087 experimental tests have been carried out using two different tube diameters (10.85 and 7.90 mm), saturation temperatures from 4.4 °C to 22.1 °C, two orientations (horizontal and vertical) and over the entire range of the vapor quality. The mass velocity ranges from 189.45 to 1695.26 kg·m^{-2}·s^{-1}.

Table 6.1: Experimental conditions and uncertainties of the present return bend pressure drop database. (1087 points)

Parameters	Range	Uncertainties
Fluids	R-410A, R-134a, HFO-1234yf	
D	10.85 and 7.90 mm	$\pm 0.6\%$
Orientation	Horizontal - Vertical	
G	189.5 to 1695.3 kg m^{-2} s^{-1}	$< 1.3\%$
T_{sat}	4.4 - 22.1 °C	± 0.1K
P$_{\mathrm{heater}}$	0 - 10 kW	± 1 W
x	0.04 - 0.98	$< 0.82\%$
p	3.48 - 14.50 bar	$\pm 0.1\%$
Δp	0 - 33.29 kPa	$\pm 0.1\%$

6.2.4.1 Results for horizontal return bends

The pressure drop along the return bend (Δp_{rb}), the regular pressure drop along the length πR ($\Delta p_{\mathrm{st}(\pi R)}$) and the singular pressure drop ($\Delta p_{\mathrm{sing}} = \Delta p_{\mathrm{curv}} + \Delta p_{\mathrm{pert,in}} + \Delta p_{\mathrm{pert,out}}$) are presented in Fig. 6.12 for the HFO-1234yf at two different conditions as a function of the vapor quality.

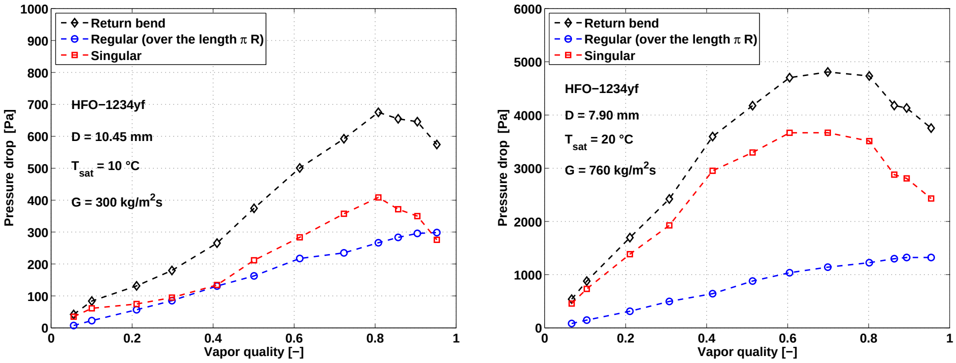

(a) (b)

Figure 6.12: Return bend, regular (over the length πR) and singular pressure drop vs. vapor quality.

Figure 6.13 shows the effect of the mass velocity at different saturation temperatures. The maximum pressure drop occurs above 60% of vapor quality at the return bend inlet. According to the flow pattern map of [Wojtan *et al.* 2005a], this maximum occurs in annular flow regime. The effects of the mass velocity G and saturation temperature T_{sat} in the total pressure drop are also observed. As the mass velocity increases, the singular pressure drop increases by the effect of the centrifugal forces acting on both phases, which is consistent with the correlation of [Padilla *et al.* 2009].

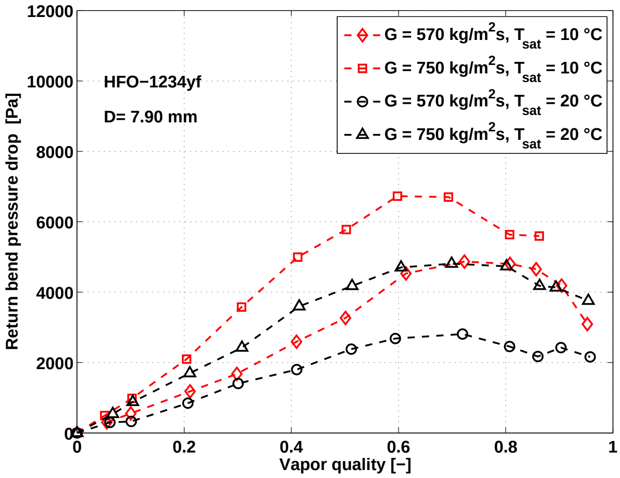

Figure 6.13: Return bend pressure drop vs. vapor quality.

6.2.4.2 Results for vertical return bends

Figure 6.14 presents the different pressure drop contributions of the return bend pressure drop ($\Delta p_{\mathrm{rb}} = \Delta p_{\mathrm{tot}} - \Delta p_{\mathrm{st,in}} - \Delta p_{\mathrm{st,out}}$) for the HFO-1234yf at two different conditions as a function of the vapor quality. These contributions are: the static pressure drop ($\Delta p_{\mathrm{static}}$), the regular pressure drop along the length πR for different orientations ($\Delta p_{\mathrm{st,vert_{rb}}(\pi R)}$) and the singular pressure drop ($\Delta p_{\mathrm{sing}} = \Delta p_{\mathrm{curv}} + \Delta p_{\mathrm{pert,in}} + \Delta p_{\mathrm{pert,out}}$). As can be noted in Fig. 6.14(a), at low vapor quality ($x < 20\%$), the contribution of the static pressure drop to the return bend pressure drop is important due to the predominant effect of the liquid phase; as the vapor quality increases, it is observed that this contribution decays and at high vapor quality it can be neglected. Figure 6.14(b) presents the results for the same fluid flowing in a smaller inner diameter ($D = 7.9$ mm) at $G = 950$ kg·m^{-2}·s^{-1}. At these conditions, the contribution of the static pressure drop is negligible.

Figure 6.15(a) presents a comparison between refrigerants HFO-1234yf, R-410A and R-134a. Results show that the pressure drop for HFO-1234yf is lower than that for R-134a. Similar behavior was observed for horizontal return bends. This behavior is the consequence of the physical properties of the refrigerants and is independent of the return bend orientation.

Figure 6.15(b) shows the orientation effect for the three refrigerants at the same experimental conditions. The maximum pressure drop occurs above 60% of vapor quality regardless of orientation. According to the flow pattern map of [Wojtan *et al.* 2005a], this maximum occurs for annular flow regime at the inlet of the bend.

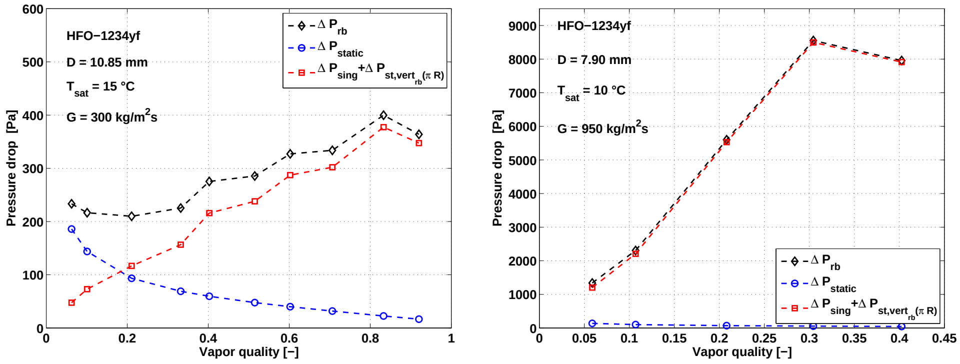

(a)

(b)

Figure 6.14: Contribution of the different pressure drops as a function of the vapor quality.

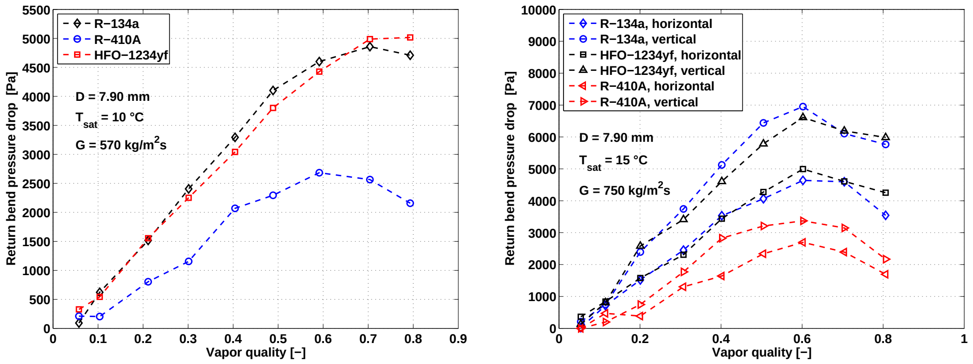

(a) Fluid comparison

(b) Orientation comparison

Figure 6.15: Return bend pressure drop vs. vapor quality. Fluid and orientation comparisons.

6.2.5 Comparison of the database to prediction methods

6.2.5.1 Predictions of the current two-phase pressure drop database for horizontal return bends

The 802 pressure drop data points measured in horizontal return bends (Δp_{rb}) for refrigerants HFO-1234yf, R-134a and R-410A are compared against four two-phase frictional pressure drop prediction methods in return bends. These methods are: [Chisholm 1983] and [Idelshik 1986], [Chen *et al.* 2004], [Domanski & Hermes 2008] and [Padilla *et al.* 2009]. These methods were introduced in section 3.2.2.4 and their experimental conditions were summarized by [Padilla *et al.* 2009].

Figure 6.16 shows the results for experimental pressure drop in return bends compared to predictions.

The best prediction was achieved by the method of [Chisholm 1983] and [Idelshik 1986] with 47.6% of the data predicted within a ±30% error band. Nevertheless, the trend of the experimental pressure drop data in return bend was not well captured by this method.

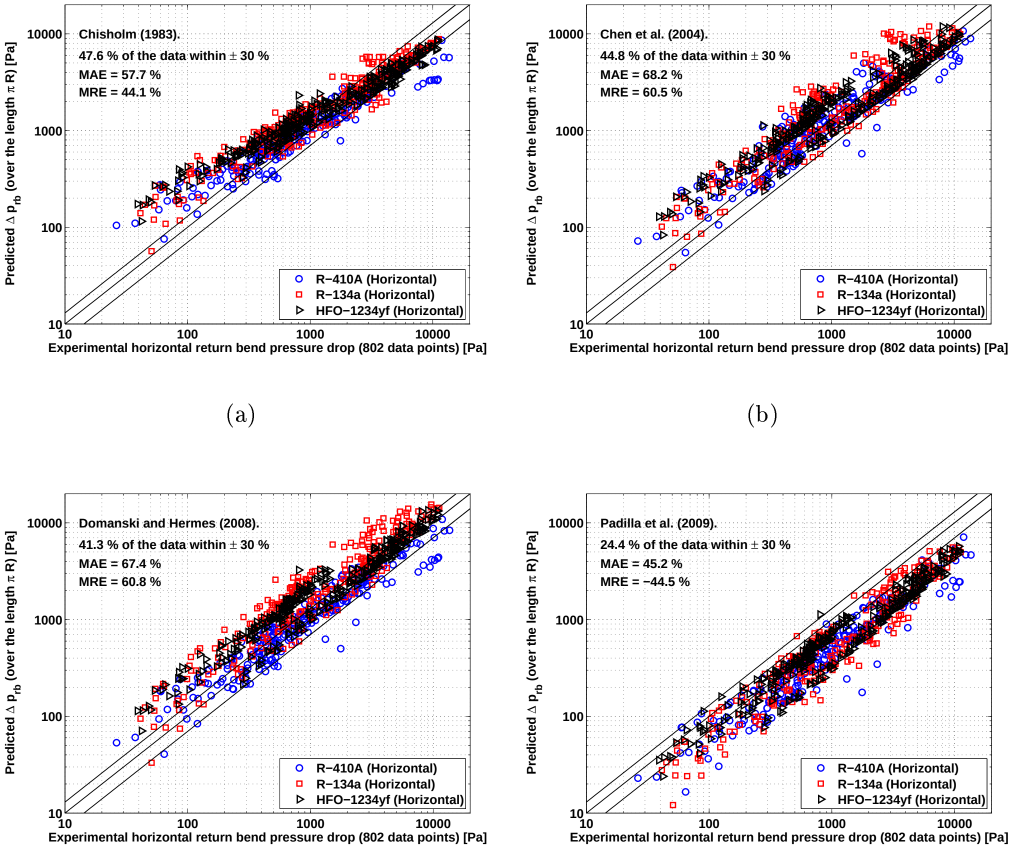

(a)

(b)

(c)

(d)

Figure 6.16: Experimental pressure drop data in horizontal return bends (over the length πR) compared to prediction methods. (802 points)

6.2.5.2 Predictions of the current two-phase pressure drop database for vertical downward flow return bends

The 285 pressure drop data points measured in vertical downward flow return bends (Δp_{rb}) for refrigerants HFO-1234yf, R-410A and R-134a are compared against the same two-phase frictional pressure drop prediction methods. Although these methods are for predicting two-phase pressure drop in horizontal return bends, it is interesting to investigate the predictions given by them on the calculation of the return bend pressure drop in vertical orientation. In this sense, the static pressure drop, which has been calculated using Eq.(6.6) has been added to the correlations.

Figure 6.17 shows the results for the experimental pressure drops in vertical return bends compared to predictions.

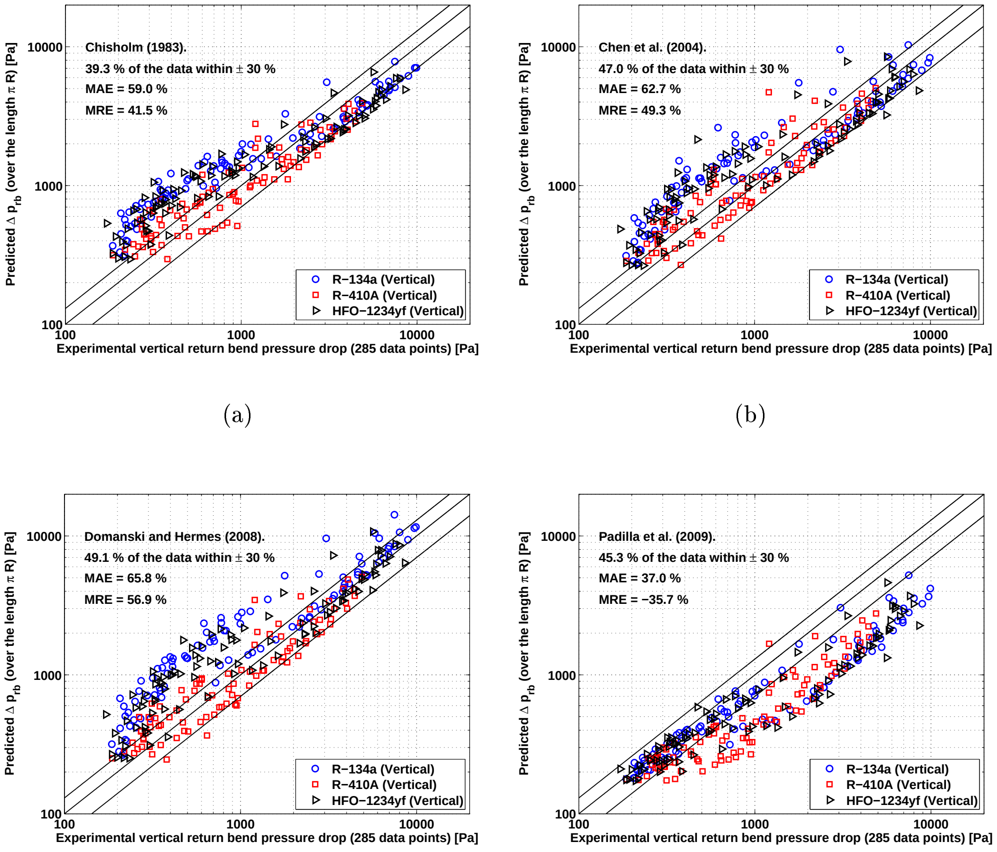

(a) (b)

(c) (d)

Figure 6.17: Experimental pressure drop data in vertical return bends (over the length πR) compared to prediction methods. (285 points)

The best prediction was achieved by the method of [Domanski & Hermes 2008] with around 49% of the data predicted within a ±30% error band. Nevertheless, the trend of the experimental pressure drop data in return bend was not well captured by these methods.

The [Padilla *et al.* 2009] prediction method gave the lower MRE with -33.2%.

To check the performance of the existing correlations, the distribution of the parameters of influence in the whole database are shown in Fig. 6.18. Figures 6.18(a) to 6.18(c) show the data distribution with respect to mass velocity, saturation temperature and vapor quality, respectively.

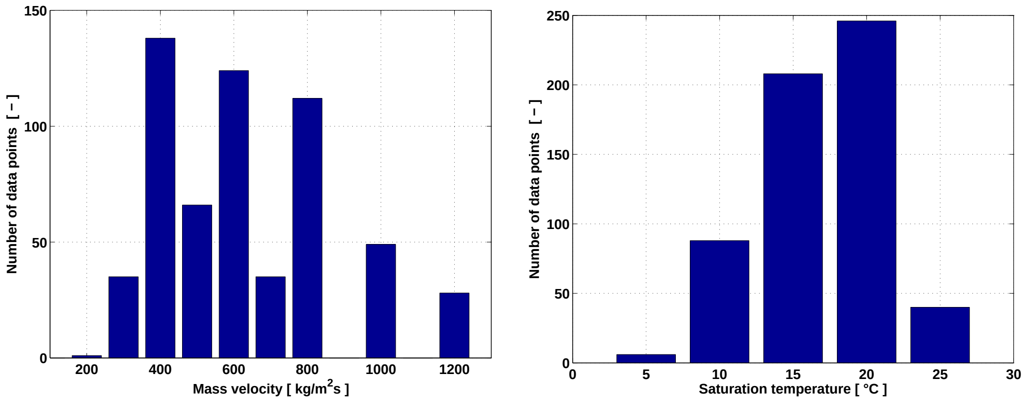

(a) Mass velocity G.

(b) Saturation temperature T_{sat}.

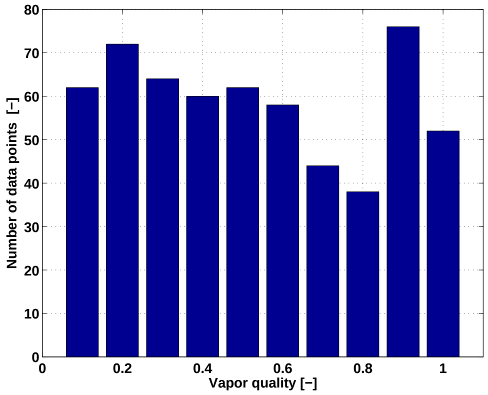

(c) Vapor quality x.

Figure 6.18: Distribution of the two-phase pressure drop database in return bends (1087 data points for HFO-1234yf, R-134a and R-410A).

6.3 New two-phase pressure drop prediction method in return bends

From the comparison carried out in the previous section, some of the methods which gave the best predictions for horizontal return bends do not seem to be valid for vertical orientation. In general, none of the prediction methods allow to explain the phenomena involved during two-phase flow in return bends. Based on the observations made in this study, the intention is to develop a new method for predicting the pressure drop in return bends using a different approach from those used in other studies. The new method is called mainly to predict the return bend pressure drop (Δp_{rb}) from the contributions of all the effects previously discussed (e.g friction, curvature, orientation, perturbation lengths, etc.).

6.3.1 Formulation

The return bend pressure drop (Δp_{rb}) is calculated by Eq.(6.3). In the case of vertical return bends, the static pressure drop ($\Delta p_{\mathrm{static}}$) is calculated using Eq. (6.6), the regular pressure drop along the bend of length πR for different orientations ($\Delta p_{\mathrm{st,vert_{rb}}(\pi R)}$) is calculated using the [Müller-Steinhagen & Heck 1986] correlation (Eq.(3.54)). Note that this method was initially developed based on horizontal and vertical orientations pressure drop data. Only the singular pressure drop ($\Delta p_{\mathrm{sing}} = \Delta p_{\mathrm{pert}} + \Delta p_{\mathrm{curv}}$) is correlated.

$$\Delta p_{\mathrm{rb}} = \Delta p_{\mathrm{st}(\pi R)} + \Delta p_{\mathrm{static}} + \Delta p_{\mathrm{sing}}$$

The new method is expected to predict the effect of the friction resistance due to the singularity (Δp_{sing}), which includes the curvature effect (Δp_{curv}) and its perturbation effect up- and downstream (Δp_{pert}). As explained in section 6.2.2, the effect of the curvature on the dynamical behavior of liquid and vapor phases, results in the generation of centrifugal forces producing an apparent buoyancy which, combined with other effects such as the flow pressure gradient, hydrodynamic lift, hydrodynamic drag and buoyancy due to gravity, govern the phenomena along the return bend, including the perturbation lengths up- and downstream of it. Since the overall effect is given by the composition of vapor and liquid flows, the following terms for the liquid and the vapor phases are considered:

$$\Delta p_{\mathrm{l}} = \rho_{\mathrm{l}} u_{\mathrm{l}}^2 = \frac{G^2(1-x)^2}{\rho_{\mathrm{l}}(1-\varepsilon)^2} \tag{6.8}$$

$$\Delta p_{\mathrm{v}} = \rho_{\mathrm{v}} u_{\mathrm{v}}^2 = \frac{G^2 x^2}{\rho_{\mathrm{v}} \varepsilon^2} \tag{6.9}$$

Two coefficients (K_{l} and K_{v}) are introduced, one for each phase. These coefficients are function of the vapor quality and the curvature ratio ($2R/D$):

$$K_{\mathrm{l}} = \left[x^a + (1-x) + b(1-x)^a\right] a \left(\frac{D}{2R}\right)^{1/a} \tag{6.10}$$

$$K_{\mathrm{v}} = \left[x^a \left(b - (1-x)\right)\right] a \left(\frac{D}{2R}\right)^{1/a} \tag{6.11}$$

where parameters $a = 3$ and $b = 0.055$ have been obtained from the least square method based on the present experimental database (1087 data points). The new prediction method is then given by the following relation:

$$\Delta p_{\mathrm{sing}} = K_{\mathrm{l}}\Delta p_{\mathrm{l}} + K_{\mathrm{v}}\Delta p_{\mathrm{v}} \tag{6.12}$$

Then, the return bend pressure drop can be predicted by:

$$\Delta p_{\mathrm{rb}} = \left[\Delta p_{\mathrm{st,vert_{rb}}(\pi R)}\right] + \left[\Delta p_{\mathrm{static}}\right] + \left[\Delta p_{\mathrm{sing}}\right] \tag{6.13}$$

Note that when $x = 0$, Eq. (6.13) becomes:

$$\Delta p_{\mathrm{rb,x=0}} = \Delta p_{\mathrm{rb,lo}} = \frac{G^2}{\rho_{\mathrm{l}}}\left[\frac{2f_{\mathrm{lo}}}{D} + \rho_{\mathrm{l}}^2 g(2R) + (1+b)a\left(\frac{D}{2R}\right)^{1/a}\right] \tag{6.14}$$

where the friction factor f_{lo} is calculated using Eq. (3.17).

6.3.2 Capability of prediction of the new method

In this section an assessment of the new developed method is carried out. To compare the performance of the new method, the entire database of this study (1087 experimental points for vertical and horizontal return bends) and the database shown in [Padilla *et al.* 2009] (325 points in the literature) have been selected. A total of 1412 points that contain information of 3 laboratories, on 4 fluids (R-12, R-134a, R-410A and HFO-1234yf), with horizontal and vertical orientations and for the entire range of vapor quality have been compared with the four prediction methods of the literature and the new prediction method. Table 6.2 presents the results of this comparison.

Table 6.2: 1412 experimental pressure drop data points for HFO-1234yf, R-410A, R-12 and R-134a refrigerants in return bends compared to different correlations from the literature and the new prediction method.

	± 30 % error band	MAE	MRE
[Chisholm 1983] and [Idelshik 1986]	41.7 (25.1) %	69.7 %	57.5 %
[Chen *et al.* 2004]	43.8 (34.7) %	71.0 %	-62.5 %
[Domanski & Hermes 2008]	43.3 (31.5) %	66.2 %	59.0 %
[Padilla *et al.* 2009]	38.4 (23.5) %	38.6 %	34.7 %
New method	**47.0** (32.1) %	36.4 %	-3.7 %

Figure 6.19 shows the comparison of 1412 data points with predictions by the new method. Around 47% of the data are predicted within a ±30% error band (32% of the data within a ±20% error band). The mean relative error is less than 5%.

Fig. 6.20 presents the pressure drop in return bend as a function of the vapor quality. The experimental data are plotted and compared to different prediction methods from the literature as well as the new prediction method. Note that for each refrigerant, the predictions of the proposed correlation show good agreement with the shape of the experimental pressure drop profile.

In addition to the previous comparisons, simulations have been performed using the proposed equation. Fig. 6.21(a) shows the effect of the mass velocity and saturation temperature on the predicted return bend pressure drop (Δp_{rb}). The range of mass velocity and saturation temperature have been voluntarily extrapolated in order to check if any particular behavior might occur. Fig. 6.21(b) presents the effect of $2R/D$ on the predicted return bend pressure drop. It is observed that when $(2R/D)$ increases, $\Delta p_{\mathrm{sing}} \Rightarrow 0$ and

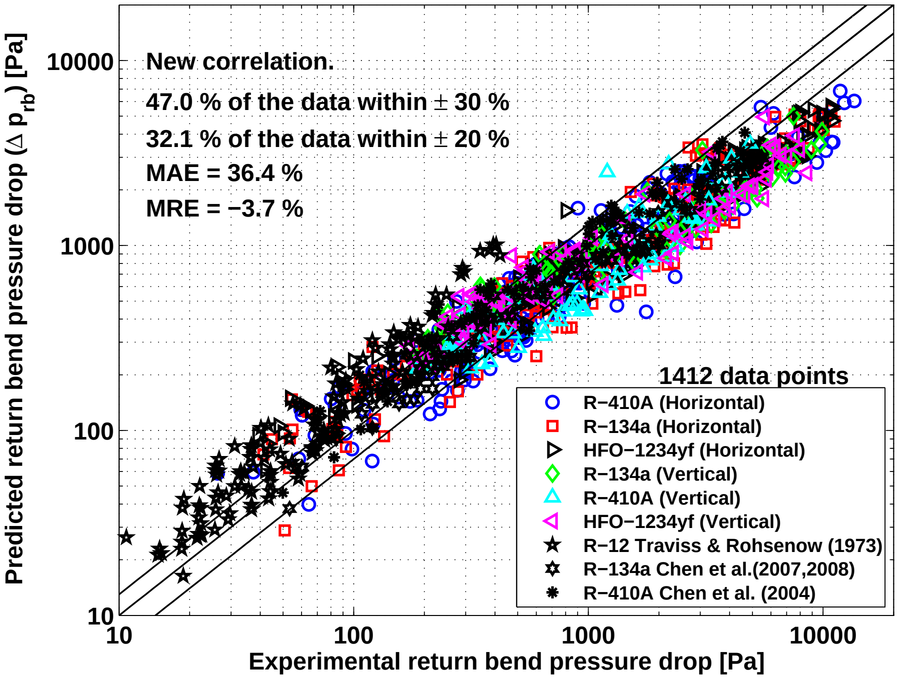

Figure 6.19: Comparison of 1412 data points with predictions by the proposed correlation.

$\Delta p_{\mathrm{rb}} \Rightarrow \Delta p_{\mathrm{st}}$. Finally, Fig. 6.21(c) presents the effect of the orientation. Note that for vertical orientation, at values of x close to 0, Δp_{rb} increases due to the effect of gravity acting on the liquid phase. This effect decreases with the increasing vapor quality, and becomes negligible for high values of x.

Eq. 6.13 presents many advantages:

- It contains only two empirical constants.
- It has been developed based on a large database (1412 data points) including the fourth generation HFO-1234yf and the well know third generation R-134a, R-410A and R-12 refrigerants in both horizontal and vertical orientations.
- Based on the visual observations, various effects including centrifugal forces acting on both phases and buoyancy due to gravity have been considered in the formulation of the new method.
- This correlation does not assume a homogeneous flow.
- The physical limits in the new method are correct. Note that when $R \rightarrow D/2$, the effect of the curvature on the singular pressure drop reaches it maximum value ($\Delta p_{\mathrm{curv}} = \Delta p_{\mathrm{curv,max}}$), and when $R \rightarrow \infty$, $(D/2R) = 0$, giving $\Delta p_{\mathrm{sing}} = 0$. In addition, when $x = 0$ or $x = 1$, the resulting pressure drop tends toward the single phase pressure drop in return bend.
- The relation has been developed considering commercial tube diameters from 7.9 to 10.85 mm, $(2R/D)$ from 3.68 to 4.05, a wide range of mass velocities (189 to 1695

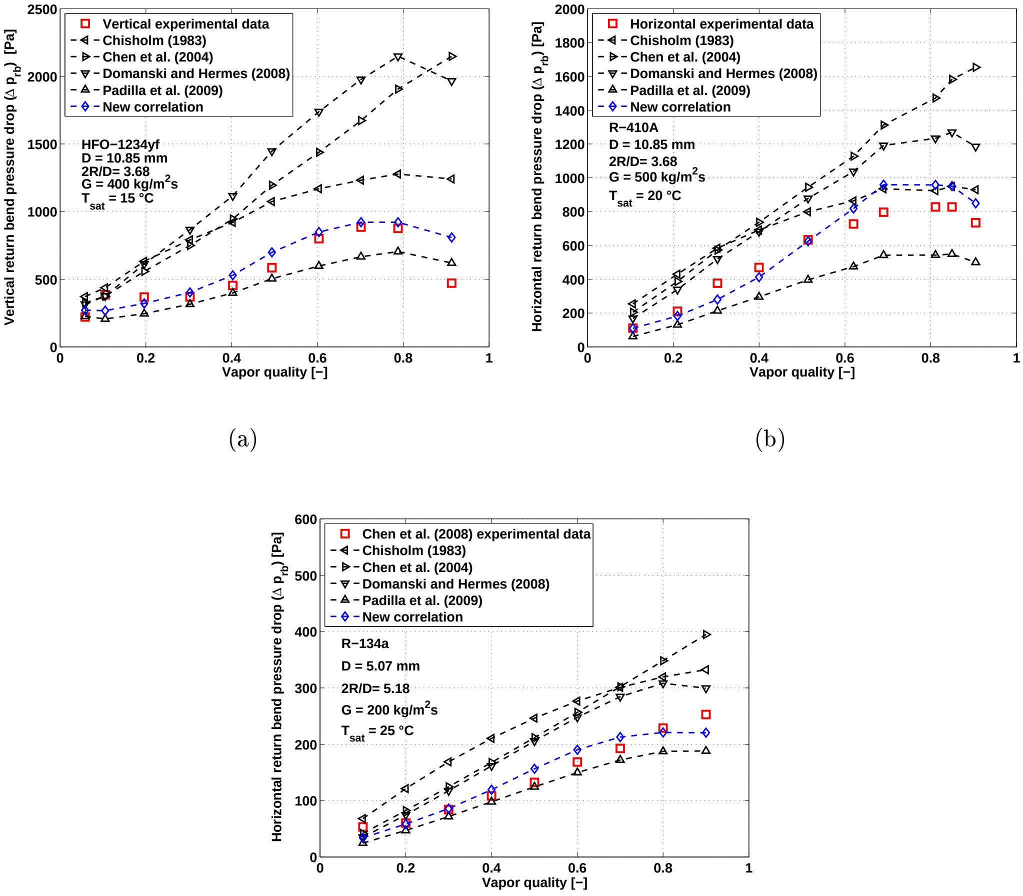

(a)

(b)

(c)

Figure 6.20: Pressure drop in return bend as a function of the vapor quality using the experimental data compared to different prediction methods.

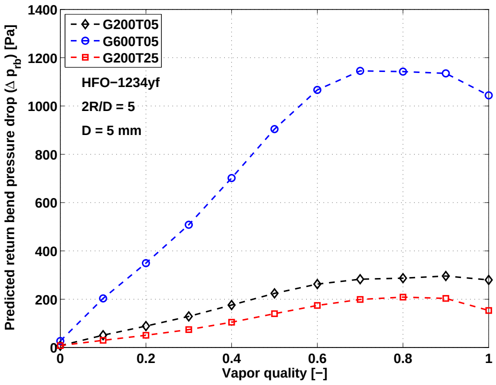

(a)

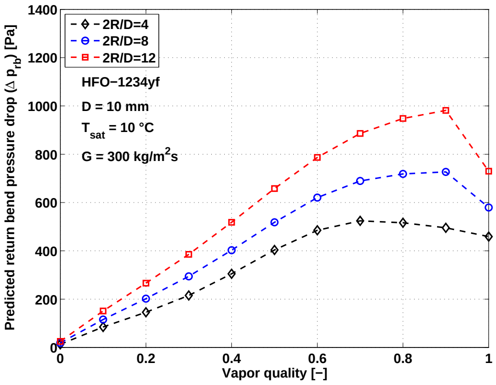

(b)

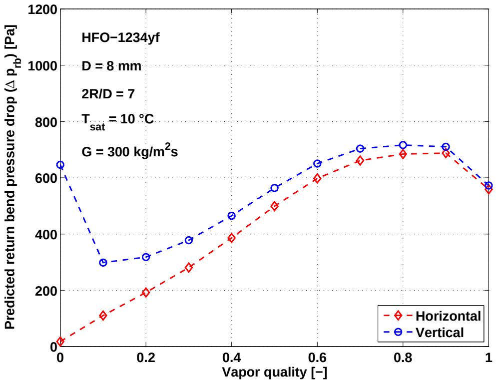

(c)

Figure 6.21: Predicted return bend pressure drop evolution as a function of the vapor quality.

kg m^{-2} s^{-1}) and saturation temperatures from 4.4°C to 22°C, which constitute a relatively large range of experimental conditions.

- The term $[\Delta p_{\text{static}}]$ represents the contribution of the static pressure drop given by a vertical orientation.
- The term $[\Delta p_{\text{sing}} + \Delta p_{\text{pert}}]$ takes into account the contribution of the curvature effect due to the singularity and its perturbation effects up- and downstream on the return bend pressure drop.

6.3.3 Predictions for single-phase flow in return bend

Knowing that Eq. (6.13) has been developed from two-phase flow experimental data, it is especially interesting to evaluate its performance on the particular case of single phase flow prediction in return bends. Very little information related to single-phase pressure drop prediction in return bends using refrigerants as working fluid has been found in the literature. [Chen *et al.* 2005] presented single-phase pressure drop data for R-410A in a copper wavy tube having an inner diameter of 3.25 mm and a curvature radius of 6.35 mm. The authors reported that the ratio of frictional factor between U-bend in wavy tube[1] and straight tube ($f_{\text{rb}}/f_{\text{st}}$) is about 1.5 to 2.5 for $\text{Re}_{\text{lo}} = 2500$ to 25000. They also presented an expression for $f_{\text{rb}} = 2.737\text{Re}_{\text{lo}}^{-0.56}$, which allows to predict $\Delta p_{\text{rb,lo}}$, as shown below:

$$\Delta p_{\text{rb,lo}} = \frac{G^2}{\rho_{\text{l}}}\left[\frac{2f_{\text{rb}}L}{D}\right] \tag{6.15}$$

Considering that $\Delta p_{\text{lo}} = \dfrac{G^2}{\rho_{\text{l}}}\Phi$, Fig. 6.22 presents a comparison between the multiplier Φ obtained for regular pressure drop in straight tubes (Eq. (3.54)), the new prediction method (Eq. (6.14)) and that obtained from [Chen *et al.* 2005] method (Eq. (6.15)).

Note that at low values of Re_{lo}, the single-phase predictions given by the method of [Chen *et al.* 2005] and the new method are similar. However, at high values of Re_{lo}, Φ_{Chen} tends toward Φ_{st} while remains around 2.5 times of these obtained for straight tube, which is in agreement with the results previously reported.

The Φ_{Chen} multiplier does not seems to be valid because it only considers the effect of the friction (regular pressure drop) which becomes lower than that for straight tube at high liquid Reynolds values, which has no physical meaning. On the contrary, at high values of Re_{lo} where the effect of the friction is small when comparing to the curvature effect, Φ_{New} and Φ_{st} follow a parallel evolution.

6.4 Chapter conclusions

In this chapter, two-phase flow regimes for HFO-1234yf and R-134a in a 6.70 mm inner diameter glass return bend have been investigated with a high-speed high-resolution camera for both horizontal and vertical orientations. The different flow regimes observed were: slug, intermittent and annular flows.

The dynamical behavior of vapor bubbles or slugs in vertical downward flow return bend was reported. A simplified analysis of the forces acting on the bubble has been proposed to better understand the observations. The detachment is mainly controlled by the apparent buoyancy and hydrodynamic lift. The re-attachment is controlled by the apparent buoyancy

---

[1] U-type wavy tubes (hairpin) with consecutive 180° return bends are widely employed in the condenser and evaporator of the refrigerating systems.

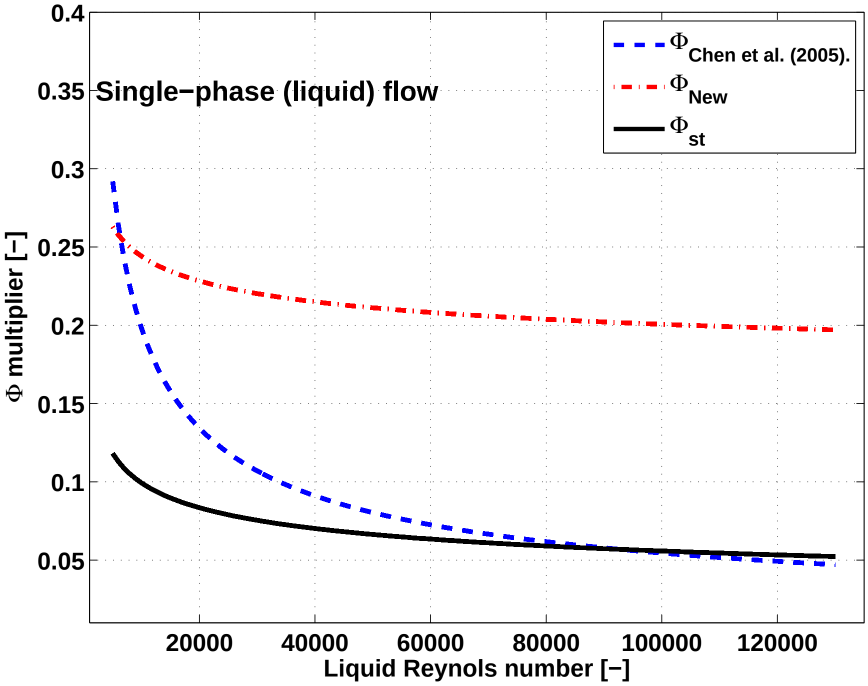

Figure 6.22: Φ multiplier comparison as a function of liquid Reynolds number (Re_{lo}).

and the radial component of buoyancy due to gravity. In general, the secondary flow in the liquid phase influences the trajectory of the small bubbles while it is probably negligible in the case of vapor slugs.

In addition, to determine the perturbation lengths up- and downstream of the return bend, an experimental study has been carried out by measuring the return bend pressure drop at different pressure tap locations up- and downstream of the singularity. In both horizontal and vertical cases, it is noted that there was no significant difference in the return bend pressure drop between any position from $20D$ to $50D$ downstream of the return bend. Concerning the perturbation length upstream of the return bend, in both cases (horizontal and vertical) there was found a significant difference in the return bend pressure drop between the pressure taps located at $5D$ and $10D$.

A new pressure drop database for horizontal and vertical return bends has been presented for HFO-1234yf, R-134a and R-410A refrigerants. 802 data points for horizontal and 285 data points for vertical return bends were determined by subtracting the inlet and outlet regular pressure drops in straight tube from the total pressure drop. It has been shown that the return bend pressure drop increases when the mass velocity increases because of the increasing effect of the centrifugal force acting on both phases. These experimental data have been compared against correlations found in the literature.

An improved prediction method for return bend pressure drop including important parameters such as void fraction, curvature ratio and effect of the orientation (i.e vertical orientation) has been developed from the present experimental data. This new method allows to predict single- and two-phase pressure drop in return bends in a wide range of conditions.

CHAPTER 7

Two-phase flow in sudden contractions

Contents

This chapter presents qualitative two-phase flow visualizations of R-134a in the test section described in section 4.2.1.3. In addition, the perturbation lengths up- and downstream of the sudden contraction are investigated. Furthermore, 360 pressure drop data points measured for two-phase flow of HFO-1234yf, R-134a and R-410A refrigerants in horizontal sudden contractions are presented and compared against 6 prediction methods from the literature.

Based on the present database, a new method is proposed for predicting the pressure drop in sudden contractions, which is the sum of the pressure drop due to the flow acceleration in a geometrical change of flow cross-section (change in momentum) and the frictional pressure drop due to the singularity and its perturbation effects up- and downstream (proposed equation).

7.1 Experimental procedure

7.1.1 Data reduction

In order to obtain the values of the sudden contraction pressure drop Δp_c, the total pressure drop and the straight tube (regular) pressure drops have been measured. Figure 7.1 shows a synthesis of the idealized pressure profile along the flow path in a sudden contraction.

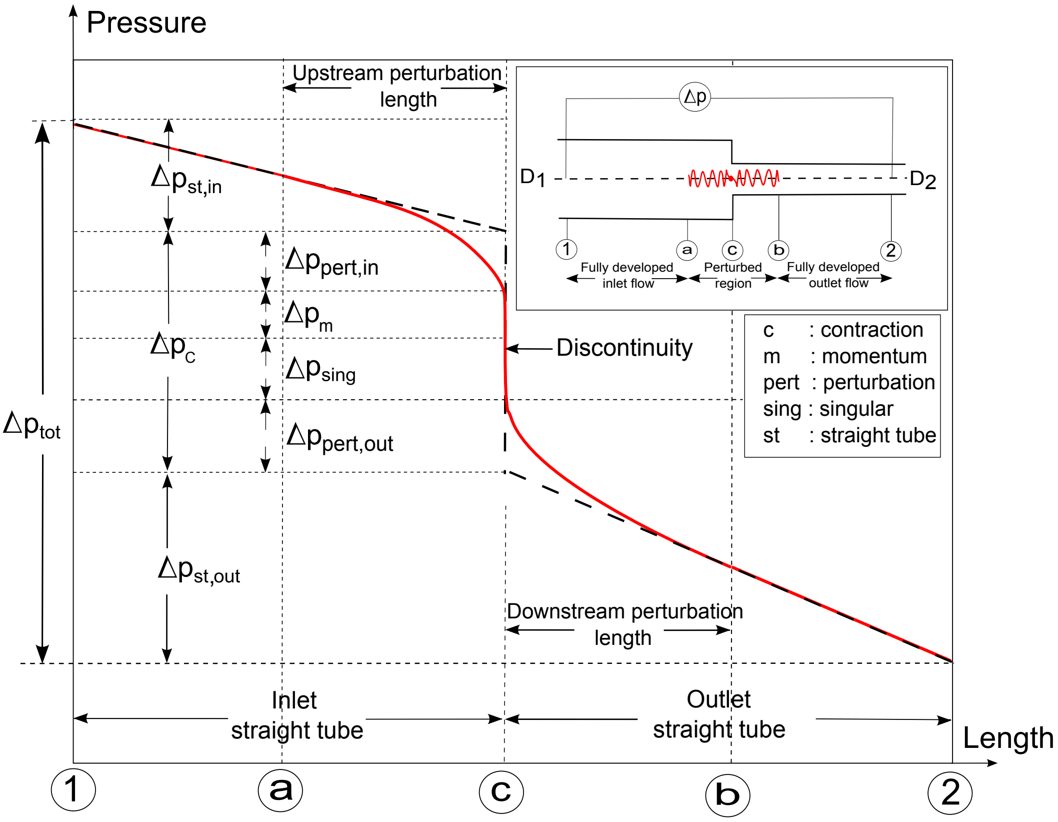

Figure 7.1: Idealized pressure profile along a sudden contraction.

Δp_{tot} corresponds to the total pressure drop experimentally measured over the length L_3. This term is expressed with the following relation:

$$\Delta p_{\text{tot}} = \Delta p_{\text{st,in}} + \Delta p_{\text{c}} + \Delta p_{\text{st,out}} \tag{7.1}$$

The term $\Delta p_{\text{st,in}} + \Delta p_{\text{st,out}}$ is calculated as:

$$\Delta p_{\text{st,in}} + \Delta p_{\text{st,out}} = \left(-\frac{\mathrm{d}p}{\mathrm{d}z}\right)_{\text{st},D_1} L_3' + \left(-\frac{\mathrm{d}p}{\mathrm{d}z}\right)_{\text{st},D_2} L_3'' \tag{7.2}$$

The straight tube (regular) pressure gradients are experimentally measured along the length L_0 and L_6 (see Fig. 4.9) for inner tube diameters of 10.85 mm and 7.90 mm. These gradients are calculated using Eq.(5.1).

The term Δp_{c} corresponds to the sudden contraction pressure drop and is expressed as the sum of the contributions of the the singular pressure drop (Δp_{sing}), the pressure drop due to the flow acceleration across a geometrical area change (Δp_{m}) and the perturbations upstream and downstream of the sudden contraction along the transitional region ($\Delta p_{\text{pert}} = \Delta p_{\text{pert,in}} + \Delta p_{\text{pert,out}}$).

$$\Delta p_{\text{c}} = \Delta p_{\text{sing}} + \Delta p_{\text{m}} + \Delta p_{\text{pert}} \tag{7.3}$$

In the experiments, as explained in [Padilla *et al.* 2011a], the maximum pressure drop measured from the outlet of the electrical heater (where the vapor quality is calculated) to the outlet of the test section can reach up to 0.84 bar. This pressure drop is not negligible and provokes a flashing effect (see section 2.6.3.1) and a temperature difference. As explained in section 5.1.2, from the outlet of the electrical heater to the outlet of the test section, the Δx and ΔT_{sat} variations due to the flashing effect have been taken into account. The flashing effect is calculated using the relation (2.50) and both vapor quality and saturation temperature are recalculated at the inlet of each straight tube and the sudden contraction. However, the variation of the vapor quality due to the flashing effect along the pressure drop measurement lengths is small enough to assume the vapor quality to be constant along these lengths.

Considering that x do not vary along the pressure drop measurement lengths, the term Δp_{m} is calculated from Eq. (2.34) and expressed as follows:

$$\Delta p_{\mathrm{m}} = \frac{x^2}{\rho_{\mathrm{v}}}\left[\frac{G_2^2}{\varepsilon_2} - \frac{G_1^2}{\varepsilon_1}\right] + \frac{(1-x)^2}{\rho_{\mathrm{l}}}\left[\frac{G_2^2}{(1-\varepsilon_2)} - \frac{G_1^2}{(1-\varepsilon_1)}\right] \tag{7.4}$$

and the void fraction (ε) is calculated using the [Steiner 1993] version of [Rouhani & Axelsson 1970] correlation (Eq. 3.68).

7.2 Experimental results

7.2.1 Two-phase flow visualization in horizontal sudden contraction

Flow regimes of R-134a have been observed in the test section described in section 4.2.1.3. As shown in Fig. 7.2, the different flow regimes observed were: slug, intermittent and annular flows. For slug flow regime (Fig. 7.2(f)), as seen in the side view, the flow in the straight tube upstream of the sudden contraction is strongly influenced by gravity that acts to stratify the liquid to the bottom of the tube and the vapor to the top. Regarding the annular flow observations (Figures 7.2(a) and 7.2(b)), for different vapor qualities, visualization results show that the liquid forms a continuous film around the perimeter of the tube and the interface between the liquid annulus and the vapor core is disturbed by small amplitude waves with some droplets dispersed in the vapor core. This flow behavior beyond the sudden contraction is found similar to the behavior observed in straight tubes.

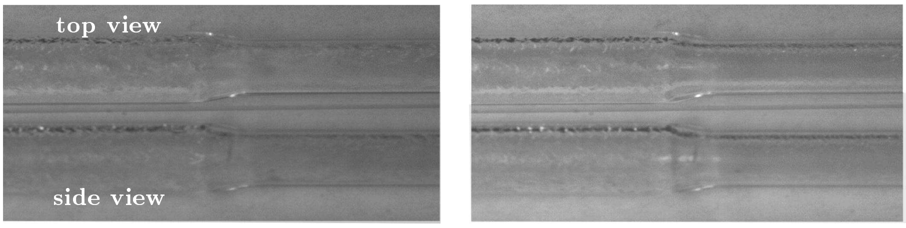

(a) Annular flow at $G_1 = 200$ kg·m^{-2}·s^{-1}, $T_{\mathrm{sat}} = 10$°C and $x = 40\%$.

(b) Annular flow at $G_1 = 200$ kg·m^{-2}·s^{-1}, $T_{\mathrm{sat}} = 10$°C and $x = 60\%$.

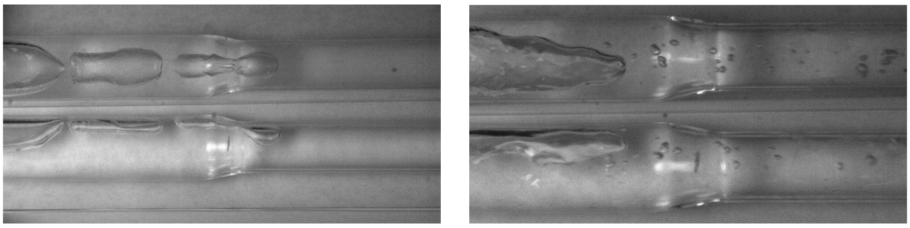

(c) Slug flow at $G_1 = 300$ kg·m^{-2}·s^{-1}, $T_{\mathrm{sat}} = 9$°C and $x = 2\%$.

(d) Slug flow at $G_1 = 300$ kg·m^{-2}·s^{-1}, $T_{\mathrm{sat}} = 9$°C and $x = 5\%$.

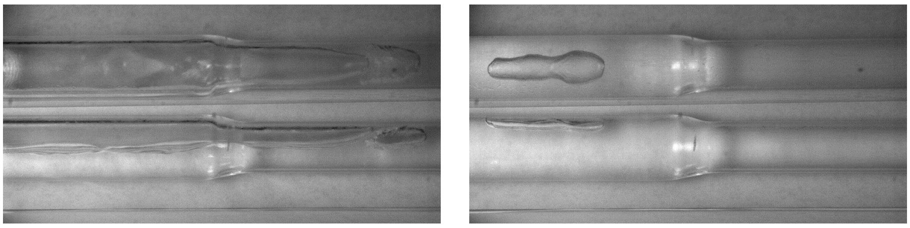

(e) Intermittent flow at $G_1 = 300$ kg·m^{-2}·s^{-1}, $T_{\mathrm{sat}} = 9$°C and $x = 10\%$.

(f) Slug flow at $G_1 = 200$ kg·m^{-2}·s^{-1}, $T_{\mathrm{sat}} = 9$°C and $x = 2\%$.

Figure 7.2: Side and top views of the R-134a flow patterns in a horizontal sudden contraction. $D_1 = 10$ mm, $\sigma_{\mathrm{A}} = \dfrac{D_2^2}{D_1^2} = 0.49$.

Figure 7.3 shows the progress of R-134a vapor slug flowing along a sudden contraction. In these figures it can be seen the effect of the vapor slug acceleration at the inlet of the singularity.

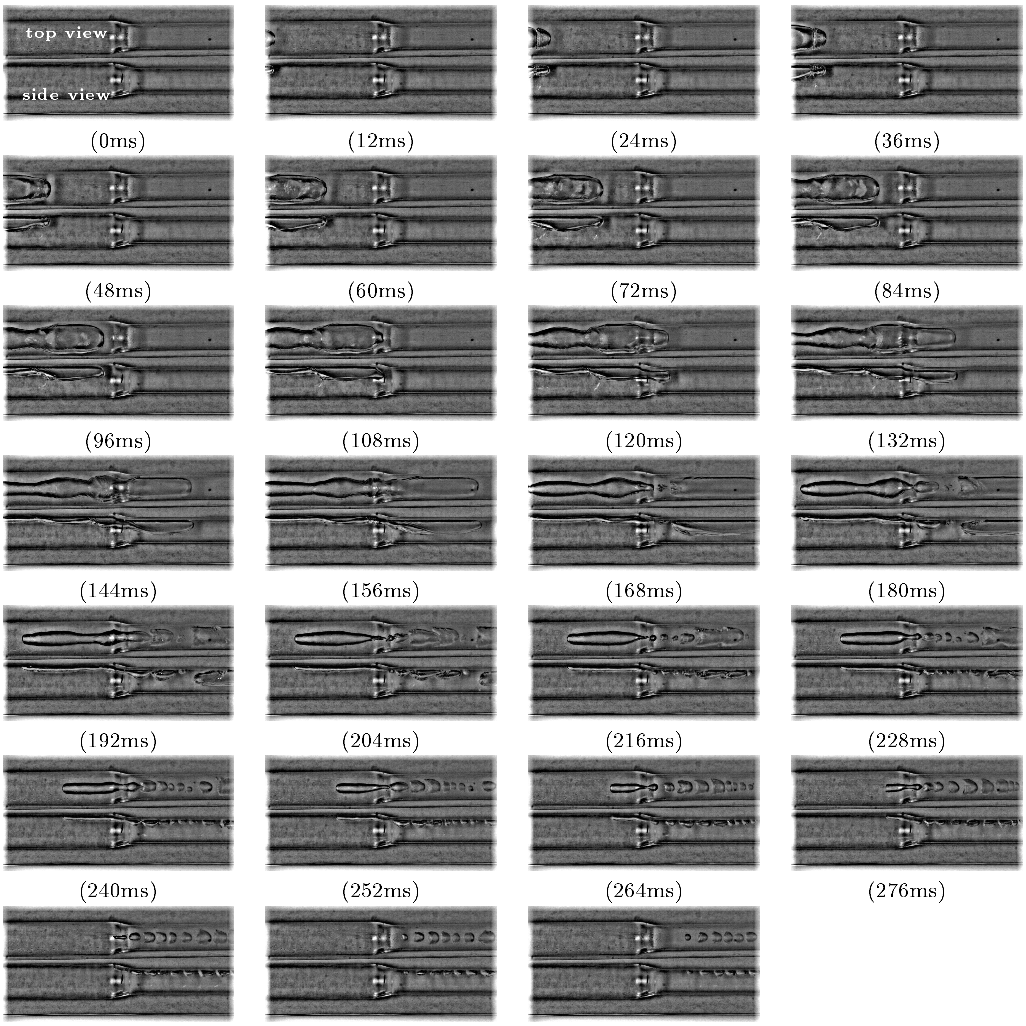

(0ms) (12ms) (24ms) (36ms)

(48ms) (60ms) (72ms) (84ms)

(96ms) (108ms) (120ms) (132ms)

(144ms) (156ms) (168ms) (180ms)

(192ms) (204ms) (216ms) (228ms)

(240ms) (252ms) (264ms) (276ms)

(288ms) (300ms) (312ms)

Figure 7.3: Side and top views progress of R-134a slug flow along a sudden contraction for $x = 1\%$, $G_1 = 200$ kg·m^{-2}·s^{-1}, $T_{\text{sat}} = 8$ °C, $D_1 = 10.0$ mm and $\sigma_A = \dfrac{D_2^2}{D_1^2} = 0.49$.

At the beginning of the singularity, approximately $1D_1$ upstream of the change of cross-section, the flow acceleration enlarges the vapor slug , and in some cases, the slug breaks into a succession of small bubbles. In some occasions, these bubbles coalesce to form again a vapor slug approximately $1D_2$ downstream of the change of cross-section, but usually, the small bubbles follow the vapor slug head from a distance of about $2D_2$. It is also important to note that the change of cross-section induces a flow acceleration which causes, in many cases, a flow pattern change.

During slug and intermittent flow (Figures 7.2(c) to 7.2(e)), an hydraulic jump is observed in the liquid phase as a result of its "collision" with the singularity. When the void fraction is small, this jump in the liquid phase is one of the causes observed, along with the flow acceleration due to the area change, which produces the breakdown of the vapor slugs mentioned above.

7.2.2 Dynamical behavior of bubbles and vapor slugs during a slug flow regime in a sudden contraction

As mentioned before, some typical flow regimes are observed during flow boiling in the experiments. The working fluid undergoes slug flow, intermittent flow and annular flow. Different flow patterns would perform distinct dynamical behavior as liquid and vapor pass through a sudden contraction. Figure 7.4(a) presents the evolution of a small bubble of R-134a (approx. equivalent radius 1.0 mm) moving along the sudden contraction. The flow conditions are $G = 200$ kg·m^{-2}·s^{-1}, $T_{\text{sat}} = 8$ °C and $x = 1\%$.

As can be observed, the side view reveals the effect of buoyancy on the bubble which slides from the horizontal inlet tube attached to the top side wall of the tube. This behavior continues beyond the sudden contraction in the outlet tube following the liquid flow direction. The top view shows the bubble trajectory almost centered in the tube. The effect of the acceleration due to a change of cross-section in the singularity can be observed as the bubble elongates when passing through the singularity.

Figures 7.4(b) and 7.4(c), present the evolution of a vapor slug head and vapor slug tail respectively. As can be noted in Fig. 7.4(b), the vapor slug head elongates when passing along the singularity due to the effect of the flow acceleration. It is also observed that the vapor slug head recovers its rounded shape after a distance of $3D_2$ of the singularity. Regarding the vapor slug tail behavior, Fig. 7.4(c) shows that when the thickness of the tail is small, the tail detaches from the vapor slug, leaving small bubbles behind it.

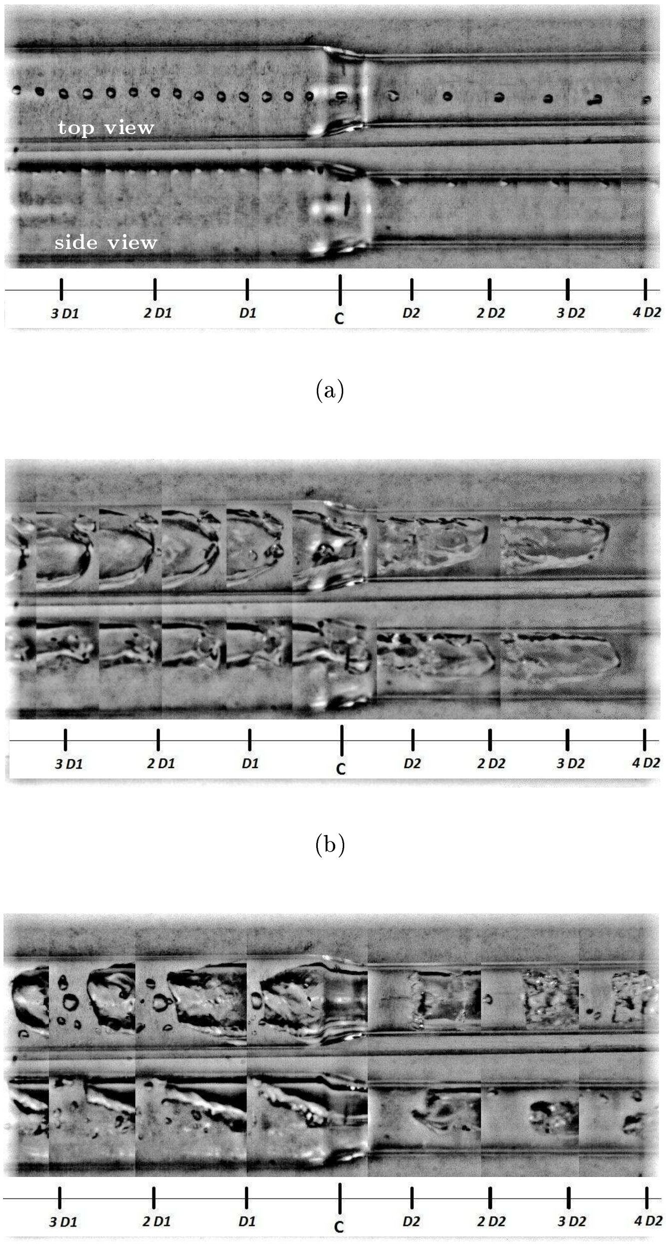

(a)

(b)

(c)

Figure 7.4: Image reconstitution of bubble, slug head and slug tail behaviors and trajectories in an horizontal sudden contraction. Test conditions are $x = 2\%$, $G_1 = 200$ kg·m^{-2}·s^{-1}, $T_{\text{sat}} = 9$ °C, $D_1 = 10.0$ mm and $\sigma_{\text{A}} = 0.49$. (Time lapse 12 ms).

7.2.3 Determination of the perturbation lengths up- and downstream of the sudden contraction

A similar procedure explained in section 6.2.3 has been conducted to determine the perturbation lengths up- and downstream of the sudden contraction (sections a-a' and b-b', see Fig. 7.1). The test section depicted in Fig. 4.8 has been used to measure these lenghts.

The pressure drops presented in this section correspond to the sudden contraction pressure drop ($\Delta p_{\mathrm{c}} = \Delta p_{\mathrm{tot}} - \Delta p_{\mathrm{st,in}} - \Delta p_{\mathrm{st,out}}$).

Figure 7.5 presents the results of the sudden contraction pressure drop measurements for R-134a and R-410A refrigerants at four different pressure tap positions downstream of the singularity.

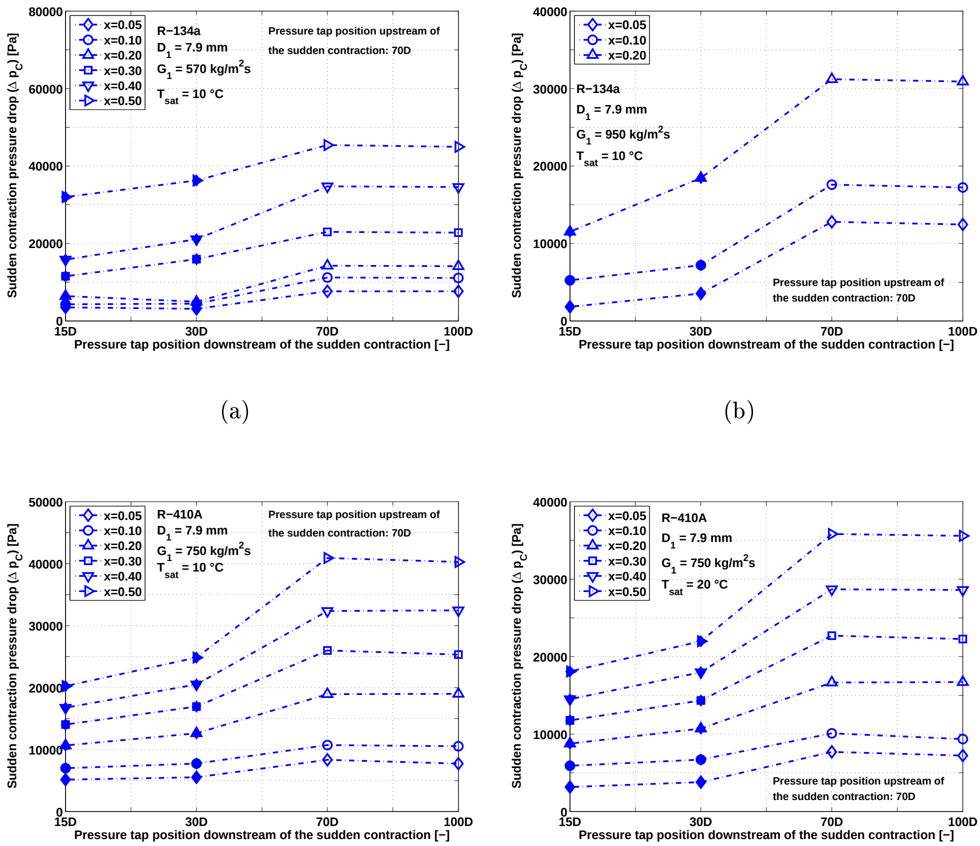

(a) (b)

(c) (d)

Figure 7.5: Sudden contraction pressure drop measured at four different pressure tap positions downstream of the singularity. Filled markers correspond to measurements affected by the perturbation.

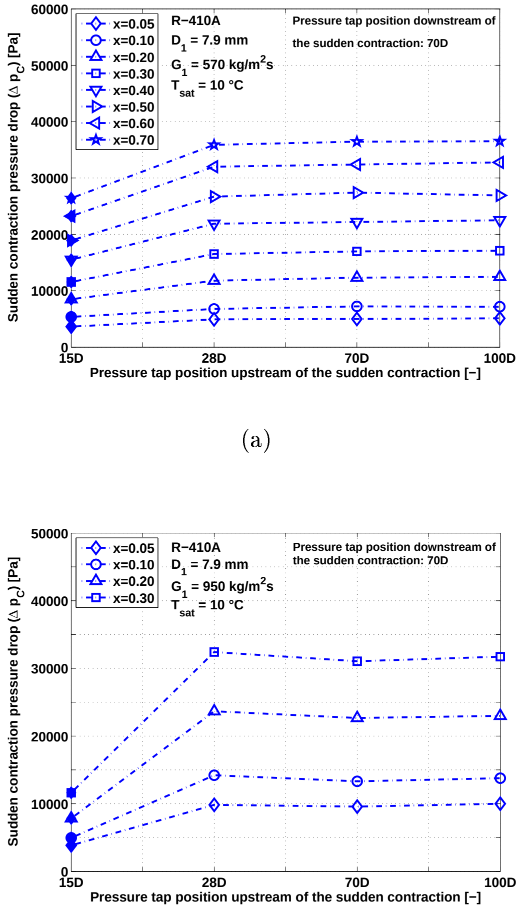

(a)

(b)

Figure 7.6: Sudden contraction pressure drop measured at four different pressure tap positions upstream of the singularity. Filled markers correspond to measurements affected by the perturbation.

Each measurement presented in Figs. 7.5 and 7.6 correspond to a mean of 30 data points measured during about 3 min. To compare the results obtained from one to the other, the Wilcoxon method ([Wilcoxon 1950]) that has been used on the determination of the perturbation lengths in return bends (Section 6.2.3) was used in all experiments for the perturbation lengths determination in sudden contractions. The significance criterion for two independent samples was set at $p = 0.05$.

For both fluids at the experimental conditions showed in this figure, it can be noted that there was no significant difference in the sudden contraction pressure drop as measured with the pressure drop tap located beyond $70D_2$ downstream of the singularity ($p > 0.05$). Nevertheless, there was found a significant difference in the sudden contraction pressure drop between the pressure taps located at $15D_2$ and $30D_2$ ($p < 0.05$), and this difference was found to be increasing with the increase of the vapor quality. Note that the effect of the saturation temperature on the sudden contraction pressure drop is shown in Figs. 7.5(c) and 7.5(d)

Figure 7.6 shows the sudden contraction pressure drop (Δp_c) for R-410A with a mass velocity of $G_1 = 570$ kg·m^{-2}·s^{-1} and $G_1 = 950$ kg·m^{-2}·s^{-1} for various locations of the upstream pressure tap. For these conditions, there was no significant difference in the sudden contraction pressure drop between each pressure tap position above $28D_1$ upstream of the singularity ($p > 0.05$). The results for both mass velocities show that there is a significant difference in the sudden contraction pressure drop ($p < 0.05$) when measuring at the pressure tap located at $15D_1$ upstream of the singularity for all the vapor qualities tested. In Figs. 7.5 and 7.6, the positions affected by the perturbations are represented by a filled marker.

7.2.4 Two-phase pressure drop in sudden contractions

Table 7.1 summarizes the experimental conditions of the sudden contraction pressure drop database presented by [Padilla *et al.* 2012b] database along with the corresponding uncertainties. The 360 experimental tests have been carried out using three different tube diameters (10.85, 7.90 and 5.30 mm), saturation temperatures from 4.4°C to 20.4°C, and over a broad range of vapor quality. The mass velocity (G_1) ranges from 188.71 to 966.14 kg· m^{-2}· s^{-1}. The working fluids are the fourth generation refrigerant HFO-1234yf and the well-known third generation refrigerants R-134a and R-410A.

Table 7.1: Experimental conditions and uncertainties of the present sudden contraction pressure drop database.

Parameters	Range	Uncertainties
Fluids	HFO-1234yf, R-134a and R-410A	
D_1	10.85 and 7.90 mm	±0.6%
D_2	7.90 and 5.30 mm	±0.6%
σ_A	0.53 and 0.45	±0.5%
G_1	188.7 to 966.1 kg m^{-2} s^{-1}	±1.3%
T_{sat}	4.4 - 20.4 °C	±0.1 K
P_{heater}	0 - 10 kW	±1 W
x	0.04 - 0.96	±0.82%
p	4.12 - 13.03 bar	±0.1%
Δp	0 - 190 kPa	±0.1%

Figure 7.7(a) presents the different pressure drop contributions of the sudden contraction pressure drop ($\Delta p_c = \Delta p_m + \Delta p_{pert} + \Delta p_{sing}$) for HFO-1234yf and R-410A at two different conditions. These contributions are: the pressure drop due to the flow acceleration in a geometrical area change (Δp_m) and the singular pressure drop (Δp_{sing}) plus the pressure drops due to perturbation up- and downstream of the singularity ($\Delta p_{pert} = \Delta p_{pert,in} + \Delta p_{pert,out}$).

As can be noted in these figures, the contribution of Δp_m increases with the increase of the vapor quality, while in the contribution of the $\Delta p_{sing} + \Delta p_{pert}$ there is a maximum. This maximum occurs for a vapor quality around 0.65. Figure 7.7(b) presents the results for the R-410A flowing at $G_1 = 200$ kg·m^{-2}·s^{-1}. As can be seen, at a lower mass velocity, the contribution of Δp_m is less than that for $\Delta p_{sing} + \Delta p_{pert}$.

This contribution predominates only at high vapor qualities when the maximum in the

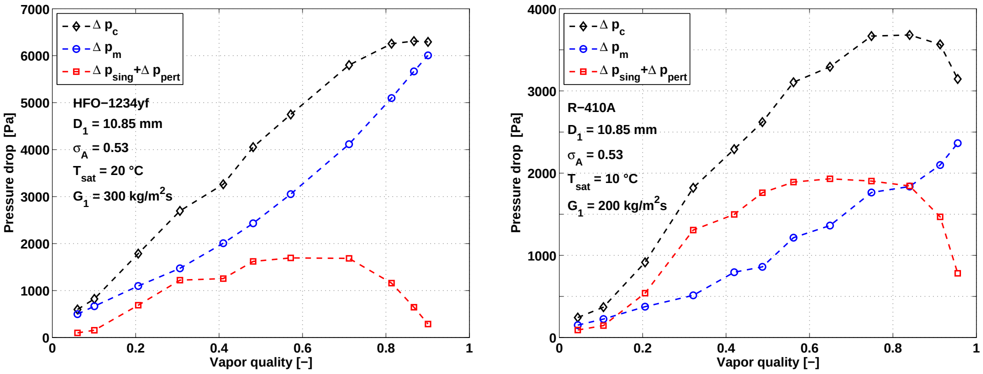

(a) (b)

Figure 7.7: Pressure drop contributions vs. vapor quality.

$\Delta p_{\text{sing}} + \Delta p_{\text{pert}}$ has been reached. Nevertheless, the behavior of the contributions on the sudden contraction pressure drop is very similar for both refrigerants at two different experimental conditions. Figure 7.8 presents a comparison between refrigerants HFO-1234yf, R-410A and R-134a for two different experimental conditions.

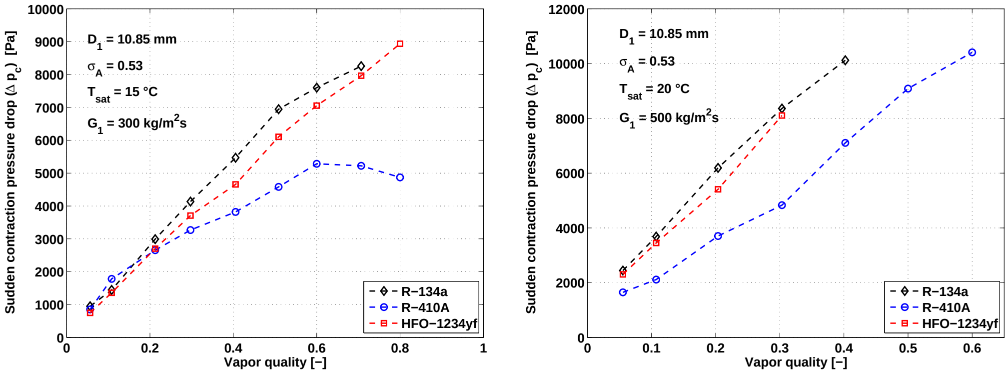

(a) (b)

Figure 7.8: Sudden contraction pressure drop vs. vapor quality for different refrigerants.

Results show that the pressure drop of HFO-1234yf is lower than that of R-134a at high vapor qualities, which is linked to the physical properties of the refrigerants. The maximum pressure drop occurs above 60% of vapor quality. According to the flow pattern map of [Wojtan *et al.* 2005a], this maximum occurs in annular flow regime in the straight tube that constitutes the sudden contraction inlet.

7.2.5 Comparison to prediction methods

The 360 pressure drop (Δp_c) data points measured in two sudden contractions for refrigerants HFO-1234yf, R-410A and R-134a are compared against 6 two-phase pressure drop prediction methods. These prediction methods are those of [Collier & Thome 1994], [Chisholm 1983], [Schmidt & Friedel 1997], [Abdelall *et al.* 2005], [Chen *et al.* 2008a] and [Chen *et al.* 2009]. All these methods allow the calculation of the sudden contraction pressure drop in horizontal orientation.

Figure 7.9 shows the results for experimental pressure drop in the sudden contraction compared to predictions. The results of the comparison are also summarized in Table 7.2.

Table 7.2: Experimental pressure drop data points for HFO-1234yf, R-410A and R-134a refrigerants in sudden contractions compared to different correlations from the literature

	± 30 % error band	MAE	MRE
[Collier & Thome 1994]	2.8 %	49.2 %	-49.2 %
[Chisholm 1983]	1.9 %	111.6 %	111.6 %
[Schmidt & Friedel 1997]	11.9 %	41.0 %	-41.0 %
[Abdelall *et al.* 2005]	54.2 %	28.8 %	-17.0 %
[Chen *et al.* 2008a]	2.8 %	49.5 %	-49.5 %
[Chen *et al.* 2009]	0.0 %	62.0 %	-62.0 %

The best prediction was achieved by the method of [Abdelall *et al.* 2005] with 54% of the data predicted within a ±30% error band. None of the other methods was able to predict the sudden contraction pressure drop with refrigerants as working fluid.

Similarly to the return bend database, the distribution of the parameters of influence in the sudden contraction database are shown in Fig. 7.10. Figures 7.10(a) to 7.10(c) show the data distribution with respect to mass velocity, saturation temperature and vapor quality, respectively.

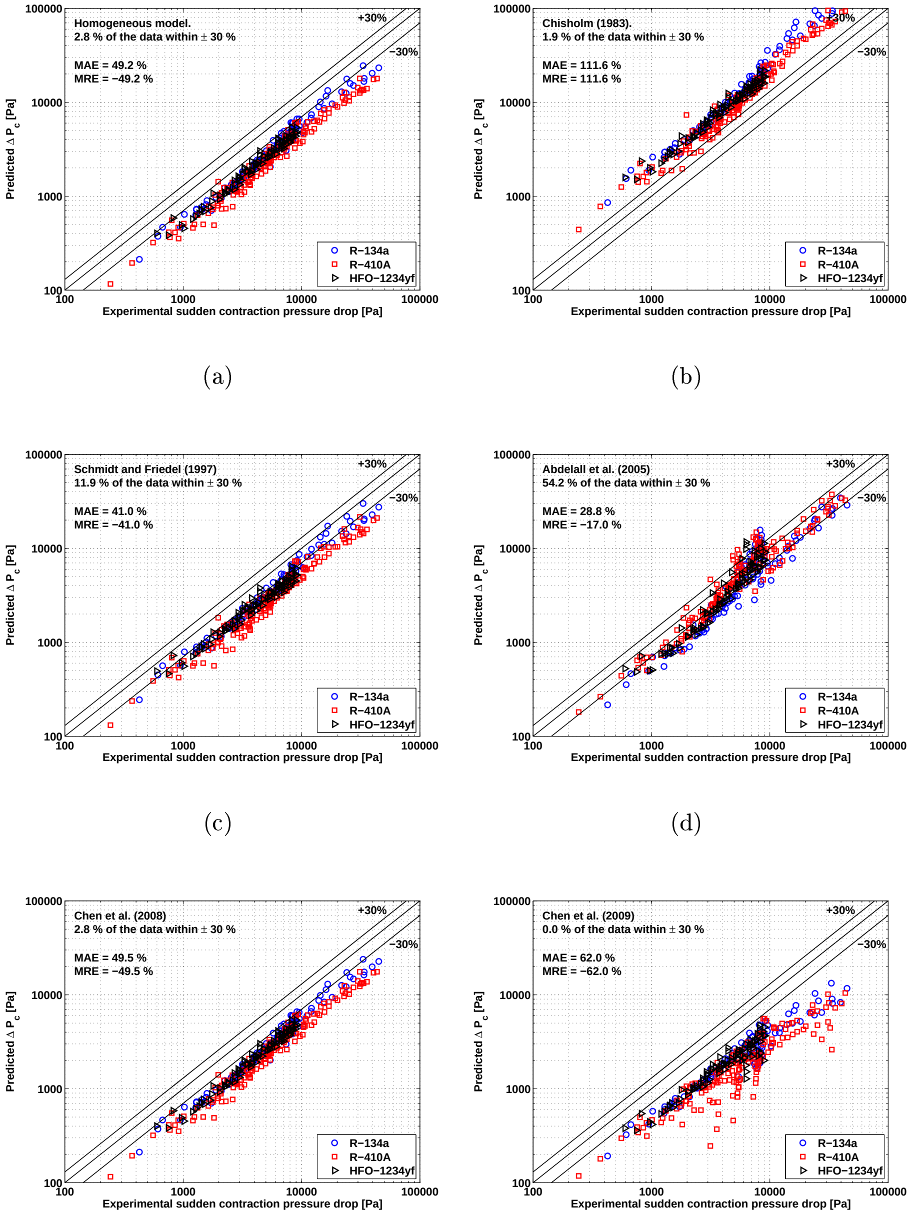

(a) (b)

(c) (d)

(e) (f)

Figure 7.9: Experimental pressure drop data in sudden contractions compared to prediction methods. (360 points)

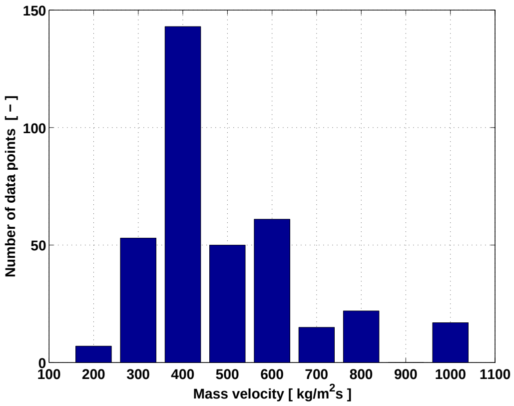

(a) Mass velocity G.

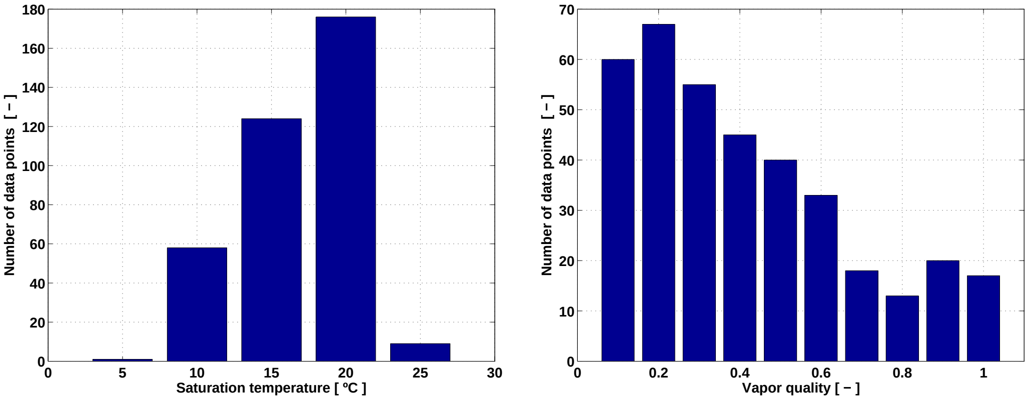

(b) Saturation temperature T_{sat}.

(c) Vapor quality x.

Figure 7.10: Distribution of the database (360 data points for HFO-1234yf, R-134a and R-410A).

7.3 New two-phase pressure drop prediction method in sudden contraction

From the comparison carried out in the previous section, only the method proposed by [Abdelall *et al.* 2005] was able to predict to a certain extend the experimental database for the HFO-1234yf, R-134a and R-410A refrigerants. Based on the observations made in this study, the intention is to develop a new method for predicting the pressure drop in sudden contractions using a different approach from those used in other studies.

7.3.1 Formulation

The pressure drop due to the flow acceleration in a geometrical area change (Δp_{m}) will be calculated using Eq.(7.4) and subtracted from the sudden contraction pressure drop. Only the term ($\Delta p_{\mathrm{sing}} + \Delta p_{\mathrm{pert}}$) will be correlated.

$$\Delta p_{\mathrm{c}} = \Delta p_{\mathrm{sing}} + \Delta p_{\mathrm{m}} + \Delta p_{\mathrm{pert}}$$

and the term Δp_{m}, is calculated as follows:

$$\Delta p_{\mathrm{m}} = \frac{x^2}{\rho_{\mathrm{v}}}\left[\frac{G_2^2}{\varepsilon_2} - \frac{G_1^2}{\varepsilon_1}\right] + \frac{(1-x)^2}{\rho_{\mathrm{l}}}\left[\frac{G_2^2}{(1-\varepsilon_2)} - \frac{G_1^2}{(1-\varepsilon_1)}\right]$$

The void fraction (ε) is calculated using the [Steiner 1993] version of [Rouhani & Axelsson 1970] correlation (Eq. (3.68)), given by:

$$\varepsilon = \frac{x}{\rho_{\mathrm{v}}}\left[(1+0.12(1-x))\left(\frac{x}{\rho_{\mathrm{v}}} + \frac{1-x}{\rho_{\mathrm{l}}}\right) + \frac{1.18(1-x)[g\sigma(\rho_{\mathrm{l}}-\rho_{\mathrm{v}})]^{0.25}}{G\rho_{\mathrm{l}}^{0.5}}\right]^{-1}$$

The new method will predict the effect of the friction resistance due to the singularity (Δp_{sing}) and its perturbation effects up- and downstream (Δp_{pert}). Since this effect is linked to the contribution of both vapor and liquid flows, the following terms for the liquid and the vapor phases are considered:

$$\Delta p_{\mathrm{l}} = \frac{G_2^2(1-x)^2}{\rho_{\mathrm{l}}(1-\varepsilon_2)^2} \tag{7.5}$$

$$\Delta p_{\mathrm{v}} = \frac{G_2^2 x^2}{\rho_{\mathrm{v}}\varepsilon_2^2} \tag{7.6}$$

Two coefficients (K_{l} and K_{v}) are introduced, one for each phase. These coefficients are function of the vapor quality and the passage cross-section area ratio (σ_{A}):

$$K_{\mathrm{l}} = [b(1-x)(1-x^a)](1-\sigma_{\mathrm{A}})^c \tag{7.7}$$

$$K_{\mathrm{v}} = \left[ax^b + bx^a(1-x)\right](1-\sigma_{\mathrm{A}})^c \tag{7.8}$$

where parameters $a = 0.017$, $b = 2$ and $c = 1/4$ have been obtained from the least square method based on the present experimental database. The new prediction method is then given by the following relation:

$$\Delta p_{\mathrm{sing}} + \Delta p_{\mathrm{pert}} = K_{\mathrm{l}}\Delta p_{\mathrm{l}} + K_{\mathrm{v}}\Delta p_{\mathrm{v}} \tag{7.9}$$

Then, the sudden contraction pressure drop can be predicted by:

$$\Delta p_{\mathrm{c}} = [\Delta p_{\mathrm{m}}] + [\Delta p_{\mathrm{sing}} + \Delta p_{\mathrm{pert}}] \tag{7.10}$$

Note that when $x = 0$, Eq. (7.10) becomes:

$$\Delta p_{\mathrm{c,x=0}} = \Delta p_{\mathrm{cl}} = \frac{G_2^2}{\rho_{\mathrm{l}}} \left[(1-\sigma_{\mathrm{A}}^2) + b(1-\sigma_{\mathrm{A}})^c\right] \tag{7.11}$$

For single phase flow, the pressure drop is normally expressed by the loss coefficient K multiplied by the kinetic energy of the flow:

$$\Delta p_{\mathrm{cl}} = \frac{K\rho_{\mathrm{l}} u_{\mathrm{l}}^2}{2} = \frac{KG_2^2}{2\rho_{\mathrm{l}}} \tag{7.12}$$

By comparing Eq. (7.11) with (7.12), the loss coefficient given by the new prediction method can be found as:

$$K_{\mathrm{cl}} = 2\left[(1-\sigma_{\mathrm{A}}^2) + b(1-\sigma_{\mathrm{A}})^c\right] \tag{7.13}$$

Although the loss coefficient for single phase K_{cl} has been obtained from two-phase flow data, the single phase pressure drop predictions obtained using Eq.(7.11) show a good agreement with those presented by [Chisholm 1983] (Eq. 3.88). For instance, for $\sigma_{\mathrm{A}} = 0.4$, $K_{\mathrm{Chisholm}} = 6.7$ and $K_{\mathrm{cl}} = 5.20$.

7.3.2 Predictions of the new method

Figure 7.11 shows a comparison of 360 data points with predictions by the proposed correlation. More than 94% of the data are predicted within a ±30% error band (84 % of the data within a ±20% error band). The mean relative error is 0.7%. The prediction is satisfactory.

Eq. 7.10 presents many advantages:

- It contains only three empirical constants.
- It has been developed based on a large database (360 data points) including the fourth generation HFO-1234yf and the well know third generation R-134a and R-410A refrigerants.
- Based on the visual observations, unlike single-phase flow, a two-phase flow does not contract behind the edge of the transition at least in a range of vapor quality between 4 and 97%. No parameter is therefore included in the new correlation to take into account a would-be *vena-contracta* phenomenon.
- This correlation does not assume a homogeneous flow.
- The physical limits in the new method are correct. Note that when $\sigma_{\mathrm{A}} = 1$, $\Delta p_{\mathrm{c}} = 0$. In addition, when $x = 0$ or $x = 1$, the resulting expressions for pressure drop calculation tend toward the single phase pressure drop in sudden contraction.
- The relation has been developed considering commercial tube diameters from 5.3 to 10.85 mm, σ_{A} from 0.45 to 0.53, a wide range of mass velocities (189 to 966 kg m^{-2} s^{-1}) and the saturation temperatures from 4.4°C to 20.4°C.
- The term $[\Delta p_{\mathrm{m}}]$ represents the contribution to the pressure drop of the flow acceleration effect due to a change of cross-section.

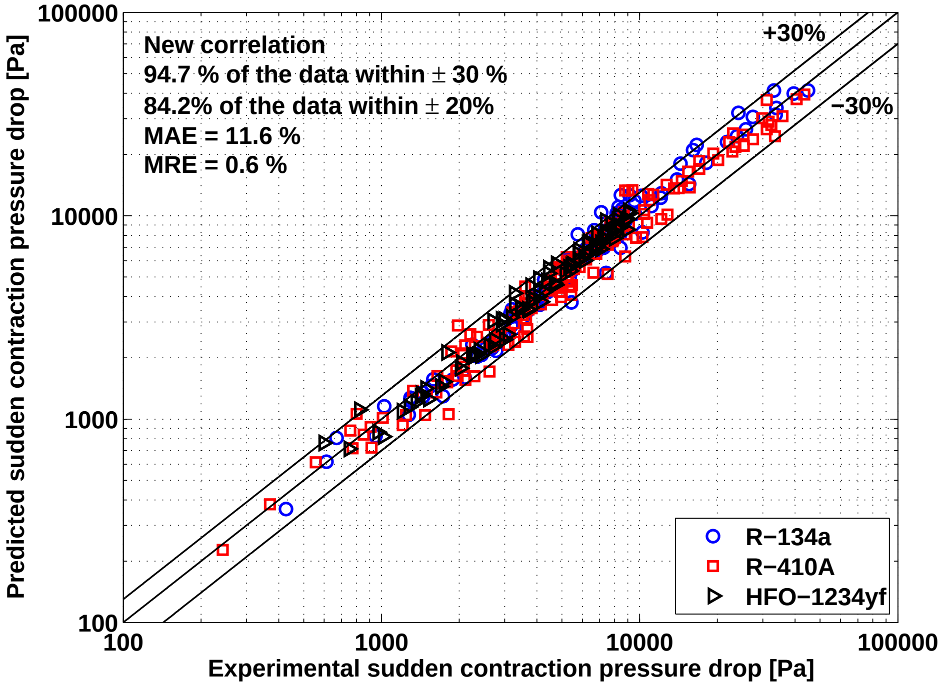

Figure 7.11: Comparison of 360 data points with predictions by the proposed correlation.

- The term $[\Delta p_{\mathrm{sing}} + \Delta p_{\mathrm{pert}}]$ takes into account the contribution of the friction resistance due to the singularity and its perturbation effects up- and downstream on the sudden contraction pressure drop.

Fig. 7.12 presents the pressure drop in sudden contraction as a function of the vapor quality. The experimental data are plotted and compared to different prediction methods from the literature as well as the new prediction method. Note that for each refrigerant, the predictions of the proposed correlation show good agreement with the shape of the experimental pressure drop profile.

Figure 7.13 shows some simulations that have been performed using the proposed equation. Fig. 7.13(a) shows the effect of the mass velocity and saturation temperature on the predicted sudden contraction pressure drop (Δp_{c}). The range of mass velocity and saturation temperature have been voluntarily extrapolated in order to check if any particular behavior might occur. Fig. 7.13(b) presents the effect of σ_{A} on the predicted sudden contraction pressure drop. Note that when σ_{A} increases up to the physical limit $\sigma_{\mathrm{A}} = 1$, $\Delta p_{\mathrm{c}} \Rightarrow 0$.

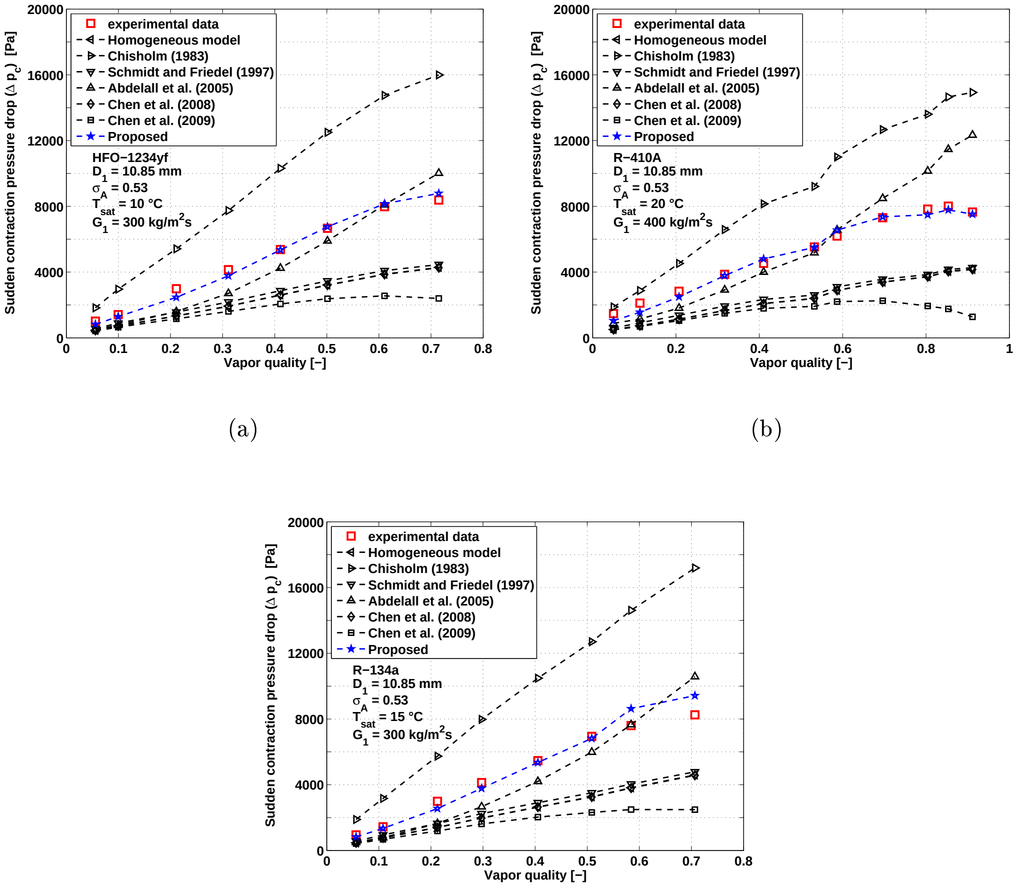

(a) (b)

(c)

Figure 7.12: Pressure drop in sudden contraction as a function of the vapor quality using the experimental data compared to different prediction methods.

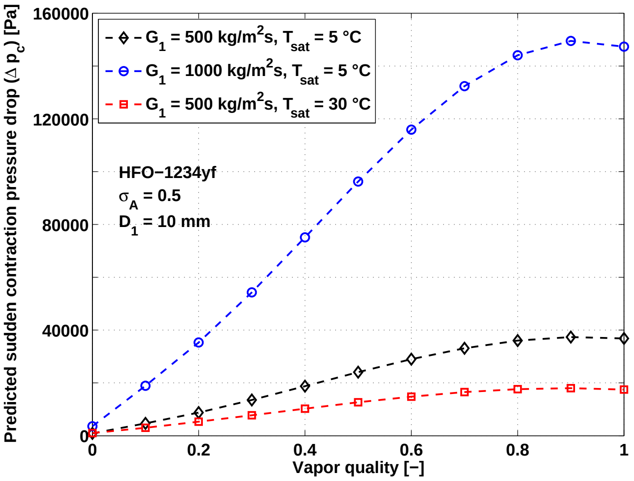

(a)

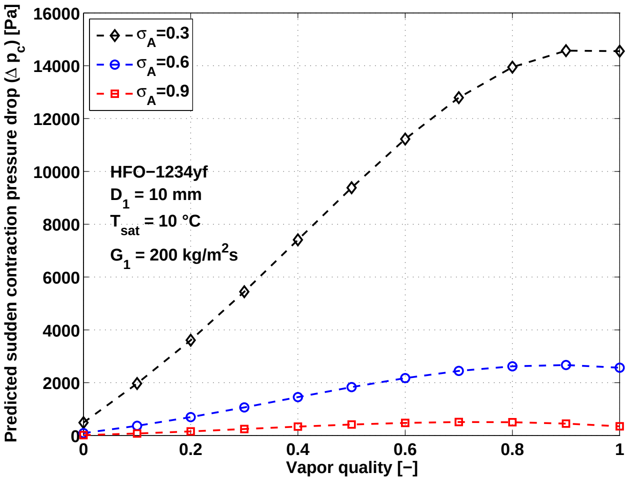

(b)

Figure 7.13: Predicted sudden contraction pressure drop evolution as a function of the vapor quality.

7.4 Chapter conclusions

In this chapter, visualizations of the two-phase flow regimes of R-134a in a 10 mm glass tube including a sudden contraction of cross-section ratio (σ_{A}) equal to 0.49 have been performed with a high-speed high-definition camera. The different flow regimes observed were: slug, intermittent and annular flows. Observations in the contraction section show that the distribution of the phases is influenced by a combination of the acceleration of both phases and the effect of the liquid phase hydraulic jump in the singularity. It was observed that the vapor slug head in the contraction section elongates due to the effect of the flow acceleration. Beyond the contraction section, the vapor slug head recovers its rounded shape after a distance of $3D_2$ of the singularity. From the vapor slug tail visualizations, it was observed that when the thickness of the tail is small, the tail detaches from the vapor slug, leaving small bubbles behind it.

The perturbation lengths up- and downstream of the singularity were experimentally investigated and their contribution to the pressure drop was identified. For two different fluids such as R-134a and R-410A refrigerants, the results obtained show that there is no significant difference for the sudden contraction pressure drop measured above $70D_2$ downstream and above $28D_1$ upstream of the singularity.

360 pressure drop data points measured in horizontal sudden contractions have been presented for the fourth generation HFO-1234yf and third generation R-134a and R-410A refrigerants. The sudden contraction pressure drop was determined by subtracting the inlet and outlet regular pressure drop in straight tube from the total pressure drop. These experimental data have been compared against 6 prediction methods from the literature. Only the method of [Abdelall *et al.* 2005] gives prediction over 50 % of the data predicted within a ± 30 % error band.

Based on the experimental database developed in this PhD work, a new method is proposed for predicting the pressure drop in sudden contractions. This new method represents the sum of the pressure drop due to the flow acceleration in a geometrical area change (Δp_{m}) and the frictional pressure drop due to the singularity and to the perturbation it induces up- and downstream (proposed equation). This relation includes only 3 empirical constants and shows the correct physical limits when $\sigma_{\mathrm{A}} \to 1$, $x = 0$ and $x = 1$. More than 94% of the data are predicted within a ±30% error band. The mean absolute error is around 12% and the mean relative error is 0.7%.

CHAPTER 8

Conclusion

Contents

This chapter concludes the present PhD thesis by giving a brief synthesis of the main results obtained in this experimental investigation on flow boiling of third and fourth generation refrigerants in singularities such as return bends and sudden contractions. Aspects meriting further investigation, as well as recommendations concerning the experimental system will be detailed.

8.1 Synthesis

An extensive review of the existing two-phase flow models to predict pressure drops in singularities such as sudden contractions and return bends showed a general trend that the two-phase pressure drop prediction methods available for air-water mixtures in singularities are not suitable for refrigerants. For these fluids, the prediction methods available give very little information about the physics of the phenomena involved. In general, these methods are still based on numerous empirical constants and do not take into account some important geometrical parameters such as void fraction.

In order to reach the main objectives of this PhD work, the existing flow boiling test facility used by [Branescu 2000] has been successfully modified and adapted to the different test conditions and measurement methods. The present study involved boiling refrigerants that were tested in a wide range of conditions for straight tubes, horizontal and vertical return bends and sudden contractions. These experimental conditions were chosen to obtain experimental values over a wide range of test parameters so that the effect of each parameter may be easily identified. The range of experimental conditions covered were: three refrigerants (third and fourth generation), three internal tube diameters, two return bend curvature ratios, two sudden contraction cross-sectional area ratios, more than ten mass velocities over a large range of vapor quality. The campaign led to acquire 884 experimental two-phase pressure drop values for straight tubes, 802 data points for horizontal return bends, 285 data points for vertical return bends and 360 data points for sudden contractions, covering a wide range of experimental conditions and four flow regimes.

8.2 Concluding remarks

The analysis of the results obtained leads to the following conclusions, classified according to the objectives of the thesis announced in Section 1.3:

8.2.1 Two-phase flow visualization

- Two-phase flow regime visualizations of refrigerants have been carried out with a high-speed high-definition camera. The different flow regimes observed were: slug, intermittent and annular flows. For straight tubes and also for sudden contraction, a mirror has been placed in order to simultaneously investigate both top and side views. For return bends, visualizations have been carried out for horizontal and vertical downward flow orientation. The general conclusion is that no major difference was observed between the refrigerants studied for the experimental conditions considered. In addition, it was found that the [Wojtan *et al.* 2005a] flow pattern map was able to satisfactorily predict the HFO-1234yf flow regimes.

- Observations in the curved section of the vertical return bend showed that the distribution of the phases is influenced by a combination of the gravity and the centrifugal forces. In this sense, the dynamical behavior of a bubble and a vapor slug in vertical downward flow return bend was reported. An analysis of the forces acting on the bubbles has been proposed. This model allows to better understand the different forces acting on the vapor phase. The detachment is mainly controlled by the apparent buoyancy and hydrodynamic lift. The re-attachment is controlled by the apparent buoyancy and the radial component of buoyancy due to gravity. In general, the secondary flow in the liquid phase influences the trajectory of the small bubbles while it is probably negligible in the case of vapor slugs.

- Two-phase flow regime visualizations of R-134a in a sudden contraction showed that the distribution of the phases was influenced by a combination of the acceleration of both phases and the effect of the hydraulic jump of the liquid phase in the singularity. The side view revealed the effect of buoyancy on the bubble which slides from the horizontal inlet tube attached to the top side wall of the tube. The top view showed the bubble trajectory almost centered in the tube. The effect of the acceleration due to a change of cross-section across the singularity can be observed as the bubble elongates when passing along the singularity. The evolution of the vapor slug head and vapor slug tail have been discussed. As a concluding remark, the vapor slug head elongates when passing along the singularity due to the effect of the flow acceleration given by the area change. Regarding the vapor slug tail behavior, for smaller thickness of the tail, the tail detaches from the vapor slug, leaving small bubbles.

8.2.2 Effects of the perturbation length on the two-phase pressure drop

The perturbation lengths up- and downstream of the singularities were specifically studied. For return bends, in both horizontal and vertical cases, it is noted that there is no significant difference in the return bend pressure drop above $20D$ downstream of the return bend. Concerning the perturbation length upstream of the return bend, in both cases (horizontal and vertical) there was found a significant difference in the return bend pressure drop between the pressure taps located at $5D$ and $10D$.

The results obtained for the sudden contraction show that there is no significant difference for the sudden contraction pressure drop measured above $70D_2$ downstream and above $28D_1$ upstream of the singularity. These lengths have been considered in the design of the test sections for pressure drop measurements.

8.2.3 Development of prediction tools from an original experimental database

The third objective of this PhD work was to develop a pressure drop database for third and fourth generation refrigerants which allowed to develop reliable pressure drop predictive methods for singularities. Based on the previous visualizations and perturbation lengths studies, two-phase pressure drops in straight tubes, return bends and sudden contraction have been measured. This experimental database allowed to better understand the physics involved in the refrigerant flow boiling, especially the effect of mass velocity, saturation temperature, inner diameter, return bend curvature ratio, orientation, sudden contraction cross-section ratio and fluid properties (density, viscosity, etc).

Based on the experimental database and flow regime visualizations developed in this PhD work, two new prediction methods were proposed for predicting the pressure drop in return bends and in sudden contractions, respectively. These new methods represent the sum of each contribution of the pressure drop. In this sense, two diagrams which represent the idealized pressure drop profile showing the contributions of the effects considered to develop the new prediction methods have been introduced for both return bends and sudden contraction.

The new methods developed for predicting two phase pressure drop in singularities include few empirical constants and show the correct physical limits. The predictions given by these new methods on their respective database were generally satisfactory.

8.3 Perspectives

As some of the aspects of this work are new and complex, further research definitely needs to be carried out. Although the new prediction methods developed in this PhD thesis show good agreement to the present experimental database, future work should extend comparison of these new models to other refrigerants and databases. Specific areas that should be given priority for future works are suggested below:

- The bubble detachment mechanism in vertical return bends are not completely assessed yet. In addition, the interaction between adjacent bubbles should be studied in future work. Specific experiments devoted to that subject should be performed.
- The two-phase prediction methods developed in this work are able to successfully predict the present experimental data. However, some of the geometric parameters of the singularities such as the straight tube orientation, the return bend curvature ratio ($2R/D$) and the sudden contraction cross-sectional area ratio (σ_A) in this database are limited. In order to further study the effect of these parameters on the pressure drop, is highly recommended to extend the existing database including a wider range of these parameters.
- Finally, based on the simultaneous visualizations in straight tubes, a new technique for measuring void fraction is in development ([Wallet *et al.* 2012]). This method gives good agreement when compared with predictions given by methods of the literature. Further investigation in this area is needed to develop a reliable method

for measuring void fraction along the singularities that allows to improve the new two-phase pressure drop prediction methods being developed for singularities such as return bends and sudden contractions.

Appendix A
Nomenclature

A	cross-section area	(m^2)
a	correlation parameter	
b, B	correlation parameter	
C	correlation parameter	
c	specific heat capacity	(J·K^{-1})
C_o	distribution parameter	
D	tube diameter	(m)
E	internal energy	(J)
e	internal energy per unit of mass	(J·kg^{-1})
F	force	(N)
f	friction factor	
G	mass velocity	(kg·m^{-2}·s^{-1})
g	gravity acceleration	(m·s^{-2})
H	vertical height	(m)
h	enthalpy	(J·kg^{-1})
J	superficial velocity	(m·s^{-1})
K	correlation parameter	
L	length	(m)
M	Correlation parameter	
$\dot{m}$	mass flow rate	(kg·s^{-1})
MAE	Mean absolute error	(%)
	$\text{MAE}=\frac{1}{N}\sum_1^N \left\lvert\frac{\text{predicted value}-\text{experimental value}}{\text{experimental value}}\right\rvert \times 100$	
MRE	Mean relative error	(%)
	$\text{MRE}=\frac{1}{N}\sum_1^N \left(\frac{\text{predicted value}-\text{experimental value}}{\text{experimental value}}\right) \times 100$	
P	perimeter	(m)
P	electrical power	(kW)
p	Wilcoxon p-value	
p	pressure	(Pa)
$\dot{Q}$	volumetric flow rate	(m^3·s^{-1})
Q	heat transfered	(J·m^{-1})
q	heat per unit of length	(W·m^{-1})
R	curvature radius	(m)
R	experimental result	
S	velocity ratio	
S	interfacial shear force	(N)
u	actual velocity	(m·s^{-1})
X	experimental variable	
x	vapor quality	
Y	correlation parameter	
V	weighted mean drift flux velocity	(m·s^{-1})

Abbreviations

ASHRAE	american society of heating, refrigeration and air conditioning engineers
CFC	chlorefluorocarbon
COP	coefficient of performance

CVC&R	chauffage, ventilation, climatisation et réfrigération
GWP	global warming potential
HCFC	hydrochlorefluorocarbon
HFO	hydrofluoroolefin
HFC	hydrofluorocarbon
HVAC&R	heating, ventilation, air conditioning and refrigeration
ODP	ozone depletion potential
TC	thermo-couple
VI	virtual instrument

Dimensionless numbers

Bo	Bond number
Fr	Froude number
Re	Reynolds number
We	Weber number
X	Martinelli parameter

Greeks

α	correlation parameter	
ε	cross-sectional void fraction	
γ	correlation parameter	
Γ	mass transfer	$(\mathrm{kg{\cdot}m^{-1}{\cdot}s^{-1}})$
λ	data predicted within error bands	
μ	dynamic viscosity	$(\mathrm{Pa{\cdot}s})$
Ω	correlation parameter	
Φ	two-phase multiplier	
ϕ	heat flux	$(\mathrm{W{\cdot}m^{-2}})$
$\dot{\phi}$	specific rate of internal heat generation	$(\mathrm{W{\cdot}m^{-3}})$
Ψ	curvature multiplier	
ρ	density	$(\mathrm{kg{\cdot}m^{-3}})$
σ	surface tension	$(\mathrm{N{\cdot}m^{-1}})$
σ_{A}	sudden contraction cross-sectional area ratio	
θ	inclination angle	(rad)

Sub and superscripts

a	acceleration
annular	annular flow
c	contraction
crit	critic
curv	curvature
dryout	dryout flow pattern
eq	equivalent
f	frictional
F	Friedel parameter
F	friction
h	homogeneous
heater	electrical heater
in	inlet
iD	interface peripheral fraction
l	liquid
lD	liquid cross-sectional fraction
lo	liquid only

Ltt	liquid turbulent, turbulent
m	momentum
M	maximum
mist	mist flow pattern
mix	mixture
o	turning of the flow
out	outlet
p	constant pressure
pert	perturbation
rb	return bend
sat	saturation
sing	singular
sp	single-phase
st	straight tube
static	static head
strat	stratified flow pattern
tot	total
tp	two-phase
Vtt	vapor turbulent, turbulent
v	vapor
vD	vapor cross-sectional fraction
vj	weighted mean drift flux velocity indexes
w	wall
wavy	stratified-wavy flow pattern
x	constant vapor quality
z	orientation

Appendix B

Single-phase energy balance

Energy balance

In order to validate the Joule heating in the electrical heater as well as the insulation around it, and single-phase energy balance test has been carried out with R-410A.

Energy Q_{in} supplied by the electrical heater

The electrical power supplied by Joule effect by the refrigerant electrical heater is:

$$Q_{\text{in}} = UI \tag{B.1}$$

The uncertainty related to Q_{in} is given by the following equation:

$$\Delta Q_{\text{in}} = Q_{\text{in}} \left(\frac{\Delta U}{U} + \frac{\Delta I}{I} \right) \tag{B.2}$$

The power supplied Q_{in} is directed measured by the HIOKI 3193 POWER HiTESTER described in Chapter 4. The accuracy given by the manufacturer is ±0.001 kW.

Sensible energy inside the liquid Q_{out}

The energy acquired by the liquid is given by the increase of the liquid enthalpy:

$$Q_{\text{out}} = \dot{m} \left(h_{\text{l,out}} - h_{\text{l,in}} \right) \tag{B.3}$$

The corresponding absolute error is thus:

$$\Delta Q_{\text{out}} = Q_{\text{out}} \left(\frac{\Delta h_{\text{l,out}} + \Delta h_{\text{l,in}}}{h_{\text{l,out}} - h_{\text{l,in}}} + \frac{\Delta \dot{m}}{\dot{m}} \right) \tag{B.4}$$

Energy balance $Q_{\text{in,out}}$

The energy balance is defined by:

$$Q_{\text{in,out}} = Q_{\text{in}} - Q_{\text{out}} \tag{B.5}$$

The uncertainty is :

$$\Delta Q_{\text{in,out}} = \Delta Q_{\text{in}} + \Delta Q_{\text{out}} \tag{B.6}$$

APPENDIX C

Refrigerant properties

Fluid properties

This appendix provides information about physical properties of refrigerants R-134a, R-410A and HFO-1234yf such as saturation temperature (T_{sat}), enthalpy (h), density (ρ), viscosity (μ) and surface tension (σ). These properties have been obtained from the NIST thermodynamic properties of refrigerants and refrigerant mixtures database [McLinden *et al.* 2007]. The thermodynamic property tables of the refrigerant HFO-1234yf have been generated using the REFPROP software with the last updated properties library.

Table C.1: Physical properties of refrigerant R-134a.

T_{sat} (°C)	ρ_{l} (kg· m^{-3})	ρ_{v} (kg· m^{-3})	μ_{l} (Pa· s)	μ_{v} (Pa· s)	h_{l} (J·kg^{-1})	h_{v} (J·kg^{-1})	σ (N·m^{-1})
4	1281.5	16.6	0.000258	0.0000109	205397.8	400917.1	0.01099
5	1278.1	17.1	0.000254	0.0000109	206753.5	401490.5	0.01084
6	1274.8	17.7	0.000251	0.0000110	208112.2	402061.5	0.01070
7	1271.4	18.3	0.000248	0.0000110	209473.8	402629.9	0.01056
8	1268.0	18.9	0.000245	0.0000111	210838.4	403195.7	0.01042
9	1264.5	19.6	0.000242	0.0000111	212206.0	403758.7	0.01028
10	1261.1	20.2	0.000239	0.0000111	213576.7	404319.0	0.01014
11	1257.6	20.9	0.000236	0.0000112	214950.6	404876.4	0.01000
12	1254.1	21.6	0.000233	0.0000112	216327.7	405430.8	0.00986
13	1250.6	22.3	0.000230	0.0000113	217708.1	405982.2	0.00972
14	1247.1	23.0	0.000227	0.0000113	219091.8	406530.5	0.00958
15	1243.5	23.7	0.000224	0.0000114	220478.8	407075.6	0.00944
16	1240.0	24.5	0.000221	0.0000114	221869.3	407617.4	0.00930
17	1236.4	25.3	0.000219	0.0000114	223263.2	408155.9	0.00917
18	1232.8	26.1	0.000216	0.0000115	224660.6	408691.0	0.00903
19	1229.1	26.9	0.000213	0.0000115	226061.7	409222.6	0.00889
20	1225.5	27.8	0.000211	0.0000116	227466.3	409750.6	0.00876
21	1221.8	28.6	0.000208	0.0000116	228874.7	410274.9	0.00862
22	1218.1	29.5	0.000205	0.0000117	230286.7	410795.5	0.00848
23	1214.4	30.4	0.000203	0.0000117	231702.6	411312.2	0.00835
24	1210.6	31.4	0.000200	0.0000118	233122.3	411825.1	0.00822
25	1206.8	32.4	0.000198	0.0000118	234545.9	412334.0	0.00808

Table C.2: Physical properties of refrigerant R-410A.

T_{sat} (°C)	ρ_l (kg· m^{-3})	ρ_v (kg· m^{-3})	μ_l (Pa· s)	μ_v (Pa· s)	h_l (J·kg^{-1})	h_v (J·kg^{-1})	σ (N·m^{-1})
4	1153.6	34.7	0.000161	0.0000129	206118.0	422467.0	0.00839
5	1149.5	35.8	0.000159	0.0000130	207658.1	422741.9	0.00823
6	1145.3	36.9	0.000157	0.0000130	209203.6	423009.1	0.00808
7	1141.1	38.1	0.000155	0.0000131	210754.8	423268.2	0.00793
8	1136.9	39.3	0.000153	0.0000132	212311.7	423519.0	0.00777
9	1132.6	40.5	0.000151	0.0000132	213874.5	423761.3	0.00762
10	1128.3	41.7	0.000149	0.0000133	215443.4	423994.8	0.00747
11	1124.0	43.0	0.000147	0.0000134	217018.7	424219.1	0.00732
12	1119.6	44.4	0.000145	0.0000134	218600.3	424434.0	0.00717
13	1115.2	45.7	0.000143	0.0000135	220188.7	424639.3	0.00702
14	1110.8	47.1	0.000141	0.0000136	221783.9	424834.4	0.00687
15	1106.3	48.6	0.000139	0.0000137	223386.1	425019.3	0.00672
16	1101.7	50.1	0.000137	0.0000137	224995.5	425193.5	0.00657
17	1097.1	51.6	0.000135	0.0000138	226612.4	425356.7	0.00642
18	1092.5	53.2	0.000134	0.0000139	228236.9	425508.5	0.00628
19	1087.8	54.9	0.000132	0.0000140	229869.3	425648.6	0.00613
20	1083.1	56.5	0.000130	0.0000141	231509.7	425776.7	0.00599
21	1078.4	58.3	0.000128	0.0000141	233158.4	425892.4	0.00584
22	1073.5	60.1	0.000126	0.0000142	234815.7	425995.2	0.00570
23	1068.6	61.9	0.000125	0.0000143	236481.7	426084.9	0.00555
24	1063.7	63.8	0.000123	0.0000144	238156.6	426161.0	0.00541
25	1058.7	65.8	0.000121	0.0000145	239840.8	426223.1	0.00527

Table C.3: Physical properties of refrigerant HFO-1234yf.

T_{sat} (°C)	ρ_l (kg· m^{-3})	ρ_v (kg· m^{-3})	μ_l (Pa· s)	μ_v (Pa· s)	h_l (J·kg^{-1})	h_v (J·kg^{-1})	σ (N·m^{-1})
4	1163.5	20.1	0.000199	0.0000120	202707.2	42139.0	0.00881
5	1160.3	20.8	0.000197	0.0000120	203355.8	43451.6	0.00868
6	1157.0	21.4	0.000195	0.0000120	204002.5	44767.8	0.00856
7	1153.8	22.1	0.000192	0.0000120	204647.4	46087.7	0.00843
8	1150.5	22.8	0.000190	0.0000120	205290.2	47411.4	0.00831
9	1147.2	23.5	0.000188	0.0000120	205930.9	48738.8	0.00818
10	1143.9	24.3	0.000186	0.0000120	206569.4	50070.0	0.00806
11	1140.6	25.0	0.000183	0.0000120	207205.7	51405.1	0.00793
12	1137.3	25.8	0.000181	0.0000120	207839.8	52744.0	0.00781
13	1133.9	26.6	0.000179	0.0000120	208471.4	54086.8	0.00768
14	1130.5	27.4	0.000177	0.0000120	209100.5	55433.6	0.00756
15	1127.1	28.3	0.000175	0.0000120	209727.0	56784.3	0.00743
16	1123.7	29.1	0.000173	0.0000120	210351.0	58139.1	0.00731
17	1120.2	30.0	0.000171	0.0000120	210972.1	59498.0	0.00718
18	1116.8	30.9	0.000169	0.0000120	211590.5	60861.0	0.00706
19	1113.3	31.8	0.000167	0.0000120	212206.0	62228.1	0.00693
20	1109.8	32.8	0.000165	0.0000120	212818.4	63599.5	0.00681
21	1106.3	33.8	0.000163	0.0000120	213427.7	64975.1	0.00669
22	1102.7	34.8	0.000161	0.0000120	214033.9	66355.0	0.00656
23	1099.2	35.8	0.000159	0.0000120	214636.8	67739.2	0.00644
24	1095.6	36.8	0.000157	0.0000120	215236.2	69127.8	0.00632
25	1092.0	37.9	0.000155	0.0000120	215832.2	70520.9	0.00619

Appendix D

List of Publications

Articles summited to peer reviewed journals

- M. Padilla, R. Revellin and J. Bonjour. *Prediction and simulation of two-phase pressure drop in return bends.* Int. J. Refrig., vol. 32, pages 1776–1783, 2009.
- M. Padilla, R. Revellin, P. Haberschill, A. Bensafi and J. Bonjour.*Flow regimes and two-phase pressure gradient in horizontal straight tubes: Experimental results for* HFO-*1234*yf, R-*134*a *and* R-*410*A. Exp. Thermal Fluid Sci., vol. 35, pages 1113–1126, 2011.
- M. Padilla, R. Revellin, P. Haberschill and J. Bonjour.*Two-phase pressure drop in return bends: Experimental results for* R*410*A. Int. J. Refrig., vol. doi:10.1016/j.ijrefrig.2011.03.009, 2011.
- M. Padilla, R. Revellin and J. Bonjour. *Flow regime visualization and pressure drops of* HFO-*1234*yf, R-*134*a *and* R-*410*A *during downward two-phase flow in vertical return bends.* Exp. Thermal Fluid Sci., 2012. In review.
- M. Padilla, R. Revellin and J. Bonjour. *Two-phase flow visualization and pressure drop measurements of* HFO-*1234*yf *and* R-*134*a *refrigerants in horizontal return bends.* Exp. Thermal Fluid Sci., 2012. In review.
- J. Wallet, M. Padilla, J. Bonjour and R. Revellin. *Two-phase flow of* HFO-*1234yf,* R-*134a and* R-*410*A *in sudden contractions Part* I*: Visualisation and void fraction measurements.* Int. J. Heat Fluid Flow, 2012. In review.
- M. Padilla, R. Revellin and J. Bonjour. *Two-phase flow of* HFO-*1234yf,* R-*134a and* R-*410*A *in sudden contractions Part* II*: pressure drop measurements and new prediction method.* Int. J. Heat Fluid Flow, 2012. In review.

Communications

- Padilla M, Revellin R., Haberschill F., Bonjour J. (2011). *Experimental results for* HFO-*1234yf visualization and two-phase pressure gradient in horizontal straight tubes.* The 23rd IIR International Congress of Refrigeration august 21-26 2011. Prague, Czech Republic.
- Padilla M, Revellin R., Haberschill F., Bonjour J. (2011). *Visualization and two-phase pressure gradient in return bends: experimental results for* HFO-1234yf. The 23rd IIR International Congress of Refrigeration august 21-26 2011. Prague, Czech Republic. Keynote presentation.
- Revellin R., Padilla M, Bonjour J. (2011). *Two-phase flow patterns, visualization and pressure drop in return bends: experimental results for* R-134a, R-410A and HFO-1234yf. 49th European Two-Phase Flow Group Meeting 2011. 29th May-2nd June 2011, Tel-Aviv, Israel.

- Padilla M, Revellin R., Bonjour J. (2011). *Etude expérimentale des écoulements diphasiques liquide-vapeur intra-tubulaires : Résultats pour le* HFO-1234yf. Journée des doctorants, 02/03/2010. CETHIL. Lyon. France.
- Padilla M, Revellin R., Bonjour J. (2010). *Experimental investigation of two-phase pressure gradient in return bends.* 2nd IIR Workshop on Refrigerant Charge Reduction, 14-18/06/2010. Stockholm. Suede.
- Revellin R., Padilla M, Bonjour J. (2010). *New prediction method for two-phase pressure drop in return bends.* ARCUS Workshop 2010, 08-12/02/2010. Sâo Carlos. Brazil.
- Padilla M, Revellin R., Bonjour J. (2010). *Détermination des caractéristiques thermo-hydrauliques des fluides frigorigènes sous forme diphasique dans des singularités.* Journée des doctorants, 02/03/2010. CETHIL. Lyon. France.
- Padilla M, Revellin R., Bonjour J. (2010). *Développement d'outils de prédiction pour la détermination de la chute de pression de fluides frigorigènes sous forme diphasique dans des tubes en U.* Journée Diphasique et Changement de Phase, Société Française de Thermique, 26/01/2010, CEA - Grenoble. France.
- Padilla M, Revellin R., Bonjour J. (2009). *Développement d'outils de prédiction pour la détermination des caractéristiques thermiques et hydrauliques de fluides frigorigènes en ébullition convective pour des géométries non conventionnelles.* Journée des doctorants. 09/02/2009. CETHIL. Lyon. France.

List of references

[Abdelall *et al.* 2005] E.F. Abdelall, G. Hahm, S.M. Ghiaasiaan, S.I. Abdel-Khalik, S.S. Jeter, M. Yoda and D.L. Sadowski. *Pressure drop caused by abrupt flow area changes in small channels.* Exp. Thermal Fluid Sci., vol. 29, pages 425–434, 2005. (Cited on pages 52, 55, 136, 139 and 144.)

[Al'Ferov & Shul'Zhenko 1977] N.S. Al'Ferov and Y.N. Shul'Zhenko. *Pressure drops in two-phase flows through local resistances.* Fluid Mech-Sov., vol. 6, pages 20–33, 1977. (Cited on page 54.)

[ASHRAE 2001] ASHRAE. Ashrae handbook, fundamentals. American Society of Heating, Refrigeration and Air-Conditioning Engineers, 2001. (Cited on pages ix and 22.)

[Attou & Bolle 1995] A. Attou and L. Bolle. *Evaluation of the two-phase pressure loss across singularities.* ASME FED, vol. 210, pages 121–127, 1995. (Cited on page 54.)

[Auton *et al.* 1988] T.R. Auton, J.C.R. Hunt and M. Prud'homme. *The force exerted on a body in inviscid unsteady non-uniform rotational flow.* J. Fluid Mech., vol. 197, pages 241–257, 1988. (Cited on page 45.)

[Baker 1954] O. Baker. *Design of pipelines for simultaneous flow of oil and gas.* Oil and Gas, vol. 53, pages 185–190, 1954. (Cited on page 25.)

[Bandarra Filho *et al.* 2004] E. P. Bandarra Filho, J. M. Saiz Jabardo and P. E. L. Barbieri. *Convective boiling pressure drop of refrigerant* R-134a *in horizontal smooth and microfin tubes.* Int. J. Refrig., vol. 27, pages 895–903, 2004. (Cited on page 31.)

[Bandel. 1973] J. Bandel. *Druckverlust und Wärmeügang bei der Verdampfung siedender Kältemittel im durchströmten waagerechten Rohr.* PhD thesis, University of Karlsruhe, 1973. (Cited on page 38.)

[Bankoff 1960] S. G. Bankoff. *A variable density single-fluid model for two-phase flow with particular reference to steam-water.* Int. J. Heat Mass Transfer, vol. 2, pages 265–272, 1960. (Cited on pages 34 and 91.)

[Baroczy 1965] C. J. Baroczy. *A systematic correlation for two-phase pressure drop.* Chem. Eng. Prog. Symp. Ser., vol. 62(44), pages 232–249, 1965. (Cited on page 35.)

[Batchelor 1967] G.K Batchelor. *An introduction to fluid dynamics.* Cambridge University Press, Cambridge, 1967. (Cited on page 108.)

[Bergles & Rohsenow 1964] A.E. Bergles and W.M. Rohsenow. *The determination of forced convection surface-boiling heat transfer.* ASME Journal of Heat Transfer, vol. 86(August), page 365, 1964. (Cited on page 22.)

[Bouré 1978] J. A. Bouré. Two-phase flows and heat transfer with application to nuclear design problems. Hemisphere, New York, 1978. (Cited on page 10.)

[Branescu 2000] C. Branescu. *Ebullition en convection forcée du R22 et du R407C a l'interieur de tubes horizontaux lisse et micro-ailetes.* PhD thesis, L'Institut National des Sciences Appliquées de Lyon, 2000. (Cited on pages 4, 59, 79 and 145.)

[Chaddock & Noerager 1966] J.B. Chaddock and J.A. Noerager. *Evaporation of Refrigerant 12 in a horizontal tube with constant wall heat flux.* ASHRAE Transactions, vol. 72(1), page 90, 1966. (Cited on page 23.)

[Chalfi & Ghiaasiaan 2008] T.Y. Chalfi and S.M. Ghiaasiaan. *Pressure drop caused by flow area changes in capillaries under low flow conditions.* Int. J. Multiphase Flow, vol. 34, pages 2–12, 2008. (Cited on page 55.)

[Charnay *et al.* 2011] R. Charnay, R. Revellin and J. Bonjour. *Review on two-phase pressure drop and heat transfer coefficient during flow boiling of natural and synthetic refrigerants: a parametric analysis (Keynote lecture).* In The 23rd IIR International Congress of Refrigeration, Prague, Czech Republic, 2011. (Cited on pages ix, 3, 29 and 30.)

[Chawla 1967] J. M. Chawla. *Warmeübergang und* D*ruckabfall in waagerechten* R*ohren bei der* S*tromung von verdampfenden* K*ältemitteln.* VDI-Forschungshelf, vol. 523, 1967. (Cited on pages 35 and 91.)

[Chen *et al.* 2002] I. Y. Chen, C.C. Yang and C.C. Wang. *Influence of horizontal return bend on the two-phase flow pattern in a 6.9 mm diameter tube.* Can. J. Chem. Eng., vol. 80(3), pages 478–484, 2002. (Cited on page 44.)

[Chen *et al.* 2004] I. Y. Chen, C.-C. Wang and S. Y. Lin. *Measurements and correlations of frictional single-phase and two-phase pressure drops of* R*-410*A *flow in small* U*-type return bends.* Exp. Thermal Fluid Sci., vol. 47, pages 2241–2249, 2004. (Cited on pages xiii, 43, 47, 48, 49, 50, 52, 114 and 118.)

[Chen *et al.* 2005] I. Y. Chen, C.L. Won and C.C. Wang. *Influence of oil on* R*-410A two-phase frictional pressure drop in a small* U*-type wavy tube.* International Communications in Heat and Mass Transfer, vol. 32, pages 797–808, 2005. (Cited on page 122.)

[Chen *et al.* 2007a] I. Y. Chen, Y.-S. Wu, Y.-J. Chang and C.-C. Wang. *Two-phase frictional pressure drop of* R*-134a and* R*-410*A *refrigerant-oil mixtures in straight tubes and* U*-type wavy tubes.* Exp. Thermal Fluid Sci., vol. 31, pages 291–299, 2007. (Cited on pages xiii, 43, 47, 48 and 49.)

[Chen *et al.* 2007b] I.Y. Chen, C.C. Liu, K.H. Chien and C.C. Wang. *Two-phase flow characteristics across sudden expansion in small rectangular channel.* Exp. Thermal Fluid Sci., vol. 32, pages 696–706, 2007. (Cited on page 52.)

[Chen *et al.* 2008a] I. Y. Chen, M.-C. Chu, J.-S. Liaw and C.-C. Wang. *Two-phase flow characteristics across sudden contraction in small rectangular channels.* Exp. Thermal Fluid Sci., vol. 32, pages 1609–1619, 2008. (Cited on pages 56, 57 and 136.)

[Chen *et al.* 2008b] I. Y. Chen, Y.-S. Wu, J.-S. Liaw and C.-C. Wang. *Two-phase frictional pressure drop measurements in* U*-type wavy tubes subject to horizontal and vertical arrangements.* Appl. Thermal Eng., vol. 28, pages 847–855, 2008. (Cited on pages xiii, 42, 43, 47, 48 and 49.)

[Chen *et al.* 2009] I. Y. Chen, C.-Y. Tseng, Y.-T. Lin and C.-C. Wang. *Two-phase flow pressure change subject to sudden contraction in small rectangular channels.* Int. J. Multiphase Flow, vol. 35, pages 297–306, 2009. (Cited on pages 56, 57 and 136.)

[Cheng & Wu 2006] P. Cheng and H. Y. Wu. *Mesoscale and Microscale Phase-Change Heat Transfer.* Advances in Heat Transfer, vol. 39, pages 461–563, 2006. (Cited on page 22.)

[Chicchitti *et al.* 1960] A. Chicchitti, C. Lombardi, M. Silvestri, G. Soldaini and R. Zavattarelli. *Two-phase cooling experiments-pressure drop, heat transfer and burnout measurements.* Energia Nucleare, vol. 7, no. 6, pages 407–425, 1960. (Cited on page 34.)

[Chisholm 1968] D. Chisholm. *Prediction of pressure losses of changes of section, bends and throttling devices.* NEL Rep, vol. 388, 1968. (Cited on page 53.)

[Chisholm 1973a] D. Chisholm. *Pressure gradients due to friction during the flow of evaporating two-phase mixtures in smooth tubes and channels.* Int. J. Heat Mass Transfer, vol. 16, pages 347–348, 1973. (Cited on pages 35, 91 and 94.)

[Chisholm. 1973b] D. Chisholm. *Void fraction during two-phase flow.* J. Mechanical Engineering Science, vol. 15, pages 235–236, 1973. (Cited on page 41.)

[Chisholm 1983] D. Chisholm. Two-phase flow in pipelines and heat exchangers. George Godwin, London, 1983. p. 304. (Cited on pages 46, 47, 52, 53, 54, 114, 118, 136 and 140.)

[Collier & Thome 1994] J. G. Collier and J. R. Thome. Convective boiling and condensation, third edition. Oxford University Press, Oxford, 1994. (Cited on pages ix, 23, 25, 53, 57 and 136.)

[Dean 1927] W.R. Dean. *Note on the motion of fluid in curved pipe.* Phil. Mag., vol. 4, pages 208–223, 1927. (Cited on page 44.)

[Delhaye 1990] J. M. Delhaye. Two-phase flows and heat transfer in the process industries. Hemisphere, New York, 1990. (Cited on page 10.)

[Didion 1997] D.A. Didion. *Thinking Small.* HVAC&R Research, vol. 3(2), pages 99–100, 1997. (Cited on page 2.)

[Domanski & Hermes 2008] P. A. Domanski and C. J. L. Hermes. *An improved correlation for two-phase pressure drop of* R*-22 and* R*-410*A *in 180° return bends.* Appl. Thermal Eng., vol. 28, pages 793–800, 2008. (Cited on pages 47, 50, 52, 114, 115 and 118.)

[Ford & Loth 1997] B. Ford and E. Loth. *Forces on ellipsoidal bubbles in a turbulent shear layer.* Phys. Fluids, vol. 10, pages 178–188, 1997. (Cited on page 45.)

[Friedel 1979] L. Friedel. *Improved friction pressure drop correlations for horizontal and vertical two-phase pipe flow.* In European Two-Phase Flow Group Meeting, Ispra, Italy, 1979. (Cited on pages 36, 38, 50, 58, 91 and 94.)

[Geary 1975] D. F. Geary. *Return bend pressure drop in refrigeration systems.* ASHRAE Trans., vol. 81, pages 250–264, 1975. (Cited on pages ix, 42, 43, 46, 47 and 48.)

[Geiger 1964] G.E. Geiger. *Sudden contraction losses in single and two-phase flow.* PhD thesis, University of Pittsburgh, USA, 1964. (Cited on pages 53 and 56.)

[Gouse & Coumou 1965] S.W. Gouse and K.G. Coumou. *Heat transfer and fluid flow inside a horizontal tube evaporator, Phase I.* ASHRAE Trans., vol. 71(2), page 152, 1965. (Cited on page 22.)

[Greco & Vanoli 2006] A. Greco and G. P. Vanoli. *Experimental two-phase pressure gradients during evaporation of pure and mixed refrigerants in a smooth horizontal tube. Comparison with correlations.* Int. J. Heat Mass Transfer, vol. 42, pages 709–725, 2006. (Cited on page 31.)

[Grönnerud 1979] R. Grönnerud. *Investigation of liquid hold-up, flow-resistance and heat transfer in circulation type evaporators, Part iv: two-phase flow resistance in boiling refrigerants.* In Annexe 1972-1, Bull. de l'Inst. International du Froid, 1979. (Cited on pages 31, 37, 38, 50, 58, 91 and 94.)

[Guerrieri & Talty 1956] S.A. Guerrieri and R.D. Talty. *A study of heat transfer to organic liquids in single tube boilers.* J. Heat Transfer, vol. 52(18), page 69, 1956. (Cited on page 23.)

[Haberschill *et al.* 2003] P. Haberschill, C. Branescu and M. Lallemand. *Eurotherm Seminar No 72, Pressure drop of microfinned tubes during boiling of* R-22 *and* R-407C. In Heat and mass transfer of refrigeration machines and heat pumps, pages 75–79, Valencia (Spain), 31 March - 02 April, 2003. (Cited on page 31.)

[Hashizume 1983] K. Hashizume. *Flow pattern, void fraction and pressure drop of refrigerant two-phase flow in a horizontal pipe - I: Experimental data.* Int. J. Multiphase Flow, vol. 4(5), pages 399–410, 1983. (Cited on page 26.)

[Hoang & Davis 1984] K. Hoang and M. R. Davis. *Flow structure and pressure loss for two-phase flow in return bends.* Trans. ASME, vol. 106, pages 30–37, 1984. (Cited on pages 42 and 48.)

[Hout *et al.* 2002] R. Van Hout, D. Barnea and L. Shemer. *Translational velocities of elongated bubbles in continuous slug flow.* Int. J. Multiphase Flow, vol. 28, pages 1333–1350, 2002. (Cited on page 44.)

[Husain 1975] A. Husain. *Applicability of the homogeneous flow model to two-phase flow.* PhD thesis, Univ. Cincinnati, 1975. (Cited on page 53.)

[Idelshik 1986] I. E. Idelshik. Handbook of hydraulic resistance, second ed. Hemisphere, New York, 1986. p. 640. (Cited on pages 46, 47, 52, 114 and 118.)

[Ishii 1975] M. Ishii. Thermo-fluid dynamics theory of two-phase flow. Eyrolles, Paris, 1975. (Cited on page 10.)

[Janssen 1966] E. Janssen. *Two phase pressure loss across abrupt contractions and expansions, steam water at 600 to 1400 psia.* In Int. Heat Transfer Conf., pages 12–23, 1966. (Cited on page 53.)

[Jung & Radermacher 1989] D. S. Jung and R. Radermacher. *Prediction of pressure drop during horizontal annular flow boiling of pure and mixed refrigerants.* Int. J. Heat Mass Transfer, vol. 32, pages 2435–2446, 1989. (Cited on page 31.)

[Kattan *et al.* 1998a] N. Kattan, J. R. Thome and D. Favrat. *Flow boiling in horizontal tubes: Part 1-Development of a diabatic two-phase flow pattern map.* J. Heat Transfer, vol. 120, pages 140–147, 1998. (Cited on pages 26 and 58.)

[Kattan *et al.* 1998b] N. Kattan, J. R. Thome and D. Favrat. *Flow boiling in horizontal tubes: Part 2 - new heat transfer data for five refrigerants.* J. Heat Transfer, vol. 120, pages 148–155, 1998. (Cited on page 26.)

[Kattan *et al.* 1998c] N. Kattan, J. R. Thome and D. Favrat. *Flow boiling in horizontal tubes: Part 3 - development of a new heat transfer model based on flow pattern.* J. Heat Transfer, vol. 120, pages 156–165, 1998. (Cited on page 26.)

[Kays 1950] W. M. Kays. *Loss coeffients for abrupt drops in flow cross section with low* Reynolds *number flow in single and multiple-tube systems.* Trans. ASME, vol. 73, pages 1068–1074, 1950. (Cited on page 53.)

[Kuo & Wang 1996] C-S Kuo and C-C Wang. *Horizontal flow boiling of* R-22 *and* R-407C *in a 9.52 mm microfin tube.* Appl. Thermal Eng., vol. 16, pages 719–731, 1996. (Cited on page 31.)

[Lakshmanan *et al.* 2011] P. Lakshmanan, F. Peters, N. Fries and P. Ehrhard. *Gas bubbles in simulation and experiment.* Journal of Colloid and Interface Science, vol. 354, pages 364–372, 2011. (Cited on page 45.)

[Lockhart & Martinelli 1949] R. C. Lockhart and R. W. Martinelli. *Proposed correlation of data for isothermal two-phase, two component flow in pipes.* Chem. Eng. Process., vol. 45, pages 39–48, 1949. (Cited on pages 17, 32, 91 and 94.)

[Mauro *et al.* 2007] A. W. Mauro, J. Moreno Quiben, R. Mastrullo and J. R. Thome. *Comparison of experimental pressure drop data for two-phase flows to prediction methods using a general model.* Int. J. Refrig., vol. 30, pages 1358–1367, 2007. (Cited on page 31.)

[McGee 1966] J.W. McGee. *Two-phase flow through abrupt expansions and contractions.* PhD thesis, University of North Carolina at Raleigh, USA, 1966. (Cited on page 53.)

[McLinden *et al.* 2007] M.O McLinden, S.A Klein, E.W Lemmon and A.P Peskin. NIST standard reference database 23, NIST thermodynamic and transport properties of refrigerants and refrigerant mixture. National Institute of Standards and Technology, 2007. (Cited on pages 74 and 155.)

[Meng *et al.* 2009] M. Meng, X.F. Peng, P. Ye and Y.Y. Duan. *Bubble dynamical behavior and thermal non-equilibrium during flow boiling in U-turn bends of hairpin tubes.* Chem. Eng. Process., vol. 48, pages 1177–1186, 2009. (Cited on pages 44, 105, 108 and 109.)

[Midgley & Henne 1930] T. Midgley and A.C. Henne. *Organic fluorides as refrigerants.* Ind. Eng. Chem., vol. 22, pages 542–545, 1930. (Cited on page 1.)

[Müller-Steinhagen & Heck 1986] H. Müller-Steinhagen and K. Heck. *A simple friction pressure drop correlation for two-phase flow pipes.* Chem. Eng. Proceedings., vol. 20, pages 297–308, 1986. (Cited on pages ix, 31, 38, 47, 48, 50, 51, 58, 65, 90, 91, 94, 95 and 117.)

[Moffat 1988] R.J. Moffat. *Describing the uncertainties in experimental result.* Exp. Thermal Fluid Sci., vol. 1, pages 3–17, 1988. (Cited on page 75.)

[Moreno Quibén & Thome 2007] J. Moreno Quibén and J. R. Thome. *Flow pattern based two-phase frictional pressure drop model for horizontal tubes, Part* II*: New phenomenological model.* Int. J. Heat Fluid Flow, vol. 28, pages 1060–1072, 2007. (Cited on pages 4, 31, 38, 39, 40, 58, 65, 91 and 94.)

[Ohadi & Buckley 2001] M.M. Ohadi and S.G. Buckley. *High temperature heat exchangers and microscale combustion systems: applications to thermal system miniaturization.* Exp. Thermal Fluid Sci., vol. 25, pages 207–217, 2001. (Cited on page 2.)

[Ould Didi *et al.* 2002] M. B. Ould Didi, N. Kattan and J. R. Thome. *Prediction of two-phase pressure gradients of refrigerants in horizontal tubes.* Int. J. Refrig., vol. 25, pages 935–947, 2002. (Cited on page 31.)

[Padilla *et al.* 2009] M. Padilla, R. Revellin and J. Bonjour. *Prediction and simulation of two-phase pressure drop in return bends.* Int. J. Refrig., vol. 32, pages 1776–1783, 2009. (Cited on pages ix, 47, 48, 50, 51, 52, 58, 97, 112, 114, 116 and 118.)

[Padilla *et al.* 2011a] M. Padilla, R. Revellin, P. Haberschill, A. Bensafi and J. Bonjour. *Flow regimes and two-phase pressure gradient in horizontal straight tubes: Experimental results for* HFO*1234*yf*,* R*134*a *and* R*410*A. Exp. Thermal Fluid Sci., vol. 35, pages 1113–1126, 2011. (Cited on pages ix, x, 31, 63, 82, 84, 85, 86, 88, 89, 90, 91, 92, 94, 99, 109 and 127.)

[Padilla *et al.* 2011b] M. Padilla, R. Revellin, P. Haberschill and J. Bonjour. *Two-phase pressure drop in return bends: Experimental results for* R*410*A. Int. J. Refrig., vol. doi:10.1016/j.ijrefrig.2011.03.009, 2011. (Cited on pages ix, 42, 45, 65, 66, 109 and 110.)

[Padilla *et al.* 2012a] M. Padilla, R. Revellin and J. Bonjour. *Flow regime visualization and pressure drops of* HFO-*1234*yf*,* R-*134*a *and* R-*410*A *during downward two-phase flow in vertical return bends.* Exp. Thermal Fluid Sci., 2012. in review. (Cited on page 110.)

[Padilla *et al.* 2012b] M. Padilla, R. Revellin and J. Bonjour. *Two-phase flow of* HFO-*1234yf,* R-*134a and* R-*410*A *in sudden contractions Part* II*: pressure drop measurements and new prediction method.* Int. J. Heat Fluid Flow, 2012. in review. (Cited on page 134.)

[Padilla *et al.* 2012c] M. Padilla, R. Revellin and J. Bonjour. *Two-phase flow visualization and pressure drop measurements of* HFO-*1234*yf *and* R-*134*a *refrigerants in horizontal return bends.* Exp. Thermal Fluid Sci., 2012. in review. (Cited on page 110.)

[Park & Hrnjak 2007] C. Y. Park and P. S. Hrnjak. CO_2 *and* R-401A *flow boiling heat transfer, pressure drop and flow pattern at low temperatures in a horizontal smooth tube.* Int. J. Refrig., vol. 30, pages 166–178, 2007. (Cited on page 31.)

[Peebles & Garber 1953] F.N. Peebles and H.J. Garber. *Studies on the motion of gas bubbles in liquids.* Chem. Eng. Prog., vol. 49, pages 88–97, 1953. (Cited on page 45.)

[Pierre 1964] B. Pierre. *Flow resistance with boiling refrigerants*-P*art* II *Flow resistance in return bends.* ASHRAE J., pages 73–77, 1964. (Cited on pages 42, 46 and 47.)

[Quibén 2005] J. Moreno Quibén. *Experimental and analytical study of two-phase pressure drops during evaporation in horizontal tubes.* PhD thesis, Ecole polytechnique Fédérale de Lausanne, 2005. http://library.epfl.ch/en/theses/?nr=3337. (Cited on pages ix, 27 and 28.)

[Revellin & Haberschill 2009] R. Revellin and P. Haberschill. *Prediction of frictional pressure drop during flow boiling of refrigerants in horizontal tubes: Comparison to an experimental database.* Int. J. Refrig., vol. 32, pages 487 – 497, 2009. (Cited on pages 39, 40, 48, 50, 58, 90, 91 and 94.)

[Revellin *et al.* 2009a] R. Revellin, A. Bensafi, P. Haberschill and J. Bonjour. *Establishing research priorities on pressure drops during flow boiling of fluorinated refrigerants from a literature survey and a statistical approach.* Bulletin IIR, vol. 5, pages 2–15, 2009. (Cited on pages ix, 29 and 30.)

[Revellin *et al.* 2009b] R. Revellin, S. Lips, S. Khandekar and J. Bonjour. *Local entropy generation for saturated two-phase flow.* Energy, vol. 34(9), pages 1113 – 1121, 2009. (Cited on page 16.)

[Richardson 1958] B. L. Richardson. *Some problems in horizontal two-phase two-component flow.* PhD thesis, Univ. Chicago., 1958. (Cited on page 53.)

[Roitberg *et al.* 2008] E. Roitberg, L. Shemer and D. Barnea. *Hydrodynamic characteristics of gas-liquid slug flow in a downward inclined pipe.* Chemical Engineering Science, vol. 63, pages 3605–3613, 2008. (Cited on pages 32, 44 and 107.)

[Rouhani & Axelsson 1970] S. Z. Rouhani and E. Axelsson. *Calculation of volume void fraction in subcooled and quality region.* Int. J. Heat Mass Transfer, vol. 13, pages 383–393, 1970. (Cited on pages 28, 39, 41, 58, 99, 127 and 139.)

[Rowland & Molina 1974] F. Rowland and M. Molina. *Stratospheric sink for chlorofluoromethanes: Chlorine atom catalyzed destruction of ozone.* Nature, vol. 249, pages 810–812, 1974. (Cited on page 1.)

[Schiller & Naumann 1933] L. Schiller and Z. Naumann. *A drag coefficient correlation.* Z. Ver. Deutsch. Ing., vol. 77, pages 318–320, 1933. (Cited on page 45.)

[Schmidt & Friedel 1997] J. Schmidt and L. Friedel. *Two-phase pressure drop across sudden contractions in duct areas.* Int. J. Multiphase Flow, vol. 23, pages 283–299, 1997. (Cited on pages 53, 54, 55, 57 and 136.)

[Shew *et al.* 2006] W.L. Shew, S. Poncet and J.F Pinton. *Force measurements on rising bubbles.* J. Fluid Mech., vol. 569, pages 51–60, 2006. (Cited on page 45.)

[Siedel *et al.* 2011] S. Siedel, S. Cioulachtjian, A.J. Robinson and J. Bonjour. *Electric field effects during nucleate boiling from an artificial nucleation site.* Exp. Thermal Fluid Sci., vol. 35, pages 762–771, 2011. (Cited on page 45.)

[Silva-Lima & Thome 2010] R.J. Silva-Lima and J.R. Thome. *Two-phase pressure drops in adiabatic horizontal circular smooth U-bends and contiguous straight pipes.* HVAC & R Research, vol. 16(3), pages 383–397, 2010. (Cited on page 42.)

[Steiner 1993] D. Steiner. Verein Deutscher Ingenieure VDI- Wärmeatlas (VDI Heat Atlas), chapter HBB, VDI- Gesellshaft Verfahrenstechnik und Chemieingenieurwesen. Düsseldorf, 1993. (Cited on pages 26, 28, 39, 41, 127 and 139.)

[Stokes 1851] G. Stokes. Cambridge Philos. Soc. Trans., vol. 9, pages 8–106, 1851. (Cited on page 45.)

[Sun *et al.* 2004] X. Sun, S. Paranjape, S. Kim, B. Ozar and M. Ishii. *Liquid velocity in upward and downward air-water flows.* Annals of Nuclear Energy, vol. 31, no. 4, pages 357–373, 2004. (Cited on page 44.)

[Taitel & Dukler 1976] Y. Taitel and A. E. Dukler. *A model for predicting flow regime transitions in horizontal and near horiziontal gas-liquid flow.* AIChE Journal, vol. 22, no. 1, pages 47–55, 1976. (Cited on pages 25 and 41.)

[Thome 2004] J. R. Thome. Engineering data book iii. Wolverine Tube Inc., 2004. http://www.wlv.com/products/databook/db3/DataBookIII.pdf. (Cited on pages ix, 4, 25, 26, 34 and 50.)

[Traviss & Rohsenow 1973] D. P. Traviss and W. M. Rohsenow. *The influence of return bends on the downstream pressure drop and condensation heat transfer in tubes.* In ASHRAE Semiannual Meeting, 1973. (Cited on pages xiii, 42, 47, 48 and 49.)

[Ursenbacher *et al.* 2004] T. Ursenbacher, L. Wojtan and J.R. Thome. *Dynamic void fractions in stratified types of flow, part* I*: new optical measurement technique.* Int. J. Multiphase Flow, vol. 31, 2004. (Cited on page 41.)

[Usui 1980] K. Usui. *Flow behavior and pressure drop of two-phase flow through C-shaped bend in vertical plane (I). Upward flow.* J. Nucl. Sci. Technol., vol. 17, pages 875–887, 1980. (Cited on page 43.)

[Usui 1981] K. Usui. *Flow behavior and pressure drop of two-phase flow through C-shaped bend in vertical plane (II). Downward flow.* J. Nucl. Sci. Technol., vol. 18, pages 179–190, 1981. (Cited on page 43.)

[van der Geld 2009] C.W.M van der Geld. *The dynamics of a boiling bubble before and after detachement.* Int. J. Heat Mass Transfer, vol. 45, pages 831–846, 2009. (Cited on page 108.)

[Wallet *et al.* 2012] J. Wallet, M. Padilla, J. Bonjour and R. Revellin. *Two-phase flow of* HFO*-1234yf,* R*-134a and* R*-410*A *in sudden contractions Part* I*: Visualisation and void fraction measurements.* Int. J. Heat Fluid Flow, 2012. in review. (Cited on page 147.)

[Wang & Chiang 1997] C. Wang and C. Chiang. *Two-phase heat transfer characteristics for* R-22/R-407C *in a 6.5 mm smooth tube.* Int. J. Heat Fluid Flow, vol. 18, pages 550–558, 1997. (Cited on page 31.)

[Wang *et al.* 2003] C.-C. Wang, I. Y. Chen and H.-J. Shyu. *Frictional performance of* R-*22 and* R*-410*A *inside a 5.0 mm wavy diameter tube.* Int. J. Heat Mass Transfer, vol. 46, pages 755–760, 2003. (Cited on pages 44 and 47.)

[Wang *et al.* 2005] C.-C. Wang, I. Y. Chen, P.-S. Huang and B.-C. Yang. *Visual observations of air-water two-phase flow across small diameter tubes with vertical return bends.* Can. J. Chem. Eng., vol. 83, pages 548–553, 2005. (Cited on page 44.)

[Wang *et al.* 2008] C.C. Wang, I. Y. Chen and Y.J. Chang. *A visual observation of the air-water two-phase flow in small diameter tubes subject to the influence of vertical return bends.* Chem. Eng. Res. Des., vol. 86, pages 1223–1235, 2008. (Cited on page 44.)

[Wilcoxon 1950] F. Wilcoxon. *Some rapid approximate statistical procedures.* Annals of the New York Academy of Sciences, vol. 52, no. 6, pages 808–814, 1950. (Cited on pages 110 and 133.)

[Wojtan *et al.* 2004] L. Wojtan, T. Ursenbacher and J.R. Thome. *Dynamic void fractions in stratified types of flow, part* II*: measurements for* R*-22 and* R*-410a.* Int. J. Multiphase Flow, vol. 31, 2004. (Cited on page 41.)

[Wojtan *et al.* 2005a] L. Wojtan, T. Ursenbacher and J. R. Thome. *Investigation of flow boiling in horizontal tubes: Part* I *- A new diabatic two-phase flow pattern map.* Int. J. Heat Mass Transfer, vol. 48, pages 2955–2969, 2005. (Cited on pages ix, x, 26, 27, 39, 58, 83, 84, 87, 88, 90, 95, 100, 111, 112, 135 and 146.)

[Wojtan *et al.* 2005b] L. Wojtan, T. Ursenbacher and J.R. Thome. *Measurement of dynamic void fractions in stratified types of flow.* Experimental Thermal and Fluid Science, vol. 29, pages 383–392, 2005. (Cited on page 41.)

[Wongsa-ngam *et al.* 2004] J. Wongsa-ngam, T. Nualboonrueng and S. Wongwises. *Performance of smooth and micro-fin tubes in high mass flux region of* R-134*a during evaporation.* Heat Mass Transfer, vol. 40, pages 425–435, 2004. (Cited on page 31.)

[Yeh & Yang 1968] H.C. Yeh and W.J. Yang. *Dynamics of bubbles moving in liquids with pressure gradients.* J. appl. phys., vol. 39, no. 7, pages 3156–3165, 1968. (Cited on page 44.)

[Zivi 1964] S. M. Zivi. *Estimation of steady-state steam void fraction by means of the principle of minimum entropy production.* J. Heat transfer, vol. 86, pages 247–252, 1964. (Cited on pages 41, 55 and 56.)

[Zuber & Findlay 1965] N. Zuber and J. A. Findlay. *Average volumetric concentration in two-phase flow systems.* J. Heat Transfer, vol. 87, pages 463–458, 1965. (Cited on page 41.)